Advancements in dynamic light scattering optical coherence tomography particle sizing and flowmetry

Cheishvili, K.

DOI
10.4233/uuid:8c16ece0-9169-4451-a92a-395643a1eaae

Publication date
2025

Document Version
Final published version

Citation (APA)
Cheishvili, K. (2025). *Advancements in dynamic light scattering optical coherence tomography particle sizing and flowmetry*. [Dissertation (TU Delft), Delft University of Technology]. https://doi.org/10.4233/uuid:8c16ece0-9169-4451-a92a-395643a1eaae

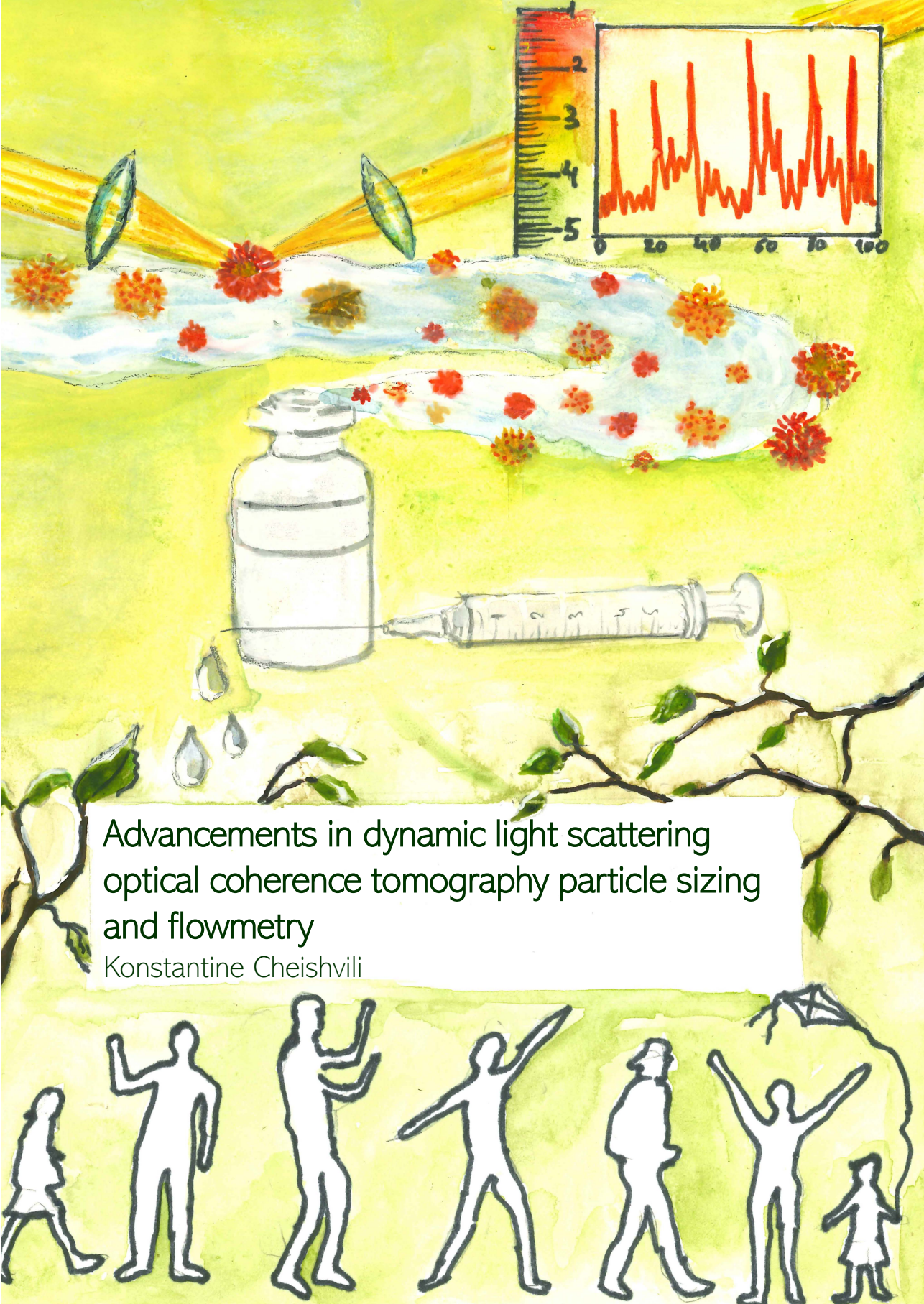

Advancements in dynamic light scattering optical coherence tomography particle sizing and flowmetry

Konstantine Cheishvili

Advancements in dynamic light scattering optical coherence tomography particle sizing and flowmetry

Advancements in dynamic light scattering optical coherence tomography particle sizing and flowmetry

Dissertation

for the purpose of obtaining the degree of doctor
at Delft University of Technology,
by the authority of the Rector Magnificus, prof. dr. ir. T.H.J.J. van der Hagen,
chair of the Board for Doctorates
to be defended publicly on Monday 20, January 2025 at 17.30 o'clock

by

Konstantine CHEISHVILI

Master of Science in Aerospace Engineering,
Delft University of Technology, Delft, The Netherlands
born in Tbilisi, Georgia.

This dissertation has been approved by the promotors.

Composition of the doctoral committee:

Rector Magnificus,	chairperson
Prof. dr. B. Rieger,	Delft University of Technology, promotor
Dr. J. Kalkman,	Delft University of Technology, promotor
Independent members:	
Prof. dr. ir. C. Poelma,	Delft University of Technology
Prof. dr. T.G. van Leeuwen,	Amsterdam UMC
Prof. dr. R. Cerbino,	Vienna University, Austria
Prof. dr. R.M. Robertson Anderson,	University of San Diego, USA
Prof. dr. S. Stallinga,	Delft University of Technology, reserve member

This work is part of the research programme NanoRheoOCT with project number 17988, which is partly financed by the Dutch Research Council (NWO).

The book cover, hand-painted by my wife, uniquely captures the essence of years of hard work and scientific discovery—often unseen yet profoundly impactful. The image of particles measured in a suspension symbolizes small-scale research, although often overlooked, driving major advancements, such as innovations in pharmaceutical production. The picture portrays people pursuing their passions and dreams. While individual contributions may not always be visible, they serve a greater purpose: helping others move forward and chase their dreams. This collective effort reflects a shared goal—that together, we can make the world a better place.

Printed by Ipskamp Printing

ISBN 978-94-6366-995-5

An electronic version of this dissertation is available at
http://repository.tudelft.nl/.

Contents

Summary ix

Samenvatting xi

1 Introduction 1
- 1.1 Process industry and quality control . . . 2
- 1.2 Particle suspensions . . . 2
  - 1.2.1 Soft matter rheology . . . 3
- 1.3 In-line nanoparticle sizing . . . 4
- 1.4 Particle sizing methods . . . 4
  - 1.4.1 Non-optical methods . . . 4
  - 1.4.2 Optical methods . . . 6
- 1.5 Optical coherence tomography . . . 13
  - 1.5.1 Doppler OCT . . . 15
  - 1.5.2 Dynamic light scattering OCT . . . 16
- 1.6 Thesis outline . . . 17
- References . . . 18

2 Wavenumber-dependent dynamic light scattering optical coherence tomography measurements of collective and self-diffusion 23
- 2.1 Introduction . . . 24
- 2.2 Theory . . . 25
  - 2.2.1 Particle diffusion . . . 25
  - 2.2.2 Particle polydispersity . . . 29
- 2.3 Methods . . . 32
  - 2.3.1 OCT systems . . . 32
  - 2.3.2 Particle suspensions . . . 33
  - 2.3.3 Diffusion measurements in dilute suspensions . . . 35
  - 2.3.4 Diffusion measurements in concentrated suspensions . . . 35
- 2.4 Results . . . 36
  - 2.4.1 Kostrosöl 10050 and Levasil CS50-28 measurements . . . 37
  - 2.4.2 Kostrosöl 8050 and 9550 measurements . . . 38
- 2.5 Discussion . . . 40
  - 2.5.1 Particle sizing . . . 41
  - 2.5.2 Polydispersity measurement . . . 43
- 2.6 Conclusion . . . 43
- 2.7 Acknowledgments . . . 44
- References . . . 44

3 Scanning dynamic light scattering optical coherence tomography for measurement of high omnidirectional flow velocities 51
3.1 Introduction . . . 52
3.2 Theory . . . 52
3.2.1 Sample geometry . . . 52
3.2.2 M-scan Doppler OCT . . . 53
3.2.3 B-scan Doppler OCT . . . 54
3.2.4 M-scan DLS-OCT . . . 54
3.2.5 B-scan DLS-OCT . . . 55
3.3 Materials and Methods . . . 56
3.3.1 OCT system . . . 56
3.3.2 Flow system . . . 57
3.3.3 M-scan OCT flow measurements . . . 58
3.3.4 B-scan OCT flow measurements . . . 59
3.4 Experimental results . . . 62
3.4.1 Flow measurements under ideal scanning alignment . . . 62
3.4.2 Omnidirectional flow measurements . . . 65
3.5 Discussion . . . 66
3.6 Conclusion . . . 69
References . . . 69

4 Sub-diffusion flow velocimetry with number fluctuation optical coherence tomography 73
4.1 Introduction . . . 74
4.2 Theory . . . 74
4.2.1 Doppler OCT . . . 75
4.2.2 Non-dilute DLS-OCT . . . 76
4.2.3 Number fluctuation DLS-OCT . . . 79
4.2.4 Flow speed sensitivity analysis . . . 81
4.2.5 Number fluctuation particle concentration estimation . . . 82
4.3 Materials and Methods . . . 83
4.3.1 OCT system . . . 83
4.3.2 Flow system . . . 83
4.3.3 Doppler OCT flow measurements . . . 84
4.3.4 Number fluctuation DLS-OCT flow measurements . . . 85
4.4 Experimental results . . . 87
4.5 Discussion . . . 91
4.6 Conclusion . . . 94
References . . . 94

5 Multi-modal optical coherence tomography flowmetry of organ-on-chip devices 97
5.1 Introduction . . . 98
5.2 Methods . . . 99
5.2.1 OCT structural imaging . . . 99
5.2.2 OCT flow measurements . . . 100

5.2.3 Doppler OCT measurements . . . 102
5.2.4 Organ-on-chip samples . . . 102
5.2.5 Computational fluid dynamics simulations . . . 103
5.3 Results . . . 104
5.3.1 Flow in a single channel OoC system . . . 104
5.3.2 Flow in the OoC well . . . 105
5.4 Discussion . . . 107
5.5 Acknowledgments . . . 108
References . . . 109

6 Precision and bias in dynamic light scattering optical coherence tomography measurements of diffusion and flow 111
6.1 Introduction . . . 112
6.2 Theory . . . 112
6.2.1 Correlation functions for particle diffusion . . . 112
6.2.2 Correlation functions for particle flow . . . 113
6.2.3 Precision of diffusion and flow estimation . . . 115
6.2.4 Bias of diffusion and flow estimation . . . 118
6.3 OCT signal simulations for flow and diffusion . . . 120
6.3.1 Simulation of diffusion . . . 120
6.3.2 Simulation of flow . . . 121
6.4 Materials and Methods . . . 122
6.4.1 OCT system . . . 122
6.4.2 Averaging strategies . . . 122
6.4.3 Diffusion measurements . . . 124
6.4.4 Flow measurements . . . 125
6.5 Results . . . 126
6.5.1 DLS-OCT diffusion measurement . . . 126
6.5.2 Non-dilute DLS-OCT flow measurement . . . 132
6.5.3 Dilute DLS-OCT flow measurement . . . 134
6.6 Discussion . . . 135
6.6.1 DLS-OCT diffusion estimation . . . 135
6.6.2 DLS-OCT flow estimation . . . 136
6.7 Conclusion . . . 137
References . . . 138

7 Measuring particle diffusion in multiple scattering media using dynamic light scattering optical coherence tomography 141
7.1 Introduction . . . 142
7.2 Theory . . . 142
7.2.1 DLS-OCT in the multiple scattering regime . . . 142
7.2.2 Intensity attenuation . . . 144

7.3 Simulations . . . 145
7.4 Materials and Methods . . . 147
7.4.1 OCT system . . . 147
7.4.2 Particle suspensions . . . 147
7.4.3 Calibration measurements . . . 148
7.4.4 Diffusion measurements . . . 149
7.4.5 Attenuation measurements . . . 150
7.5 Results . . . 150
7.6 Discussion . . . 153
7.7 Conclusion . . . 155
References . . . 155

8 Summary and outlook **159**
8.1 Summary . . . 160
8.2 Outlook on particle sizing . . . 162
8.2.1 Particle sizing in flowing suspensions . . . 162
8.2.2 Particle sizing using Doppler OCT . . . 165
8.2.3 Particle sizing in the multiple scattering regime . . . 168
8.2.4 Particle sizing using q-dependent DLS-OCT . . . 171
8.3 Outlook on number-fluctuation DLS-OCT . . . 173
8.3.1 Improving 2D flow imaging with faster B-scan rates . . . 173
8.3.2 Beam shape characterization in scattering media . . . 174
8.3.3 Effects of particle size polydispersity . . . 175
References . . . 176

Acknowledgements **179**

Curriculum Vitæ **181**

List of Publications **183**

Summary

This thesis explores the application of dynamic light scattering optical coherence tomography (DLS-OCT) for in-line particle sizing and flow measurements in particle suspensions. DLS-OCT is capable of measuring the depth-resolved particle diffusion coefficient, which can then be converted into particle size. This capability is particularly advantageous for in-line particle sizing scenarios, where the suspension is under flow, and the depth-resolved particle diffusion coefficient can be separated from the flow contribution. However, there are several other challenges associated with DLS-OCT, such as measuring: at high particle concentrations, in fast and slow flows, in multiple scattering media, and quantifying the measurement uncertainty. These challenges are addressed in this thesis.

In concentrated suspensions, the relationship between particle size and the diffusion coefficient is not well described by the simple Stokes-Einstein equation and the diffusion becomes dependent on multiple factors. Accurate determination of particle size necessitates diffusion coefficient measurements across a wide range of wavenumbers and the application of sophisticated rheological models. In Chapter 2, we address this issue with a broadband DLS-OCT system covering the wavelength range of 350–1000 nm. By inverting hard-sphere rheological models, we successfully measured the particle size and polydispersity in very dense nanoparticle suspensions. Furthermore, we demonstrated the applicability to particle sizing in suspensions that are not suitable for standard DLS-OCT measurements and showed how measurements of different diffusion modes can assess the number-based particle size polydispersity in concentrated suspensions.

DLS-OCT measurement of high flow speeds and small particle sizes in fast-flowing suspensions is problematic due to detector sampling limitations, as the rapid decay of the autocorrelation function prevents the extraction of flow speed and particle size information. To address this, in Chapter 3, we showed the incorporation of beam scanning—a standard feature in many OCT systems—to extend the capabilities of DLS-OCT flow imaging beyond its current limitations and improve particle sizing in flowing suspensions. This approach allowed us to demonstrate a two-fold improvement in the flow velocity dynamic measurement range and more accurate particle size measurement deeper within the flow channel, away from the edges. These advancements are beneficial for in-line pharmaceutical and process industry particle sizing applications, where diffusion and mixing near the edges are slower, leading to overestimation of particle size.

Particle Brownian motion imposes limitations on the minimum flow speeds measurable in particle suspensions using DLS-OCT. In Chapter 4, we address this challenge by introducing the concept of number fluctuations to DLS-OCT. This innovation enabled the successful measurement of sub-diffusion flow speeds and particle concentrations in dilute particle suspensions, both in 1D and 2D. By extending the

capability of DLS-OCT, this development also facilitates the measurement of the beam shape within the particle suspension, a task traditionally requiring complex calibration in conventional OCT systems.

In Chapter 5, we demonstrate the application of number-fluctuation DLS-OCT for measuring simultaneous 2D flow profiles in organ-on-chip (OoC) devices, overcoming limitations of conventional Doppler OCT and DLS-OCT in low-flow environments. A numerical method was employed to equalize axial and transverse OCT resolutions, eliminating the dependence on Doppler angles in the autocorrelation function and enabling accurate measurement of absolute flow velocities. Additionally, we implemented particle image velocimetry (PIV) on the OCT data to complement number-fluctuation measurements with precise in-plane velocity vector maps. This chapter underscores the effectiveness of number-fluctuation DLS-OCT in biomedical imaging, particularly for measuring extremely small flow speeds and addressing flow direction variability within OoC devices.

The lack of readily available theoretical models for estimating the uncertainty in DLS-OCT measurements of diffusion and flow is a challenge addressed in Chapter 6. We conducted a detailed assessment of precision and bias in DLS-OCT measurements, revealing that errors in autocorrelation coefficients are strongly correlated over time, which complicates accurate quantification of uncertainty in particle size and flow speed measurements. To address this challenge, we introduced a novel method of mixing different autocorrelation functions at the same time delay. This approach effectively eliminates error correlations and enables us to achieve precision levels approaching the Cramer-Rao lower bound. This advancement allows for reliable quantification of particle size and flow speed uncertainties using DLS-OCT, which is crucial for applications in the process industry where maximizing precision is essential.

Multiple scattering in DLS-OCT complicates accurate particle sizing as the models assume single backscattering. In Chapter 7, we propose a simple method to simulate multiple scattering effects on particles undergoing Brownian motion. Through simulations and experimental measurements, we demonstrated that the autocorrelation functions exhibit double-exponential decay in the multiple scattering regime. We employed a double-exponential autocorrelation fit model for all depths, significantly enhancing both the depth range of reliable particle sizing using the single-scattering model. In addition, we can perform particle sizing in the diffusing-wave spectroscopy (DWS) limit of the decorrelation rate.

The final Chapter 8 summarizes the key contributions of this thesis to particle sizing and flow measurements using DLS-OCT. It also discusses potential future research directions aimed at improving the accuracy and expanding the applicability of DLS-OCT across various sectors of the process industry.

Samenvatting

Dit proefschrift beschrijft het onderzoek naar de toepassing van dynamische lichtverstrooiing optische coherentie tomografie (DLS-OCT) voor het bepalen van de deeltjesgrootte en stroomsnelheid in stromende deeltjesoplossingen. DLS-OCT meet de diepte-afhankelijke deeltjesdiffusiecoëfficiënt, die vervolgens kan worden omgezet in deeltjesgrootte. Deze mogelijkheid is bijzonder voordelig voor het in een stroming bepalen van de deeltjesgrootte, waarbij de oplossing in beweging is en de diepte-afhankelijke deeltjesdiffusiecoëfficiënt van de stromingsbijdrage kan worden gescheiden. Echter, er zijn verschillende uitdagingen verbonden aan DLS-OCT, zoals metingen bij hoge deeltjesconcentraties, in snelle en langzame stromingen, in meervoudig verstrooiendemedia, en het kwantificeren van de meetonzekerheid, die in dit proefschift worden geaddresseerd.

In geconcentreerde oplossingen wordt de relatie tussen deeltjesgrootte en de diffusiecoëfficiënt niet goed beschreven door de eenvoudige Stokes-Einstein vergelijking en wordt de diffusiecoëfficient afhankelijk van meerdere factoren. Nauwkeurige bepaling van de deeltjesgrootte vereist diffusiecoëfficiëntmetingen over een breed scala aan golfgetallen en de toepassing van geavanceerde reologische modellen. In Hoofdstuk 2 behandelen we dit probleem door het gebruik van een breedband DLS-OCT systeem dat het golflengtebereik van 350–1000 nm bestrijkt. Door harde-bollen reologische modellen te inverteren, hebben we met succes de deeltjesgrootte en polydispersiteit gemeten in zeer dichte nanodeeltjesoplossingen. Bovendien toonden we de toepasbaarheid voor deeltjesgroottebepaling in oplossingen die niet geschikt zijn voor standaard DLS-OCT metingen en lieten we zien hoe metingen van verschillende diffusiekanalen de op aantal gebaseerde deeltjesgroottepolydispersiteit in geconcentreerde oplossingen kunnen bepalen.

DLS-OCT meting van hoge stroomsnelheden en kleine deeltjesgroottes in snelstromende oplossingen is problematisch vanwege beperkingen van de detectorbemonstering, aangezien het snelle verval van de autocorrelatiefunctie de extractie van stroomsnelheid en deeltjesgrootte-informatie verhindert. Om dit aan te pakken, hebben we in Hoofdstuk 3 laten zien dat de opname van bundelscannen—een standaardfunctie in veel OCT-systemen—de mogelijkheden van DLS-OCT stromingsbeeldvorming uitbreidt en de huidige beperkingen bij deeltjesgroottebepaling in stromende oplossingen wegneemt. Deze aanpak stelde ons in staat het dynamische meetbereik van de stroomsnelheidmeting te verdubbelen en nauwkeurigere deeltjesgroottemetingen uit te voeren dieper in het stroomkanaal weg van de randen. Deze verbeteringen zijn gunstig voor farmaceutische en procesindustrie deeltjesgroottebepaling in stromende vloeistoffen, waar diffusie en vloeistofmenging nabij de randen trager zijn, wat kan leiden tot een overschatting van de deeltjesgrootte.

De Brownse beweging van deeltjes legt beperkingen op aan de minimale stroomsnelheden meetbaar in deeltjesoplossingen met behulp van DLS-OCT. In Hoofdstuk 4 hebben we deze uitdaging aangepakt door het concept van getalfluctuaties in DLS-OCT te introduceren. Deze innovatie maakte succesvolle meting mogelijk van subdiffusie stroomsnelheden en deeltjesconcentraties in verdunde oplossingen, zowel in 1D als 2D. Deze techniek faciliteert ook de meting van de bundelvorm binnen de deeltjesoplossing, een taak die traditioneel complexe kalibratie vereist in OCT-systemen.

In Hoofdstuk 5 demonstreren we de toepassing van getalfluctuatie DLS-OCT voor het meten van gelijktijdige 2D stromingsprofielen in organ-on-chip (OoC) apparaten, waarmee de beperkingen van conventionele Doppler OCT en DLS-OCT in omgevingen met lage stroomsnelheid worden weggenomen. Hierbij gebruikten we een numerieke methode om de axiale en transversale OCT resoluties gelijk te maken, waardoor de afhankelijkheid van de stromingsbepaling op de Dopplerhoek in de autocorrelatiefunctie werd geëlimineerd en nauwkeurige meting van absolute stroomsnelheden mogelijk werd. Bovendien implementeerden we deeltjesbeeldsnelheidsmeting (PIV) op OCT-beelden om de absolute snelheid zoals verkregen door getalfluctuatiemetingen aan te vullen met nauwkeurige in het vlak snelheidsvectorafbeeldingen. Dit hoofdstuk onderstreept de effectiviteit van getalfluctuatie DLS-OCT in biomedische beeldvorming, met name voor het meten van extreem lage stroomsnelheden en variabiliteit in stroomrichting binnen OoC-apparaten aan te pakken.

Het gebrek aan eenvoudige theoretische modellen voor het schatten van de onzekerheid in DLS-OCT metingen van diffusie en stroom is een uitdaging die wordt aangepakt in Hoofdstuk 6. We voerden een gedetailleerde analyse uit van precisie en bias in DLS-OCT metingen, waarbij we ontdekten dat fouten in de autocorrelatiecoëfficiënt sterk gecorreleerd zijn in de tijd, wat een nauwkeurige kwantificering van onzekerheid in deeltjesgrootte- en stroomsnelheidsmetingen bemoeilijkt. Om dit op te lossen introduceerden we een nieuwe methode voor het mengen van verschillende autocorrelatiefuncties op dezelfde tijdsvertraging. Deze aanpak elimineert effectief foutencorrelaties en stelt ons in staat om precisieniveaus te bereiken die de Cramer-Rao ondergrens benaderen. Deze vooruitgang maakt betrouwbare kwantificering van deeltjesgrootte- en stroomsnelheids-onzekerheden mogelijk met behulp van DLS-OCT, wat cruciaal is voor toepassingen in de procesindustrie waar het maximaliseren van precisie essentieel is.

Meervoudige verstrooiing in DLS-OCT bemoeilijkt nauwkeurige deeltjesgroottebepaling omdat de modellen uitgaan van enkelvoudige terugverstrooiing. In Hoofdstuk 7 stellen we een eenvoudige methode voor om de effecten van meervoudige verstrooiing in DLS-OCT voor deeltjes die Brownse beweging ondergaan te simuleren. Simulaties en experimentele metingen tonen aan dat de autocorrelatiefuncties dubbel-exponentieel verval vertonen in het meervoudige verstrooiingsregime. Bij het gebruik een dubbel-exponentiële autocorrelatiefitmodel voor alle dieptes konden we het dieptebereik van betrouwbare deeltjesgroottebepaling met het enkelvoudige verstrooiingsmodel aanzienlijk vergroten. Ook kunnen we deeltjesgroottebepaling uitvoeren in de diffusieve golf spectroscopie (DWS) limiet van de decorre-

latiesnelheid.

Het laatste hoofdstuk 8 vat de belangrijkste bijdragen van dit proefschrift samen met betrekking tot deeltjesgroottebepaling en stromingsmetingen met behulp van DLS-OCT. Het bespreekt ook mogelijke toekomstige onderzoeksrichtingen die gericht zijn op het verbeteren van de nauwkeurigheid en het uitbreiden van de toepasbaarheid van DLS-OCT in verschillende sectoren van de procesindustrie.

1

Introduction

1

1.1. Process industry and quality control

The process industry, which involves the manufacture and processing of substances through various physical, chemical, or biological methods, is an important sector of the global economy. The process industry includes the chemical, pharmaceutical, oil and gas, and food and beverage manufacturing sectors. Each of these sectors makes goods that are essential to modern life and economic welfare. The pharmaceutical process industry is vital for public health as it develops and mass produces drugs, vaccines, and other healthcare products. The food and beverage process industry ensures the mass production of safe, nutritious, and affordable food to feed the world's population. In the oil and gas sector, the process industry fuels the global economy by providing high-quality energy carriers for transportation, heating, electricity, and industrial activities.

Quality control is of paramount importance to ensure the safety, consistency, and efficacy of manufactured products. It is also essential for optimizing processes and their efficiency to minimize waste and enhance product effectiveness. Quality control can be performed in two ways: in-line and offline. In-line quality control involves continuous monitoring and inspection of products during manufacturing, enabling immediate adjustments to the process. In contrast, offline quality control is conducted on batches of material taken from the production line or on the finished products after manufacturing, where the finished products undergo assessment to ensure they meet predefined standards. In-line quality control offers the advantage of real-time process adjustments, enhancing responsiveness and efficiency. However, offline quality control allows for a broader range of tests to be conducted on the product. Yet, in cases of nonconformity, the entire product batch may need to be discarded, generating high costs and necessitating a new start to the process.

1.2. Particle suspensions

Particles are integral components in the process industry used in a variety of forms such as suspensions, emulsions, powders, dusts, sprays, and foam. Particle suspensions refer to systems in which solid particles are dispersed in a liquid medium. These solid particles are typically insoluble and remain suspended throughout the fluid due to their Brownian and bulk motion. Nanoparticle suspensions, containing particles ranging in size from approximately 1–1000 nm, have garnered significant interest across many sectors of the process industry due to their distinct and advantageous properties [1, 2]. Nanoparticles are used in pharmaceuticals, healthcare products, food and beverages, mining processes, coatings, agricultural products, cement production, and protein engineering.

This growing interest in nanoparticle suspensions has opened up new possibilities for working with ultra-small-scale structures. Nanoparticles can be tailored to access sub-cellular structures and proteins, making them particularly useful in the medical, biological, chemical, and pharmaceutical industries. Key applications include fluorescent biological labels, drug and gene delivery systems, vaccine development, tissue engineering, phagokinetic studies, and pathogen detection [3]. In the pharmaceutical industry, nanoparticle suspensions are highly valued for their

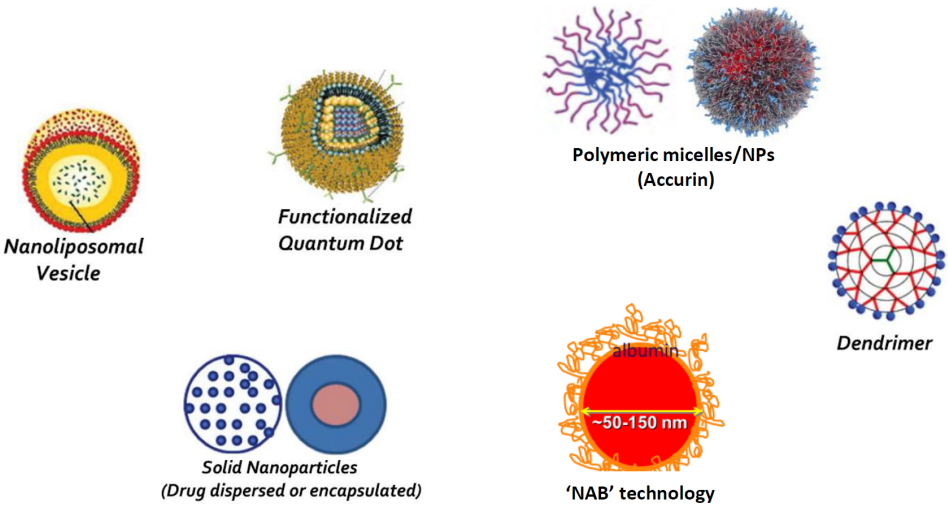

Figure 1.1: Commonly used nanoparticles in the pharmaceutical industry [4].

large surface area and small size, which make them excellent drug delivery systems [2]. They offer benefits such as improved drug solubility, extended drug release, and reduced degradation. Typical nanoparticles encountered in the pharmaceutical and medical industries are displayed in Fig. 1.1, where NPs denote nanoparticles. Nanoparticle albumin-bound (NAB) technology enhances drug delivery by binding therapeutic agents to albumin nanoparticles, thereby improving efficacy and safety. Functionalized quantum dots, dendrimers, polymeric micelles, and nonliposomal vesicles similarly enhance drug delivery by improving solubility, stability, and enabling precise targeting to specific cells. This enhances treatment efficacy and minimizes side effects.

1.2.1. Soft matter rheology

Soft matter comprises materials with properties between those of conventional solids and liquids, encompassing systems like particle suspensions. Soft matter rheology is the study of the flow and deformation of materials under applied forces. Since particle suspensions consist of solid particles dispersed in a liquid medium, their rheological behavior can be complex due to interactions between the particles and between the particles and the surrounding fluid. Key rheological parameters of particle suspensions include viscosity, particle size, particle polydispersity, particle concentration, interactions between the particles, as well as factors such as particle aggregation and sedimentation, flow, diffusion, and shear rate [5]. Understanding and controlling these rheological parameters is crucial for ensuring the quality and performance of nanoparticle suspensions. In pharmaceutical applications, nanoparticle size is critical as it directly influences the mobility of the particles and affects the efficiency of drug delivery systems. Moreover, for pharmaceuticals, particle size is strictly regulated and material costs are high [1, 6]. Therefore, accurate quantifi-

cation of particle sizes during manufacturing is an integral part of process control. Usually, particle size is determined offline with a small batch of material that can be measured over an extended period.

1.3. In-line nanoparticle sizing

In-line particle sizing is particularly significant for medical and pharmaceutical applications since they deal with flowing colloidal particle suspensions in the manufacturing process. Nanoparticle suspensions are often subjected to flow, mixing, or agitation during typical pharmaceutical processes, and in-line or in-process particle sizing is the direct and non-invasive measurement of particle size within the original particle environment. In-line particle sizing can be used for quality control and determination of rheological parameters during manufacturing. In-line particle sizing enables direct control of production processes within a constant feedback loop, significantly impacting product quality and cost. As the complexity of the suspension increases and the particle sizes decrease (e.g., through the use of nanoparticles, proteins), more advanced measurement methods are required.

For in-line particle sizing, suspension flow speed and concentration determine the measurement time and signal strength, respectively. They play a vital role in particle sizing accuracy, necessitating their quantification and effect on the measurement process [5]. At higher flow speeds, the accuracy of particle size measurement becomes lower as the measurement time decreases. At lower concentrations or in diluted particle suspensions, the amount of signal decreases, which also negatively affects the particle size measurement. On the other hand, the Brownian motion of particles sets the lower limit on the flow velocities that can be measured. Therefore, increasing the flow dynamic range, as well as the concentrations at which particle size can be measured, is crucial for in-line sizing applications. Additionally, the flow speed is directly related to the shear rate of the suspension [5], offering insights into additional rheological properties such as fluid-wall interactions, in-line refresh rate, and non-Newtonian behavior.

1.4. Particle sizing methods

In the broadest sense, particle sizing technologies can be divided into two domains: optical and non-optical methods. Here we focus on the most important techniques, emphasizing measurement methodologies rather than specific prototypes or devices. Not all methods are suitable for measuring moving particles and flow speeds, let alone for performing in-line sizing. For the optical techniques, dynamic light scattering optical coherence tomography (DLS-OCT), which is derived from dynamic light scattering (DLS), is the main focus of this thesis and is discussed in a separate chapter along with optical coherence tomography (OCT).

1.4.1. Non-optical methods

Non-optical methods encompass techniques for particle sizing that do not primarily rely on visible light scattering for analysis. In this context, electron microscopy and ultrasound are considered non-optical techniques.

The Coulter Principle, developed by Wallace H. Coulter in the 1940s, is a method for counting and sizing particles in electrolytes. As a particle passes through a small orifice, a volume of electrolyte solution is displaced causing a change in resistance, which results in the generation of a voltage pulse. The frequency of these pulses corresponds to the number of particles that traverse the opening, while the pulse amplitude is proportional to the particle's cross-section. Ensuring single-particle traversal is crucial to avoid pulse coincidence [7], necessitating low particle concentration (on the order of 0.1%) [8], and careful orifice diameter selection to maintain parallel entry angles. Although capable of swiftly measuring diameters from 0.2 to 1600 microns [9], in-line applications are limited due to reliance on aperture diameter and electrolyte solution.

Sedimentation size analysis quantifies particle sizes by measuring their settling rates in a liquid medium [10]. Two main methods, incremental and cumulative, are utilized. Incremental methods track changes in suspension concentration or density at known depths over time, while cumulative methods determine the rate at which particles settle out of suspension to derive size distribution. Gravitational sedimentation, which relies on steady-state particle velocity determined by gravitational, buoyant, and drag forces, is applicable to particles sized from 0.3 to 200 microns [10], albeit with longer measurement times for smaller particles. For particles with diameters below 0.3 microns, where Brownian motion is strong, centrifugal sedimentation is necessary, covering a size range from 0.02 to 10 microns. However, this method requires diluted samples and a high density contrast between the medium and particles, with the Reynolds number limit for sedimentation being approximately 0.25 and the suspension concentration ideally below 0.2% [10]. Measurement times vary from minutes to hours depending on particle sizes and concentration. While the original gravitational sedimentation technique is straightforward, incorporating centrifugal sedimentation increases complexity [8]. Despite advancements, practical limitations often confine sedimentation measurements to offline settings.

Ultrasound can also be used for particle sizing. Ultrasonic attenuation measurement utilizes the frequency dependence of ultrasonic velocity and/or attenuation coefficient in colloidal dispersions to obtain information about particle concentration and size distribution [11]. This technique provides sizing for particles with diameters ranging from 0.01 to 3000 microns at concentrations of 0.5-70%, with measurement times of 1-10 minutes [10]. Ultrasonic methods allow for in-line measurements, but the technique needs further development, especially for particle sizing in more concentrated emulsions. Additionally, data analysis and interpretation require knowledge of the thermophysical properties of particles and the medium, which may not always be readily available and can be challenging to obtain [11]. In addition to particle sizing, ultrasound techniques can be employed for flow measurements. The frequency of the ultrasound wave scattered from moving particles is Doppler shifted, directly related to the suspension flow speed. However, since particle sizing and flow determination require different data, simultaneous measurements are not feasible.

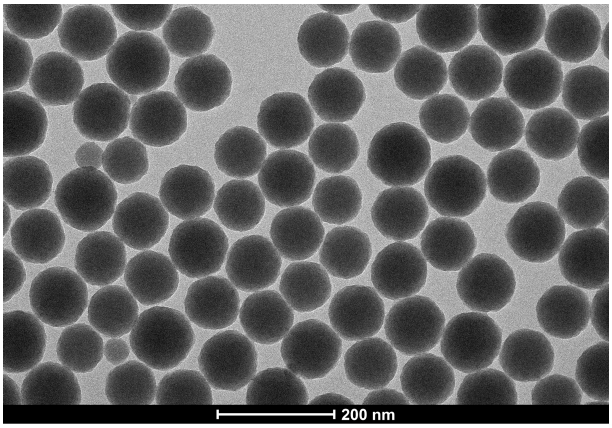

Figure 1.2: Transmission electron microscopy image of 50 nm radius silica particles.

Electron microscopy

Scanning or transmission electron microscopy (SEM or TEM) is used to measure particle sizes with resolutions of 15-20 nm for SEM and 0.3-0.5 nm for TEM [7]. However, these electron microscopy techniques necessitate thorough sample isolation, preparation, and subsequent image analysis, resulting in relatively long measurement times, typically about 1-60 minutes [10]. The particle number per image should be controlled to avoid particle overlap, as samples that are too concentrated may decrease the accuracy of particle sizing and localization. Electron microscopy methods are primarily suited for offline measurements. An example of a TEM image of 50 nm radius silica particles is given in Fig. 1.2.

1.4.2. Optical methods

The optical methods for particle sizing, whether with or without the presence of flow, encompass techniques that involve illuminating particles with visible light and collecting the scattered or transmitted light. These methods comprise both direct and indirect observation techniques. In direct observation methods, particles are directly imaged using a microscope. Indirect measurement methods rely on determining particle size through their static or dynamic scattering properties.

Optical microscopy & spectroscopy

Optical microscopy, such as widefield and confocal techniques, is one of the most common methods for visualizing small objects. Particle sizing using a microscope is usually done offline and involves sample separation, preparation, and image analysis after observing the objects. From a temporal perspective, measurements take some time, typically dozens of minutes. Direct particle observation techniques are diffraction-limited by the light wavelength, restricting measurements to objects larger than 0.3-0.5 microns. In-line sizing is not feasible since the measurements are performed offline after drying the particles. In such cases, the particle concentration must be low enough to allow separation between single particles.

Particles can be sized indirectly by measuring their mean-square displacement (MSD) using fluorescence microscopy [12]. This involves labeling particles with fluorophores, exciting them with a laser source, and capturing subsequent images at high temporal resolution. The particle MSD is determined from a sequence of these images. A subsequent fit of the MSD versus time is then related to the particle diffusion coefficient and size. While fluorescence microscopy allows in-line measurements, its applications are limited due to the necessity of fluorescent labels and restrictions on low concentration and flow speed.

Optical spectroscopic techniques, such as diffuse reflectance or transmission spectroscopy, can be used for particle sizing. These methods rely on measuring the scattering and/or absorption coefficients of particle suspensions as a function of wavelength to obtain information about the particle size distribution. In-line measurements are theoretically possible [13], but they require significant prior sample information and theoretical treatment.

Static light scattering

Static light scattering (SLS), also known as laser diffraction, relies on illuminating a particle suspension with light and collecting and analyzing time-averaged scattered light intensity. The light scattering from particles can be described by Rayleigh and/or Mie Scattering [14, 15]. When particles in a suspension are illuminated by a light source, they scatter light in all directions. The intensity of the scattered light depends on factors such as particle size, shape, refractive index, light wavelength, and polarization. Additionally, the scattered light intensity may vary with the scattering angle θ, which is the angle between the illumination beam and the direction of the scattered light collection. These parameters are often combined into a single quantity q, known as the scattering wavenumber, representing the difference between the illuminating and scattering wavevectors. Mie theory can be used to analyze scattering phenomena for various particle sizes and q values.

In a typical SLS measurement setup, as shown in Fig. 1.3, a particle suspension is illuminated using a laser beam, and the time-averaged scattered intensity is collected at different scattering angles θ. This can be achieved by moving the detector (which prolongs measurements) or by using multiple detectors at different

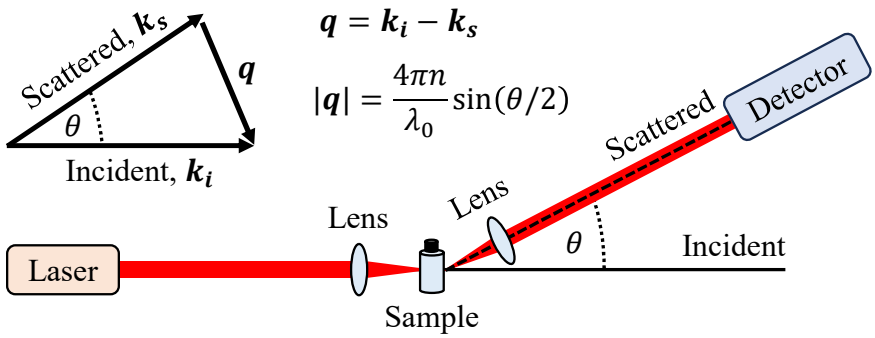

Figure 1.3: Typical measurement setup for static and dynamic light scattering experiments.

angles with respect to the source and illumination volume. Incident, scattered, and scattering wavevectors are denoted by $\mathbf{k_i}$, $\mathbf{k_s}$, and $\mathbf{q}$, respectively. When fitted with Mie theory, the distribution of scattered light intensity as a function of scattering angle can be utilized to determine particle size [16]. The weight concentration of particles in suspension is crucial for SLS, influencing both scattered light intensity and particle diameter. The effective particle sizing range is typically from 100 to 1000 nm [10, 17]. The SLS measurement time can vary; it may take minutes if the detector needs to be moved for different scattering angles or seconds if multiple detectors are used at different angles. However, this adds to the cost and complexity of the setup.

In-line measurements are possible with a multi-angle SLS detection scheme, but they are constrained by signal fluctuations caused by particle flow speed. The standard SLS measurement assumes single scattering, but in reality, especially at high particle concentrations (turbid media), multiple scattering can occur, compromising measurement accuracy as multiple scattering is not included in the scattering model. Multiple scattering effects can be removed to some extend using two simultaneous light scattering experiments performed at the same scattering vector on the same sample volume. This approach, known as cross-correlation or modulated 3D SLS, eliminates multiple scattering effects via cross-correlation of the scattering signals from the two beams [18]. However, this method is more expensive and complex compared to standard SLS.

Dynamic light scattering

Dynamic Light Scattering (DLS), also known as photon correlation spectroscopy, is a method that uses a similar setup as in SLS, see Fig. 1.3. Similar to SLS, it is also used for sizing particles in emulsions and suspensions. However, instead of examining time-averaged intensities as a function of angle, DLS records scattered light intensity fluctuations as a function of time at a fixed scattering angle θ. These intensity variations arise from the homodyne interference of the fields scattered off the particles in Brownian motion, which, in turn, depends on the particle size. As the particles move, the path length of the scattered light reaching the detector constantly changes. This causes constructive or destructive interference in the detected scattered intensity. The dynamics of these intensity fluctuations depend on the diffusional motion of the particles, which can be related to the particle size (hydrodynamic radius). The diffusional motion of the particles in the suspension is governed by the Stokes-Einstein equation

$$D_0 = \frac{k_B T}{6\pi\eta_0 a}, \tag{1.1}$$

where D_0 represents the particle diffusion coefficient, k_B is Boltzmann's constant, T is the temperature in Kelvin, η_0 is dynamic viscosity, and a is a particle hydrodynamic radius. Therefore, by determining the diffusion constant and knowing the solution temperature and viscosity, the particle size can be determined.

The detector in DLS detects the intensity of scattered field fluctuations, and subsequently, the autocorrelation of the intensity signal, $g_2(\tau)$, is calculated. This

autocorrelation function measures the resemblance of the signal with itself as a function of the time delay. The decay of the autocorrelation function indicates how quickly this resemblance diminishes and can be fitted to analytical models to determine particle size. For larger particles with a relatively low diffusion rate, the detected intensity autocorrelation decays more slowly. Conversely, for smaller particles, the intensity fluctuations are much more rapid, leading to a faster signal correlation [19].

In heterodyne DLS, where the scattered field is mixed with a local oscillator, the fluctuations of the scattered field can be measured directly. For non-interacting monodisperse spherical particles undergoing Brownian motion, the normalized scattered light electric field autocovariance, $g_1(\tau)$, is given by Eq. (1.2) according to [20, 21]:

$$g_1(\tau) = \frac{\langle E(t)E^*(t+\tau)\rangle_t}{\langle I(t)\rangle_t} = e^{-D_0 q^2 \tau}, \tag{1.2}$$

where $E(t)$ is the scattered complex field as a function of time, $I(t) = E(t)E^*(t)$ is the scattered intensity, τ is the autocorrelation lag time, and q is the scattering wavenumber, defined as [20]

$$q = \frac{4\pi n}{\lambda_0} \sin(\theta/2) . \tag{1.3}$$

Here, n is the suspension refractive index, and λ_0 is the incident laser wavelength in vacuum.

In the classical detection scheme, DLS relies on homodyne detection of scattered light intensity, i.e., the scattered light from different particles are mixed together and detected. Therefore, the normalized autocovariance of the detected light intensity is $g_2(\tau)$. Using the Siegert relation [20], the normalized intensity autocovariance, which represents the autocorrelation of the intensity signal after mean subtraction, is given by

$$g_2(\tau) = \frac{\left\langle \left(I(t) - \langle I(t)\rangle_t\right)\left(I(t+\tau) - \langle I(t)\rangle_t\right)\right\rangle_t}{\langle I(t)\rangle_t^2} = \beta\left|g_1(\tau)\right|^2 = \beta e^{-2D_0 q^2 \tau}, \tag{1.4}$$

where β is a factor that takes into account the reduction of contrast. The relation Eq. (1.4) is valid for monodisperse particles. Figure 1.4(a,b) shows simulated intensity fluctuations and the corresponding normalized second-order autocovariance function for non-interacting, sufficiently diluted particles with a radius of 100 nm. The decay rate of $g_2(\tau)$ is a pure single exponential. For a suspension containing non-interacting polydisperse particles (i.e., particles of different sizes), the autocorrelation function is the sum of correlation functions for the different particle sizes [19]. Generally, DLS is accurate and reliable for measuring monodisperse particles or a single mean particle radius. To determine particle dimensions using DLS measurements, knowledge of the viscosity and temperature of the suspension is necessary. Additionally, the DLS setup is quite sensitive to specular reflections,

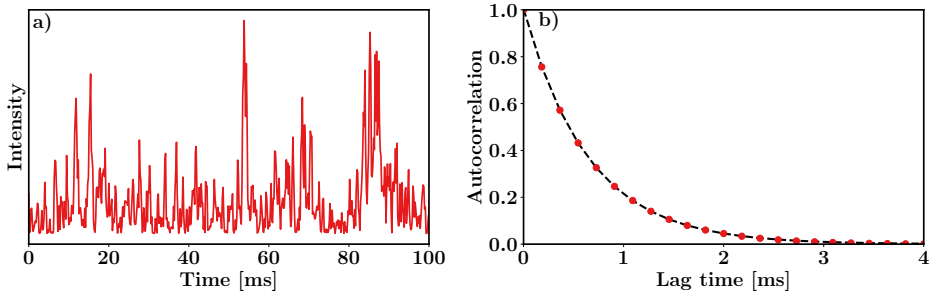

Figure 1.4: DLS simulations using 100 nm radius particles. (a) Intensity fluctuations as a function of time. (b) Normalized second-order autocovariance function along with the fit using Eq. (1.4).

as the scattered signal intensity from particles is usually low, especially for smaller particles.

DLS can measure particle sizes ranging from a few nanometers to 1000 nanometers [10, 17]. Smaller particles do not scatter light sufficiently, while larger particles may tend to settle out from the suspension and exhibit no measurable diffusional motion. The optical limitations for DLS are less severe than for the SLS technique, but there is an additional requirement that the sample properties remain stationary on the timescale of a measurement, typically ranging from 0.1 to 5 minutes [10]. For accurate capture of diffusive dynamics with DLS, the detector must possess both high sensitivity and a high acquisition rate. DLS particle sizing is also limited to low particle concentration samples [19]. With increasing particle concentrations, hydrodynamic and direct particle interactions become important, and the simple diffusional model is no longer sufficient to describe the physics. Moreover, in such cases, DLS also suffers from multiple scattering, which is not included in the underlying models that rely on the assumption of a single scattered light. Two-color [22, 23] or cross-correlation [24] DLS have been developed to overcome the limit imposed by multiple scattering. However, these require a more complex setup with at least two scattering arms. Very low sample concentrations, on the other hand, lead to fluctuations in particle count within the measurement volume for which Eq. (1.4) does not hold. Typical particle volume fractions studied in DLS are in the range of 0.001-0.01%. To measure very high volume fractions, diffusing-wave spectroscopy (DWS) is employed, representing an extreme case of DLS that assumes a very dense and opaque medium.

Similar to SLS, real-time measurements are possible with DLS. DLS models have been extended [25] to compensate for the bulk particle motion, which, when uncompensated for, leads to the underestimation of the particle size. However, this compensation is effective only when the suspension flow speed is uniform across the entire scattering volume. This imposes further limitations on DLS, as the flow profile in typical in-line applications is not uniform.

Diffusing-wave spectroscopy

Diffusing-wave spectroscopy (DWS) extends DLS to highly multiple scattering media. Both techniques involve detecting varying scattered light intensity and correlating it with particles' diffusive motion. While DLS assumes a single scattering signal, DWS takes a completely different approach. In DWS, light is supposed to undergo a large number of scattering events from particles in the suspension. In this limit, the direction of scattered light is entirely randomized, and dynamics are treated with statistical approximations [26]. DWS employs two approximations. The first is that it describes light propagation through the suspension in the extreme multiple scattering limit, where each photon is scattered multiple times and the photon's path can be described as a random walk. The simplest description of light propagation is through the diffusion approximation [26], which neglects interference effects and assumes that light diffuses as it travels through the medium. The second approximation is that individual light scattering instances are approximated through a contribution of an average scattering event, with the path length determining the number of average scattering events.

From an experimental perspective, DWS also measures the autocorrelation function and relates it to particle sizes. Since DWS is an extreme case of DLS with a very concentrated and turbid sample, its setup is similar to DLS. However, the collected light intensity is lower, hence requiring more powerful light sources for accurate particle sizing. In the case of transmission DWS, it is crucial to ensure no unscattered light passes through the sample. This requires a large sample thickness and high particle concentration, which, in turn, increases light absorption and necessitates higher optical power compared to DLS. In DWS, scattered light intensity from large path lengths (more multiple scattering) decorrelates faster than from smaller path lengths, offering a method to differentiate between single scattering and multiple scattering contributions. In backscattering DWS, it is important not to measure contributions to the autocorrelation function from single scattering events, which have longer characteristic decay times. Since DWS deals with multiple scattered light, which decorrelates faster, there are more requirements on the detection electronics. Additionally, multiply scattered light loses its polarization and produces an autocorrelation function of lesser magnitude.

In practice, DLS is a more powerful and quantitative tool for measuring particle size because it has fewer technical limitations. DWS requires more prior information and its accuracy is rather limited. Unlike DLS, DWS cannot characterize polydisperse suspensions [27]. However, when multiple scattering dominates and DLS cannot be relied upon, DWS can still provide information about particle size. Simple diffusion models for DWS also do not account for particle-particle interactions. While these interactions can be considered by modifying underlying models, due to the higher particle concentrations of the sample, accounting for hydrodynamic interactions is more critical for DWS performance than for DLS. The typical particle size range for DWS is 100–3000 nm, with concentrations of at least 10–20% [28].

Photon density wave spectroscopy

Photon Density Wave (PDW) spectroscopy is a novel optical method suitable for particle sizing. In PDW, the light from a laser diode is intensity-modulated in the

MHz-GHz frequency range and guided into a sample using a fiber [29]. The light coming out of the fiber acts as a point source. Due to the intensity modulation, a photon density wave is created, representing a variation in the number of photons per unit volume as a function of time [29]. The PDW wave propagates spherically from the fiber tip, creating a coherent density wave in the medium. At some distance from the light source fiber, the detection fiber is located, collecting and guiding part of the light to the detector. The amplitude and phase of the detected signal are then analyzed. This analysis provides information on the absorption and reduced scattering coefficients of the suspension. The reduced scattering coefficient can be further converted into the particle size using Mie and/or other scattering theories. The PDW technique is most effective when applied to highly turbid and concentrated samples for the PDW wave to fully develop. Particle size measurements in the range 50-200 nm [30, 31] have been reported in industrial settings. The temporal resolution of the measurements is typically a few minutes.

Differential dynamic microscopy

Differential dynamic microscopy (DDM) is an alternative to DLS that can be used to measure particle sizes indirectly. Instead of detecting the total scattered power, DDM relies on obtaining consecutive 2D brightfield images as a function of time. A differential signal $d(\mathbf{r}, t, \tau)$ is generated by subtracting two images acquired at different times, the first one at time t and the second one at $t + \tau$ [32, 33], with

$$d\left(\mathbf{r}, t, \tau\right) = I\left(\mathbf{r}, t + \tau\right) - I\left(\mathbf{r}, t\right) . \tag{1.5}$$

Here, $I(\mathbf{r}, t)$ represents the image intensity distribution, which is a function of both time and lateral position. Squaring the Fourier transform of the differential $d(\mathbf{r}, t, \tau)$ and measuring the time average gives the so-called image structure function,

$$F_d\left(\mathbf{q}, \tau\right) = \left\langle \left| d\left(\mathbf{q}, t, \tau\right) \right|^2 \right\rangle_t , \tag{1.6}$$

where $\mathbf{q}$ is a wave vector in the Fourier domain and where $\langle\rangle_t$ indicates averaging over t.

The variation of the image intensity distribution with the time delay between the images is related to the translational and Brownian motion of the imaged particles. For spherical particles in Brownian motion, the image structure function takes the form [34]

$$F_d\left(\mathbf{q}, \tau\right) = A\left(\mathbf{q}\right)\left[1 - e^{-D_0 q^2 \tau}\right] + B\left(\mathbf{q}\right) , \tag{1.7}$$

where $q = |\mathbf{q}|$ is the azimuthally isotropic scattering vector magnitude, which is the Fourier pair of the radial position in the intensity image. Therefore, DDM allows access to q-dependent diffusive dynamics by distinguishing between various spatial frequencies in the intensity image.

In contrast to standard DLS, DDM involves more complicated optics due to the 2D image acquisition scheme and operation in a transmission configuration. As the characteristic correlation decay increases with decreasing particle size, a fast imaging system is required for sizing small particles. Using DDM, researchers have

reported measurements of particles ranging in size from a few nanometers to a few microns [34, 35]. It is crucial to note that sample thickness, particle concentration, and speed must be high enough to enable tracking of particle motion in consecutively acquired images, as well as the transmission of sufficient light without multiple scattering. Similar to SLS and DLS, DDM can be extended by incorporating multiple cameras in a cross-differential mode [36]. This allows researchers to decrease the lag time between acquired images and investigate faster particle dynamics.

When applying DDM to a flowing sample, flow effects quickly dominate over diffusive dynamics, leading to an underestimation of particle size. Flow-DDM has been developed [37] to address these limitations. However, this improvement only works for spatially uniform flows, as it is based on an average particle drift velocity. In typical in-line sizing applications, where flow speed varies as a function of space, this further constrains the effective particle sizing depth range and, consequently, the sample thickness. Therefore, implementing DDM for in-line particle sizing is likely more challenging due to limited sample thickness, spatial variation in flow velocity, and the use of a complex optical system.

Doppler-based techniques

In Doppler-based methods, the Doppler effect is utilized to measure the velocity and/or size of particles. In phase Doppler anemometry (PDA) [10], a laser beam is split into two parallel beams that are then focused on a point within a measurement zone, forming stationary interference fringes of alternating high and low intensity. When a particle passes through these fringes, it scatters light. The intensity of the scattered light has high-frequency oscillations known as Doppler burst signals. The frequency of these oscillations (Doppler frequency) is proportional to the particle's velocity. Particle size is determined by measuring the phase shift between the Doppler burst signals received by multiple detectors, with the phase shift directly related to the particle diameter. This method allows simultaneous and precise measurement of both the size and velocity of particles in a flow. The typical particle size range is from 0.5 μm to several millimeters[10]. The measurement volume is small, confined to the area where the laser beams overlap. The setup of PDA is complex and costly.

Laser Doppler anemometry (LDA), also known as laser Doppler velocimetry (LDV), is insensitive to particle size and can only measure the velocity or concentration of a suspension [8]). It operates based on the Doppler effect, detecting the frequency shift of laser light scattered by moving particles. By analyzing this frequency shift and its frequency broadening, LDA provides information about suspension concentration and flow velocity. While it can be applied in-line, it is not suitable for particle sizing.

1.5. Optical coherence tomography

Optical coherence tomography (OCT), also known as low-coherence interferometry (LCI), utilizes a low-coherence light source in a Michelson interferometer configuration to measure path-length-resolved sample reflectivity profiles with micrometer resolution and lengths of up to a few millimeters [38]. In OCT, light from a low

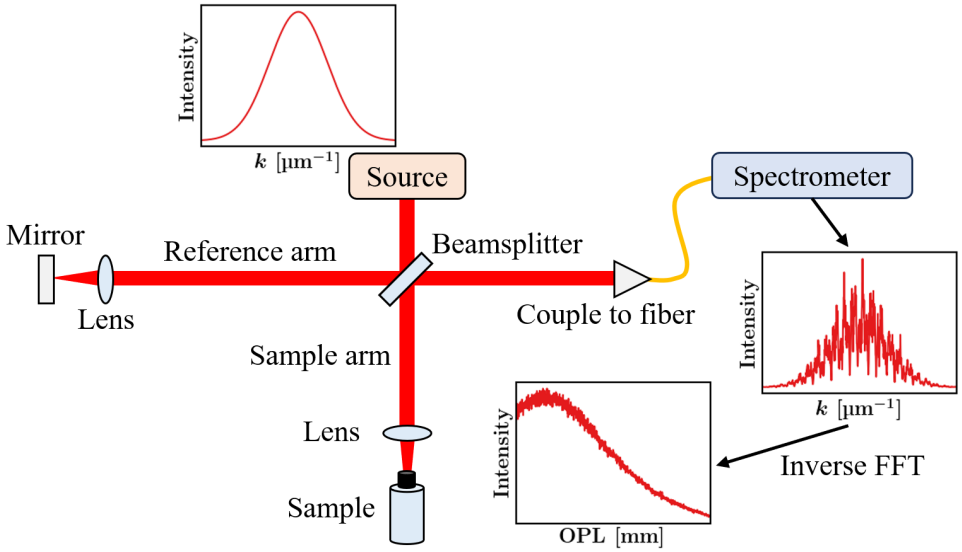

Figure 1.5: Schematic representation of a spectral-domain OCT setup.

temporal-coherence broad-bandwidth source is split via a beam splitter. One part of the beam is directed towards the sample, and the second portion is directed towards the reference mirror. Scattered light from the sample (sample beam) and a reflection from the reference mirror (reference beam) are recombined via the beam splitter onto a detector. The measured interference signal is a function of the sample and reference electric field amplitudes. The interference between the two beams arises only when the path-length difference between them is less than the light coherence length. The axial resolution of OCT is inversely proportional to the spectral bandwidth of the light source, with broader bandwidths providing better resolution.

OCT measurements can be realized in two different ways: time-domain and Fourier-domain OCT. In time-domain OCT, light interference is detected using a single photodiode, and path-length-resolved information about sample scattering is obtained by scanning the position of the reference mirror. Interference will be produced only at specific reference mirror positions (within the accuracy of the light coherence length). The magnitude of the interference burst is related to the sample reflectivity. Thus, by varying the reference mirror position in accordance with the sample depth, the sample reflectivity profile can be obtained. Initial implementations were with time-domain OCT, but it is currently being superseded by more advanced Fourier-domain OCT.

In Fourier-domain OCT, the position of the reference mirror is fixed. However, path-length-dependent information is encoded within the spectrum of the interference pattern. The schematic of a Fourier-domain OCT setup is given in Fig. 1.5. The OCT signal, or path-length-dependent reflectivity/scattering amplitude, is calculated by an inverse Fourier transformation of the interference spectrum [38].

Fourier-domain OCT can be achieved using two approaches: swept-source and spectral-domain OCT. In the swept-source method, the incident light is a laser with a tunable frequency. The incident light frequency is scanned as a function of time, and the interference signal is detected using a single photodiode. This produces a frequency-dependent interference signal, which is then Fourier-transformed to obtain the path-length resolved OCT signal. In spectral-domain OCT, a broadband light source is used. However, in this case, the interference spectrum is spectrally resolved in space using an interferometer. This provides a frequency-domain interference signal, which is then transformed to the optical path-length domain. Compared to time-domain OCT, Fourier-domain OCT provides several advantages: higher signal-to-noise ratio, lower measurement time, and a fixed reference mirror [38]. Fourier-domain OCT does not require moving the mirrors to obtain axial sample scans. However, the beams can be tilted to perform lateral 2D path-resolved scans of the sample as well. The Fourier transform of the interference spectrum, which is the OCT signal, is a complex-valued signal and can be expressed as a combination of the signal amplitude and phase [39].

Optical coherence tomography can be used to determine various properties of a particle suspension through both static and dynamic measurements. In static measurements, sample properties are derived from the depth-resolved OCT intensity profile, while in dynamic measurements, the time-dependent OCT signal is used to probe particle motion and relate it to their properties. The advantage of dynamic measurements over static measurements is that they require less a priori sample information or calibration. OCT has been utilized for measuring the complex refractive index [40], particle concentration [41], attenuation coefficient [42–44], scattering anisotropy [45], flow speed [46, 47], particle size and polydispersity [5, 48] of colloidal suspensions.

1.5.1. Doppler OCT

Doppler OCT enables the determination of spatially-resolved flow speed within particle suspensions [49]. The Doppler frequency shift observed in the Fourier-domain spectral OCT signal corresponds to a phase change in the spatial OCT signal. This phase change is directly proportional to the flow velocity component along the optical axis of the beam. An advantage of Doppler OCT is its capability to provide spatially resolved flow speed measurements across the entire OCT imaging depth.

Doppler OCT is considered the gold standard for flow measurements in particle suspensions and finds widespread use in in-line medical and clinical applications. However, it is important to note that while Doppler OCT excels in flow measurement, the average Doppler phase shift is insensitive to particle size [20, 21]. Consequently, similar to Laser Doppler Anemometry (LDA), Doppler OCT isn't suitable for particle sizing applications. Due to its origin in the Doppler frequency shift, lateral flows cannot be measured with Doppler OCT. The minimum flow that Doppler OCT can measure is limited by particle diffusion as this adds a random phase to the phase from the axial motion. The maximum flow speed that can be measured is limited by phase wrapping and fringe washout [49].

1

1.5.2. Dynamic light scattering OCT

Fourier-domain OCT can be employed in conjunction with DLS for particle sizing and flow measurement, denoted as DLS-OCT. Initially, DLS-OCT was used for quantitative diffusion imaging and particle sizing [48], where particles down to 46 nm in size and with weight concentrations of up to 10% were measured. Later, DLS-OCT was employed to measure flow speeds of particle suspensions [46, 47, 50, 51]. Since the correlation functions of flow and diffusion multiply, particle size and flow speed measurements affect each other. This is particularly interesting for in-line particle sizing during process control [5]. There is a significant bias in measuring the particle size of flowing suspensions when the flow decorrelation is not accounted for [50, 52]. Similarly, it is difficult to accurately estimate small flow velocities with DLS-OCT due to particle diffusion. This is more problematic with smaller particles, due to faster Brownian motion, which results in similar order-of-magnitude decorrelation rates for diffusion and flow. In addition, diffusion measurements for flowing particles with large bulk velocity are sampling-limited due to fast flow decay rates.

The combination of OCT and DLS offers several advantages. First, it improves the signal-to-noise ratio using heterodyne detection through the mixing of the sample field with a reference beam, whereas conventional DLS relies on homodyne detection. Second, the autocorrelation decay rate for the field is halved compared to the homodyne case [20, 21]. Third, Fourier-domain OCT provides depth-resolved information, enabling simultaneous DLS-type measurements for multiple depths within a suspension. This allows for the characterization of flow profiles and particle sizes as a function of depth [53], which standard DLS techniques cannot achieve. Fourth, DLS-OCT provides complex depth-resolved fields, while conventional DLS only yields intensity information. This also allows the use of phase-resolved Doppler measurements [49]. Fifth, coherence gating rejects multiply scattered light with a path-length difference larger than the light coherence length, enabling measurements in concentrated and highly scattering media.

Typical depth-resolved DLS-OCT diffusion and flow speed measurements are shown in Fig. 1.6(a) and (b). Here, diffusion coefficient or flow speed profiles are obtained simultaneously as a function of depth (OPL). Note that diffusion and

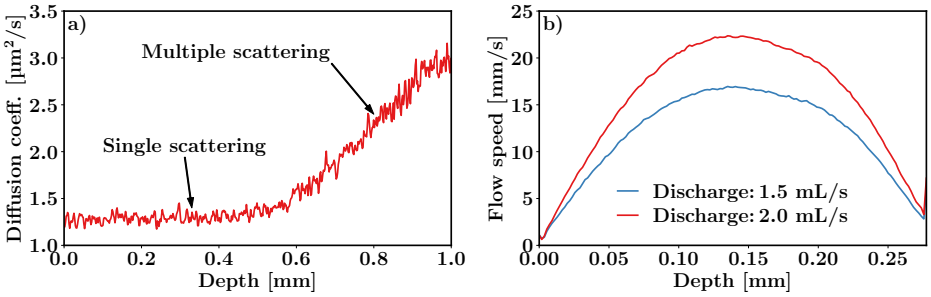

Figure 1.6: DLS-OCT measurements in Intralipid. (a) Diffusion coefficient and (b) flow speed for different discharge rates as a function of depth (OPL).

flow measurements were performed on different samples in cuvettes with different thicknesses, and hence, they have different depth ranges. Typical measurement times are in the order of a few seconds, making DLS-OCT suitable for in-line sizing applications. Even though coherence gating in DLS-OCT does not remove multiple scattering, it enables the determination of the single-scattering regime from the depth-resolved data. This is visible from the apparent increase in the estimated diffusion coefficient with depth in Fig 1.6(a). With standard DLS, it is impossible to determine with certainty whether single or multiple scattering is observed, leading to the restriction of its use to dilute suspensions. By utilizing DLS-OCT, this limitation is overcome.

Despite the fact that DLS-OCT can measure particle size in dense suspensions, this does not alter the fundamental limit of the applicability of the Stokes-Einstein equation (1.1) to dilute particle suspensions. For increasing particle concentrations, the diffusion coefficient of hard-sphere particles becomes dependent on the scattering wavenumber q, particle volume fraction f_v, and the time over which the motion is probed [54]. Therefore, DLS-OCT particle sizing in such high concentration samples requires inversion of the hard-sphere diffusion models [54–56] and measurements in spectral-domain using the OCT system with a relatively large q-range. Such DLS-OCT measurements have not yet been realized.

In contrast to Doppler OCT [57–60], there is very little information about the sensitivity and precision of DLS-OCT measurements of particle diffusion and flow. These aspects are crucial for ensuring reliable measurements, particularly in medical and pharmaceutical applications. While the effects of noise and bias in OCT on the measured autocorrelation function have been reported [61], their influence on the underlying parameters remains unclear. Therefore, to gain a better understanding of the fundamental limits of particle sizing and flow measurement, it is important to quantify the precision and bias of DLS-OCT.

1.6. Thesis outline

In this thesis we address the challenges associated with particle sizing and flow measurements using dynamic light scattering optical coherence tomography.

In chapter 2, we address the issue of particle interactions for particle sizing in concentrated nanoparticle suspensions. For this purpose, we developed a broadband DLS-OCT system covering the wavelength range of 350–1000 nm. We inverted hard-sphere rheological models and successfully measured particle size and polydispersity in nanoparticle suspensions with a particle concentration of 50 wt.%. Furthermore, we demonstrated the applicability of in-line particle sizing in suspensions that are not suitable for standard DLS-OCT measurements.

In chapter 3, we developed a scanning DLS-OCT system for measuring high flow speeds and improving particle sizing under flow conditions. We demonstrated a two-fold improvement in the flow velocity dynamic range when scanning the OCT beam along the flow. We also showed that we can measure the particle size of flowing suspensions more accurately deeper within the flow channel, further away from the edges. This can be beneficial in typical pharmaceutical applications where diffusion and mixing near the edges are slower, leading to overestimation of particle

size.

In chapter 4, we incorporate number fluctuations into DLS-OCT to measure extremely low flow speeds and particle concentrations in diluted nanoparticle suspensions. We demonstrated the ability to measure flow velocities below the particle diffusion and Doppler OCT limits by incorporating number fluctuations into the second-order autocorrelation function. Furthermore, the inclusion of number fluctuations in the DLS-OCT analysis can improve the accuracy of in-line particle sizing in dilute suspensions. Number fluctuations can also be implemented in more concentrated particle suspensions, for instance, using an OCT system with higher resolution.

In chapter 5, we demonstrate the application of number-fluctuation DLS-OCT for simultaneous 2D flow measurements below the diffusion and Doppler OCT limits on an organ-on-chip (OoC) device. In addition to number fluctuations, we implemented particle image velocimetry (PIV) on the OCT data and successfully measured the distribution of the complete in-plane velocity vectors. This chapter further showcases the usability of number-fluctuation DLS-OCT for measuring extremely small flow speeds in biomedical imaging and its advantages over Doppler OCT.

In chapter 6, we assess the precision and bias in DLS-OCT measurements of diffusion and flow. We show that errors in autocorrelation coefficients are strongly correlated, thereby hindering the ability to quantify the uncertainty in particle sizing. To overcome this issue, we mix different autocorrelation functions at the same time delay. Once the error correlations are removed, the precision in particle diffusion and flow speed matches the Cramer-Rao lower bound. This enables precise uncertainty quantification in particle sizing and flow speed measurements using DLS-OCT.

In Chapter 7, we address the problem of multiple scattering in DLS-OCT. We propose a simple method to perform multiple scattering simulations for particles undergoing Brownian motion and demonstrate that the autocorrelation functions in the multiple scattering regime exhibit double-exponential decay, corresponding to different numbers of scattering events. Experimental measurements corroborate these findings. Employing a double-exponential fit model improves both the depth range of single-scattering particle sizing and the accuracy of DWS particle size estimation.

Chapter 8 summarizes this thesis, discusses its contributions to particle sizing and flow measurements using DLS-OCT, and provides an outlook for future work.

References

[1] A. K. Kulshreshtha, O. N. Singh, and G. M. Wall, *Pharmaceutical Suspensions: From Formulation Development to Manufacturing* (Springer, 2010).

[2] S. Jacob, A. B. Nair, and J. Shah, *Emerging role of nanosuspensions in drug delivery systems,* Biomaterials Research **24**, 1 (2020).

[3] O. Salata, *Applications of nanoparticles in biology and medicine,* Journal of Nanobiotechnology **2**, 1 (2004).

[4] R. Besseling, *A new innovative pat tool for inline particle sizing of concentrated, flowing nanosuspensions,* InProcess-LSP (2018).

[5] R. Besseling, M. Damen, J. Wijgergans, M. Hermes, G. Wynia, and A. Gerich, *New unique PAT method and instrument for real-time inline size characterization of concentrated, flowing nanosuspensions,* European Journal of Pharmaceutiral Sciences **133**, 2005 (2019).

[6] B. Y. Shekunov, P. Chattopadhyay, H. H. Y. Tong, and A. H. L. Chow, *Particle size analysis in pharmaceutics: principles, methods and applications,* Pharmaceutical Research **24**, 203–227 (2007).

[7] T. Allen, *Particle Size Measurement* (Springer, 1981).

[8] W. Boyes, *Instrumentation Reference Book* (Butterworth-Heinemann, 2010).

[9] B. Coulter, *Coulter principle short cource,* (2014).

[10] H. G. Merkus, *Particle Size Measurements* (Springer, 2009).

[11] D. J. McClements, *Ultrasonic measurements in particle size analysis,* Encyclopedia of Analytical Chemistry (2006).

[12] N. Ruthardt, D. C. Lamb, and C. Bräuchle, *Single-particle tracking as a quantitative microscopy-based approach to unravel cell entry mechanisms of viruses and pharmaceutical nanoparticles,* Molecular Therapy **19**, 1199 (2011).

[13] O. H. A. Abildgaard, J. R. Frisvad, V. Falster, A. Parker, N. J. Christensen, A. B. Dahl, and R. Larsen, *Noninvasive particle sizing using camera-based diffuse reflectance spectroscopy,* Applied Optics **55**, 3840 (2016).

[14] R. B. Miles, W. R. Lempert, and J. N. Forkey, *Laser rayleigh scattering,* Meas. Sci. Technol. **12**, R33 (2001).

[15] C. F. Bohren and D. R. Huffman, *Absorption and Scattering of Light by Small Particles* (John Wiley & Sons, 1983).

[16] I. Kolokolnikov, E. Nepomnyashchaya, and E. Velichko, *Static light scattering for determination of physical parameters of macro- and nanoparticles,* Journal of Physics **1410**, 012168 (2019).

[17] L. Ogendal, *Light Scattering: A brief introduction*, Tech. Rep. (University of Copenhagen, 2019).

[18] I. D. Block and F. Scheffold, *Modulated 3D cross-correlation light scattering: improving turbid sample characterization,* Review of Scientific Instruments **81**, 123107 (2010).

[19] J. Stetefeld, S. A. McKenna, and T. R. Patel, *Dynamic light scattering: a practical guide and applications in biomedical sciences,* Biophys Rev **8**, 409 (2016).

[20] C. S. Johnson and D. A. Gabriel, *Laser Light Scattering* (Dover Publications, 1994).

[21] B. J. Berne and R. Pecora, *Dynamic Light Scattering* (Dover Publications, 2000).

[22] P. N. Segrè and P. N. Pusey, *Scaling of the dynamic scattering function of concentrated colloidal suspensions,* Physical Review Letters **77**, 771 (1996).

[23] P. N. Segrè and P. N. Pusey, *Dynamics and scaling in hard-sphere colloidal suspensions,* Physica A **235**, 9 (1997).

[24] F. Westermeier, B. Fischer, W. Roseker, G. Grübel, G. Nägele, and M. Heinen, *Structure and short-time dynamics in concentrated suspensions of charged colloids,* The Journal of Chemical Physics **137**, 114504 (2012).

[25] A. B. Leung, K. I. Suh, and R. R. Ansari, *Particle-size and velocity measurements in flowing conditions using dynamic light scattering,* Applied Optics **45**, 2186 (2006).

[26] W. Brown, *Dynamic Light Scattering* (Oxford University Press, 1993).

[27] D. J. Pine, D. A. Weitz, J. X. Zhu, and E. Herbolzheimer, *Diffusing-wave spectroscopy: dynamic light scattering in the multiple scattering limit,* Journal De Physique **51**, 2101 (1990).

[28] F. Scheffold, *Particle sizing with diffusing wave spectroscopy,* Journal of Dispersion Science and Technology **23**, 591 (2002).

[29] *Fiber-optical Particle Sizing by Photon Density Wave Spectroscopy* (Spie, 2014).

[30] L. Bressel, R.Hass, and O.Reich, *Particle sizing in highly turbid dispersions by photon density wave spectroscopy,* Journal of Quantitative Spectroscopy & Radiative Transfer **126**, 122 (2013).

[31] R. Hass, M. Münzberg, L. Bressel, and O. Reich, *Industrial applications of photon density wave spectroscopy for in-line particle sizing,* Applied Optics **52**, 1423 (2013).

[32] R. Cerbino and V. Trappe, *Differential dynamic microscopy: Probingwave vector dependent dynamics with a microscope,* Physical Review Letters **100**, 188102 (2008).

[33] R. Cerbino and P. Cicuta, *Perspective: Differential dynamic microscopy extracts multi-scale activity in complex fluids and biological systems,* The Journal of Chemical Physics **147**, 110901 (2017).

[34] D. Germain, M. Leocmach, and T. Gibaud, *Differential dynamic microscopy to characterize Brownian motion and bacteria mobility,* American Journal of Physics **84**, 202 (2015).

[35] C. Guidolin, C. Heim, N. B. P. Adams, P. Baaske, V. Rondelli, R. Cerbino, and F. Giavazzi, *Protein sizing with differential dynamic microscopy,* Macromolecules **56**, 8290 (2023).

[36] M. Arkoa and A. Petelin, *Cross-differential dynamic microscopy,* Soft Matter **15**, 2791 (2019).

[37] J. A. Richards, V. A. Martinez, and J. Arlt, *Particle sizing for flowing colloidal suspensions using flow-differential dynamic microscopy,* Soft Matter **17**, 3945 (2021).

[38] W. Drexler and J. G. Fujimoto, *Dynamic Light Scattering* (Springer, 2008).

[39] J. Kalkman, *Fourier-domain optical coherence tomography signal analysis and numerical modeling,* International Journal of Optics **2017**, 1 (2017).

[40] P. N. A. Speets and J. Kalkman, *Experiment and theory of the complex refractive index of dense colloidal media,* Applied Optics **41**, 214 (2024).

[41] K. Cheishvili and J. Kalkman, *Sub-diffusion flow velocimetry with number fluctuation optical coherence tomography,* Optics Express **31**, 3755 (2023).

[42] B. Ghafaryasl, K. A. Vermeer, J. Kalkman, T. Callewaert, J. F. de Boer, and L. J. van Vliet, *Analysis of attenuation coefficient estimation in Fourier-domain OCT of semi-infinite media,* Biomedical Optics Express **11**, 6093 (2020).

[43] B. Ghafaryasl, K. A. Vermeer, J. Kalkman, T. Callewaert, J. F. de Boer, and L. J. van Vliiet, *Attenuation coefficient estimation in Fourier-domain OCT of multi-layered phantoms,* Biomedical Optics Express **12**, 2744 (2021).

[44] P. N. A. Speets and J. Kalkman, *Measuring optical properties of clear and turbid media with broadband spectral interferometry,* Applied Optics **62**, 4349 (2023).

[45] V. M. Kodach, D. J. Faber, J. van Marle, T. G. van Leeuwen, and J. Kalkman, *Determination of the scattering anisotropy with optical coherence tomography,* Optics Express **19**, 6131 (2011).

[46] V. J. Srinivasan, H. Radhakrishnan, E. H. Lo, E. T. Mandeville, J. Y. Jiang, S. Barry, and A. E. Cable, *OCT methods for capillary velocimetry,* Biomedical Optics Express **3**, 612 (2012).

[47] J. Lee, W. Wu, J. Y. Jiang, B. Zhu, and D. A. Boas, *Dynamic light scattering optical coherence tomography,* Optics Express **20**, 22262 (2012).

[48] J. Kalkman, R. Sprik, and T. G. van Leeuwen, *Path-length-resolved diffusive particle dynamics in spectral-domain optical coherence tomography,* Physical Review Letters **105**, 198302 (2010).

[49] E. Koch, J. Walther, and M. Cuevas, *Limits of Fourier domain Doppler-OCT at high velocities,* Sensors and Actuators A **156**, 8 (2009).

[50] N. Weiss, T. G. van Leeuwen, and J. Kalkman, *Localized measurement of longitudinal and transverse flow velocities in colloidal suspensions using optical coherence tomography,* Physical Review E **88**, 042312 (2013).

[51] B. K. Huang and M. A. Choma, *Resolving directional ambiguity in dynamic light scattering-based transverse motion velocimetry in optical coherence tomography,* Optics Letters **39**, 521 (2014).

[52] N. Weiss, T. G. van Leeuwen, and J. Kalkman, *Simultaneous and localized measurement of diffusion and flow using optical coherence tomography,* Optics Express **23**, 3448 (2015).

[53] A. Wax, C. Yang, R. Dasari, and M. S. Feld, *Path-length-resolved dynamic light scattering: modeling the transition from single to diffusive scattering,* Applied Optics **40**, 4222–4227 (2001).

[54] C. W. J. Beenakker and P. Mazur, *Self-diffusion of spheres in a concentrated suspension,* Physica A **120**, 388 (1983).

[55] U. Genz and R. Klein, *Collective diffusion of charger spheres in the presence of hydrodynamic interaction,* Physica A **171**, 26 (1991).

[56] C. W. J. Beenakker and P. Mazur, *Diffusion of spheres in a concentrated suspension ii,* Physica A **126**, 349 (1984).

[57] S. Yazdanfar, C. Yang, M. V. Sarunic, and J. A. Izatt, *Frequency estimation precision in Doppler optical coherence tomography using the Cramer-Rao lower bound,* Optics Express **13**, 410 (2005).

[58] H. C. Hendargo, R. P. McNabb, A. Dhalla, N. Shepherd, and J. A. Izatt, *Doppler velocity detection limitations in spectrometer-based versus swept-source optical coherence tomography,* Biomedical Optics Express **2**, 2175 (2011).

[59] C. S. Kim, W. Qi, J. Zhang, Y. J. Kwon, and Z. Chen, *Imaging and quantifying Brownian motion of micro- and nanoparticles using phase-resolved Doppler variance optical coherence tomography,* Journal of Biomedical Optics **18**, 030504 (2013).

[60] M. G. O. Gräfe, M. Gondre, and J. F. de Boer, *Precision analysis and optimization in phase decorrelation OCT velocimetry,* Biomedical Optics Express **10**, 1297–1314 (2019).

[61] N. Uribe-Patarroyo, A. L. Post, S. Ruiz-Lopera, D. J. Faber, and B. E. Bouma, *Noise and bias in optical coherence tomography intensity signal decorrelation,* OSA Continuum **3**, 709 (2020).

2

Wavenumber-dependent dynamic light scattering optical coherence tomography measurements of collective and self-diffusion

We demonstrate wavenumber-dependent DLS-OCT measurements of collective and self-diffusion coefficients in concentrated silica suspensions across a broad q-range, utilizing a custom home-built OCT system. Depending on the sample polydispersity, either the collective or self-diffusion is measured. The measured collective-diffusion coefficient shows excellent agreement with hard-sphere theory and serves as an effective tool for accurately determining particle sizes. We employ the decoupling approximation for simultaneously measuring collective and self-diffusion coefficients, even in sufficiently monodisperse suspensions, using a high-speed Thorlabs OCT system. This enables particle size and volume fraction determination without the necessity of wavenumber-dependent measurements. We derive a relationship between the particle number-based polydispersity index and the ratio of self and collective mode amplitudes in the autocorrelation function and utilize it to measure the particle number-based polydispersity index. Notably, the polydispersity determined in this manner demonstrates improved sensitiv-

This chapter has been published as: **Konstantine Cheishvili**, Rut Besseling, Michiel Hermes, and Jeroen Kalkman, *Wavenumber-dependent dynamic light scattering optical coherence tomography measurements of collective and self-diffusion*, Optics Express 32(11), 19963-19983 (2024).

ity to smaller particle sizes compared to the standard intensity-based DLS cumulant analysis performed on dilute samples.

2.1. Introduction

Colloidal dispersions are widely used in chemical, pharmaceutical, and food industries, as well as in the domains of biology and medicine. Dynamic light scattering (DLS) is one of the most popular experimental techniques for studying colloidal systems [1–3]. It is a relatively simple and versatile technique that relies on the measurement of fluctuations in scattered light to obtain information about the diffusive motion of colloidal particles, predominantly used to obtain colloidal size characteristics. However, conventional DLS is limited to samples that are not in flow and have a low concentration of scatterers that have little multiple scattering. Dynamic light scattering optical coherence tomography (DLS-OCT) incorporates coherence gating to obtain a depth-resolved particle diffusion coefficient [4]. In DLS-OCT coherence gating suppresses multiple scattering and allows to study diffusive dynamics in more concentrated samples [5–7] and under flow [8–10].

In low-concentration particle suspensions, particle interactions are negligible, and the diffusion coefficient is inversely proportional to the particle hydrodynamic radius via the Stokes-Einstein relation. However, there is generally no such simple relation for concentrated samples. Concentrated particle suspension dynamics has been an active area of research for many years [11] and rheological models have been developed for highly concentrated charge-stabilized hard-sphere particle suspensions. These models describe particle diffusion through collective and self-diffusion mechanisms over short and long time scales [12–15]. Collective diffusion describes the relaxation of concentration gradients over specific length scales and thus depends on the scattering wavenumber q, while self-diffusion describes the mean squared displacement (MSD) of individual colloid particles. Conventional DLS has been utilized to measure the collective and/or self-diffusion coefficient of concentrated hard-sphere particle suspensions using an index-matching procedure [16–18]. This is a non-trivial process that requires extensive sample preparation to minimize multiple scattering and make self-diffusion measurable. Two-color [11, 14] or cross correlation [19] DLS has been employed to measure the collective diffusion coefficient over a large q-range in concentrated samples. While these methods effectively suppress multiple scattering, they require a more complex setup with at least two different scattering arms or wavelengths and involves laborious subsequent measurement of different incident and/or scattering vectors to obtain wavenumber-dependent dynamics.

In this work, we employ DLS-OCT to measure the q-dependent particle diffusion in dense suspensions in the spectral domain. DLS-OCT is generally used for conducting spatially resolved coherence-gated measurements of diffusion and flow by Fourier transformation over all wavenumbers. Nonetheless, when operated in the spectral domain, it can provide heterodyne correlation measurements at the different wavelengths of the OCT bandwidth and thus can be employed to simultaneously measure wavenumber-dependent diffusion over the entire bandwidth. This is akin to conducting parallel DLS measurements at different wavelengths or scattering an-

gles. However, the limited spectral width of typical OCT systems makes the q-range relatively small. In this study, we employ a custom-built broad bandwidth DLS-OCT system to measure wavenumber-dependent dynamics in a single measurement over a large q-range. From the scattering wavenumber dependency of the decorrelation, we measured the long- and short-time collective and self-diffusion coefficients in concentrated silica suspensions in a straightforward manner and correlated them with particle size and polydispersity.

2.2. Theory

2.2.1. Particle diffusion

In dilute particle suspensions with a particle volume fraction $f_v \to 0$, direct and hydrodynamic interactions between the particles are negligible [20]. The diffusion coefficient for non-interacting particles undergoing Brownian motion is given by the Stokes-Einstein equation

$$D_0 = \frac{k_B T}{6\pi\eta_0 a}, \tag{2.1}$$

where k_B is the Boltzmann constant, T is the absolute temperature, η_0 is the suspension dynamic viscosity, and a is the particle hydrodynamic radius. For charge-stabilized particle suspensions with a sufficient salt concentration, the hydrodynamic radius is the particle radius [16].

In concentrated suspensions, particle motion is affected by the presence of surrounding particles. For these suspensions we differentiate between short-time ($t \ll \tau_0$) and long-time ($t \gg \tau_0$) diffusive regimes, as well as between collective and self-diffusion. Here, t is the time over which the motion is probed (lag time in DLS-OCT correlation functions), while τ_0 is the interaction time defined as $\tau_0 = a^2/D_0$ [20, 21]. In the short-time regime, particle motion is primarily influenced by solvent-mediated hydrodynamic interactions between the particles. In the long-time regime, excluded volume interactions and direct electrostatic interactions additionally affect the diffusion (in different ways for collective and self-diffusion and at different time scales). Self-diffusion pertains to the mean squared displacement of individual colloid particles, while collective diffusion involves the relaxation of concentration gradients across specific length scales. Dynamic light scattering (DLS) on a monodisperse particle suspension measures the collective diffusion coefficient for a particular length scale related to the wavelength and angle of the experiment [20].

In the dilute limit, there is no difference between the two different time scales or collective and self-diffusion. However, due to the interactions described above in concentrated systems, both collective and self-diffusion coefficients become functions of the particle volume fraction due to both hydrodynamic and direct interactions, and a function of time, represented by the transition from short to long-time dynamics [21–24]. Furthermore, the collective diffusion coefficient becomes a function of the scattering wavenumber, $q = 4\pi n \sin(\theta/2)/\lambda_0$, where λ_0 is the illuminating light wavelength, n is the suspension refractive index, and θ is the angle between the illumination and scattering directions. The wavenumber dependence

of collective diffusion reflects the fact that, due to particle interactions, the diffusion of a density fluctuation in the suspension can strongly depend on the length scale of that fluctuation.

Self-diffusion

Self-diffusion describes how an individual particle diffuses in the presence of other Brownian particles. Therefore, it can only be detected when individual particles are optically distinguishable, either due to the polydispersity of particle scattering properties in the suspension, or by index-matching the majority of particles within the solvent, leaving only a small fraction of optically contrasting particles of interest that determine the scattered light fluctuations. Index matching ensures that the light-scattering particles do not interact with each other but do interact with other non light-scattering particles. Since self-diffusion depends solely on the motion of a single particle, the self-diffusion coefficient, $D_s(t)$, depends only on time and volume fraction and not on the scattering wavenumber. It equals the collective diffusion coefficient in the limit of infinite q[25]. The self-diffusion coefficient is proportional to the slope of the particle mean-squared displacement curve[20] and, for hard spheres, is given by [15, 20, 26]

$$D_s(t) = D_s^s - (D_s^s - D_s^l)\frac{2\sigma}{\sqrt{\pi}}\left[\frac{t}{\tau_M}\right]^{1/2} \quad \text{as} \quad t \to 0+, \tag{2.2}$$

and

$$D_s(t) = D_s^l + (D_s^s - D_s^l)\frac{\sigma}{2\sqrt{\pi}}\left[\frac{\tau_M}{t}\right]^{3/2} \quad \text{as} \quad t \to \infty, \tag{2.3}$$

where D_s^l is the long-time self-diffusion coefficient, D_s^s is the short-time self-diffusion coefficient, τ_M is the relaxation time of the velocity autocorrelation function [27], and σ is the width of the relaxation rate spectrum [26]. For dilute particle suspensions, $D_s(t) = D_0$, the characteristic time for structural rearrangements $\tau_M = \tau_0$, and $\sigma = \sqrt{2}$ [20, 26]. For more concentrated suspensions such analytical relations for τ_M and σ are not available. Based on simulations Cichocki and Hinsen [26, 27] suggested that $\tau_M \lesssim \tau_0$ and $\sigma \gtrsim \sqrt{2}$.

It has been reported that the time-dependent part in Eqs. (2.2) and (2.3) has a small relative amplitude, making it problematic to observe in typical light scattering experiments and even in simulations [20, 22, 26, 27]. Therefore, we simplify the time-dependent self-diffusion coefficient into a constant short-time self-diffusion [21–24]

$$D_s(t \ll \tau_0) \approx D_s(t \to 0) = D_s^s, \tag{2.4}$$

and a constant long-time self-diffusion

$$D_s(t \gg \tau_0) \approx D_s(t \to \infty) = D_s^l, \tag{2.5}$$

for times shorter or longer with respect to τ_0, respectively. For hard-sphere particle suspensions, D_s^s can be computed numerically using Eq. (7.2) derived by Beenakker

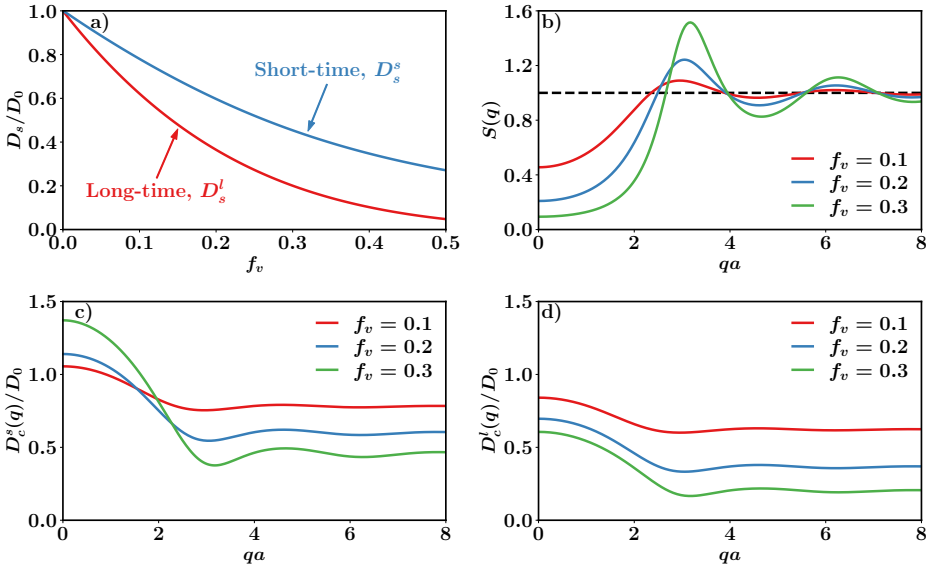

Figure 2.1: Diffusion coefficients and structure factors for hard-sphere particles. (a) Self-diffusion coefficients D_s^l and D_s^s as a function of volume fraction. (b) Structure factor $S(q)$, where the dashed line corresponds to $f_v = 0$. (c) Short- and (d) long-time collective diffusion coefficients.

and Mazur [12, 28], while D_s^l can be calculated analytically using [16]

$$D_s^l = D_0 \frac{(1 - f_v)^3}{1 + 1.5f_v + 2f_v^2 + 3f_v^3}. \tag{2.6}$$

Both D_s^s and D_s^l are plotted in Fig. 2.1(a) as a function of f_v. They decrease with increasing f_v, but D_s^s is consistently larger than D_s^l. It has been further suggested that D_s^l can be determined more accurately using [16, 29–32]

$$D_s^l = D_0 \frac{\eta_0}{\eta}, \tag{2.7}$$

where η is the measured low-shear viscosity of a concentrated particle suspension.

Collective diffusion

Collective diffusion describes a simultaneous motion of many Brownian particles due to concentration gradients in a suspension [20]. The term "collective" refers to the coherent displacement of particles from a region of high concentration to region of low concentration [33]. In addition to dependence on t and f_v, the collective diffusion coefficient $D_c(q,t)$ also depends on the scattering wavenumber q. It has been demonstrated that the time dependency in $D_c(q,t)$ solely arises from the mean-square displacement of individual particles [11, 14, 34], establishing its relation to self-diffusion. Assuming uniform time-dependency across all wavenumbers,

the collective diffusion coefficient can be factorized into the product of wavenumber and time-dependent factors [11, 14, 35], resulting in

$$D_c(q,t) = D_c^s(q)\frac{D_s(t)}{D_s^s}, \tag{2.8}$$

where $D_c^s(q)$ is the short-time collective diffusion coefficient given by [13]

$$D_c^s(q) = D_0\frac{H(q)}{S(q)}, \tag{2.9}$$

with $H(q)$ the hydrodynamic mobility function, and $S(q)$ the static structure factor. For hard-sphere particles, $H(q)$ can be obtained from the Beenakker-Mazur or so the called δY theory [12, 13, 28], and $S(q)$ can be determined using the Percus-Yevick approximation [36–38]. For dilute suspensions, i.e. for suspension for which $f_v \to 0$, $S(q) = H(q) = 1$ and $D_c(q,t) = D_0$. Figure 2.1(b,c) shows theoretical curves for $S(q)$ and $D_c^s(q)$, respectively, for hard-sphere particles as a function of the dimensionless wavenumber qa and f_v. At low qa values, $S(q)$ is small, reflecting the suppression of long wavelength density fluctuations in concentrated suspensions, while at large qa, it approaches unity. The short-time collective diffusion is highest at low qa and converges to D_s^s at large qa.

Since the time-dependency in collective diffusion arises from self-diffusion, we can use the same approximation as in Eq. (2.4, 2.5) and simplify $D_c(q,t)$ for shorter times into

$$D_c(q, t \ll \tau_0) \approx D_c(q, t \to 0) = D_c^s(q) = D_0\frac{H(q)}{S(q)}, \tag{2.10}$$

and for longer times into

$$D_c(q, t \gg \tau_0) \approx D_c(q, t \to \infty) = D_c^l(q) = D_0\frac{H(q)}{S(q)}\frac{D_s^l}{D_s^s}. \tag{2.11}$$

The long-time collective diffusion coefficient $D_c^l(q)$ is given in Fig. 2.1(d) as a function of qa and f_v. The long-time collective diffusion coefficient is consistently smaller than its short-time counterpart due to the direct electrosteric interactions that hamper particle movement; these interactions are not yet operative at short times [21].

Dynamic light scattering optical coherence tomography (DLS-OCT) can be used to measure the wavenumber-dependent collective diffusion coefficient of a particle suspensions by analyzing temporal fluctuations in the scattered light intensity for different wavenumbers detected by the OCT spectrometer. When the reference power is much larger than the sample power (at least an order of magnitude larger), DLS-OCT measures the collective diffusion coefficient using a heterodyne detection scheme [20]. When the optical properties of the particles are identical and the particles are monodisperse, all intensity fluctuations arise from microscopic density changes. The normalized autocovariance of q-dependent spectral intensity fluctuations, which is the heterodyne correlation function, is given by

$$g_1(q,\tau) = \frac{S_c(q,\tau)}{S(q)} = \frac{1}{1+\frac{1}{\mathrm{SNR}(q)}}e^{-D_c(q)q^2\tau} = A(q)e^{-D_c(q)q^2\tau}, \tag{2.12}$$

where SNR(q) is the signal-to-noise ratio as defined in [39], τ is the lag time, $A(q)$ is the autocovariance amplitude containing the effect of a diminishing SNR, $S(q,\tau)$ is the collective dynamic structure factor [20], and $D_c(q)$ is the short- or long-time collective diffusion coefficient. Here we have neglected the time dependence of the collective diffusion coefficient based on Sec. 2.2.1. Whether $D_c^s(q)$ or $D_c^l(q)$ is measured depends on the DLS-OCT acquisition time and particle size (through τ_0). Equation (2.12) is also known as the first-order autocorrelation function and decorrelates with a decay rate of $D_c(q)q^2$ in contrast to the scattered intensity correlation function obtained from spatially resolved OCT intensity measurements, which decays at twice this rate [5, 10]. Note that the collective diffusion rate is q-dependent in contrast to the self-diffusion which is q-independent.

2.2.2. Particle polydispersity

In the previous section, single-size monodisperse particles were assumed. However, particle polydispersity significantly affects the DLS-OCT correlation measurements. We distinguish between size polydispersity, particularly relevant for dilute samples, and optical polydispersity, which holds broader significance and becomes more relevant when measuring particle diffusion in concentrated suspensions.

Particle size polydispersity

When particle sizes in a suspension are not identical, the sample is polydisperse in size. For large size polydispersities single exponential fits using Eq. (2.12) underestimate the decay rate[40]. In dilute suspensions, size polydispersity affects $g_1(q,t)$ by introducing additional higher-order correlation terms (in time) in the exponent in Eq. (2.12), where the magnitude of these terms is related to the degree of polydispersity [20]. For dilute particle suspensions, size polydispersity can be accounted for in the correlation function using cumulant or Laplace analysis [40]. In the cumulant analysis, instead of using D_0 in the exponent of Eq. (2.12), the temporal evolution of the exponent is expanded as a polynomial as proposed in[40],

$$g_1(q,\tau) = A(q)e^{-D_0q^2\tau+\frac{\mu_2}{2}\tau^2-\frac{\mu_3}{3!}\tau^3+\frac{\mu_4}{4!}\tau^4-\dots}, \tag{2.13}$$

where μ_j corresponds to the j^{th} order in the cumulant analysis. Including the second order in τ in the expansion, the intensity-averaged polydispersity index is then defined as [2, 40]

$$\text{PDI}_I = \frac{\mu_2}{\left(D_0q^2\right)^2} = \frac{\sigma_I^2}{\langle a\rangle_I^2}, \tag{2.14}$$

where $\langle a\rangle_I$ and σ_I represent the mean and standard deviation (width) of intensity-averaged particle radius distribution, respectively. The second equality hols true only for Gaussian-distributed particle sizes [41]. For perfectly monodisperse particles, $\text{PDI}_I = 0$.

When measuring diffusion of particles small compared to the wavelength of DLS-OCT, the Rayleigh scattered intensity is proportional to the squared volume of the particle [42]. In this case, the first-order autocorrelation function measures quantities averaged over the squared volume of the particle, and $\text{PDI}_I = \text{PDI}_{v^2}$.

Theoretically, the measured polydispersity index may vary as a function of q due to the scattering anisotropy in DLS-OCT. However, for small particles with isotropic scattering properties this effect can be neglected [43].

Optical polydispersity

Optical polydispersity refers to the variation of optical properties of the particle scattering amplitude and includes the size polydispersity [20]. Even if all particles are identical and statistically equivalent, their scattering amplitudes can vary due to non-uniform illumination intensity and light scattering directions caused by a nonzero system numerical aperture (NA). Variations in particle size, shape, and refractive index significantly increase the optical polydispersity. In an optically perfect monodisperse system, intensity fluctuations arise solely from microscopic density changes. However, optical polydispersity gives rise to variations in the scattering intensity that are not related to microscopic density changes. For example, when two optically distinct particles interchange their positions, the scattered intensity changes but the microscopic density remains unchanged [20]. This intensity fluctuation is solely related to self-diffusion. The autocovariance of these intensity fluctuations is related to the self-diffusion of these particles instead of the collective diffusion. As a result, for optically polydisperse systems, an additional self-diffusion term appears in $g_1(q,t)$. For particles with a narrow size distribution, $g_1(q,t)$ can be approximated using the decoupling approximation [20, 23, 44, 45]

$$g_1(q,\tau) = \underbrace{A_c(q)e^{-D_c(q)q^2\tau}}_{\text{collective term}} + \underbrace{A_s(q)e^{-D_s q^2\tau}}_{\text{self-term}}, \tag{2.15}$$

where $D_c(q)$ and D_s are the short- or long-time collective and self-diffusion coefficients. Higher-order terms in the exponents, similar to Eq. (2.13), due to the size polydispersity are neglected. The mode amplitudes $A_c(q)$ and $A_s(q)$ are the relative weights of the collective and self-diffusion terms and given by [20]

$$A_c(q) = \frac{\langle B(q)\rangle_N^2}{\left(\langle B^2(q)\rangle_N - \langle B(q)\rangle_N^2 + \langle B(q)\rangle_N^2 S(q)\right)\left(1+\frac{1}{\mathrm{SNR}(q)}\right)}, \tag{2.16}$$

and

$$A_s(q) = \frac{\langle B^2(q)\rangle_N - \langle B(q)\rangle_N^2}{\left(\langle B^2(q)\rangle_N - \langle B(q)\rangle_N^2 + \langle B(q)\rangle_N^2 S(q)\right)\left(1+\frac{1}{\mathrm{SNR}(q)}\right)}, \tag{2.17}$$

where $B(q)$ is the particle scattering amplitude and $\langle..\rangle_N$ denotes number-averaged quantities. The collective term of Eq. (2.15) is often called "coherent" due to a scattering contribution from coherent particle motions, while the self term is referred to as "incoherent" due to the unrelated scattering from individual particles [19, 35, 46]. The self and collective modes in Eq. (2.15) become evident only at high particle concentrations when the collective and self-diffusion coefficients are different. In dilute particle suspensions there is always only one mode because $D_c(q) = D_s = D_0$, and Eq. (2.15) simplifies into Eq. (2.12).

In suspensions where particles are made from the same material, we assume that the variation in refractive index between particles can be neglected [47]. In typical low-NA OCT systems, the beam intensity and scattering angle variations among the particles are also negligible. In this case, the optical polydispersity arises solely from the size polydispersity. If we further assume that particles are much smaller than the wavelength ($a \ll \lambda$) such that the scattering process is described by Rayleigh scattering [42, 48], we find that $B(q) \propto a^3$ [49]. For particles with a number-based Gaussian size distribution, the ratio of the self and collective mode amplitudes is given by

$$\frac{A_s(q)}{A_c(q)} = \frac{\langle B^2(q)\rangle_N - \langle B(q)\rangle_N^2}{\langle B(q)\rangle_N^2} = \frac{15\cdot \mathrm{PDI}_N^3 + 36\cdot \mathrm{PDI}_N^2 + 9\cdot \mathrm{PDI}_N}{9\cdot \mathrm{PDI}_N^2 + 6\cdot \mathrm{PDI}_N + 1}, \tag{2.18}$$

where PDI_N is the particle number-based polydispersity index defined as

$$\mathrm{PDI}_N = \frac{\sigma_N^2}{\langle a\rangle_N^2}, \tag{2.19}$$

with $\langle a\rangle_N$ and σ_N being the mean and the standard deviation (width) of the number-averaged particle radius distribution. The ratio of the self and collective mode amplitudes contains information about the sample's number polydispersity. As expected, the self mode vanishes for a perfectly monodisperse particle suspension ($\mathrm{PDI}_N = 0$), resulting in the simplification of Eq. (2.15) into Eq. (2.12).

Figure 2.2(a) shows simulated volume-based and intensity-based polydispersity indices (PDI_v and PDI_I, respectively) for particles characterized by a Gaussian number-based size distribution with a number polydispersity index PDI_N. For the considered PDI_N values, both volume-based and intensity-based distributions exhibit a Gaussian shape. Up to $\mathrm{PDI}_N = 0.02$, all three polydispersity indices are similar. PDI_v and PDI_I remain close even up to $\mathrm{PDI}_N = 0.04$, but they start to deviate for larger PDI_N values.

In Figure 2.2(b), it is illustrated that the quantity $\frac{\langle a\rangle_v}{\langle a\rangle_N}$, the ratio of volume- to number-averaged particle radii, is nearly proportional to PDI_N, serving as a good

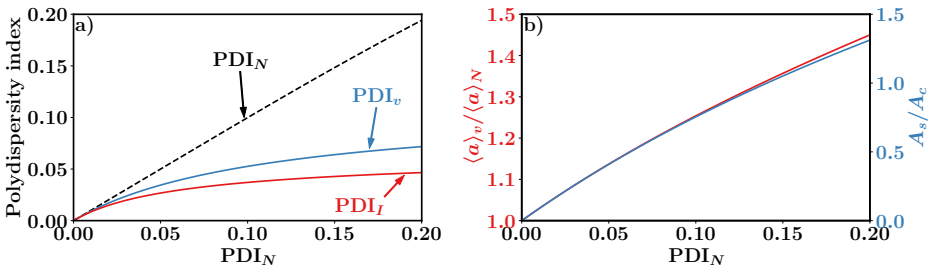

Figure 2.2: Simulated Gaussian number-based particle size distribution: (a) comparison of number, volume, and intensity-based polydispersity indices. (b) Ratios $\frac{\langle a\rangle_v}{\langle a\rangle_N}$ and $\frac{A_s}{A_c}$ as functions of PDI_N.

indicator for the number-based polydispersity index. For a number-based Gaussian size distribution, the relationship is given by

$$\frac{\langle a \rangle_v}{\langle a \rangle_N} = \frac{3 \cdot \mathrm{PDI}_N^2 + 6 \cdot \mathrm{PDI}_N + 1}{3 \cdot \mathrm{PDI}_N + 1}. \tag{2.20}$$

Furthermore, in Fig. 2.2(b), we can observe how the ratio of the self and collective modes increases with higher PDI_N. At $\mathrm{PDI}_N = 0.14$, which corresponds to a PDI_I of approximately 0.04 for a Gaussian number distribution, the self and collective terms become equal. Consequently, for samples with much larger PDI_I, we anticipate A_s from Eq. (2.15) to be significantly larger than A_c.

2.3. Methods

2.3.1. OCT systems

Dynamic light scattering experiments were performed using two OCT systems. A custom-built relatively slow ultra-broadband OCT system and a fast relatively narrowband Thorlabs GANYMEDE II HR series spectral domain OCT. The latter, based on a stable superluminescent diode, has been described in detail in our previous work [10, 39]. Both OCT systems have a backscattering configuration with NA $= 0.05$ and were operated in M-scan mode where subsequent A-scans were acquired at a fixed sample position. All measurements were performed at room temperature. Table 2.1 summarizes important parameters for both OCT systems. Figure 2.3(a) shows the layout of our custom setup. Maximum imaging depths for custom and Thorlabs OCT setups were 0.27 and 1.87 mm, respectively.

The custom spectral-domain OCT setup was built using a supercontinuum laser from NKT Photonics with an emission spectrum from visible to mid-infrared range.

Setup	k_0 range [µm^{-1}]	FWHM$_\lambda$ [nm]	FWHM$_z$ [µm]	Rate [kHz]
Custom	$6.49 - 15.64$	217	0.6	4.5
Thorlabs	$6.23 - 7.82$	112	3.1	36.0

Table 2.1: System parameters for the custom-built and Thorlabs OCT setup.

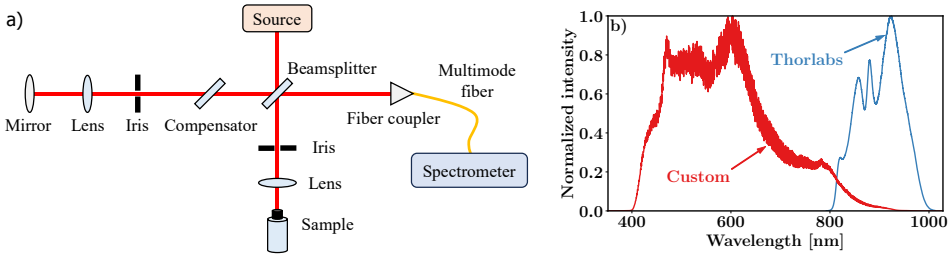

Figure 2.3: (a) Schematic overview of the custom-made OCT system. (b) DC spectra of the custom-built and Thorlabs OCT system.

Data was acquired with a high-speed spectrometer (Ocean FX, Ocean Optics) covering a wavelength range of $350-1000$ nm. The optics was designed for the same wavelength range, utilizing achromatic lenses (AC254-050-AB-ML, $f = 50$ mm, Thorlabs), a plate beamsplitter (BSW26R, Thorlabs), a beamsplitter compensator (BCP42R, Thorlabs), and silver mirrors (PF10-03-P01, Thorlabs). Backscattered sample and reference beams were coupled into a multi-mode fiber connected to the spectrometer. Since the coherence length and NA are very low, the optical variation in q due to a varying scattering angle is much smaller than the variation in q due to spectral sampling in k_0. Therefore, it can be assumed that the scattering angle is 180° and the scattering wavenumber q in the correlation analysis is $q = 2nk_0$.

Reference spectra of both OCT systems are shown in Fig. 2.3(b). The custom-built setup has a lower temporal sampling rate but much larger wavelength range than the Thorlabs OCT system. The custom-built setup has a higher noise level due to several reasons. First, the supercontinuum source has a higher noise floor and worse sensitivity roll-off characteristics [50] compared to the superluminescent diode used in the Thorlabs system. Second, the custom setup uses a multimode fiber to deliver the interfered light to the spectrometer whereas the Thorlabs system is solely based on single-mode fibers. The interference between different fiber modes increases the noise level. It was not possible to use the single-mode fiber with our custom setup due to the single-mode fiber's limited spectral transmission bandwidth.

2.3.2. Particle suspensions

Four concentrated and NaCl charge-stabilized aqueous silica suspensions were procured. The manufacturer-provided silica mass fraction in each sample was 50 wt.%. All relevant manufacturer-provided sample properties are summarized in Table 2.2. Particle surface (Zeta) potential measurements were not provided; they were obtained separately, along with transmission electron microscope (TEM) images. The obtained TEM images are shown in Fig. 2.9 in Appendix 2.7. The measured Zeta potentials are strongly negative, indicating that the suspensions are very stable against coalescence [51].

For Kostrosöl samples manufactured and supplied by Chemiewerk Bad Köstritz GmbH (CWK), the particle size distribution (PSD) properties were determined by the manufacturer using a CPS Disc Centrifuge (CPS Instruments, USA), and they are provided in Appendix 2.7. Both volume and number-averaged distributions are

Sample	$\langle a \rangle_v$ [nm]	PDI_v	$\frac{\langle a \rangle_v}{\langle a \rangle_N}$	Zeta [mV]	η [cP]
Kostrosöl 8050	38.2	0.027	1.645	-43.3 ± 2.4	5.9
Kostrosöl 9550	37.5	0.033	1.033	-36.7 ± 2.8	6.0
Kostrosöl 10050	49.7	0.018	1.195	-45.1 ± 0.8	4.7
Levasil CS50-28	-	-	-	-51.7 ± 0.7	-

Table 2.2: Manufacturer provided and measured sample properties.

depicted. The volume-based PSDs for all samples exhibit a single peak around the mean particle size, resembling normal or log-normal size distributions. In the case of Kostrosöl 9550, the number-based PSD is similar. However, in Kostrosöl 8050 and 10050, additional peaks in the number-based PSDs are observed due to the presence of a large number of smaller particles. While these smaller particles scatter almost no light and are negligible in the volume-averaged scheme, they are significant in the number-based PSD.

Levasil CS50-28, manufactured by Nouryon and supplied by Inprocess-LSP, was provided to us as a more polydisperse sample with a particle radius range of 5-75 nm. However, detailed information about the particle properties is not available. DLS measurements from literature report an average particle radius of 55 nm [52]. However, it's important to note that this value may vary from batch to batch.

In Table 2.2, $\langle a \rangle_v$ is the mean radius, and PDI_v denotes the polydispersity index of the volume-based particle radius distribution measured by the manufacturer. Since the exact shapes of the distributions in Appendix 2.7 are unavailable to us, the volume-based polydispersity index was approximated by dividing the square of the full width at half maximum (FWHM_v) by the square of the mean radius. The quantity $\frac{\langle a \rangle_v}{\langle a \rangle_N}$, as provided by the manufacturer and shown in Fig. 2.10 in Appendix 2.7, represents the ratio of volume-averaged to number-averaged particle radius. As illustrated in Fig. 2.2(b), this ratio is directly related to the number-based polydispersity in Eq. (2.19).

The particle volume fraction f_v is necessary for calculating the theoretical collective and self-diffusion coefficients. Even though our particles are charge-stabilized, we did not know the exact thickness of the electric double layer around them, which can significantly affect f_v [16]. For that reason we diluted our original suspensions with a small amount of highly concentrated LiCl solution (mixing ratio 110:1). This did not affect the silica weight content when rounded to the nearest integer but resulted in approximately 14 mM LiCl concentration in the suspensions. At this salt concentration the thickness of the electrical double layer can be neglected and the particles can be treated as hard-spheres [16, 53]. To determine f_v we have used the simplest approach based on the particle mass and density [54] with

$$f_v = \left[1 + \frac{\rho_s}{\rho_w}(w_s^{-1} - 1)\right]^{-1}, \tag{2.21}$$

where w_s is the manufacturer stated silica mass fraction in the suspension, $\rho_s \approx 2.0$ g/mL and $\rho_w = 1.0$ g/mL are the silica particle and water densities [55], respectively. Based on Eq. (2.21) and $w_s = 0.5$, and for all provided samples the maximum volume fraction is $f_v \approx 0.33$.

The mean sample refractive index n was calculated by finding the refractive indices of water and silica separately and then mixing them using the Lorentz-Lorenz formula [56, 57]. The refractive index of water as a function of wavelength and temperature was calculated using [58], and the refractive index of silica at the room temperature as a function of wavelength was estimated using [59]. Since all suspensions have the same f_v, we assume that their refractive indices are identical.

2.3.3. Diffusion measurements in dilute suspensions

Dilute suspensions were prepared using the demineralized water with a silica weight content of 1 wt.% corresponding to $f_v \approx 0.005$. This is sufficiently low to neglect particle interactions and multiple scattering. The LiCl concentration was maintained at the same level as in dense suspensions. In dilute suspensions D_0 is constant and does not depend on q. Therefore, all DLS-OCT measurements were performed in the depth-domain using the Ganymede OCT system. The dilute suspensions were used to determine D_0 and PDI_I for all samples. In order to convert D_0 to the particle hydrodynamic radius, the viscosity of the dilute aqueous solution, η_0, was calculated using Eq. (21) from [60].

Every OCT acquisition consisted of 20 subsequent M-scans, each containing 32768 temporal sampling points. The measured interference spectrum was first resampled to a linearly-sampled wavenumber domain and then apodized using a Gaussian filter. After apodization, the measured FWHM_z was 4.67 µm, exceeding the unapodized FWHM_z value in Table 2.1. From the complex OCT data the average of 20 first-order normalized autocorrelation functions was calculated at every depth. The depth-resolved $g_1(z,\tau)$ was noise-corrected [61, 62] and averaged over the depth range with SNR > 10 inside the sample. The resultant average $g_1(\tau)$ was fitted using Eq. (2.13) with $A = 1/(1+\mathrm{SNR}^{-1})$, $D_c = D_0$, and μ_j as free parameters. The second- or fourth-order nonlinear fits were performed depending on the sample polydispersity [40] for the range of τ for which $g_1(\tau) > 0.01$. The intensity-averaged particle size and PDI_I were subsequently calculated using Eq. (2.1) and Eq. (2.14).

2.3.4. Diffusion measurements in concentrated suspensions

Wavenumber-domain DLS-OCT measurements were performed either with the custom or Thorlabs OCT system. Due to temporal sampling and sensitivity limitations, only the samples with the largest particles, Kostrosöl 10050 and Levasil CS50-28, could be measured using the custom setup. The small particles, Kostrosöl 8050 and 9550, were measured using the Thorlabs system. Two additional suspensions were made by mixing both samples in each pair with 1:1 mixing ratio. In total 20 measurements were performed with 8192 and 32768 temporal sampling points for the custom and Thorlabs systems, respectively.

Wavenumber-dependent DLS-OCT data processing steps are shown in Fig. 2.4. Similar to the dilute case, we initially obtain the complex OCT signal from the spectral interference. Then we compute the average depth-resolved $g_1(z,\tau)$ and determine its decay rate as a function of depth. We identify the depth region with a constant diffusion coefficient and without the effects of multiple scattering or sensitivity roll-off [63]. We apodize the complex OCT signal in this region using the Tukey window function and transform it back to the wavenumber-domain via the forward Fourier transformation. As a result we obtain a fully real-valued spectral interference signal. Subsequently, the average temporal autocovariances are computed and fitted for every k_0 to determine the wavenumber-dependent diffusion coefficient.

In concentrated suspensions, particle size polydispersity can affect both the collective [20, 24] and self-diffusion [64, 65] coefficients. For purely exponential

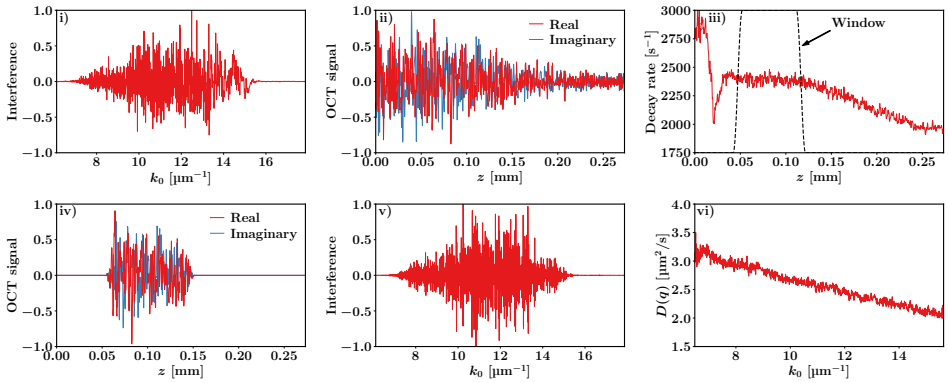

Figure 2.4: Overview of the processing steps in DLS-OCT for obtaining the wavenumber-dependent diffusion coefficient in a single acquisition. The data are from the custom-built setup where we measured the collective diffusion coefficient in the Kostrosöl 10050 sample, containing 100 nm particles at $f_v = 0.33$.

decays Eq. (2.12) is used to fit with autocovariance amplitude and the diffusion coefficient as fit parameters. For $g_1(q,\tau)$ with a non-exponential behaviour we use Eq. (2.15) to fit with A_c, A_s, D_c, and D_s as fit parameters.

2.4. Results

Table 2.3 presents the results obtained from dilute particle suspensions using the Thorlabs OCT system. Diffusion coefficients were obtained by fitting Eq. (2.13), and particle radii were determined using the Stokes-Einstein relation. The errors in radii were calculated by propagating the assumed temperature uncertainty of half a degree and incorporating statistical errors. Polydispersity indices were then calculated using Eq. (2.14). Interaction times, calculated using $\tau_0 = \langle a \rangle_I^2 / D_0$, are also given. In general, the intensity-averaged particle sizes and PDI_I align well with the volume-averaged values provided by the manufacturer in Table 2.2. The measured PDI_I values for Kostrosöl samples are comparable in magnitude and slightly lower than the corresponding PDI_v from the manufacturer. This observation is consistent with our expectations for relatively monodisperse samples, as indicated in

Sample	$\langle a \rangle_I$ [nm]	PDI_I	τ_0 [ms]
Kostrosöl 8050	38.9 ± 1.1	0.022 ± 0.002	0.26
Kostrosöl 9550	37.4 ± 1.1	0.022 ± 0.002	0.23
8050 & 9550 1:1 mix	38.6 ± 1.2	0.023 ± 0.002	0.26
Kostrosöl 10050	48.6 ± 1.5	0.018 ± 0.002	0.51
Levasil CS50-28	51.7 ± 1.6	0.162 ± 0.003	0.62
CS50-28 & 10050 1:1 mix	49.9 ± 1.6	0.101 ± 0.004	0.56

Table 2.3: Measured parameters for dilute particle suspensions using the Thorlabs OCT system.

Fig. 2.2. In contrast to Kostrosöl samples, Levasil CS50-28 and its mixtures exhibit significantly higher levels of polydispersity.

2.4.1. Kostrosöl 10050 and Levasil CS50-28 measurements

Autocorrelation functions for dilute (depth-domain, Thorlabs OCT) Levasil CS50-28, Kostrosöl 10050, and their mixture are shown in Fig. 2.5(a). As expected from Eq. (2.13), the autocorrelation function of dilute samples deviates from the single exponential trend with increasing size polydispersity. Autocorrelation functions for concentrated (q-domain, custom OCT) Levasil CS50-28, Kostrosöl 10050, and their mixture are shown in Fig. 2.5(b). The concentrated suspensions do not exhibit a double exponential decay; instead, we observe only a single term from Eq. (2.15). We attribute this to a combination of factors, such as low sensitivity and low acquisition rate of the custom setup, very high or very low sample polydispersity, used qa range, and differences in decay rates between the collective and self-terms at longer time scales. Hence, a single exponential function was employed to fit the wavenumber-dependent diffusion coefficient $D(q)$.

The concentrated samples are analyzed in the q-domain with the custom setup which operates with an acquisition time $\Delta t = 222$ ms. This implies that we are in the long-time diffusion regime, with $\tau \gg \tau_0$ for all particles. The obtained wavenumber-dependent diffusion coefficients for concentrated suspensions with $f_v \approx 0.33$ are given in Fig. 2.6. For comparison, the theoretical D_s^l and $D_c^l(q)$ from Sec. 2.2.1 and 2.2.1 are also shown. These were calculated with hard-sphere models presented in Sec. 2.2 and a volume fraction of 0.33 and the particle radii from Table 2.3. For Kostrosöl 10050, D_s^l was estimated based on the provided sample viscosity and using Eq. (2.7). The viscosity for Levasil CS50-28 was not known, so D_s^l was calculated using Eq. (2.6). The obtained diffusion coefficients were normalized using D_0 values of the diluted suspensions, corresponding to the radii in Table 2.3. The measured $D(q)/D_0$ for Kostrosöl 10050 is wavenumber-dependent and agrees re-

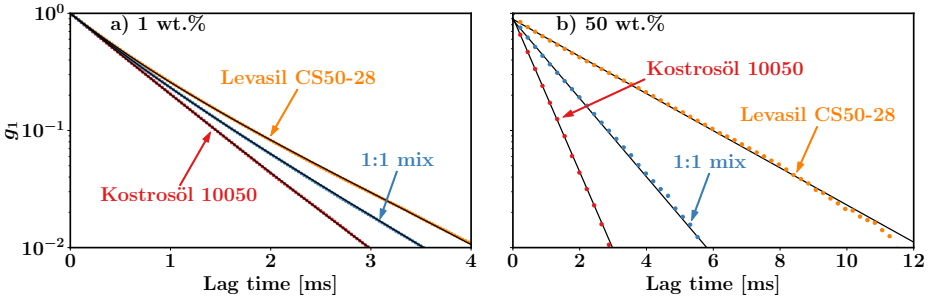

Figure 2.5: Autocorrelation function of Levasil CS50-28, Kostrosöl 10050, and their mixture. (a) Depth-averaged $g_1(\tau)$ obtained at the center wavenumber $q_c = 18.8$ µm^{-1} in dilute suspensions using the Thorlabs OCT, fitted with Eq. (2.13). (b) Wavenumber-dependent $g_1(q,\tau)$ measured in concentrated samples for $q = 22.7$ µm^{-1} using the custom OCT system, fitted with Eq. (2.12). Black solid lines represent the fits.

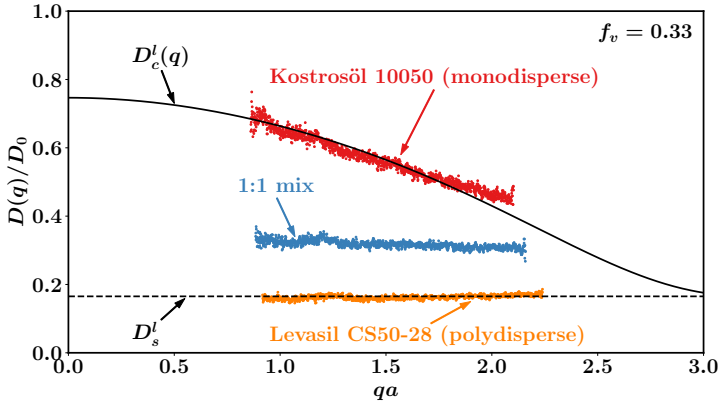

Figure 2.6: Measured q-dependent diffusion coefficient for Levasil CS50-28 (polydisperse), Kostrosöl 10050 (monodisperse), and their mixture at $f_v = 0.33$.

markably well with the long-time collective diffusion coefficient. For Levasil CS50-28 the obtained $D(q)/D_0$ is constant and matches well to the long-time self-diffusion coefficient. For the mixed sample $D(q)$ is also constant (marginally q-dependent) and lies in between D_s^l and $D_c^l(q)$. At the edges of the spectrum the obtained diffusion coefficient fluctuates, which is caused by a reduction in the signal-to-noise ratio at these wavenumbers.

2.4.2. Kostrosöl 8050 and 9550 measurements

The short-time dynamics of concentrated Kostrosöl 8050 and 9550 samples are shown in Fig. 2.7(a-i). All measurements were performed using the Thorlabs OCT system with a much higher acquisition rate and lower noise compared to the custom setup. In this case, $\Delta t = 0.028 \ll \tau_0$ ms, which implies that we are in the short-time diffusion regime. The double-exponential behavior in concentrated samples was clearly visible, which is why we used Eq. (2.15) to fit the collective and self-diffusion coefficients. Fig. 2.7(a,b,c) show the obtained first-order normalized autocovariance functions both for dilute and concentrated suspensions. The correlation functions are very similar because all samples are quite monodisperse and have similar particle sizes and concentrations. For the same reason we see in Fig. 2.7(d,e,f) that the measured $D_c(q)$ and D_s from all samples are almost identical. In this case, $D_c(q)$ matches well with the short-time collective diffusion coefficient from Eq. (2.9), and D_s matches the short-time self-diffusion coefficient from Eq. (2.4). The presence of noise is also evident, highlighting the added value of averaging over different wavenumbers.

Since the self-term becomes visible at larger lag times, it is theoretically possible that we measure D_s^l rather than D_s^s. However, the obtained results match well with the calculated values of D_s^s. The only parameters that differ among these samples are the mode amplitudes $A_c(q)$ and $A_s(q)$, as shown in Fig. 2.7(g,h,i).

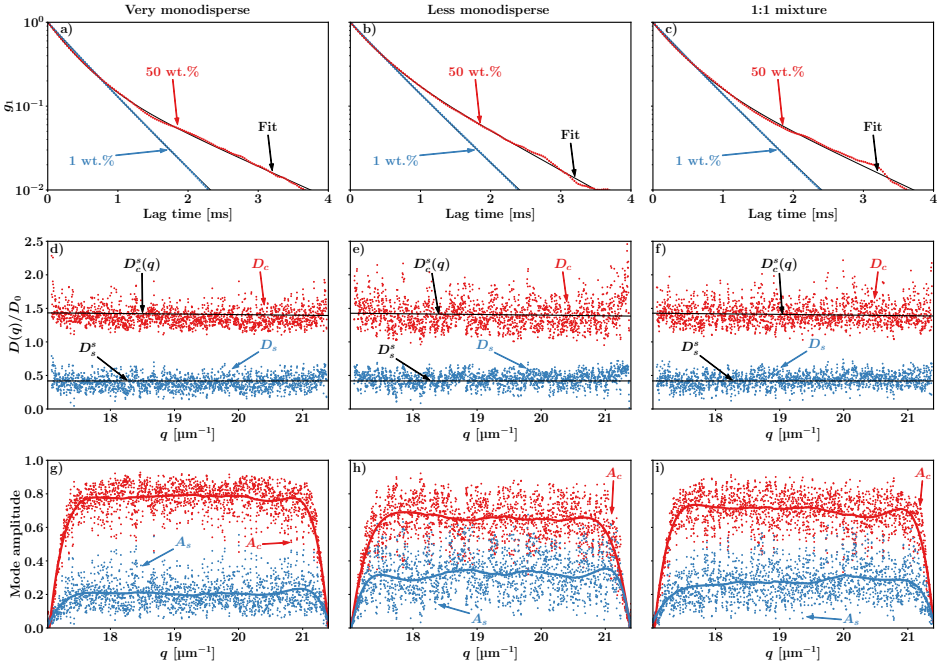

Figure 2.7: Kostrosöl 9550 (very monodisperse) and 8050 (less monodisperse), and their mixture. (a-c) Measured and fitted $g_1(q = 18.8\ \mu m^{-1}, \tau)$. (d-f) Measured and theoretical collective and self-diffusion coefficients. (g-i) Measured and smoothed collective and self mode amplitudes obtained using Thorlabs OCT.

Here, the solid curves correspond to wavenumber-smoothed data. We see that $A_c(q)$ is highest for Kostrosöl 9550 and lowest for Kostrosöl 8050, while $A_s(q)$ is highest for Kostrosöl 8050 and lowest for Kostrosöl 9550. These differences can be explained by the difference in size polydispersities between these samples. Despite having nearly identical volume-based and intensity-based polydispersity indices, the number-based particle size distribution for Kostrosöl 8050 exhibits significantly less monodispersity, as shown in Fig. 2.10(b), compared to that of Kostrosöl 9550, as illustrated in Fig. 2.10(d). Hence, the self-diffusion amplitude for Kostrosöl 8050 is larger. This contrast is highlighted by the provided $\frac{\langle a \rangle_v}{\langle a \rangle_N}$ data from Table 2.2.

Particle number-based polydispersity indices were calculated from measurements of concentrated samples using the ratio of collective and self-mode amplitudes. This approach is valid at all diffusion time scales. For each sample we calculated $\frac{A_s(q)}{A_c(q)}$ and averaged it over the wavenumber range with SNR > 10. PDI_N values were determined numerically by inverting Eq. (2.18) and the results are given in Table 2.4. Unlike the intensity-based polydispersity indices measured in dilute samples, the PDI_N obtained from concentrated suspensions differs between Kostrosöl samples indicating the variation in number polydispersity. While PDI_N is

not directly comparable with the manufacturer-provided $\frac{\langle a \rangle_v}{\langle a \rangle_N}$ from Appendix 2.7, we expect them to be almost proportional based on Fig. 2.2(b), which is exactly what we observe in Table 2.4.

Sample	PDI_N	$\frac{\langle a \rangle_v}{\langle a \rangle_N}$
Kostrosöl 8050	0.061 ± 0.002	1.645
Kostrosöl 9550	0.029 ± 0.001	1.033
Kostrosöl 8050 & 9550 1:1 mix	0.045 ± 0.001	1.379

Table 2.4: PDI_N obtained from concentrated particle suspensions using Thorlabs OCT, along with the manufacturer-provided ratio $\frac{\langle a \rangle_v}{\langle a \rangle_N}$.

2.5. Discussion

In this work we investigated q-dependent diffusion coefficients in concentrated (silica) particle suspensions at short and long times. We measured collective and/or self-diffusion coefficients in samples with similar particle sizes and varying degrees of size (and optical) polydispersities. The results were consistent with calculations based on hard-sphere diffusion theory.

We determined long-time diffusion coefficients in Levasil CS50-28 and Kostrosöl 10050 samples using a custom-built OCT system with a broad wavelength range and a relatively long sampling time. The average particle size for both samples was nearly 100 nm, but the polydispersities were different. In monodisperse Kostrosöl 10050 we measured the wavenumber-dependent collective diffusion coefficient $D_c^l(q)$. The obtained $g_1(q,\tau)$ was pure single exponential and the self-diffusion term from the decoupling approximation could not be observed. This is primarily attributed to low size and optical polydispersities of the sample. The sample Levasil CS50-28 exhibited much greater polydispersity; however, in this case, only the self-diffusion coefficient D_s^l was measured. This suggests that, in this scenario, the self-diffusion contribution to the correlation function is significantly larger compared to the collective diffusion. This is precisely what we expect when we analyze the curves in Fig. 2.2(a,b). Here, we anticipate that the PDI_N values of Levasil CS50-28 and its mixture will be very high, resulting in $A_s \gg A_c$. Therefore, it is unsurprising that only self-diffusion is measured, which also is in good agreement with the theoretical estimate. The diffusion coefficient obtained from the mixed sample remained nearly constant with q and was notably higher than D_s^l. Due to the high sample polydispersity, it is more likely that we are still measuring self-diffusion, but D_s^l deviates from the value predicted by Eq. (2.6). Therefore, similar to the method used for Kostrosöl 10050, a viscosity measurement is needed to estimate D_s^l more accurately using Eq. (2.7). Additionally, there is a possibility that both the collective and self terms were measured, but they cannot be separated. It has been suggested that when the amplitudes and the diffusion coefficients of the collective and self-diffusion modes are comparable, separating these modes becomes problematic, resulting in the measurement of a mixed diffusion coefficient [17]. Overall,

the decoupling approximation appears to work remarkably well even for moderately polydisperse samples.

We employed the fast acquisition Thorlabs OCT system to measure the short-time diffusive dynamics in Kostrosöl 8050 and 9550. These suspensions were quite monodisperse with the average particle size of approximately 75 nm. In this case, the obtained $g_1(q,\tau)$ clearly exhibited a double-exponential behavior, enabling us to measure both the self and collective terms. This is likely attributed to the utilization of a faster and more sensitive OCT system with lower q and the use of smaller particles, resulting in lower qa value. First, as illustrated in Fig. 2.1(c,d), decreasing qa increases the difference between $D_c^s(q)$ and D_s^s, making the collective and self modes more distinguishable. Second, at low qa values, self-diffusion becomes significant even for monodisperse suspensions due to a reduction in the structure factor [22]. For the Thorlabs system the wavenumber range was limited due to a narrow spectral bandwidth. Therefore, we could not clearly observe the wavenumber-dependent variations in the collective diffusion coefficient. Nevertheless, we find it feasible to measure self-diffusion even in monodisperse particle suspensions due to optical polydispersity. In this study, our primary focus was on investigating the impact of particle size variations on optical polydispersity. We did not consider refractive index dispersity, which is always present to some degree, and further contributes to increasing optical polydispersity [47].

The smallest particle radius that our custom-built DLS-OCT system can reliably measure in a dilute aqueous suspension at all wavelengths is limited by the acquisition rate of the spectrometer to around 50 nm. Additionally, the signal-to-noise ratio is constrained by the 212 µs dead time of the spectrometer. Therefore, a faster spectrometer without dead time will provide increased sensitivity and access to shorter diffusion times. Furthermore, self-interference inside the multimode fiber also decreases the experimental SNR, which could potentially be improved by altering the setup to a free-space system.

2.5.1. Particle sizing

Diffusion measurements can be used for in-line particle sizing during process control [66]. However, in concentrated particle suspensions there is no simple relation between the diffusion coefficient and the particle size. The self-diffusion coefficient is wavenumber-independent and depends both on particle size and concentration. So, without a-priori knowledge of the particle concentration, D_s cannot be used to determine the particle size. The collective diffusion coefficient, on the other hand, is wavenumber-dependent. So, when measured over a sufficient q-range, $D_c(q)$ can be used to determine both the particle size and concentration. This is only possible with large-bandwidth OCT systems covering a wide q-range, capable of capturing q-dependent variations in the collective diffusion coefficient.

For our long-time analysis, we inverted Eq. (2.11) and performed a fit for both a and f_v using the measured $D_c^l(q)$ in Kostrosöl 10050. The fitted values for particle size and volume fraction were $a = 50 \pm 2$ nm and $f_v = 0.18 \pm 0.02$, respectively. The measured and fitted $D_c^l(q)$ are shown in Fig. 2.8(a). The obtained particle radius is remarkably close to the expected value, but the volume fraction deviates

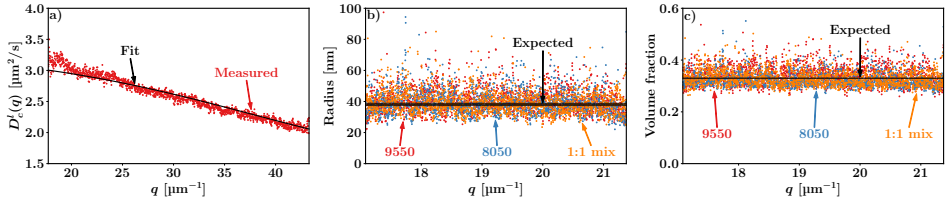

Figure 2.8: (a) Measured and fitted $D_c^l(q)$ for Kostrosöl 10050. (b) Fitted particle size and (c) volume fraction for Kostrosöl 8050, 9550, and their mixture.

considerably. This deviation is likely caused by an inaccurate estimation of the long-time self-diffusion coefficient using Eq. (2.6) in the fitting procedure. For Kostrosöl 10050, based on Eq. (2.7) and the measured viscosity, $D_s^l/D_0 = 0.21$. In contrast, according to Eq. (2.6), $D_s^l/D_0 = 0.17$. It is evident that Eq. (2.6) slightly underestimates D_s^l for Kostrosöl 10050. Since $D_c^l(q) \propto D_s^l$, using Eq. (2.6) in our fit introduces a bias into the obtained parameters. However, this bias affects f_v more because it is more sensitive to the magnitude of $D_c^l(q)$. Conversely, the particle radius is more sensitive to the slope and shape of the $D_c^l(q)$ curve, leading to a more accurate estimation.

In the short-time analysis, both the collective and self-diffusion coefficients are obtained from the fit and wavenumber-dependent measurements are not necessary to simultaneously determine the values of a and f_v. In this scenario, we have two measurements of D_s^s and D_c^s and two unknown parameters, which can be solved using a nonlinear system of equations. Consequently, we inverted $D_c^s(q)$ and D_s^s from the δY theory and utilized our measurements of the samples Kostrosöl 8050, 9550, and their mixture to determine the particle radius and volume fraction in each sample. In this case, we obtain values for a and f_v at every single q without the need to fit over the large q-range. This also allows the analysis to be conducted in the depth-domain. Figure 2.8(b) shows the fitted a as a function of q along with the expected particle radius range for these samples. The average particle sizes over the entire q-range, along with their corresponding standard deviations, for Kostrosöl 8050, 9550, and their mixture were 39 ± 9, 41 ± 9, and 39 ± 8 nm, respectively. The averaged volume fractions obtained for these samples are presented in Fig. 2.8(c) and correspond to 0.32 ± 0.03, 0.34 ± 0.04, and 0.33 ± 0.04, respectively. So there is a good agreement with the expected values for a and f_v, although the noise in Fig. 2.8(b,c) is also significant. So, even if q-dependent measurements are not available, it is possible to obtain the particle size and volume fraction in concentrated suspensions from fast correlation measurements of both the collective and self-diffusion coefficients. Regardless of which diffusion coefficient is obtained, it is always necessary to determine whether the measurement corresponds to long- or short-time particle dynamics. This determination is not trivial, as it depends not only on the acquisition speed but also on the to-be-estimated particle size. Furthermore, accurate estimates of collective and self-diffusion, crucial in determining particle size, depend on known particle interactions. While we

assumed hard-sphere interactions, in industrial scenarios, these interactions may remain unknown.

2.5.2. Polydispersity measurement

We observed that the intensity-based polydispersity index, PDI_I, measured using DLS-OCT in dilute particle suspensions, demonstrates less sensitivity towards smaller particles compared to its number-based counterpart, PDI_N. This difference arises from the influence of particle size on the measured PDI_I, which depends on both the scattering intensities and decay rates of the particles. Smaller particles scatter less light and exhibit faster decaying autocorrelations, making them more challenging to detect.

The PDI_I values obtained from the dilute samples Kostrosöl 8050, 9550 and their mixture using the cumulant analysis were virtually identical even though the actual number-based polydispersities were knowingly different. In concentrated suspensions, where both collective and self-diffusion are measured, we used the ratio of the self over collective mode amplitudes to determine PDI_N. Our method measures PDI_N by observing exchange diffusion, where particles swap positions, leading to variations in the intensity of scattered light. This method proved to be much more sensitive to particles of all sizes and can effectively differentiate samples with very similar PDI_v and PDI_I but different PDI_N. The results obtained using this technique closely matched our expectations based on the manufacturer-provided number polydispersities. Our approach relies on assuming a normal distribution for the particle size to establish an analytic relationship between PDI_N and $\frac{A_s(q)}{A_c(q)}$. However, our method is not restricted to Gaussian distributions and can be extended to particle size distributions of any a priori assumed shape, as long as the decoupling approximation remains valid.

2.6. Conclusion

We demonstrated the application of q-dependent DLS-OCT to measure both collective and self-diffusion coefficients in concentrated silica suspensions. Depending on the sample polydispersity, we successfully measured either long-time collective or long-time self-diffusion over a broad q-range using our custom-built OCT system. The obtained long-time collective diffusion coefficient agreed well with hard-sphere theory, providing further evidence for the dynamic scaling property [14]. Fitting the particle size and volume fraction of the suspension to the q-dependent collective diffusion coefficient resulted in excellent agreement for particle size but yielded a less accurate estimate of the volume fraction.

We found the decoupling approximation to be highly effective in describing the first-order normalized autocovariance functions in both monodisperse and relatively polydisperse samples. Utilizing a high-speed yet narrow q-range Thorlabs OCT system, we simultaneously measured collective and self-diffusion even in sufficiently monodisperse samples. Using both terms allowed us to determine particle size and volume fraction at a single wavenumber. Furthermore, for a normal particle size distribution, we derived a relationship between the particle number-based

polydispersity index and the ratio of the self and collective mode amplitudes. This relationship was employed to determine the size polydispersity of concentrated suspensions. Our method exhibits considerably greater sensitivity to all particle sizes compared to the standard intensity-based cumulant analysis performed in DLS on dilute samples.

2.7. Acknowledgments

We would like to thank InProcess-LSP for their support and discussions. We also thank Chemiewerk Bad Köstritz GmbH for providing us with samples. Special thanks to Kelly Brouwer from Soft Condensed Matter group at Utrecht University for providing us with transmission electron microscopy images and Zeta potential measurements. This work was funded by NWO domain Applied and Engineering Sciences with the project number 17988.

Data availability

Data underlying the results presented in this paper and the relevant analysis routines are available at [67].

References

[1] C. Holt, T. G. Parker, and D. G. Dalgleish, *Measurement of particle sizes by elastic and quasi-elastic light scattering,* Biochimica et Biophysica Acta (BBA) - Protein Structure **400**, 283 (1975).

[2] W. Tscharnuter, *Photon correlation spectroscopy in particle sizing,* in *Encyclopedia of Analytical Chemistry*, edited by R. Meyers (John Wiley & Sons Ltd, Chichester, 2000) p. 5469–5485.

[3] V. A. Martinez, J. H. J. Thijssen, F. Zontone, W. van Megen, and G. Bryant, *Dynamics of hard sphere suspensions using dynamic light scattering and x-ray photon correlation spectroscopy: Dynamics and scaling of the intermediate scattering function,* The Journal of Chemical Physics **134**, 054505 (2011).

[4] A. Wax, C. Yang, R. Dasari, and M. S. Feld, *Path-length-resolved dynamic light scattering: modeling the transition from single to diffusive scattering,* Applied Optics **40**, 4222–4227 (2001).

[5] J. Kalkman, R. Sprik, and T. G. van Leeuwen, *Path-length-resolved diffusive particle dynamics in spectral-domain optical coherence tomography,* Physical Review Letters **105**, 198302 (2010).

[6] K. K. Bizheva, A. M. Siegel, and D. A. Boas, *Path-length-resolved dynamic light scattering in highly scattering random media: The transition to diffusing wave spectroscopy,* Physical Review E **58**, 7664 (1998).

[7] D. A. Boas, K. K. Bizheva, and A. M. Siegel, *Using dynamic low-coherence interferometry to image Brownian motion within highly scattering media,* Optics Epxress **23**, 319 (1997).

[8] N. Weiss, T. G. van Leeuwen, and J. Kalkman, *Localized measurement of longitudinal and transverse flow velocities in colloidal suspensions using optical coherence tomography,* Physical Review E **88**, 042312 (2013).

[9] J. Lee, W. Wu, J. Y. Jiang, B. Zhu, and D. A. Boas, *Dynamic light scattering optical coherence tomography,* Optics Express **20**, 22262 (2012).

[10] K. Cheishvili and J. Kalkman, *Scanning dynamic light scattering optical coherence tomography for measurement of high omnidirectional flow velocities,* Optics Express **30**, 23382 (2022).

[11] P. N. Segrè and P. N. Pusey, *Dynamics and scaling in hard-sphere colloidal suspensions,* Physica A **235**, 9 (1997).

[12] C. W. J. Beenakker and P. Mazur, *Self-diffusion of spheres in a concentrated suspension,* Physica A **120**, 388 (1983).

[13] C. W. J. Beenakker and P. Mazur, *Diffusion of spheres in a concentrated suspension ii,* Physica A **126**, 349 (1984).

[14] P. N. Segrè and P. N. Pusey, *Scaling of the dynamic scattering function of concentrated colloidal suspensions,* Physical Review Letters **77**, 771 (1996).

[15] B. Cichocki and B. U. Felderhof, *Time-dependent self-diffusion coefficient of interacting Brownian particles,* Physical Review A **44**, 6551 (1991).

[16] A. van Blaaderen, J. Peetermans, G. Maret, and J. K. G. Dhont, *Long-time self-diffusion of spherical colloidal particles measured with flourescence recovery after photobleaching,* The Journal of Chemical Physics **96**, 4591 (1992).

[17] M. M. Kops-Werkhoven and H. M. Fijnaut, *Dynamic behavior of silica dispersions studied near the optical matching point,* The Journal of Chemical Physics **77**, 2242–2253 (1982).

[18] M. M. Kops-Werkhoven, C. Pathmamanoharan, and A. Vrij, *Concentration dependence of the self-diffusion coefficient of hard, spherical particles measured with photon correlation spectroscopy,* The Journal of Chemical Physics **77**, 5913–5922 (1982).

[19] F. Westermeier, B. Fischer, W. Roseker, G. Grübel, G. Nägele, and M. Heinen, *Structure and short-time dynamics in concentrated suspensions of charged colloids,* The Journal of Chemical Physics **137**, 114504 (2012).

[20] J. K. G. Dhont, *An Introduction to Dynamics of Colloids* (Elsevier Science B.V., 1996).

[21] A. J. Banchio and G. Nägele, *Short-time transport properties in dense suspensions: From neutral to charge stabilized colloidal spheres,* The Journal of Chemical Physics **128**, 104903 (2008).

[22] A. J. Banchio, G. Nägele, and J. Bergenholtz, *Collective diffusion, self-diffusion and freezing criteria of colloidal suspensions,* The Journal of Chemical Physics **113**, 3381–3396 (2000).

[23] P. Baur, G. Nägele, and R. Klein, *Nonexponential relaxation of density fluctuations in charge-stabilized colloids,* Physical Review E **53**, 6224 (1996).

[24] P. N. Segré, O. P. Behrend, and P. N. Pusey, *Short-time Brownian motion in colloidal suspensions: Experiment and simulation,* Physical Review E **52**, 5070 (1995).

[25] W. van Megen, R. H. Ottewill, S. M. Owens, and P. N. Pusey, *Measurement of the wave-vector dependent diffusion coefficient in concentrated particle dispersions,* The Journal of Chemical Physics **82**, 508–515 (1985).

[26] B. Cichocki and K. Hinsen, *Dynamic computer simulation of concentrated hard sphere suspensions,* Physica A **187**, 133 (1992).

[27] B. Cichocki and K. Hinsen, *Dynamic computer simulation of concentrated hard sphere suspensions,* Physica A **166**, 473 (1990).

[28] U. Genz and R. Klein, *Collective diffusion of charger spheres in the presence of hydrodynamic interaction,* Physica A **171**, 26 (1991).

[29] J. Brady, *The long-time self-diffusivity in concentrated colloidal dispersions,* Journal of Fluid Mechanics **272**, 109 (1994).

[30] P. N. Segré, S. P. Meeker, P. N. Pusey, and W. C. K. Poon, *Viscosity and structural relaxation in suspensions of hard-sphere colloids,* Physical Review Letters **75**, 958 (1995).

[31] A. Imhof, A. van Blaaderen, G. Maret, J. Mellema, and J. K. G. Dhont, *A comparison between the long-time self-diffusion and low shear viscosity of concentrated dispersions of charged colloidal silica spheres,* The Journal of Chemical Physics **100** (1994).

[32] A. J. Banchio, J. Bergenholtz, and G. Nägele, *Rheology and dynamics of colloidal suspensions,* Physical Review Letters **82**, 1792 (1999).

[33] *Scattering Methods for Condensed Matter Research: Towards Novel Applications at Future Sources*, Lecture Notes of the 43rd IFF Spring School 2012, Vol. 33 (Forschungszentrum Jülich GmbH, 2012).

[34] A. J. C. Ladd, H. Gang, Z. X. Zhu, and D. A. Weitz, *Time-dependent collective diffusion of colloidal particles,* Physical Review Letters **74**, 318 (1995).

[35] A. J. Banchio, M. Heinen, P. Holmqvist, and G. Nägele, *Short- and long-time diffusion, and dynamic scaling in suspensions of charged colloidal particles,* The Journal of Chemical Physics **148**, 134902 (2018).

[36] M. S. Wertheim, *Exact solution of the Percus-Yevick integral equation for hard spheres,* Physical Review Letters **10**, 321 (1963).

[37] E. Leutheusser, *Exact solution of the Percus-Yevick equation for a hard-core fluid in odd dimensions,* Physica A **127**, 667 (1984).

[38] D. J. Kinning and E. L. Thomas, *Hard-sphere interactions between spherical domains in diblock copolymers,* Macromolecules **17**, 1712–1718 (1984).

[39] K. Cheishvili and J. Kalkman, *Sub-diffusion flow velocimetry with number fluctuation optical coherence tomography,* Optics Express **31**, 3755 (2023).

[40] A. G. Mailer, P. S. Clegg, and P. N. Pusey, *Particle sizing by dynamic light scattering: Non-linear cumulant analysis,* Journal of Physics Condensed Matter **27** (2015).

[41] K. N. Clayton, J. W. Salameh, and S. T. Wereley, *Physical characterization of nanoparticle size and surface modification using particle scattering diffusometry,* Biomicrofluidics **10**, 054107 (2016).

[42] R. B. Miles, W. R. Lempert, and J. N. Forkey, *Laser rayleigh scattering,* Meas. Sci. Technol. **12**, R33 (2001).

[43] P. N. Pusey and W. van Megen, *Detection of small polydispersities by photon correlation spectroscopy,* The Journal of Chemical Physics **80**, 3513 (1984).

[44] G. Nägele and P. Baur, *Long-time dynamics of charged colloidal suspensions: hydrodynamic interaction effects,* Physica A **245**, 297 (1997).

[45] W. van Megen and S. M. Underwood, *Tracer diffusion in concentrated colloidal dispersions. iii. mean squared displacements and self-diffusion coefficients,* The Journal of Chemical Physics **91**, 552–559 (1989).

[46] P. N. Pusey, *Intensity fluctuation spectroscopy of charged Brownian particles: the coherent scattering function,* Journal of Physics A: Mathematical and General **11**, 119 (1978).

[47] J. Buitenhuis, J. K. G. Dhont, and H. N. W. Lekkerkerker, *Static and dynamic light scattering by concentrated colloidal suspensions of polydisperse sterically stabilized boehmite rods,* Macromolecules **27**, 7267 (1994).

[48] P. N. Pusey, H. M. Fijnaut, and A. Vrij, *Mode amplitudes in dynamic light scattering by concentrated liquid suspensions of polydisperse hard spheres,* The Journal of Chemical Physics **77**, 4270 (1982).

[49] A. van Veluwen, H. N. W. Lekkerkerker, C. G. de Kruif, and A. Vrij, *Influence of polydispersity on dynamic light scattering measurements on concentrated suspensions,* The Journal of Chemical Physics **89**, 2810 (1988).

[50] M. Jensen, I. B. Gonzalo, R. D. Engelsholm, M. Maria, N. M. Israelsen, A. Podoleanu, and O. Bang, *Noise of supercontinuum sources in spectral domain optical coherence tomography,* Journal of the Optical Society of America B **36**, A154 (2019).

[51] A. Barron and W. Algozeeb, *Physical Methods in Chemistry and Nano Science* (MiDAS Green Innovations, 2020).

[52] K. Kolmana, O. Nechyporchuka, M. Perssona, K. Holmberga, and R. Bordesa, *Preparation of silica/polyelectrolyte complexes for textile strengthening applied to painting canvas restoration,* Colloids and Surfaces A **532**, 420 (2017).

[53] J. Gapinski, A. Patkowski, A. J. Banchio, P. Holmqvist, G. Meier, M. P. Lettinga, and G. Nägele, *Collective diffusion in charge-stabilized suspensions: Concentration and salt effects,* The Journal of Chemical Physics **126**, 104905 (2007).

[54] W. C. K. Poon, E. R. Weeks, and C. P. Royall, *On measuring colloidal volume fractions,* Soft Matter **8**, 21 (2012).

[55] M. Godin, A. K. Bryan, T. P. Burg, K. Babcock, and S. R. Manalisa, *Measuring the mass, density, and size of particles and cells using a suspended microchannel resonator,* Applied Physics Letters **91**, 123121 (2007).

[56] W. Heller, *Remarks on refractive index of mixture rules,* The Journal of Physical Chemistry **69**, 1123–1129 (1965).

[57] P. N. A. Speets and J. Kalkman, *Measuring optical properties of clear and turbid media with broadband spectral interferometry,* Applied Optics **62**, 4349 (2023).

[58] *Water refractive index in dependence on temperature and wavelength: A simple approximation*, Vol. 5068 (2003).

[59] I. H. Malitson, *Interspecimen comparison of the refractive index of fused silica,* Journal of the Optical Society of America **55**, 1205 (1965).

[60] N. Cheng, *Formula for viscosity of glycerol-water mixture,* Industrial and Engineering Chemistry Research **47**, 3285 (2008).

[61] N. Uribe-Patarroyo, A. L. Post, S. Ruiz-Lopera, D. J. Faber, and B. E. Bouma, *Noise and bias in optical coherence tomography intensity signal decorrelation,* OSA Continuum **3**, 709 (2020).

[62] K. Cheishvili, B. Rieger, and J. Kalkman, *Precision and bias in dynamic light scattering optical coherence tomography measurements of diffusion and flow,* Biomedical Optics Express **15**, 1288 (2024).

[63] J. Kalkman, *Fourier-domain optical coherence tomography signal analysis and numerical modeling,* International Journal of Optics **2017**, 1 (2017).

[64] W. Schaertl and H. Sillescu, *Brownian dynamics simulations of colloidal hard spheres. effects of sample dimensionality on self-diffusion,* Journal of Statistical Physics **74**, 687–703 (1994).

[65] J. Kovář and I. Fortelný, *Effect of polydispersity on the viscosity of a suspension of hard spheres,* Rheologica Acta **23**, 454 (1984).

[66] R. Besseling, M. Damen, J. Wijgergans, M. Hermes, G. Wynia, and A. Gerich, *New unique PAT method and instrument for real-time inline size characterization of concentrated, flowing nanosuspensions,* European Journal of Pharmaceutiral Sciences **133**, 2005 (2019).

[67] K. Cheishvili, *Wavenumber-dependent DLS-OCT data and analysis routines,* https://doi.org/10.5281/zenodo.8425185 (2024).

Appendix

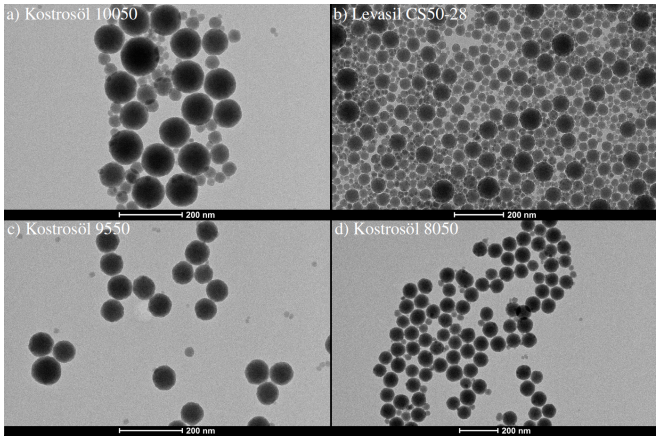

Figure 2.9: TEM images of (a) Kostrosöl 10050, (b) Levasil CS50-28, (c) Kostrosöl 9550, and (d) Kostrosöl 8050.

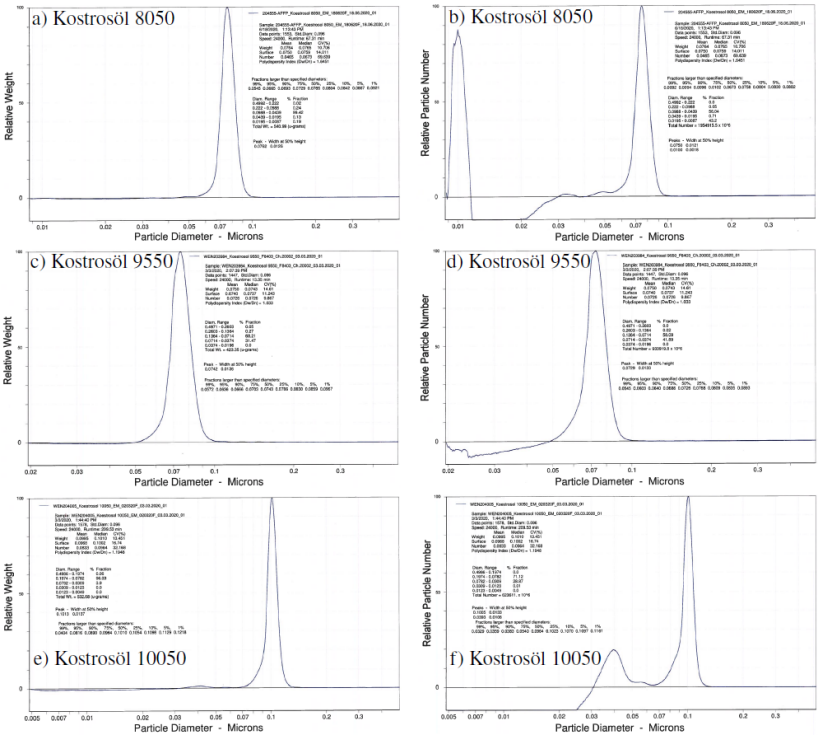

Figure 2.10: Volume (left column) and number-based (right column) PSDs for Kostrosöl (a,b) 8050, (c,d) 9550, and (e,f) 10050, determined by disc centrifuge.

3

Scanning dynamic light scattering optical coherence tomography for measurement of high omnidirectional flow velocities

We show scanning dynamic light scattering optical coherence tomography (OCT) omnidirectional flow measurements. Our method improves the velocity measurement limit over conventional correlation-based or phase-resolved Doppler OCT by more than a factor of 2. Our technique is applicable without a-priori knowledge of the flow geometry as our method works both for non-zero Doppler angle and non-ideal scan alignment. In addition, the method improves the particle diffusion coefficient estimation for particles under flow.

This chapter has been published as: **Konstantine Cheishvili** and Jeroen Kalkman, *Scanning dynamic light scattering optical coherence tomography for measurement of high omnidirectional flow velocities*, Optics Express 30(13), 23382-23397 (2022). The technique described in this chapter, *Scanning OCT off-wall particle sizing*, has also been successfully patented by TU Delft under the Patent WO2023146400A1 in 2023.

3.1. Introduction

Dynamic light scattering optical coherence tomography (DLS-OCT) relies on the measurement of fluctuations of scattered light and coherence gating to obtain simultaneous depth-resolved information about diffusive and translational motion of particles. This information is extracted from the temporal autocorrelation of the OCT signal for every voxel in depth. Initially, DLS-OCT was used for particle sizing [1] where the particle size is determined from the estimated diffusion coefficient using the Stokes-Einstein relation.

Flow measurements with OCT have been performed using the phase-resolved Doppler OCT, lateral resonant Doppler OCT [2], and M-scan correlation-based DLS-OCT [3–5]. The axial velocity of Doppler OCT is limited by phase wrapping. In the correlation-based measurements, the maximum transverse velocity is limited by the decorrelation rate, which depends on the spatial resolution of the system [6]. The axial velocity range is limited by interference fringe washout [7] and the coherence length of the source. When measuring the diffusion of particles under flow, the decorrelation in the flow causes uncertainty in the estimated diffusion coefficient [8], which, in case of high flows, cannot be measured at all.

In this work we apply beam scanning in DLS-OCT to improve the maximum measurable velocity limit for omnidirectional flows. We extend the existing theoretical models [3, 9] for the OCT signal autocorrelation and incorporate the motion of the beam into it. We show that when scanning the OCT beam in the direction of the flow, the dynamic velocity range is significantly increased. We demonstrate that the B-scan correlation-based DLS-OCT method is capable of measuring a far higher range of velocities than standard Doppler OCT, lateral resonant Doppler OCT [2] or conventional correlation analysis (M-scan) with stationary beam.

3.2. Theory

3.2.1. Sample geometry

The geometry for OCT flow measurements is shown in Fig. 3.1(a). The propagation of the optical beam is in the z direction. The flow is in a channel oriented at an

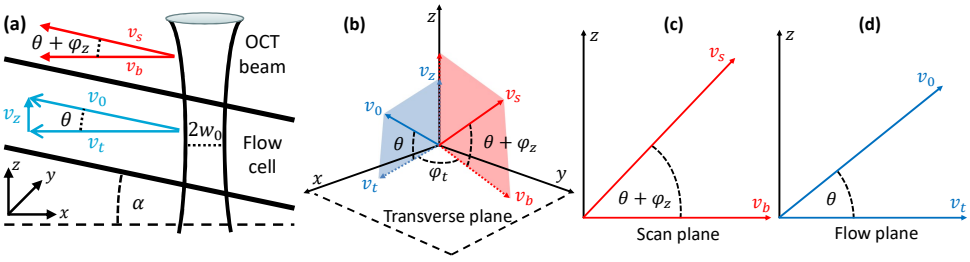

Figure 3.1: Geometry of the flow and the scanning OCT setup. (a) The flow and the OCT beam layout. (b) The flow vectors in the flow plane (blue) and scan vectors in the scan plane (red). (c) The scan plane with scan vector and its transverse projection. (d) The flow plane with flow vector and its transverse projection.

angle α with respect to the x-y plane. This angle can, due to refraction of the light, be different from the orientation of the flow direction at angle θ. In general, we assume the flow to be laminar with transverse, $v_t(z)$, and axial, $v_z(z)$, velocity components as a function of depth. Given a total flow $v_0(z)$, the flow components are expressed as $v_t(z) = v_0(z)\cos\theta$ and $v_z(z) = v_0(z)\sin\theta$. The OCT beam is a Gaussian beam characterized by the waist w_0 in focus, defined as a distance from the beam center where the field amplitude is e^{-1} of its maximum value. The OCT beam can be scanned in the direction of the flow with speed v_b in the x-y plane. The 3D scan speed along the flow is v_s, which, in general ($\theta \neq 0°$), is larger, than v_b. The more general case of 3D flow measurements with scanning OCT is shown in Fig. 3.1(b-d). Here φ_t is the angle between projections of the scan and flow vectors in the transverse plane, and φ_z is the difference between the angles that the scan and flow vectors make to their corresponding transverse projections.

Quantitative OCT flow measurements have been performed with different techniques. Here we discuss four different techniques, namely

- M-scan Doppler OCT
- B-scan Doppler OCT
- M-scan DLS-OCT
- B-scan DLS-OCT

where the last method is the new method developed by us.

3.2.2. M-scan Doppler OCT

The most used method for measuring the axial flow velocity is phase-resolved Doppler OCT. Due to the Doppler effect, the frequency of light scattered from a particle undergoing axial motion is shifted. The Doppler shift in the scattered light leads to a phase change of the OCT signal, $\Delta\phi(z)$. From the phase change the axial depth-resolved velocity $v_z(z)$ is determined using [10]

$$v_z(z) = \frac{\Delta\phi(z)}{q\Delta t}, \tag{3.1}$$

where Δt is the sampling time, and $q = 2nk_0$ is the scattering wavenumber for the backscattering probe configuration with the medium refractive index n and the vacuum wavenumber k_0. The total and axial flow velocities are related with the expression $v_0(z) = v_z(z)/\sin\theta$. The maximum velocity that can be estimated using Eq. (3.1) is limited by the Nyquist sampling criterion as

$$v_{z_{\max}} = \frac{\pi}{q\Delta t}. \tag{3.2}$$

However, Eq. (3.2) is only true for flows at low transverse velocity [10]. At high transverse velocities, because of the changing intensity of the illuminating beam on the moving particles, the phase change does not increase linearly with the velocity and approaches a constant value. This makes it impossible to determine the velocity for high lateral flow speeds.

3.2.3. B-scan Doppler OCT

As Koch et al. highlighted, transverse movements during the detector integration time as small as 20% of the beam diameter can lead to erroneous velocity measurements [10]. To correct for the deviation from Eq. (3.1) due to the short transit time of the particle through the beam, Walther and Koch suggested a method of laterally scanning the beam along the flow and performing the Doppler analysis on numerically aligned OCT data [2]. Synchronizing the OCT beam movement with the direction of the flow reduces the effective transverse velocity and its effect on the phase shift. While this method can be quite effective with uniform flows, its usability is reduced for flows where the transverse velocity components vary over depth. In that case, the transverse velocity effects cannot be fully suppressed for all depths using a single B-scan.

3.2.4. M-scan DLS-OCT

While the Doppler methods only can determine axial flows, correlation-based DLS-OCT methods can be used to determine both axial and transverse flows. For a Gaussian illuminating beam and Gaussian-shape spectral envelope, the depth-dependent autocovariance of the OCT complex signal in a backscattering geometry is given by [3, 4, 8, 9]

$$g_1(z,\tau) = A_1(z) e^{iqv_z(z)\tau} e^{-Dq^2\tau} e^{-\frac{v_z(z)^2\tau^2}{2w_z^2}} e^{-\frac{v_t(z)^2\tau^2}{w_0^2}}, \tag{3.3}$$

where D is the diffusion coefficient, w_z is the coherence function waist (e^{-1} distance) in the sample, and τ is the correlation time lag. For the Gaussian source spectrum with a wavenumber standard deviation σ_k and the sample refractive index n the coherence function waist is given by $w_z^{-1} = \sqrt{2}\sigma_k n$. The parameter $A_1(z)$ is the autocovariance amplitude containing the effect of a diminishing signal-to-noise in depth [11] and takes values between 0 and 1. Note that the decorrelation only depends on the in-focus beam radius w_0 [8, 12, 13] which makes depth-dependent analysis relatively straightforward. The decorrelation of the OCT signal magnitude is a factor two higher [1, 8] than the field decorrelation and can be expressed with the second-order autocovariance [14, 15]:

$$g_2(z,\tau) = |g_1(z,\tau)|^2 = A_2(z) e^{-2Dq^2\tau} e^{-\frac{v_z(z)^2\tau^2}{w_z^2}} e^{-\frac{2v_t(z)^2\tau^2}{w_0^2}}, \tag{3.4}$$

where $A_2(z)$ is a depth-dependent amplitude factor. Equation (3.4) is valid with the assumption that the average number of particles in the scattering volume, N, is sufficiently large ($N \gtrsim 100$) [12, 14, 16].

In this paper we focus on the second-order autocovariance function, $g_2(z,\tau)$, that does not depend on phase, is easier to implement, and can also be implemented in phase-unstable OCT systems. When the autocovariance function is used for estimating the flow, the e^{-1} decay time of the autocorrelation must be equal or larger than the temporal sampling time Δt. From this requirement, the maximum measurable transverse and axial flow speeds are

$$v_{t_{\max}} = \frac{w_0}{\sqrt{2}\Delta t}, \tag{3.5}$$

$$v_{z_{\max}} = \frac{w_z}{\Delta t}, \tag{3.6}$$

respectively. These equations are derived under the assumption of ideal δ-function sampling. However, when the measurements are performed while integrating over a specific detector time, defined by $T = \Delta t / C$ (where C is the multiplicative constant larger or equal to 1), the axial motion of a sample during the integration time causes a significant SNR degradation that limits the axial velocity to

$$v_{z_{\max}} = \frac{\pi C}{q \Delta t}. \tag{3.7}$$

Equations (3.5) and (3.6) limit the maximum measurable transverse and axial velocity components from a correlation perspective: when the effective particle displacements become comparable to the transverse and axial resolutions, the acquired signals become completely decorrelated within a single acquisition time [6]. Equation (3.7) limits the axial velocity due to fringe washout at the detector [7]. For the spectrometer-based OCT systems, the detector integration time is comparable to the sampling time, i.e, $C \gtrsim 1$. Such systems operate in the visible and infrared wavelength ranges with $q/\pi \gg w_z^{-1}$, therefore limiting the axial velocity by the fringe washout through Eq. (3.7), rather than by the axial resolution through Eq. (3.6).

3.2.5. B-scan DLS-OCT

To circumvent the limit imposed by Eq. (3.5) we propose the implementation of flow quantification using B-scan correlation-based DLS-OCT. When moving the OCT beam in any direction with a constant velocity while acquiring the signal, $v_t(z)$ and $v_z(z)$ in Eq. (3.4) must be replaced with the effective transverse $\Delta v_t(z)$ and axial $\Delta v_z(z)$ velocities, given by

$$\begin{aligned}\Delta v_t(z)^2 &= \left[v_0(z)\cos\theta - v_s \cos\varphi_t \cos\left(\varphi_z + \theta\right)\right]^2 + \left[v_s \sin\varphi_t \cos\left(\theta + \varphi_z\right)\right]^2 \\ &= v_0(z)^2 \cos^2\theta - 2v_0(z)v_s \cos\varphi_t \cos\theta \cos\left(\theta + \varphi_z\right) + v_s^2 \cos^2\left(\theta + \varphi_z\right),\end{aligned} \tag{3.8}$$

$$\Delta v_z(z)^2 = \left[\left(v_0(z)\sin\theta - v_s \sin\left(\theta + \varphi_z\right)\right]^2, \tag{3.9}$$

where v_s is the effective scan speed in 3D along the flow, φ_t and φ_z are the angles defining the scan direction relative to the flow, shown in Fig. 3.1(a-d). When the effective scan direction is sufficiently aligned with the flow velocity, so that $\cos\varphi_t \approx 1$ and $\theta + \varphi_z \approx \theta$, Eq. (3.8) and (3.9) are simplified into

$$\Delta v_t(z) = \left(v_0(z) - v_s\right)\cos\theta = \Delta v_0(z)\cos\theta, \tag{3.10}$$

$$\Delta v_z(z) = \left(v_0(z) - v_s\right)\sin\theta = \Delta v_0(z)\sin\theta, \tag{3.11}$$

which shows that with an ideal scan alignment, the ratio of the effective transverse and axial velocity components remains unchanged irrespective of the beam scan speed v_s. This simplification allows calculation of flow velocities by adding effective flow and scan speeds. Therefore, an autocovariance model of the OCT signal

magnitude for the general case of beam scanning incorporating the beam motion can be written as

$$g_2(z,\tau) = A_2(z)e^{-2Dq^2\tau}e^{-\frac{(v_0(z)-v_S)^2\sin^2\theta\,\tau^2}{w_z^2}}e^{-\frac{2(v_0(z)-v_S)^2\cos^2\theta\,\tau^2}{w_0^2}}, \tag{3.12}$$

with the limitation that the axial intensity profiles are the same for all lateral B-scan acquisitions. For Eq. (3.12), the axial velocity limit is unchanged and limited by the fringe washout via Eq. (3.7). However, the transverse velocity limit is modified; Eq. (3.5) is now limited by the relative velocity Δv_t rather than the absolute velocity v_t. This implies that for flows uniform along the length of the B-scan, the maximum measurable flow is limited by the absolute difference between flow and scan speeds. The application of lateral scanning in correlation analysis can give a significant improvement because for a typical OCT flow geometry the transverse flow is much higher than the axial flow and the limitation caused by the transverse flow, Eq. (3.5), is more restrictive than that for axial flow, Eq. (3.7). For a flow profile $v_t(z)$ the most optimum scan speed is such that the decorrelation rate is at its maximum for the highest and lowest flows, i.e., the effective scan speed v_s is a mid-range flow velocity $v_s\cos\theta = \frac{\max[v_t(z)]+\min[v_t(z)]}{2}$. This scan speed will cause maximum and equal decorrelation rates for the maximum and minimum flow speeds. Hence, with optimal scan speed, the maximum transverse velocity is limited to

$$v_{t_{\max,B}} = \frac{\sqrt{2}w_0}{\Delta t} + \min[v_t(z)], \tag{3.13}$$

or stated differently,

$$v_{t_{\max,B}} = 2\cdot v_{t_{\max,M}} + \min[v_t(z)], \tag{3.14}$$

which shows that for measuring flow profiles where a minimum velocity is zero, the B-scan flow measurement limit is a factor of 2 larger than the conventional M-scan DLS-OCT flow limit. This equation is valid within the small angle approximation between scan and flow vectors. However, to obtain the actual flow speeds, the effective scan speed needs to be added to the velocities determined with correlation after acquisition. For flows with a non-uniform transverse component, assuming that the beam can be moved at sufficiently high velocities, the maximum flow that can be determined with B-scanning is at least twice the flow that can be determined without. However, this has no effect on the axial velocity limit imposed by the fringe washout.

3.3. Materials and Methods

3.3.1. OCT system

The experiments were performed using a Thorlabs GANYMEDE II HR series spectral domain OCT System, with a bandwidth centered around 900 nm with an axial resolution of $l_c = 3$ µm in air. The OCT system was operated both in M-scan and B-scan modes. In M-scan mode, subsequent A-scans were acquired at a fixed sample position. In B-scan mode, the beam was moved in the transverse plane,

perpendicular to the illumination direction, while acquiring A-scans. Because of the telecentric scan arrangement, the scanned beam remains perpendicular to the transverse plane for all lateral positions. The acquisition rate was set at 36 kHz for all experiments. The OCT axial resolution and axial decorrelation were determined using the wavenumber spectrum standard deviation, σ_k, of the measured reference spectrum. The acquired signal spectrum was measured with a spectrometer with 2048 pixels. After acquisition, the measured spectrum was first apodized using a Gaussian filter and then resampled to a linearly-sampled wavenumber domain. After the apodization, the measured axial resolution in air and coherence function waist in sample were $l_c = 3.5$ and $w_z = 2.5$ µm, respectively.

The OCT system is operated with a scan lens (LSM04-BB, Thorlabs) in a confocal setup with a focal spot size of $w_0 = 6$ µm in air, defined as the e^{-1} radius of the field function. The NA of the system was 0.05. The manufacturer-provided waist size in air was validated by measuring the axial confocal response of a reflector moving through the beam focus. The measured values were around $w_0 = 5 - 6$ µm. However, depending on the angle of incidence, refractive index contrast and Gaussian beam parameters, w_0 varies somewhat because of the passage of the beam through the interfaces [17]. Therefore, for each experiment, w_0 was calibrated by performing a B-scan with a known transverse scan speed on a static sample, and then fitting w_0 from Eq. (3.4) using the correlation analysis. This gave results similar as for the confocal measurement, but slightly lower ($w_0 = 4.5$ µm). For maximizing the number of particles within the scattering volume, the region of interest in the dept range was moved away from the focus by approximately 0.5 mm [12]. Since for the given OCT setup the coherence length and the NA are very low, it can be assumed that the scattering angle is $180°$ and the scattering wavenumber q in the correlation analysis is constant at $q = 2nk_0$.

3.3.2. Flow system

The flow was generated using a syringe pump with variable discharge rate (Fusion 100, Chemyx) and a 60 mL syringe (BD Plastipak). The flow passes through a quartz rectangular flow cell with internal dimensions of 0.2 mm thickness and 10 mm width (type 45-F, Starna Scientific). For each experiment, the flowing sample consisted of 5 mL 20% Intralipid (Fresenius Kabi) solution dissolved in 200 mL water, resulting in a total particle volume fraction of approximately 0.5%. The refractive index of the solution was determined by measuring the OCT amplitude signal of the flow cell filled with the sample and numerically solving the following equation

$$\cos\left[\sin^{-1}\left(\frac{\sin\alpha}{n}\right)\right] = \frac{hn}{L}, \tag{3.15}$$

where h is the known flow cell thickness, L is the measured peak-to-peak optical path length difference between the flow cell surfaces, and α is the angle between the cuvette and a plane normal to the optical beam. The obtained refractive index was $n = 1.38$. As a reference, velocity profiles for the set pump discharge rates were calculated using the analytical solution for the Poiseuille flow in a rectangular

channel [18]

$$v\left(y=\frac{w}{2},z\right)=\frac{40\cdot Q}{3\pi^3 hw\left(1-0.63\frac{h}{w}\right)}\sum_{m=1,m\,\text{odd}}^{\infty}\frac{\sin\left(\frac{m\pi z}{h}\right)}{m^3}, \tag{3.16}$$

where the velocity, in mm/s, is given as a function of depth z at the flow cell half-width, w is a width of the flow cell and Q is the pump discharge rate in mL/s. All flow cell dimensions are in mm. In the analytical solution, the maximum velocities are observed at the half-width of the cell. Therefore, the OCT beam was positioned as close as possible to this location. In the transverse plane, the flow and B-scan directions were aligned as good as possible. In the axial plane, the angle α was fitted to the surface as shown in Fig. 3.2 and numerical alignment was performed using the voxel-shifting technique.

3.3.3. M-scan OCT flow measurements

In the M-scan mode, depending on the expected flow velocities, the measurement time series lengths were chosen between $N = 240$ and $N = 2845$ matching the lengths of the associated B-scan lengths. Each M-scan measurement was repeated 100 times. The beam was stationary during the whole signal acquisition period.

M-Scan Doppler OCT flow measurements

Axial velocities were determined using the depth-dependent and time-averaged phase changes from $240 - 2845$ adjacent A-scans using Eq. (3.1) with

$$\Delta\phi(z)=\left\langle\tan^{-1}\left[\frac{\mathrm{Im}\big(a(z,t)\times a^*(z,t+\Delta t)\big)}{\mathrm{Re}\big(a(z,t)\times a^*(t,t+\Delta t)\big)}\right]\right\rangle_t, \tag{3.17}$$

where $a(z,t)$ and $a(z,t+\Delta t)$ represent the complex OCT data at times t and $t+\Delta t$, respectively. Total flow velocities were determined by diving the axial velocities with $\sin\theta$.

M-scan DLS-OCT flow measurements

The M-scan correlation analysis was performed by fitting the autocovariance function using only $v_0(z)$ and $A_2(z)$ as free parameters. Prior to fitting, several reference measurements were performed. First, an M-scan measurement was performed with only diffusion and no flow. The diffusion coefficient D was determined from the fit of Eq. (3.4) to the autocovariance of the M-scan OCT signal amplitude from the stationary fluid. This measurement was performed for every time series length from $N = 240$ to $N = 2845$ to account for the statistical bias in D caused by the time series length [11]. The statistically corrected diffusion coefficient was subsequently used in all following analysis as a fixed parameter. Depending on the time series length, the measured diffusion coefficients were $1.47 - 3.80 \times 10^{-12}$ m^2/s.

Afterwards, one B-scan measurement was made under no-flow condition. From the a-priori known set B-scan velocity, the beam waist w_0 was determined using a fit of Eq. (3.4). Depending on the measurement, the obtained w_0 values were

$4.26 - 4.51$ µm. The beam waist was used in all following analysis as a fixed parameter. In the last calibration step, the Doppler angle θ was determined by using w_0, D and $v_z(z)$, obtained from the phase-resolved Doppler analysis, in combination with Eq. (3.4), fitting $v_t(z)$, and then finding the depth-averaged angle $\theta = \left\langle \arctan \frac{v_z(z)}{v_t(z)} \right\rangle_z$. This measurement was performed in M-scan mode using a low discharge rate to avoid phase wrapping. After the calibration, OCT M-scan flow measurements were performed. The total velocity, $v_0(z)$, was fitted using Eq. (3.4) on the averaged data, incorporating the calibrated D, w_0, and θ.

3.3.4. B-scan OCT flow measurements

In B-scan mode, the OCT beam was scanned while acquiring the data. The length of a time series (the number of acquired A-scans) could not be set at will, but is dependent on the scan speed, the A-scan acquisition rate, and the scan distance. With the A-scan acquisition rate at 36 kHz and the scan distance fixed to 1 mm to ensure identical sample uniformity for all measurements, the time series consisted of 240 to 2845 successive A-scans for scan speeds of 12.7 to 150.8 mm/s, respectively. One M-scan measurement was performed for obtaining the background noise of the signal amplitude in the depth domain. This amplitude was subtracted from all measurements before the numerical alignment.

B-Scan Doppler OCT flow measurements

The obtained signal was numerically aligned as described in Sec. 3.3.4. Afterwards, axial velocities were determined using the depth-dependent and time-averaged phase changes from Eq. (3.1). Total flow velocities were determined as in the M-scan Doppler mode. In the B-scan mode, the Doppler method suffered less from the effects of transverse velocities when using the depth-domain alignment compared to the frequency-domain alignment.

B-scan DLS-OCT flow measurements for scanning along an in-plane flow

For B-scan correlation-based flow measurements, the transverse scan direction of the OCT beam was aligned to the flow direction as much as possible, with $\cos\varphi_t \approx 1$ and $\theta \approx \theta + \varphi_z$. In this limiting case the only fitting parameters are $v_0(z)$ and $A_2(z)$. The scan speed was chosen to be close to the expected mid-range velocity within the flow profile, calculated analytically from the pump discharge rate, the dimensions of the flow channel, and Eq. (3.16). The same calibration measurements were used as in the M-scan mode.

B-scan DLS-OCT flow measurements for scanning along an out-of-plane flow

The application of B-scan DLS-OCT is most straightforward for a flow perpendicular to the beam. However, in the more general case of oblique flow, the same path length in the B-scan corresponds to different physical depths in the flow, and hence, direct implementation of the correlation analysis is not possible. Therefore, the data has to be numerically aligned to have identical sample locations on identical depths for all transverse points of the B-scan.

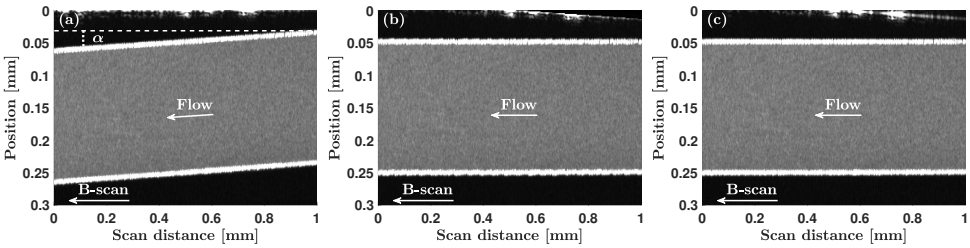

Figure 3.2: OCT numerical image alignment. (a) Original depth-resolved B-scan image. (b) B-scan alignment in the spatial domain. (c) B-scan alignment in the frequency domain.

Numerical alignment is either achieved using a spatial shift of the OCT signal in the depth domain obtained after the inverse Fourier transformation of the spectrum, or, equivalently, by using a phase multiplication in the frequency domain before the inverse Fourier transform. Figure 3.2 shows the numerical alignment process. In the depth-domain, the spatial shift is accomplished by circularly shifting depth voxels by an integer number $\Delta_z(t)$ as a function of time t according to

$$\Delta_z(t) = \text{nint}\left(\frac{nv_b t \tan\alpha}{\delta z}\right), \tag{3.18}$$

$$I(z_j, t) \Longrightarrow I(z_{j+\Delta_z(t)}, t), \tag{3.19}$$

where t is the acquisition time, α is a physical flow cell tilt angle, and δz is the voxel size interval [19]. The rounding operation is necessary as the voxels can only be shifted by an integer number. Depending on the scan direction, the voxels are shifted upwards or downwards. A fully equivalent result can be obtained in the frequency domain using

$$I(k, t) \Longrightarrow I(k, t)e^{-i2knv_b t \tan\alpha}, \tag{3.20}$$

$$I(k, t) \xrightarrow{\mathcal{F}^{-1}} I(z, t), \tag{3.21}$$

After aligning the scan and flow directions, the effective scan speed, v_s, is the effective speed at which the beam scans along the oblique flow. It is required for fitting Eq. (3.12) and can be expressed as

$$v_s = \frac{v_b}{\cos\alpha}. \tag{3.22}$$

The validity of the autocovariance model in Eq. (3.12) relies on the assumption of stationarity. This is only truly valid if the intensity fluctuations for any given depth voxel do not have an explicit dependence on time and that the average intensity remains constant. At non-zero tilt angles α these conditions are not met while B-scanning, because adjacent pixels correspond to different flow speeds and therefore are described by different random processes. The numerical re-alignment is performed to remedy this effect and make sure that adjacent pixels in time correspond to the same position in the flow channel and therefore have the same flow

speeds. However, this process introduces a mismatch between the signal levels of adjacent pixels. First, the aligned pixels in time correspond to different locations within the axial confocal PSF. Second, due to the sensitivity roll-off the OCT signal is different for these pixels. Third, depending on the axial velocity distribution, the signal decay due to the fringe washout effect may also differ. Therefore, before performing the numerical re-alignment, at each lateral position, the OCT signal intensity was normalized with the averaged depth-dependent OCT signal at that location. It was assumed that for the normalization a sufficient number of B-scans was recorded to extinguish signal fluctuations due to particle motion.

Figure 3.3 shows the processing steps for obtaining velocities. After numerically aligning the flow measurements, the autocovariance at a depth z at the center of a flow cell, where the velocity is highest was fitted using Eq. (3.12) using D, w_0, w_z and θ as input parameters to obtain the effective velocity, as shown in Fig. 3.3(a). The B-scan autocovariance decays slower than the M-scan counterpart because the scan is along the flow. Noise decorrelates in a single time step, therefore, $g_2(h/2, \tau = 0)$ is omitted from the fit. The fitted autocovariance amplitude is slightly lower for the B-scan measurement. We attribute this to the fact that the transverse beam motion degrades the OCT signal [20].

Figure 3.3(b) shows the obtained effective velocity for all depths in the flow channel. As can be seen the parabolic flow profile is mirrored at an effective velocity close to zero. The jitter velocity v_e causes the "dips" in the flow velocity profile to have a small offset. For B-scan correlation analysis, the fitted velocity is the difference between the flow and effective scan speeds, or the effective velocity, Δv_0. The flow velocity $v_0(z)$ was then obtained using

$$(v_0(z) - v_s)^2 + v_e^2 = \Delta v_0(z)^2 \,, \tag{3.23}$$

with v_s the scan velocity along the flow and v_e a non-zero fitted velocity when $v_s = v_0(z)$. Ideally, with a well-calibrated diffusion coefficient and the beam motion perfectly aligned with the flow, it is expected from the Eq. (3.10-3.12) that $v_e = 0$. However, due to small scan misalignments, galvo instability, and jitter there is additional decorrelation that leads to an offset v_e. Since v_e is much smaller than v_s and $v_0(z)$ it is only observed as $v_0(z) \approx v_s$. Therefore, v_e is obtained as the average of both minima from Fig. 3.3(b). After finding v_e, $v_0(z)$ is determined

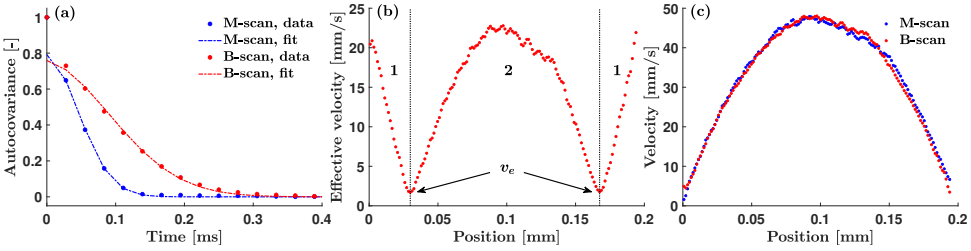

Figure 3.3: (a) M-scan and B-scan correlation functions at $z = h/2$ with the flow rate 1/15 mL/s and $\theta = 0.39°$. (a) Measured autocovariance, $g_2(h/2, \tau)$. (b) Measured $\Delta v_0(z)$ from B-scan. (c) Measured and reconstructed $v_0(z)$ from both M-scan and B-scan analysis, respectively.

by solving the quadratic equation (3.23). This equation has two solutions that are mirror reflections over the line where the effective velocity equals v_s. To find the correct value the velocity profile is split into two regions. In the region 1 the flow speed is lower than the effective scan speed, while in the region 2 the flow speed is higher than the effective scan speed. So, the solution $v_0(z) < v_s$ is chosen for the region 1 and the solution $v_0(z) > v_s$ is chosen for the region 2. Equation (3.23) can also be solved explicitly, i.e., without any assumptions for $v_0(z)$ or v_e, if two or more B-scans are performed at different speeds for the same flow velocities.

Figure 3.3(c) shows the obtained full flow profile compared to the flow profile measured with M-scan DLS-OCT. Clearly, the same flow profile is obtained.

B-scan DLS-OCT flow measurements for arbitrary scan direction and out-of-plane flow

The most general application of our method is under the condition that the flow is not in the transverse plane and that the B-scan angle is not exactly aligned with the transverse flow direction. In this case flow measurements were performed in the B-scan mode similar to the aligned condition. The scan distance was kept the same but the measurement averaging was increased from 100 to 200 scans. No assumptions were made for the angles φ_t and φ_z. The scan direction was at an angle of about $\varphi_t \approx 10^\circ$ from the flow direction. In this case, only the background noise and the beam waist calibration measurements were performed. For each flow speed, B-scans at 5 different scan speeds were acquired. Due to the purposeful misalignment, flow and scan vectors never fully match and the decorrelation rate was nonzero for every depth. Since the diffusive term is only important when the scan and flow velocities coincide (yielding low decorrelation), it was neglected here. For every acquired B-scan a total decorrelation rate $\Gamma(z)$ was obtained by fitting

$$g_2(z,\tau) = A_2(z)e^{-\Gamma(z)\tau^2} \tag{3.24}$$

to the depth-resolved OCT signal amplitude, with

$$\Gamma(z) = \frac{\Delta v_z(z)^2}{w_z^2} + \frac{2\Delta v_t(z)^2}{w_0^2}, \tag{3.25}$$

with $\Delta v_t(z)$ and $\Delta v_z(z)$ defined in Eq. (3.8-3.9). First, $\Gamma(z)$ is fitted for all five B-scan measurements at all depths. Second, an overdetermined system of equations is constructed with unknowns $v_0(z)$, θ, φ_t and φ_z. The total number of equations equals five times the number of samples in depth. Finally, the system of equations is solved simultaneously for all depths using a nonlinear least-squares method, yielding the values for $v_0(z)$, θ, φ_t and φ_z.

3.4. Experimental results

3.4.1. Flow measurements under ideal scanning alignment

Three sets of flow measurements were performed for θ values of 0.39°, 0.94° and 1.58°. For each angle, the pump discharge rates were varied from $1/30$ to $1/3$ mL/s.

Figure 3.4 shows velocity profiles obtained with M-scan Doppler OCT, M-scan DLS-OCT, B-scan Doppler OCT, and B-scan DLS-OCT, where each column corresponds to the same method. For improved data visibility, only the profiles with less than 20% relative error between the expected and measured integrated flow profiles, as well as less than 20% relative mean squared error with respect to the expected velocity profiles, are shown. Dashed parabolic curves are the theoretical velocities at the center of the cuvette, while the horizontal lines represents the maximum velocities

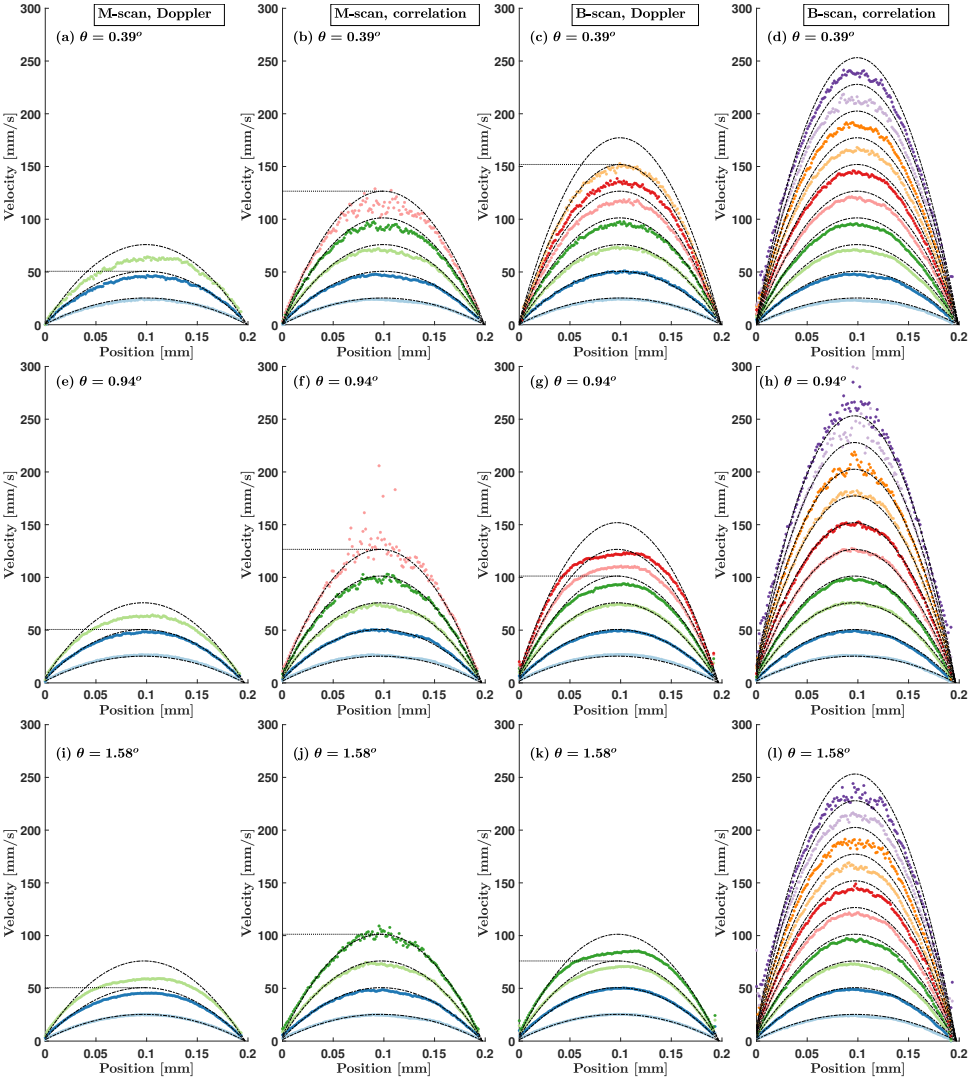

Figure 3.4: Flow profiles measured using different methods (columns) and angles (rows). (a-d) $\theta = 0.39°$. (e-h) $\theta = 0.94°$. (i-l) $\theta = 1.58°$.

that can be measured by any given method.

Figure 3.4(a,e,i) shows the M-scan Doppler OCT flow measurements. With increasing discharge rate, the phase shift approaches a constant value due to phase distortion and the profiles become inaccurate, which is consistent with the results from Koch et al. [10]. At larger angles the Doppler flow becomes less noisy. Since the flow cell is oriented almost perpendicular to the beam optical axis, the axial velocity is proportional to the Doppler angle ($\sin\theta \approx \theta$), while the transverse velocity is almost unaffected by the angle ($\cos\theta \approx 1$). The M-scan Doppler OCT has the lowest velocity dynamic range, for the current settings limited to 51 mm/s. Using simulations based on the models from [10], expected velocities at which the phase shifts, for the given geometry, deviate from the linear phase increment are above 50 mm/s, which is consistent with our observations.

Figure 3.4(b,f,j) shows the M-scan DLS-OCT flow measurements. Depending on the Doppler angle, the maximum velocity is 101-127 mm/s. The expected maximum velocity from Eq. (3.5-3.6) is approximately 115 mm/s, which is consistent with our observations. The velocity values become more noisy for higher discharge rates. In this case the velocity limit is dictated by Eq. (3.5-3.6), because the fringe washout limit has not been reached. The maximum measurable velocity slightly decreases with increasing θ. This is expected, since the coherence function waist is slightly smaller than the Gaussian beam waist. Therefore, for the same flow rate, the decorrelation becomes more rapid with increasing axial velocity. This method has a higher velocity limit compared to M-scan Doppler OCT. The flow limit for M-scan DLS-OCT is approximately a factor 2 higher than for M-scan Doppler OCT.

Figure 3.4(c,g,k) shows B-scan Doppler OCT flow measurements. Due to the reduced transverse velocity components, the velocity dynamic range has increased to a maximum flow rate of 76-127 mm/s (depending on the Doppler angle). This is consistent with the theoretical estimate of roughly 100 mm/s (double the M-scan Doppler flow limit). Deviations of the velocity increase with increasing θ values, as the phase shift approaches a constant value at lower discharge rates. Due to non-uniformity of the flow, transverse components at all depths cannot be simultaneously suppressed. This method performs similar to the M-scan DLS-OCT.

Figure 3.4(d,h,l) shows the results obtained using B-scan DLS-OCT. It has by far the highest velocity dynamic range yielding a maximum flow rate of up to 250 mm/s and a maximum speed that is unaffected by the Doppler angle, as long as the fringe washout limit is not reached. The theoretical maximum measurable velocity according to Eq. (3.5-3.6) and (3.13-3.14) is approximately 230 mm/s. This is consistent with our observation of a flow limit around 250 mm/s.

The measured profiles are in good agreement with analytical predictions, especially for $\theta = 0.94°$. However, since the flow cell is tilted, the refracted beam travels at an angle to the surface normal and with a small offset from the half-width. Therefore, for different experiments, deviations from the theoretical profiles are expected. Slightly increased noise in high flow rates for $\theta = 0.94°$ is caused by an insufficient B-scan speed that isn't set exactly at the mid-range flow velocity. Insufficiently fast scanning is not an issue for $\theta = 0.39°$ and $\theta = 1.58°$, because for these angles the measured velocities are slightly lower due to probing a different

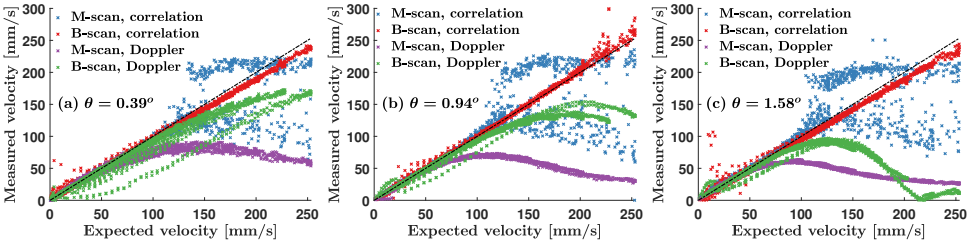

Figure 3.5: Measured versus expected flow velocities for all methods for (a) $\theta = 0.39°$, (b) $\theta = 0.94°$, and (c) $\theta = 1.58°$.

position in the flow.

To compare all flow methods simultaneously all measured velocities at a fixed angle are plotted against the expected velocities in Fig. 3.5(a-c). The black dashed curve corresponds to the expected value. For all angles, B-scan DLS-OCT follows the expected flow up to 250 mm/s. The second best method is B-scan Doppler OCT. This shows consistent flow measurements up to 76-152 mm/s, depending on the angle. Its accuracy gets worse for larger Doppler angles. M-scan DLS-OCT measurements have a dynamic range from zero up to 101-127 mm/s and are less dependent on the angle. M-scan Doppler OCT measurements level off at a maximum flow rate of 51 mm/s.

With increasing θ, M-scan and B-scan Doppler measurements deviate from the expectations at lower velocities. For the M-scan DLS-OCT measurements, the fit error becomes very large after reaching the limiting velocities. It is only the B-scan DLS-OCT measurements that show a linear behaviour for all considered flow rates. It worth noting that the B-scan methods have the same sensitivities at the highest and lowest flow speeds where the apparent velocities (due to scanning) are equal. Therefore, for these methods, higher errors are expected near the minimum and maximum flow velocities, which are visible in Fig. 3.5.

3.4.2. Omnidirectional flow measurements

Figure 3.6 shows the applicability of our method to the general situation of flow under non-zero Doppler angle and non-aligned B-scanning. Flow is measured in B-scan mode for discharge rates of $1/5$ and $1/6$ mL/s. The angle between the transverse projections of scan and flow directions, φ_t, was approximately $10°$ and φ_z was unknown. For each flow rate, 5 different scan speeds were used. For the purpose of comparison with the ideal scanning assumption, θ was also determined experimentally and found to be $1.5°$.

Figure 3.6(a) shows the fitted decorrelation parameter, $\Gamma(z)$, for every scan speed and flow rate. The variation in the magnitude of $\Gamma(z)$ for the same flow rate is due to different scan speeds used. Due to the non-aligned scanning the dips in the $\Gamma(z)$ are smoothed out as compared to Fig. 3.3(b). Figure 3.6(b) shows the flow profile obtained by solving the overdetermined system of equations for $\Gamma(z)$ without any assumptions on the angles. Uncertainties in velocity are highest at the positions of the two minima. At these positions, the system of equations is

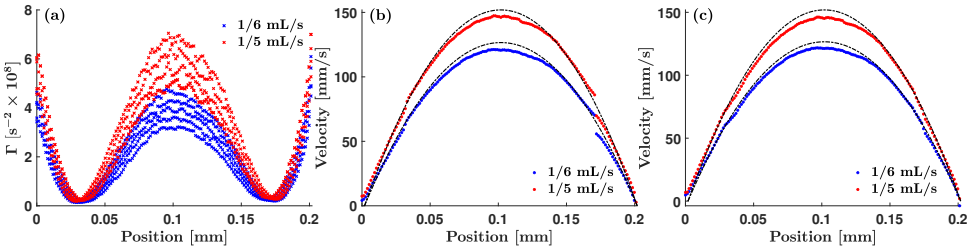

Figure 3.6: B-scan DLS-OCT flow measurements with arbitrary scan and flow directions. (a) Obtained decorrelation parameter, $\Gamma(z)$. (b) Flow profiles obtained without any assumption on the angles, averaged over all B-scan rates. (c) Velocity profiles obtained using the small angle assumption with $\theta = 1.5°$.

underdetermined because there is a very little variation in fitted decay rates for different scan speeds. As a result, multiple solutions for $v_0(z)$ could be possible at these locations leading to slightly wrong values. Outside of these locations the velocity profile is correctly estimated.

For comparison, flow profiles were also determined from the same data using $\cos\varphi_t \approx 1$, $\varphi_z + \theta \approx \theta$ and $\theta = 1.5°$. As can be seen from Fig. 3.6(c), the obtained profiles match well with the ones determined without any assumptions. This suggests that φ_t of around $10°$ degrees is still sufficiently small as to not violate the small angle approximation. The obtained results show that omnidirectional velocity profiles unambiguously can be determined without any underlying assumptions on the geometry if multiple B-scans are performed. The absence of any assumptions or careful alignment only requires the acquisition multiple B-scans and, hence, a longer acquisition time.

3.5. Discussion

Our results show that using B-scan DLS-OCT, aided with numerical data alignment, the transverse flow velocity dynamic range can be significantly increased. Moreover, our method works for arbitrary flow direction. The advantage of our method is in situations where the M-scan decorrelation limit is reached, where the Doppler angle is low, and the fringe washout limit is not reached.

For well-aligned B-scan DLS-OCT flow measurement there are minor deviations for Doppler angles of $\theta = 0.39°$ and $\theta = 1.58°$ from the theoretically calculated flow profiles. This is attributed to the uncertainties in the beam waist calibration, beam offset from the center and its alignment with the flow, as well as the pump stability. During the waist calibration measurement the beam moves over a tilted flow cell by the B-scan distance. This alters the Gaussian beam distribution within the flow cell during the scan due to the varying sample geometry [17]. Therefore, the fitted waist, which is assumed to be constant over the scan length, slightly varies over the length of the scan. This is by far the largest source of error and can be minimized by decreasing the scan distance and/or lowering the objective NA. Another source of uncertainty is the pump stability. Lastly, the position of the sample arm beam can be less than ideal. In our analysis we assumed that the beam is positioned

at the center of the flow cell in both directions. Deviations in the alignment would alter the measured flow profiles within the cell. This source of error is more severe for the B-scan methods where stationarity of the flow and diffusion dynamics along the scan is assumed.

The obtained velocity results show that the fringe washout axial velocity limit had not been reached during the experiments. B-scan DLS-OCT can measure higher flows in any geometry compared to conventional M-scan Doppler-OCT, M-scan DLS-OCT, and B-scan Doppler OCT. The optimal choice of the scan speed is important for improving the flow imaging range. The largest gain is made when the effective scan speed is in between the maximum and minimum flow speeds. In this case, according to Eq. (3.14), the maximum measurable velocity limit is at least factor 2 times higher. For the most simple analysis, the scan direction must be sufficiently close to the flow direction. However, it is worth noting that the small angle assumption produces correct results for angles as much as 10°, underlining the robustness of the method. A limitation of the method is that the flow should be uniform over the scan distance with the assumption of stationarity. Hence, the method is most appropriate for somewhat larger vessels where the diameter is much larger than the scan range. On the other hand, the scan range can be chosen arbitrarily small, while being limited by the inertia of the galvos to obtain a constant speed over small scan ranges.

Implementation of the more general case of arbitrary scan angle shows that the fitted decorrelation parameters at certain depths cannot be well determined from the measurements at different scan speeds. This is caused by the fact that the system of equations is underdetermined at those locations. This error can be decreased by increasing the number of scan velocity measurements or by fitting the velocity and angles at each depth separately [5] (instead of fitting the whole velocity profile and angles simultaneously). The latter would require a significantly larger number of B-scans, because in this case the depth-resolved equations need to be solved independently. It is worth noting that the accuracy of B-scan DLS-OCT is higher when using the Doppler angle as a fixed parameter. The Doppler angle multiplies the alignment angles from Eq. (3.8-3.9), increasing the fit error.

Our method for arbitrary scan angles can be applied for determining the transverse and axial velocity components in omnidirectional flows as neither the Doppler angle nor the φ_t and φ_z angles need to be zero. For finding the individual transverse flow components in the x- and y-directions, multiple scans in at least two linearly independent directions must be performed [5]. Our method accuracy increases with more scans at the expense of measurement time. Even when scanning at an angle with respect to the flow, it can access velocity ranges inaccessible by conventional techniques. However, it is important to note that the scan component perpendicular to the flow direction accelerates the decorrelation and adversely affects the maximum measurable velocity limits. Therefore, to achieve the highest flow measurement gain, scanning along the flow direction is favorable. Any flow measurement gain is achieved when the decorrelation reduction due to the scan component along the flow is higher than the above-mentioned decorrelation penalty.

The numerical alignment is essential in implementing B-scan DLS-OCT methods and it minimizes φ_z. In principle, the OCT signal needs to be normalized by the confocal response and sensitivity roll-off before performing the numerical alignment. For typical flow geometries with relatively low tilt angles, these functions are slowly varying at the length scales of voxel shifts and the normalization can be dropped. However, in the limit of high axial velocities, the fringe washout causes a significant decrease in the signal level [7].

Another important application of the B-scan correlation analysis is improving the accuracy in measuring the diffusion coefficient of flowing particles from their decorrelation. This is of particular importance for in-line particle sizing during process control [21]. Estimation of the diffusion coefficient under flow using the M-scan DLS-OCT becomes problematic when the flow decorrelation is at a similar rate as the diffusion decorrelation or when it entirely dominates the decorrelation [8]. This is a problem in particular for high flow rates and/or slow diffusion (large particles). By scanning along the flow, the effective flow decorrelation is minimized and the diffusion coefficient can be determined more accurately. For fast flowing suspensions in the channel, estimation of the diffusion coefficient is only possible very close to the channel walls, in a limited number of depth voxels, where the flow velocity is low. However, a close proximity to the walls creates additional unwanted effects for particles (stickiness, particle-wall interactions) and their behaviour deviates from the free diffusion. When scanning along the flow, these limitations can be removed. First, the apparent flow velocity can be minimized not near the walls but well inside the channel. These locations depend on the combination of flow and effective scan speeds. Second, the number of depth voxels where the flow decorrelation is minimal can be more than doubled.

Figure 3.7 shows the obtained normalized diffusion coefficients for the particles in the solution under flow for $\theta = 0.39^{\circ}$ at discharge rates of 1/30 mL/s and 1/15 mL/s. The black curves correspond to static diffusion measurements (no flow), blue curves correspond to the conventional M-scan diffusion measurements under flow, and red curves correspond to B-scan diffusion measurements under flow. The fitted diffusion coefficients are given with 95% confidence intervals indicated

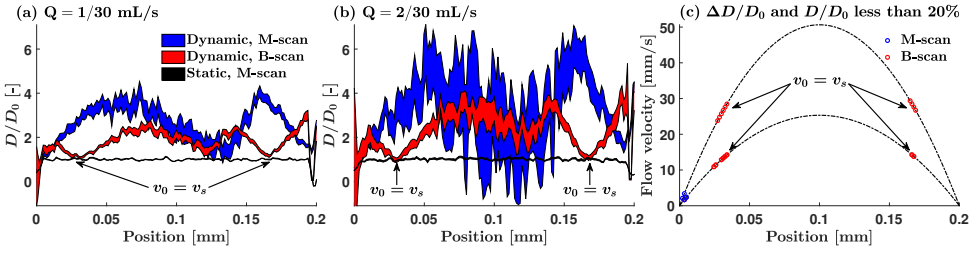

Figure 3.7: Diffusion estimation under static and flow conditions with or without scanning. (a) Normalized diffusion coefficient for 1/30 mL/s discharge rate. (b) Normalized diffusion coefficient for 1/15 mL/s discharge rate. The areas in the curve represent 95% confidence intervals. The locations where the effective scan speed equals the flow speed are indicated. (c) Locations in the flow profile where the relative error of the diffusion coefficient is less than 20%.

by the area between the two lines. For M-scan diffusion measurement the obtained diffusion coefficients become less reliable as the flow velocity increases. With the B-scan measurements, D can be estimated accurately inside the channel further away from its walls indicated by the arrows and with a higher accuracy at more depth voxels than in the M-scan mode. The advantage of our method is greater with faster flows and for samples with a larger diffusion coefficient. The measured diffusion coefficient is most accurate when the B-scan angle is aligned with the flow direction and the numerical alignment is not required. If the latter cannot be avoided, the frequency domain alignment is preferred to the spatial alignment.

3.6. Conclusion

We have implemented the B-scan correlation-based DLS-OCT method for measuring omnidirectional flows. Our method extends the maximum measurable velocity limit by at least a factor of 2 compared to the standard M-scan DLS-OCT or Doppler OCT techniques. We have shown that our method can be applied to flow geometries where a proper scan alignment is not possible. In addition, we have demonstrated that the suggested method can be used to estimate a diffusion coefficient more accurately under flow conditions.

Data availability

Data underlying the results presented in this paper and the relevant analysis routines are available at [22].

References

[1] J. Kalkman, R. Sprik, and T. G. van Leeuwen, *Path-length-resolved diffusive particle dynamics in spectral-domain optical coherence tomography,* Physical Review Letters **105**, 198302 (2010).

[2] J. Walther and E. Koch, *Flow measurement by lateral resonant Doppler optical coherence tomography in the spectral domain,* Applied Sciences **7**, 382 (2017).

[3] N. Weiss, T. G. van Leeuwen, and J. Kalkman, *Localized measurement of longitudinal and transverse flow velocities in colloidal suspensions using optical coherence tomography,* Physical Review E **88**, 042312 (2013).

[4] J. Lee, W. Wu, J. Y. Jiang, B. Zhu, and D. A. Boas, *Dynamic light scattering optical coherence tomography,* Optics Express **20**, 22262 (2012).

[5] B. K. Huang and M. A. Choma, *Resolving directional ambiguity in dynamic light scattering-based transverse motion velocimetry in optical coherence tomography,* Optics Letters **39**, 521 (2014).

[6] X. Liu, Y. Huang, J. C. Ramella-Roman, S. A. Mathews, and J. U. Kang, *Quantitative transverse flow measurement using OCT speckle decorrelation analysis,* Optics Letters **38**, 805 (2013).

[7] H. C. Hendargo, R. P. McNabb, A. Dhalla, N. Shepherd, and J. A. Izatt, *Doppler velocity detection limitations in spectrometer-based versus swept-source optical coherence tomography,* Biomedical Optics Express **2**, 2175 (2011).

[8] N. Weiss, T. G. van Leeuwen, and J. Kalkman, *Simultaneous and localized measurement of diffusion and flow using optical coherence tomography,* Optics Express **23**, 3448 (2015).

[9] N. Uribe-Patarroyo, M. Villiger, and B. E. Bouma, *Quantitative technique for robust and noise-tolerant speed measurements based on speckle decorrelation in optical coherence tomography,* Optics Express **22**, 24411 (2014).

[10] E. Koch, J. Walther, and M. Cuevas, *Limits of Fourier domain Doppler-OCT at high velocities,* Sensors and Actuators A **156**, 8 (2009).

[11] N. Uribe-Patarroyo, A. L. Post, S. Ruiz-Lopera, D. J. Faber, and B. E. Bouma, *Noise and bias in optical coherence tomography intensity signal decorrelation,* OSA Continuum **3**, 709 (2020).

[12] T. W. Taylor and C. M. Sorensen, *Gaussian beam effects on the photon correlation spectrum from a flowing Brownian motion system,* Applied Optics **25**, 2421 (1986).

[13] M. G. O. Gräfe, M. Gondre, and J. F. de Boer, *Precision analysis and optimization in phase decorrelation OCT velocimetry,* Biomedical Optics Express **10**, 1297–1314 (2019).

[14] B. J. Berne and R. Pecora, *Dynamic Light Scattering* (Dover Publications, 2000).

[15] C. S. Johnson and D. A. Gabriel, *Laser Light Scattering* (Dover Publications, 1994).

[16] D. P. Chowdhury, C. M. Sorensen, T. W. Taylor, J. F. Merklin, and T. W. Lester, *Application of photon correlation spectroscopy to flowing Brownian motion systems,* Applied Optics **23**, 4149 (1984).

[17] R. R. Vardanyan, V. K. Dallakyan, U. Kerst, and C. Boit, *Laser beam transmission and focusing inside media,* Journal of Contemporary Physics **46**, 218 (2011).

[18] H. Bruus, *Acoustofluidics 1: Governing equations in microfluidics,* Lab on a Chip **11**, 3742–3751 (2011).

[19] J. Kalkman, *Fourier-domain optical coherence tomography signal analysis and numerical modeling,* International Journal of Optics **2017**, 1 (2017).

[20] S. H. Yun, G. J. Tearney, J. F. de Boer, and B. E. Bouma, *Motion artifacts in optical coherence tomography with frequency domain ranging,* Optics Express **12**, 2977 (2004).

[21] R. Besseling, M. Damen, J. Wijgergans, M. Hermes, G. Wynia, and A. Gerich, *New unique PAT method and instrument for real-time inline size characterization of concentrated, flowing nanosuspensions,* European Journal of Pharmaceutiral Sciences **133**, 2005 (2019).

[22] K. Cheishvili, *Scanning DLS-OCT data and analysis routines,* https://doi.org/10.5281/zenodo.6425084 (2022).

4

Sub-diffusion flow velocimetry with number fluctuation optical coherence tomography

We have implemented number fluctuation dynamic light scattering optical coherence tomography (OCT) for measuring extremely slow, sub-diffusion flows of dilute particle suspensions using the second-order autocovariance function. Our method has a lower minimum measurable velocity than conventional correlation-based OCT or phase-resolved Doppler OCT as the velocity estimation is not affected by the particle diffusion. Similar to non-dilute correlation-based OCT our technique works for any Doppler angle. With our analysis we can quantitatively determine the concentration of particles under flow. Finally, we demonstrate 2D sub-diffusion flow imaging with a scanning OCT system at high rate by performing number fluctuation correlation analysis on subsequent B-scans.

This chapter has been published as: **Konstantine Cheishvili** and Jeroen Kalkman, *Sub-diffusion flow velocimetry with number fluctuation optical coherence tomography*, Optics Express 31(3), 3755-3773 (2023).

4.1. Introduction

Dynamic light scattering optical coherence tomography (DLS-OCT) relies on the measurement of fluctuations of scattered light and coherence gating to obtain simultaneous depth-resolved information about diffusive and translational motion of particles. This information is extracted from the temporal autocorrelation of the OCT signal for every voxel in depth. Initially, DLS-OCT was used for quantitative diffusion imaging [1] and quantitative flow imaging of non-dilute particle suspensions [2–4].

DLS-OCT has the advantage over the phase resolved Doppler OCT that a flow can be measured for zero Doppler angle. However, for both methods the velocity sensitivity is limited by signal-to-noise ratio (SNR) [5] and the Brownian motion of the flowing particles [2, 6]. In that case the Doppler phase shifts and the scattered light intensity fluctuations are small, are buried in the noise, or are overwhelmed by the phase/intensity changes caused by Brownian motion. Hence, it is challenging to measure sub-diffusion transverse flow rates. However, for very dilute suspensions particle motion gives rise to additional fluctuations in the scatterred intensity at longer time scales compared to particle diffusion [7, 8] and enables measurement of a sub-diffusion flow velocity.

In this work we utilize particle number fluctuations of dilute suspensions in DLS-OCT to improve the minimum measurable velocity of omnidirectional flows. We combine and extend the existing theoretical models for the normalized second-order OCT signal autocovariance and incorporate number fluctuations into them. We show that when using number fluctuations, the minimum measurable velocity of DLS-OCT is freed from the constraint imposed by diffusion. Hence, lower flow velocities can be measured compared to conventional non-dilute DLS-OCT or Doppler OCT.

4.2. Theory

The typical geometry for point scanning OCT flow measurements is visualized in Fig. 4.1. The propagation of the optical beam is along the z direction. The flow is

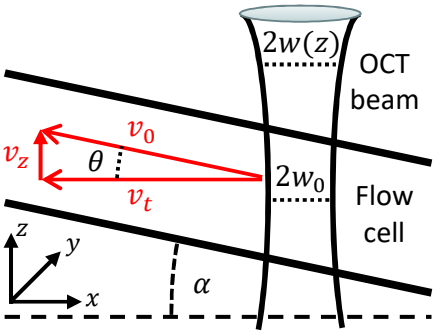

Figure 4.1: Geometry of the OCT sample arm and the fluid flow.

in a channel oriented at an angle α with respect to the x-y plane. This angle can, due to refraction of the light, be different from the orientation of the flow direction at angle θ. In general, we assume the flow to be laminar with transverse, $v_t(z)$, and axial, $v_z(z)$, velocity components as a function of depth. Given a total flow $v_0(z)$, the flow components are expressed as $v_t(z) = v_0(z)\cos\theta$ and $v_z(z) = v_0(z)\sin\theta$. The OCT beam is a Gaussian beam characterized by a waist w_0 in focus, and the local beam waist $w(z)$ at location z along the optical axis. The beam waist is defined as a distance from the beam center where the beam intensity is e^{-2} of its maximum value. The combination of the Gaussian-shaped lateral intensity and the axial coherence function gives the OCT point spread function (PSF) in the z and r-directions

$$I(r,z) = e^{-\frac{4r^2}{w^2(z)}} e^{-\frac{2z^2}{w_z^2}}, \tag{4.1}$$

where r is the radial distance from the beam center, z is the axial position, and w_z is the coherence function waist (e^{-2} intensity distance) in the sample. The additional factor 2 in the radial PSF function is due to coupling efficiency of the scattered light in a confocal setup [2, 9]. For the Gaussian source spectrum with a wavenumber standard deviation σ_k and sample refractive index n, the coherence function waist is given by $w_z^{-1} = \sqrt{2}\sigma_k n$.

In this work we discuss three different techniques for performing quantitative OCT flow measurements, namely

- Doppler OCT
- Non-dilute DLS-OCT
- Number fluctuation DLS-OCT

where the last method is the new method developed by us.

4.2.1. Doppler OCT

The most commonly used method for measuring the axial flow velocity is phase-resolved Doppler OCT. The Doppler effect gives a frequency shift to the light scattered from a particle undergoing axial motion. The Doppler frequency shift of the spectral OCT signal is equivalent to a phase change of the spatial OCT signal, $\Delta\phi(z)$. From the phase change the axial depth-resolved velocity $v_z(z)$ is determined using [10]

$$v_z(z) = \frac{2\pi f_D(z)}{q} = \frac{\Delta\phi(z)}{q\Delta t}, \tag{4.2}$$

where f_D is the Doppler frequency shift of the scattered light, Δt is the sampling time, and $q = 2nk_0$ is the scattering wavenumber for the OCT backscattering probe configuration with the medium refractive index n and the vacuum wavenumber k_0. The total and axial flow velocities are related through $v_0(z) = v_z(z)/\sin\theta$. For a shot-noise limited OCT system, the smallest observable change in the phase

measurement, $\delta\phi_{\text{sens}}$, can be obtained using [5, 11, 12]:

$$\delta\phi_{\text{sens}} = \frac{2}{\pi}\int_0^{\pi/2} \tan^{-1}\left(\sqrt{\frac{I_n}{I_s}}\sin\phi_{\text{rand}}\right) d\phi_{\text{rand}} \approx \frac{2}{\pi\sqrt{\text{SNR}}}, \tag{4.3}$$

where ϕ_{rand} is the random phase of the shot noise with uniform probability distribution over the range from 0 to 2π and $\text{SNR} = \frac{\langle I_s\rangle}{\langle I_n\rangle}$ is the measurement signal-to-noise ratio with I_s and I_n being the OCT signal and noise intensities, respectively. The minimum axial velocity that for a given signal-to-noise ratio can be estimated is obtained by replacing $\Delta\phi$ in Eq. (4.2) with $\delta\phi_{\text{sens}}$ from Eq. (4.3), which results in

$$v_{z_{\text{min, SNR}}} = \frac{2^{3/2}}{\pi q \Delta t\sqrt{\text{SNR}\cdot M}}, \tag{4.4}$$

where the additional factor of $\sqrt{2}$ in the nominator arises because the estimated velocity is proportional to the numerical difference between the measured phase and a reference phase[5]. The variable M in the denominator is the number of statistically independent phase change measurements for calculating the axial velocity. Averaging increases the flow sensitivity by a factor of $\sqrt{M}$.

The axial velocity sensitivity of Doppler OCT is further limited by the particle diffusion[6, 13, 14]. Particle diffusion causes frequency broadening of the Doppler shifted scattered light resulting in a particle diffusion broadened Lorentzian [15, 16]. For a single wavelength heterodyne system the full width at half maximum (FWHM) of the particle diffusion broadened Lorentzian is Dq^2/π, where D is the particle diffusion coefficient. However, in Fourier domain OCT the Doppler phase is calculated by multiplying/dividing intensities from different pixels on the camera, resulting in a twice as big FWHM, i.e., $\text{FWHM} = 2Dq^2/\pi$ [1]. Using this FWHM as a measure of the frequency sensitivity together with Eq. (4.2), we obtain the minimum measurable axial velocity in the presence of the particle diffusion:

$$v_{z_{\text{min, Diff}}} = \frac{4Dq}{\sqrt{M}}. \tag{4.5}$$

Assuming that both noise and diffusion are independent and not correlated, the overall axial velocity sensitivity can be expressed as

$$v_{z_{\text{min}}} = \sqrt{v^2_{z_{\text{min, SNR}}} + v^2_{z_{\text{min, Diff}}}}, \tag{4.6}$$

with the total velocity sensitivity given by $v_{0_{\text{min}}} = v_{z_{\text{min}}}/\sin\theta$.

4.2.2. Non-dilute DLS-OCT

Non-dilute DLS-OCT is based on light intensity fluctuations and is sensitive to both axial and transverse flows. For a Gaussian illuminating beam and Gaussian-shaped spectral envelope, the normalized depth-dependent autocovariance of the OCT

complex signal in a backscattering geometry, including the effect of SNR, is given by [2, 3, 17–19]

$$g_1(z,\tau) = \frac{1}{1+\frac{1}{\mathrm{SNR}(z)}} e^{iqv_z(z)\tau} e^{-Dq^2\tau} e^{-\frac{v_0^2(z)\sin^2\theta\,\tau^2}{2w_z^2}} e^{-\frac{v_0^2(z)\cos^2\theta\,\tau^2}{w_0^2}}, \qquad (4.7)$$

where τ is the autocovariance time lag. In Eq. (4.7) the effect of a gradient of the axial velocity on the autocovariance function is neglected. Note that the transverse decorrelation in Eq. (4.7) only depends on the in-focus beam radius w_0 [8, 18, 20]. The decay rate of the OCT signal intensity or magnitude is a factor two higher [1, 18] than the field decorrelation and can be expressed with the normalized second-order autocovariance [15, 16]

$$g_2(z,\tau) = |g_1(z,\tau)|^2 = \frac{1}{\left(1+\frac{1}{\mathrm{SNR}(z)}\right)^2} e^{-2Dq^2\tau} e^{-\frac{v_0^2(z)\sin^2\theta\,\tau^2}{w_z^2}} e^{-\frac{2v_0^2(z)\cos^2\theta\,\tau^2}{w_0^2}}, \qquad (4.8)$$

where we have used the Siegert relation (for a normalized second-order autocovariance the Siegert relation does not contain a constant offset). In deriving $g_2(z,\tau)$ we have assumed that the average number of particles in the scattering volume, N, is sufficiently large ($N \gtrsim 100$) [7, 8, 16]. This ensures that the particle probability distribution in the scattering volume and the scattered light fluctuations follow Gaussian statistics. This requirement is almost always satisfied for typical OCT resolutions and particle concentrations. Deviation from the Gaussian approximation requires extremely dilute samples and/or very small scattering volumes that can be achieved with extremely high spatial resolution. In this work we focus on the normalized second-order autocovariance function $g_2(z,\tau)$ for flow measurements as it does not depend on phase, is easier to implement, and can also be implemented in phase-unstable OCT systems.

Diffusion and flow decay functions multiply each other in $g_2(z,\tau)$. Therefore, to accurately determine the flow velocity, the flow decay must dominate over the diffusion decay. This depends on the dynamic time constants τ_{v_0} and τ_D (e^{-1} decay times) of flow and diffusion decorrelations, respectively. Hence, for the flow decay to dominate we require that $\tau_{v_0} \ll \tau_D$ [2], where

$$\tau_D = (2Dq^2)^{-1}, \qquad (4.9)$$

and

$$\tau_{v_0} = \left(v_0 \sqrt{\frac{\sin^2\theta}{w_z^2} + \frac{2\cos^2\theta}{w^2(z)}} \right)^{-1}. \qquad (4.10)$$

By combining and inverting Eq. (4.9-4.10) we obtain the relation

$$v_0 \sqrt{\frac{\sin^2\theta}{w_z^2} + \frac{2\cos^2\theta}{w_0^2}} \gg 2Dq^2. \qquad (4.11)$$

In the limiting case when both decays are equally strong, the minimum measurable diffusion-limited velocity for the normalized second-order autocovariance function is

$$v_{0_{\text{min, Diff}}} = 2Dq^2 \left[\frac{\sin^2\theta}{w_z^2} + \frac{2\cos^2\theta}{w_0^2} \right]^{-1/2} . \tag{4.12}$$

A finite signal-to-noise ratio further limits the minimum velocity that can be determined using intensity-based non-dilute DLS-OCT. The SNR-limited smallest observable relative change in the intensity can be obtained using [5]

$$\frac{\delta I_{\text{sens}}}{I_s} = \frac{2}{\pi\sqrt{M}} \int_0^{\pi/2} \frac{I_n}{I_s} \cos^2\phi_{\text{rand}}\, d\phi_{\text{rand}} = \frac{1}{2\text{SNR}\sqrt{M}} , \tag{4.13}$$

where the sensitivity improvement by a factor of $\sqrt{M}$ comes from recording M statistically independent observations, which we assume has the same effect for both non-dilute DLS-OCT and Doppler OCT methods.

To estimate the limit imposed by the SNR on the DLS-OCT flow sensitivity the change of the intensity of light scattered by particles is considered. The amount of scattered light varies as the particles undergo bulk motion with respect to the illuminating beam described by Eq. (4.1). The expected relative intensity change in a single time step due to transverse and axial particle motion can be estimated by moving the particle within the corresponding PSF by a distance traveled during the acquisition time Δt. Calculation of the relative intensity change requires splitting the analysis in a transverse and axial part and averaging over all possible particle locations. The expected relative intensity changes are

$$\frac{\delta I_t}{I_s} = \frac{\int_{-\infty}^{\infty} \left| e^{-\frac{4r^2}{w^2(z)}} - e^{-\frac{4(r+v_0\Delta t\cos\theta)^2}{w^2(z)}} \right| dr}{\int_{-\infty}^{\infty} e^{-\frac{4r^2}{w^2(z)}}\, dr} = \text{erf}\left(\frac{2v_0\Delta t\cos\theta}{w(z)} \right) \tag{4.14}$$

and

$$\frac{\delta I_z}{I_s} = \frac{\int_{-\infty}^{\infty} \left| e^{-\frac{2z^2}{w_z^2}} - e^{-\frac{2(z+v_0\Delta t\sin\theta)^2}{w_z^2}} \right| dz}{\int_{-\infty}^{\infty} e^{-\frac{2z^2}{w_z^2}}\, dz} = \text{erf}\left(\frac{\sqrt{2}v_0\Delta t\sin\theta}{w_z} \right) \tag{4.15}$$

for transverse and axial particle motions, respectively. Here we have neglected prefactors of exponential functions as they are identical both for nominator and denominator and cancel out. Finally, the expected relative intensity change due to a particle displacement with velocity v_0 after time step Δt can be determined by combining transverse and axial parts into

$$\frac{\delta I_0}{I_s} = \sqrt{\left(\frac{\delta I_t}{I_s}\right)^2 + \left(\frac{\delta I_z}{I_s}\right)^2} . \tag{4.16}$$

In the autocorrelation analysis, the particle flow limit is determined by the flow for which the relative intensity change is larger than or equal to, the smallest observable relative intensity change. Therefore, the SNR-limited minimum measurable velocity can be determined by solving the equation

$$\frac{\delta I_0}{I_s} = \frac{\delta I_{\text{sens}}}{I_s} \tag{4.17}$$

or equivalently

$$\sqrt{\text{erf}\left(\frac{2v_{0_{\text{min, SNR}}}\Delta t \cos\theta}{w(z)}\right)^2 + \text{erf}\left(\frac{\sqrt{2}v_{0_{\text{min, SNR}}}\Delta t \sin\theta}{w_z}\right)^2} = \frac{1}{2\text{SNR}\sqrt{M}}, \tag{4.18}$$

and finding the unknown $v_{0_{\text{min, SNR}}}$. The minimum total velocity limit is then

$$v_{0_{\text{min}}} = \sqrt{v_{0_{\text{min, SNR}}}^2 + v_{0_{\text{min, Diff}}}^2}. \tag{4.19}$$

Note that this a rough estimate using only a single change in the scattered light intensity and assuming a factor $\sqrt{M}$ improvement for M observations. In DLS-OCT the determination of the flow is performed using a fit to the normalized autocovariance function requiring a multitude of points that could further affect the actual velocity sensitivity. In addition, the sampling time Δt should be smaller than the transit time affecting the effective number of points that could be used for the fit.

4.2.3. Number fluctuation DLS-OCT

Chowdhury et al. [7] suggested that in the limit of low number of particles in the scattering volume, the dilute case with $N \ll 100$, the DLS-OCT relations for the normalized second-order autocovariance function do not apply any more as they are derived for an infinite number of particles, i.e., $g_2(z,\tau) \neq |g_1(z,\tau)|^2$. For a low number of particles in the scattering volume, additional correlations appear in the intensity due to fluctuations in the total number of scaterrers in the detected volume [21]. In this low particle number limit, the normalized second-order autocovariance function containing the effect of number fluctuations is given by

$$g_2(z,\tau) = \underbrace{\left|g_1(z,\tau)\right|^2}_{\text{Gaussian term}} + \underbrace{\langle \delta N(0)\delta N(\tau)\rangle}_{\text{number fluctuation term}}, \tag{4.20}$$

where the first term is known as the Gaussian, non-dilute, or coherent term, while the second term is known as the non-Gaussian, number fluctuation, dilute, number density, or incoherent term [7, 8, 15, 16]. Following the derivation of Chowdhury et al. [7] and Taylor and Sorensen [8], incorporating the effects of SNR [19] and a light beam with a Gaussian lateral and axial PSF, the total normalized second-order

autocovariance function $g_2(z,\tau)$ can be obtained as

$$g_2(z,\tau) = \frac{1}{\left(1+\frac{1}{\mathrm{SNR}(z)}\right)^2}\frac{2^{3/2}\langle N\rangle}{2^{3/2}\langle N\rangle+1}\left[e^{-2Dq^2\tau}e^{-\frac{v_0^2(z)\sin^2\theta\tau^2}{w_z^2}}e^{-\frac{2v_0^2(z)\cos^2\theta\tau^2}{w_0^2}}\right.$$
$$\left.+\underbrace{\frac{1}{2^{3/2}\langle N\rangle}e^{-\frac{v_0^2(z)\sin^2\theta\tau^2}{w_z^2}}e^{-\frac{2v_0^2(z)\cos^2\theta\tau^2}{w^2(z)}}}_{\text{number fluctuation term}}\right], \tag{4.21}$$

where $\langle N\rangle$ is the average number of particles in the scattering volume. In OCT, $\langle N\rangle$ corresponds to the depth-resolved number of particles per scattering volume and is a function of axial position z through the shape of the probing beam. Equation (4.21) is based on the same assumptions as Eq. (4.8), except that there is no restriction on the number of particles. Number fluctuations only affect $g_2(z,\tau)$ and have no influence on $g_1(z,\tau)$ [7, 8]. The number fluctuation term in Eq. (4.21) does not depend on diffusion, i.e., flow and diffusion decorrelations are decoupled. In general, there are diffusional number fluctuations in $g_2(z,\tau)$ [21, 22], however, the relevant time delays for these fluctuations are much larger than flow decorrelation times as they depend on the ratio of lateral resolution over diffusional displacement. With typical spatial resolutions and diffusion coefficients, these diffusive fluctuations can be neglected in the presence of flow. In contrast to the non-dilute case, the number fluctuation decay rate depends on the local beam waist, $w(z)$, and not the beam waist in focus, w_0. The expected number of particles in the scattering volume, $\langle N\rangle$, is a function of the PSF and the particle volume fraction f_v and is given by

$$\langle N\rangle = \frac{3f_vV_s}{4\pi a^3}, \tag{4.22}$$

where a is the particle radius and V_s is the scattering volume which appears as the normalization factor in $g_2(\tau,z)$. The depth-dependent V_s, found by integrating the intensity PSF over all space, is [8]:

$$V_s = 2\pi\int_0^\infty e^{-\frac{4r^2}{w^2(z)}}rdr\int_{-\infty}^\infty e^{-\frac{2z^2}{w_z^2}}dz \approx \frac{\pi^{3/2}w^2(z)w_z}{2^{5/2}}, \tag{4.23}$$

where the factor 2π in front of the integral originates from rotational symmetry of the lateral PSF. Since the coherence function waist w_z is much smaller than length scales at which the local beam waist varies significantly, $w(z)$ was assumed to be constant within the integral over the axial PSF. Combining Eq. (4.22-4.23) we find

$$\langle N\rangle = \frac{3f_v\sqrt{\pi}w^2(z)w_z}{2^{9/2}a^3}. \tag{4.24}$$

Since the OCT signal is discrete in depth, $w(z)$ is also assumed to be constant within every voxel.

For sufficiently small $\langle N\rangle$ and flow decorrelation much smaller than diffusion decorrelation ($\tau_{v_0} \gg \tau_D$), as given by Eq. (4.9-4.10), the normalized second-order

autocovariance function at larger time delays, when the Gaussian term has already decayed, is completely dominated by the number fluctuations term given by

$$g_2(z,\tau \gg \tau_D) \approx \frac{1}{\left(1+\frac{1}{\mathrm{SNR}(z)}\right)^2}\frac{1}{2^{3/2}\langle N\rangle+1} e^{-\frac{v_0^2(z)\sin^2\theta\tau^2}{w_z^2}} e^{-\frac{2v_0^2(z)\cos^2\theta\tau^2}{w^2(z)}}, \quad (4.25)$$

Therefore, for slowly flowing dilute samples, $g_2(z,\tau)$ decorrelation at larger time delays is independent of the particle diffusion and depends only on the particle flow speed. In this regime, the minimum measurable velocity is limited only by SNR. The minimum measurable velocity can be obtained by neglecting the diffusion and using only the SNR part from Eq. (4.19) in Sec. 4.2.2.

4.2.4. Flow speed sensitivity analysis

Theoretical velocity sensitivities of Doppler OCT, non-dilute DLS-OCT, and number fluctuation DLS-OCT for Doppler angles of up to 10° are plotted in Fig. 4.2, The sensitivity is quantified as δv_0 indicating the minimum measurable flow velocity and plotted versus SNR. The calculated sensitivities are based on the diffusion coefficient of 9.08×10^{-13} m^2/s, which is equivalent to a particle radius of 242 nm (average of the measurements in Table 4.1). In the calculations the following experimental values, as given in Sec. 4.3, were used: $M = 6\times30999$, $w(z)$, w_0, and Δt. Non-dilute and number fluctuation DLS-OCT methods show minimal dependence on θ as these methods work for any angle. In contrast, the Doppler OCT sensitivity strongly

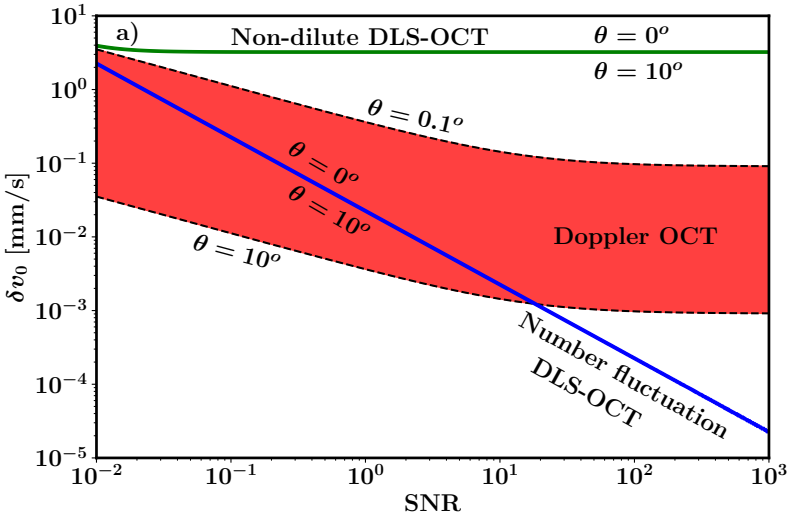

Figure 4.2: Velocity sensitivities as a function of SNR and θ for Doppler OCT, non-dilute DLS-OCT, and number fluctuation DLS-OCT.

depends on the Doppler angle with large angles resulting in a large phase shift and therefore a higher sensitivity (lower δv_0).

According to Eq. (4.4-4.6), the sensitivity of Doppler OCT is limited by SNR and particle diffusion, with both factors being independent of each other. In Fig. 4.2 we see that the Doppler OCT sensitivity levels off at higher SNR values (SNR > 10) as the diffusive limit is reached. At this stage it is no longer possible to improve the velocity sensitivity by increasing the SNR. Equations (4.12,4.17-4.19) show that non-dilute DLS-OCT is also limited by the same factors, but its diffusion limitation is much more restrictive. This is clearly visible in Fig. 4.2 where the sensitivity of this method is almost independent of SNR.

For the number fluctuation DLS-OCT the minimum measurable velocity follows the same derivation as for DLS-OCT, only there is no dependence on diffusion in Eq. (4.19). Figure 4.2 shows that its velocity sensitivity is only a function of SNR and does not level off to a constant value as it does in a diffusion-limited scenario like Doppler OCT or non-dilute DLS-OCT. For SNRs higher than 10 number fluctuation DLS-OCT has a higher sensitivity than Doppler OCT even at relatively large θ. The amount of improvement is related to the Doppler angle due to dependence of Doppler OCT sensitivity on θ.

4.2.5. Number fluctuation particle concentration estimation

Number fluctuations in DLS-OCT also can be used to determine particle concentration in a sample through the dependence of $g_2(z,\tau)$ on $\langle N\rangle$. For time delays with negligible number fluctuation flow decorrelation, the normalized second-order autocovariance function can be approximated as

$$g_2(z,\tau \ll \tau_{v_0}) \approx \frac{2^{3/2}\langle N\rangle}{2^{3/2}\langle N\rangle + 1}\left|g_1(z,\tau \ll \tau_{v_0})\right|^2 + \frac{1}{\left(1+\frac{1}{\mathrm{SNR}(z)}\right)^2}\frac{1}{2^{3/2}\langle N\rangle + 1}, \quad (4.26)$$

where the limiting time delay τ_{v_0} is given by Eq. (4.10). From Eq. (4.26) we can obtain the particle concentration by solving for $\langle N\rangle$

$$\langle N\rangle \approx \frac{\frac{1}{\left(1+\frac{1}{\mathrm{SNR}(z)}\right)^2} - g_2(z,\tau \ll \tau_{v_0})}{2^{3/2}\left[g_2(z,\tau \ll \tau_{v_0}) - \left|g_1(z,\tau \ll \tau_{v_0})\right|^2\right]}, \quad \text{with} \quad (4.27)$$

$$\frac{1}{\left(1+\frac{1}{\mathrm{SNR}(z)}\right)^2} = \left|g_1(z,\tau=0)\right|^2. \quad (4.28)$$

Here $g_1(z,\tau=0)$ is an extrapolation of the fit to the first-order normalized autocovariance function at $\tau = 0$. Note that $\langle N\rangle$ can be determined for any $\tau \ll \tau_{v_0}$, but that for practical applications it is averaged over all relevant times. Alternatively, $\langle N\rangle$ can also be calculated using

$$\langle N\rangle = \frac{\left|g_1(z,\tau=0)\right|^2}{2^{3/2}g_2(z,\tau=0)_{\langle N\rangle}} - 2^{-3/2}, \quad (4.29)$$

where $g_2(z,\tau=0)_{\langle N\rangle}$ is the extrapolation of the fit to the number fluctuation term ($\tau \gg \tau_D$) of the second-order normalized autocovariance function at $\tau = 0$.

4.3. Materials and Methods

4.3.1. OCT system

The experiments were performed using a Thorlabs GANYMEDE II HR series spectral domain OCT System, which has been described in detail in our previous work [23]. The acquisition rate was 5.5 kHz. The same datasets and time series were used both in number fluctuation DLS-OCT and Doppler OCT analyses. The OCT axial resolution and axial decorrelation were determined using the wavenumber spectrum standard deviation, σ_k, of the measured reference spectrum. The acquired signal spectrum was measured with a spectrometer with 2048 pixels. After acquisition, the measured spectrum was first resampled to a linearly-sampled wavenumber domain and then apodized using a Gaussian filter. After the apodization, the measured coherence function waist in sample was $w_z = 2.11$ µm. We have neglected the effect of a gradient of the axial velocity on the autocovariance function for two reasons [24]. First, the Doppler angles in this work are low ($\theta < 2°$). Second, our optical resolution is high both in axial and transverse directions. Hence, the flow velocity within PSF can be assumed to be constant.

The OCT system is operated with a scan lens (LSM04-BB, Thorlabs) in a confocal setup with a manufacturer provided focal spot size of $w_0 = 6$ µm in air which was validated by axial confocal response measurements, defined as the e^{-2} radius of the intensity function. The measured values were around $w_0 = 5 - 6$ µm. The NA of the system was 0.05. Depending on the angle of incidence, refractive index contrast and Gaussian beam parameters, w_0 and $w(z)$ vary somewhat because of the passage of the beam through the interfaces [25]. Therefore, for each experiment, $w(z)$ was calibrated using the procedure described in Sec. 4.3.4. For minimizing the number of particles within the scattering volume, $\langle N\rangle$, the beam waist was placed at the center of the flow channel in depth [8]. Since for the given OCT setup the coherence length and the NA are very low, it can be assumed that the scattering angle is $180°$ and the scattering wavenumber q in the correlation analysis is constant at $q = 2nk_0$.

Determination of the particle number density $\langle N\rangle$ using Eq. (4.27- 4.29) requires a-priori knowledge or an estimate of the system SNR. In this work we estimated the SNR at every depth using a fit to the measured $g_1(z,\tau)$, as described in Sec. 4.3.4. If required, the depth-resolved SNR can be measured a-priori according to the procedure described in [6]. We used this approach to verify the obtained SNR values in the particle suspension that were around $3 - 30$.

4.3.2. Flow system

The flow was generated using a syringe pump with variable discharge rate (Fusion 100, Chemyx, Inc.) and a 1 mL syringe (BD Plastipak). The flow passes through a quartz rectangular flow cell with internal dimensions of 0.5 mm thickness and 10 mm width (type 45-F, Starna Scientific). Every experiment was performed using a

0.005% volume fraction of dilute suspension of monodisperse polystyrene particles in water. The particles were supplied by InProcess-LSP with an expected radius of 257 nm. Since the particle solution was extremely dilute, the refractive index and viscosity of the sample as a function of wavelength were assumed to be identical to water at room temperature and calculated using equations from [26, 27]. The sample temperature was assumed to be $21°C$, corresponding to a water refractive index of $n = 1.33$. As a reference, velocity profiles for the set pump discharge rates were calculated using the analytical solution for the Poiseuille flow in a rectangular channel [28]

$$v(y,z) = \frac{Q}{75\pi^3 hw(1-0.63\frac{h}{w})} \sum_{m=1,m\,\text{odd}}^{\infty} \frac{\sin\left(\frac{m\pi z}{h}\right)}{m^3}\left[1 - \frac{\cosh\left(m\pi\frac{y}{h}\right)}{\cosh\left(m\pi\frac{w}{2h}\right)}\right], \quad (4.30)$$

$$v(y=0,z) \approx \frac{Q}{75\pi^3 hw\left(1-0.63\frac{h}{w}\right)} \sum_{m=1,m\,\text{odd}}^{\infty} \frac{\sin\left(\frac{m\pi z}{h}\right)}{m^3}, \quad (4.31)$$

where the velocity, in mm/s, is given as a function of depth z and lateral position y, w is the width of the flow cell in mm, h is the flow cell thickness in mm ($h < w$) and Q is the pump discharge rate in µL/s. In the analytical solution, the maximum velocities are observed at the half-width of the cell at $y = 0$. Therefore, in 1D measurements, the OCT beam focal plane was positioned as close as possible to this location to ensure a maximum decorrelation. We performed 1D flow measurements for discharges in the range of $0 - 3.33$ µL/s at three different Doppler angles. The corresponding expected flow velocities in the channel were in between $0 - 1$ mm/s. For 2D measurements only one Doppler angle was considered.

4.3.3. Doppler OCT flow measurements

Doppler OCT analysis was performed as follows: First, OCT spectra were acquired with a time series length of 31000, resulting in an acquisition time of $5 - 6$ seconds and a sampling time of $\Delta t = 5500^{-1}$ s. This measurement was repeated 6 times, resulting in $M = 6 \times 30999$ phase/intensity changes. For each time series a DC component was calculated by averaging all spectra. Second, the interference spectra were computed by subtracting the DC component from the acquired spectra. Third, a complex depth-resolved OCT signal was obtained using the inverse Fourier transformation of the interference spectra. Finally, axial velocities were determined with Eq. (4.2) using a phase estimation through

$$\Delta\phi(z) = \left\langle \tan^{-1}\left[\frac{\text{Im}\big(a(z,t)\times a^*(z,t+\Delta t)\big)}{\text{Re}\big(a(z,t)\times a^*(t,t+\Delta t)\big)}\right]\right\rangle_t, \quad (4.32)$$

where $a(z,t)$ and $a(z,t+\Delta t)$ represent the complex OCT data at times t and $t+\Delta t$, respectively. The $\langle . \rangle_t$ denotes the time averaging. All phase measurements were used in the analysis. Total flow velocities were determined by dividing the axial velocities with $\sin\theta$. The Doppler angle calibration procedure is described in Sec. 4.3.4.

4.3.4. Number fluctuation DLS-OCT flow measurements

In number fluctuation DLS-OCT the first three processing steps were the same as in the Doppler OCT analysis from Sec. 4.3.3. However, instead of determining the OCT phase, the magnitude of a complex OCT signal was calculated. Normalized temporal fluctuations of the scattered signal magnitude from dilute and non-dilute samples are shown in Fig. 4.3(a). The non-dilute OCT signal shows relatively small deviations from the mean. In contrast, the number-fluctuation OCT signal shows much larger signal variations, with a clear spike-like behavior due to particles moving in and out of the focal area. With the non-dilute sample, complex field fluctuations due to the Brownian motion of the particles follows Gaussian statistics. Hence, the field magnitude fluctuations have a Rayleigh distribution as shown in Fig. 4.3(b). In the dilute regime the OCT signal magnitude is directly proportional to the number of particles where the number of particles in the scattering volume follows the Poisson distribution [7, 8]. Therefore, it is expected that the magnitude fluctuations due to number fluctuations are also Poisson distributed, as shown in Fig. 4.3(b).

After determining field magnitude fluctuations for each acquisition, a normalized second-order autocovariance of the mean-subtracted signal magnitude was calculated at every depth. The autocovariance functions were averaged for all 6 acquisitions. Finally, Eq. (4.33) was fitted to the averaged autocovariance functions with

$$g_2(z,\tau>\tau_N) = A(z)e^{-\frac{v_0^2(z)\sin^2\theta\tau^2}{w_z^2}}e^{-\frac{2v_0^2(z)\cos^2\theta\tau^2}{w^2(z)}}, \tag{4.33}$$

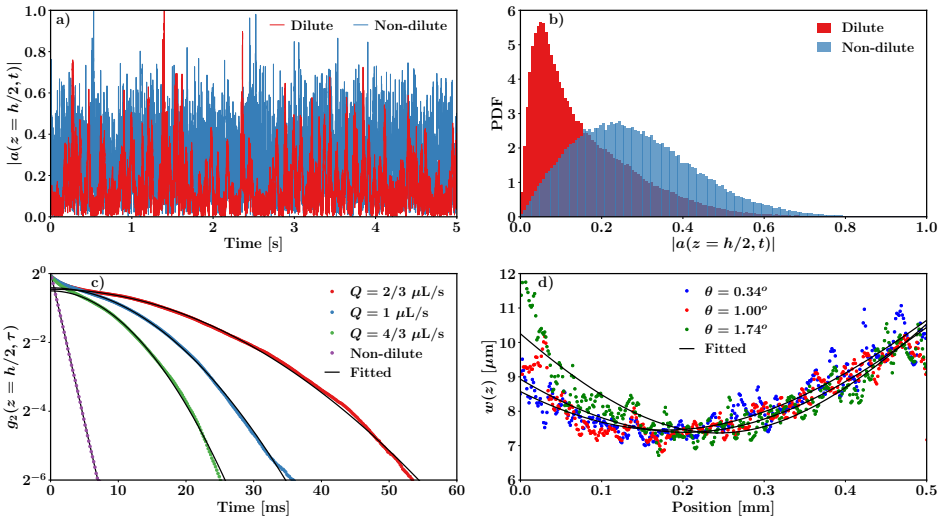

Figure 4.3: (a-b) Time trace and distribution of the OCT signal magnitude from non-dilute (0.5%) and dilute (0.005%) samples at $Q = 1$ μL/s and $\theta = 0.34°$. (c) Measured and fitted $g_2(z,\tau)$ for non-dilute and dilute samples at different flow rates and $\theta = 0.34°$. (d) Measured and fitted beam waist at different Doppler angles.

where the choice of free parameters depended on whether calibration or flow measurements were performed. In our fitting procedure only the number fluctuation term was fitted. To ensure that the diffusive term in the measured autocovariance had decayed sufficiently, only $g_2(z,\tau > \tau_N)$ was considered, where τ_N was the time delay with $g_2(z,\tau > \tau_N) > 10 \cdot |g_1(z,\tau > \tau_N)|^2$. Examples of the measured and fitted second-order autocovariance functions from the dilute sample at different discharge rates are shown in Fig. 4.3(c). For comparison, a diffusion-dominated $g_2(z,\tau)$ from the same, but more concentrated, sample is also shown. In non-dilute DLS-OCT $g_2(z,\tau)$ decays exponentially (linearly on a logarithmic scale) at low flow speeds. In number fluctuation DLS-OCT the decay is much slower and quadratic on a logarithmic scale, where the effect of a particle diffusion is visible for the Gaussian term at very small time delays with $\tau < \tau_N$. As Fig. 4.3(c) shows, the fit models match very well with the number fluctuation term of the normalized autocovariance functions at different flow rates.

To perform quantitative number fluctuation measurements, the beam waist $w(z)$ and the Doppler angle θ were determined in a two-step procedure. During the first step, a beam waist calibration was performed, as described in [23]. The beam was moved with a-priori known velocity over a stationary sample while the spectra were acquired. The local beam waist $w(z)$ was determined using a fit of Eq. (4.33) to the measured $g_2(z,\tau > \tau_N)$ with $A(z)$ and $w(z)$ being the free parameters. The obtained beam profiles for different Doppler angles are shown in Fig. 4.3(d). Here the beam shapes were fitted using $w(z) = w_0\sqrt{1 + ((z - z_0)/z_R)^2}$, with w_0, z_0, and z_R being the free parameters. The fitted beam waist values are given in table 4.1.

In the second step, the Doppler angle was determined. For this purpose any flow measurement with a sufficient Doppler signal could be used. Here $v_z(z)$ was determined using the phase-resolved Doppler analysis from Sec. 4.3.3. Then Eq. (4.33) was fitted to the measured $g_2(z,\tau > \tau_N)$, incorporating the known $w(z)$ and $v_z(z)$ while using $A(z)$ and $v_t(z)$ as free parameters. The depth-averaged angle was then determined using $\theta = \langle \arctan(v_z(z)/v_t(z)) \rangle_z$. The obtained Doppler angles are given in table 4.1. After these two calibration steps, flow measurements could be performed for the given geometry at any discharge rate. For each flow rate Eq. (4.33) was fitted to the measured $g_2(z,\tau > \tau_N)$ using $A(z)$ and $v_0(z)$ as the only fit parameters.

The number of particles in the scattering volume was obtained without any a-priori calibration or SNR measurements. Particle number density under flow was determined at the discharge rates of $1/12$ and $1/6$ µL/s using Eq. (4.29), incor-

Mode	θ [°]	a [nm]	w_0 [µm]
1D	0.34 ± 0.01	233 ± 8	7.45 ± 0.03
1D	1.00 ± 0.05	247 ± 11	7.39 ± 0.03
1D	1.74 ± 0.02	246 ± 11	7.37 ± 0.05
2D	1.84 ± 0.08	NA	7.79 ± 0.07

Table 4.1: Measured Doppler angle, particle radius, and beam waist for the four experimental conditions.

porating the fitted and extrapolated values $g_2(z,\tau=0)_{\langle N\rangle}$ and $g_1(z,\tau=0)$. The number fluctuation term of $g_2(z,\tau)$ was fitted using Eq. (4.33), and $g_1(z,\tau)$ was fitted using Eq. (4.34)

$$|g_1(z,\tau)| = \frac{1}{1+\frac{1}{\mathrm{SNR}(z)}} e^{-Dq^2\tau}, \tag{4.34}$$

with $\mathrm{SNR}(z)$ and D being the free parameters. Here we have neglected the contribution from the flow decorrelation, because $g_1(z,\tau)$ is diffusion-dominated at these flow rates and independent of number fluctuations. As a reference, the particle diffusion coefficient D was determined from the fit of Eq. (4.34) to the measured $g_1(z,\tau)$ from the stationary fluid at all Doppler angles. The diffusion coefficient is irrelevant for flow or number density measurements with the number fluctuation term of $g_2(z,\tau)$. However, it is required for determining the particle size which is used for calculating the theoretical $\langle N\rangle$ from a known particles' volume fraction. Particle radii determined using the Stokes-Einstein relation are given in table 4.1 and match the particle radius of 257 nm from the provider reasonable well.

2D flow measurements with number fluctuation DLS-OCT were performed by lateral scanning of the OCT beam along the flow cell, perpendicular to the flow direction. Even though the channel width was 10 mm, only 2 mm was imaged due to sampling limitations and the presence of aberrations. For resolving the transverse flow profile the scanning location was chosen near the flow cell edge. For 2D measurements 2000 consecutive B-scans were acquired with 100 lateral points in each scan, resulting in the total acquisition time of 44 s. Data processing steps were the same as before. However, instead of correlating the field magnitude fluctuations at a single position, the temporal autocovariance at each location in the B-scan was performed. This reduced the effective sampling rate from 5.5 kHz to approximately 45 Hz at each location in the 2D measurement. This sampling rate was still sufficiently fast to determine the flow from the number fluctuation autocovariance and enabled the implementation of number fluctuation flow imaging in conventional B-scan mode.

4.4. Experimental results

Three sets of 1D measurements were performed at the center of the flow cell for θ values of $0.34°$, $1.00°$ and $1.74°$. For each angle, the pump discharge rate was varied from $1/12$ to $10/3$ µL/s. Figure 4.4 shows velocity profiles obtained with number fluctuation DLS-OCT (top row) and phase-resolved Doppler OCT (bottom row). The parabolic curves represent the expected velocity profiles according to Eq. (4.31), the flow channel dimensions and the discharge rate. To quantitatively compare both methods, all measured velocities at a fixed angle are plotted against the expected velocities in Fig. 4.5, where the black curves corresponds to the expected values.

Figures 4.4(a,d) and 4.5(a) show number fluctuation DLS-OCT and Doppler OCT flow measurements for $\theta = 0.34°$. The Doppler OCT sensitivity is very low, making it impossible to accurately measure flow velocities for these low axial speeds. This is clearly indicated by the spread of measurements in Fig. 4.5(a). The number

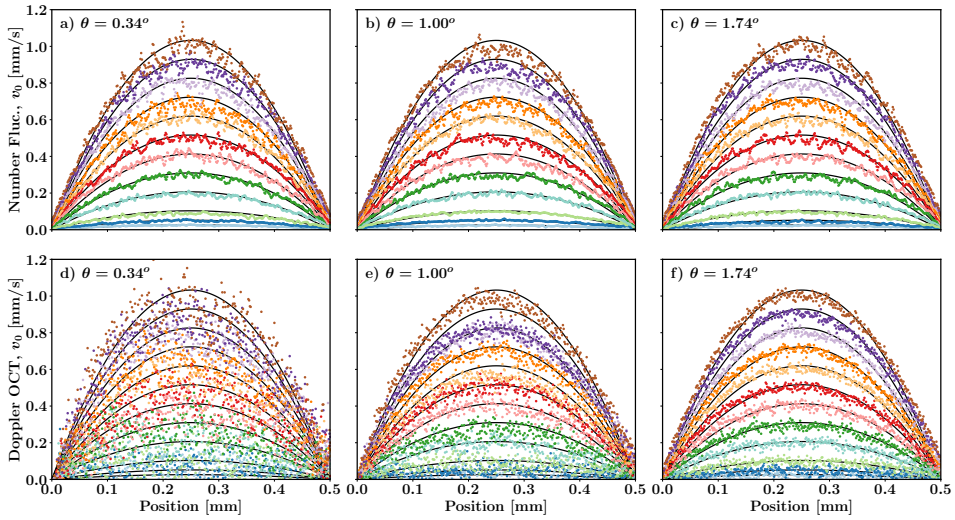

Figure 4.4: Flow profiles measured using different methods. (a-c) Number fluctuation DLS-OCT. (d-f) Phase-resolved Doppler OCT.

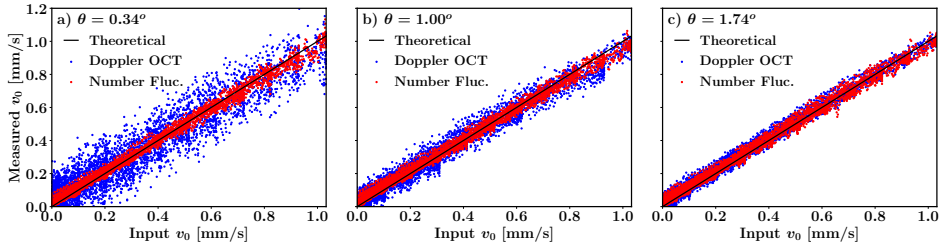

Figure 4.5: Measured versus input velocities for (a) $\theta = 0.34°$, (b) $\theta = 1.00°$, and (c) $\theta = 1.74°$.

fluctuation DLS-OCT method, on the other hand, can accurately determine flow velocities for all considered flow speeds.

Figures 4.4(b,e) and 4.5(b) show the same measurements for $\theta = 1.00°$. In this case, the Doppler OCT sensitivity is higher but still insufficient to fully resolve the flow for the different discharge rates. The spread of measurements in Fig. 4.5(b) is therefore also lower compared to Fig. 4.5(a). The accuracy of the number fluctuation DLS-OCT method is unchanged. This is indicated by accurate reconstruction of flow profiles in Fig. 4.4(b) and low spread of measurements in Fig. 4.5(b).

Figures 4.4(c,f) and 4.5(c) show the flow measurements for $\theta = 1.74°$. In this case the sensitivity of Doppler OCT is much better due to the larger axial flow component. Performance is comparable to number fluctuation DLS-OCT for higher discharge rates, but very low velocities are still poorly resolved. For low flow velocities, number fluctuation DLS-OCT technique has a superior performance compared

to Doppler OCT and also can work for zero Doppler angle.

The sensitivity of Doppler OCT strongly depends on the Doppler angle, and the minimum measurable velocity decreases with increasing θ. For number fluctuation DLS-OCT, the sensitivity is independent of the Doppler angle, which is in agreement with our expectations from Sec. 4.2.1 and 4.2.3. Number fluctuation DLS-OCT can accurately determine flow velocities for all considered flow speeds whereas the flow profiles cannot be accurately measured using non-dilute DLS-OCT, as the profile velocities are well below the limit set by diffusion, which is approximately 3.3 mm/s for our experimental setup and used Doppler angles.

In figure 4.6 we compare the measured accuracy with the expected velocity sensitivities according to the theory outlined in Sec. 4.2.1-4.2.3. The maximum velocity (at the center of the profile) was calculated for each discharge rate according to Eq. (4.31) and plotted on the x-axis. For each discharge, the velocity uncertainty was estimated by calculating the velocity profile standard deviation with respect to the best fit parabolic curve. For direct comparisons with the theoretical minimum measurable velocities, an SNR range of 3–30 was used as determined from the measurement data. Fig. 4.6(a) shows that for Doppler OCT, the obtained absolute axial velocity sensitivity is independent of Doppler angle and maximum profile velocity (discharge rate), and the minimum measurable axial velocities are slightly higher than expected. Invariance of the axial velocity sensitivity with respect to the discharge rate is expected, since it is independent of the Doppler phase shift magnitude. In Fig. 4.6(b) we see that the velocity sensitivity for number fluctuation DLS-OCT is independent of θ but changes with increasing maximum profile velocity. At low flow rates, corresponding to long decorrelation times, the measured sensitivities have the same order of magnitude as the theoretical ones for intensity fluctuations. However, the deviation increases at higher velocities when the number of relevant fit points becomes lower and fit errors increase. Figure 4.6(c) shows the estimation of the total velocity. Clearly, number fluctuation DLS-OCT is more accurate for low flow rates as would be expected from the calculated flow sensitivity advantage for constant SNR as shown in Fig. 4.2. In addition, the flow estimate does not depend on Doppler angle. This makes it easier to quantify the total flow, which is the relevant parameter.

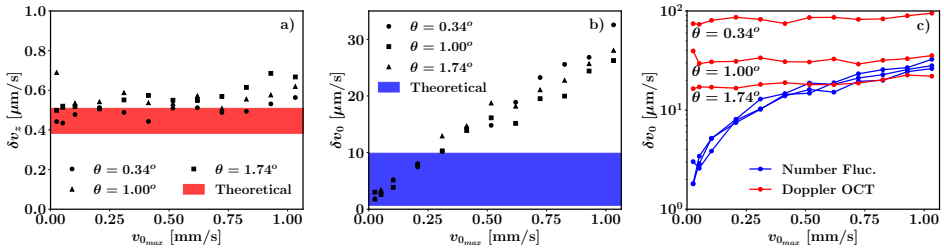

Figure 4.6: (a) Measured and expected axial velocity sensitivities for Doppler OCT, (b) measured and expected total velocity sensitivities for number fluctuation DLS-OCT, and (c) measured total velocity sensitivities for both methods versus the maximum profile velocity.

The number of particles in the scattering volume, $\langle N \rangle$, was obtained using Eq. (4.29) for the lowest two discharge rates, $1/12$ and $1/6$ µL/s, respectively. The expected number of particles was calculated using Eq. (4.24) incorporating the particle radius from Table 4.1 and other optical/sample properties. Figure 4.7 shows that the obtained number of particles in the focal area, $\langle N \rangle$, matches well with the expected distribution at positions close to beam waist. Deviations increase towards the flow cell edges where the SNR is lower and the local beam waist is larger. There is no explicit dependence on the Doppler angle and the average number of particles within the scattering volume is much lower than 1. As expected, $\langle N \rangle$ is minimum near the beam waist and is higher away from focus. Almost identical results are obtained when measuring SNR a-priori or when Eq. (4.27-4.28) are used. The measured number of particles per scattering volume can easily be converted to volume fraction using the particle size and scattering volume. Values of $\langle N \rangle$ from the central portions of Fig. 4.7 with a higher SNR correspond to particle volume fractions

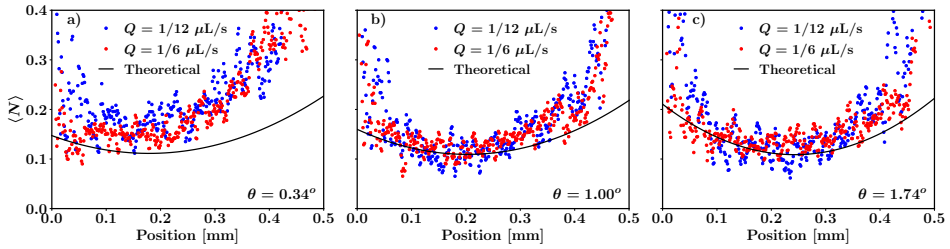

Figure 4.7: Depth-resolved number of particles in the scattering volume for (a) $\theta = 0.34°$, (b) $\theta = 1.00°$, and (c) $\theta = 1.74°$.

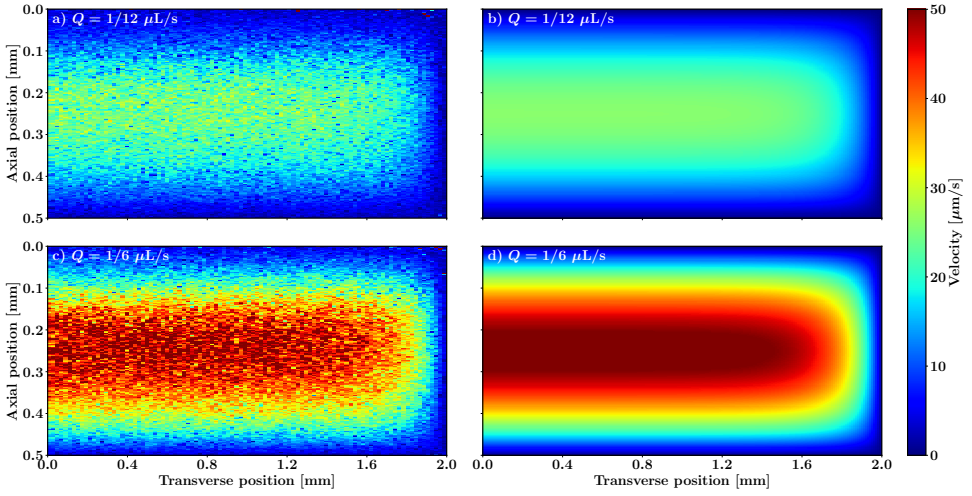

Figure 4.8: Measured (a) and expected (b) 2D velocity profiles for $Q = 1/12$ µL/s. Measured (c) and expected (d) flow profiles for $Q = 1/6$ µL/s.

$0.004 - 0.007\%$. This is in good agreement with the expected volume fraction of 0.005%.

2D flow measurements were performed at the flow cell edge for $\theta = 1.84°$ and the pump discharge rates of $1/12$ and $1/6$ µL/s. Figure 4.8 shows transverse and axial velocity profiles obtained using number fluctuation DLS-OCT (left column) and expected flow profiles according to Eq. (4.30) (right column). The obtained velocity distributions are in good agreement with the expected values and both the transverse and the axial flow profiles are clearly visible. The transverse flow profile is uniform except very close to the flow cell edge at distances less than 0.4 mm, whereas the axial velocity profile has a much larger degree of variation. Due to the limitations imposed by particle diffusion, flow profiles for such low flow velocities can be obtained neither by Doppler OCT nor by non-dilute DLS-OCT.

4.5. Discussion

Our results show that number fluctuation DLS-OCT can significantly improve the velocity sensitivity compared to current Doppler OCT flow measurements. While phase-resolved Doppler OCT and non-dilute DLS-OCT are ultimately limited by particle diffusion, our method allows sub-diffusion flow velocity measurements with a sensitivity only limited by the SNR. Moreover, our method works for arbitrary Doppler angle and has a clear advantage in situations where the number density of scattering particles in the sample is very low while sufficient light is scattered. The advantage of number fluctuation DLS-OCT decreases with increasing Doppler angles. As Fig. 4.2 shows, Doppler OCT can be more sensitive at high θ values. The exact crossover point depends on system parameters and resolution. However, sufficiently increasing the Doppler angle is difficult due to several reasons: First, with larger θ, beam refraction effects and a sensitivity loss in depth become more pronounced. Second, higher flow speeds can cause phase wrapping and distortion [10], leading to incorrect phase estimation. Third, in certain applications θ may be limited to small angles due to geometric constraints, for example in medical and ophthalmic imagining. Therefore, it is preferable to use low Doppler angles at which our method has a superior performance than Doppler OCT. The low angle also allows to neglect gradient effects on the normalized autocovariance function [24].

In very dilute samples the number of scattering particles is very low. However, due to bulk flow, scatterers always move from one OCT voxel to another, which has a temporal averaging effect over the whole acquisition period. So, even though the average number of scatterers per voxel is around $0.1 - 0.2$, there is still a sufficient scattered signal from each voxel for capturing number fluctuations. In fact, with our OCT system we could measure even more dilute samples. Yet, going to lower concentrations reduces SNR and makes OCT flow measurements more difficult. To estimate phase changes accurately with Doppler OCT at low flow speeds and low θ, we averaged over long acquisition times. Relatively large time traces are also needed to reduce the statistical bias [19] of $g_2(z,\tau)$ in number fluctuation DLS-OCT when dealing with slow flows. In this work, the measurement time series length was chosen based on an accurate flow estimation for the lowest considered discharge rate. However, the time series length could in principle be reduced for

faster flows allowing for faster 1D and 2D imaging. We have also noticed that acquiring several time traces for averaging was more critical for Doppler OCT than for number fluctuation DLS-OCT.

The flow profiles obtained for Doppler and number fluctuation DLS-OCT methods match well with the expected flow velocities. Uncertainties in the flow can be attributed to the beam waist calibration, beam offset from the center of the flow channel and the pump stability [23], which have an effect especially at very low discharge rates. As Fig. 4.6 shows, the sensitivity of Doppler OCT for varying velocity is constant, implying that systematic errors are minimal and do not increase with increasing flow rates. Small deviations from the expected sensitivity range could be caused by a fact that the system is not shot-noise limited or the phase stability is less than ideal. In contrast to our derived model, the velocity uncertainties in number fluctuation DLS-OCT increase as a function of flow (discharge) rate, indicating that the method accuracy drops for larger velocities. The theoretical framework for SNR-based sensitivity analysis of number fluctuation DLS-OCT given in Sec. 4.2.3 is based on the minimum measurable relative intensity change when particles move during a single time step and assuming a factor $\sqrt{M}$ over M measurements. It does not take into account additional factors introduced when computing the normalized autocovariance of intensity fluctuations, such as the statistical or the fit model bias due to a limited number of time series points. As the flow speed increases, the autocovariance decay becomes more rapid and there are fewer sampling points available for fitting. In addition, with increasing flow velocity the difference in decay rates between the Gaussian and number fluctuation terms in $g_2(z,\tau)$ decreases, making extraction of the number fluctuation term more difficult. Our theoretical model gives an estimation of the order of magnitude of the minimum measurable velocity. It can be further extended by including the above-mentioned factors for more accurate flow measurement sensitivity analysis. For best performance, number fluctuation DLS-OCT should be implemented in the diffusion-dominated regime for very low flow rates with

$$v_0\sqrt{\frac{\sin^2\theta}{w_z^2}+\frac{2\cos^2\theta}{w_0^2}} \ll 2Dq^2\,. \tag{4.35}$$

In contrast, for faster flows where

$$v_0\sqrt{\frac{\sin^2\theta}{w_z^2}+\frac{2\cos^2\theta}{w_0^2}} \gg 2Dq^2\,, \tag{4.36}$$

non-dilute DLS-OCT or even scanning DLS-OCT [23] are more suitable methods. With intermediate flow regimes where

$$v_0\sqrt{\frac{\sin^2\theta}{w_z^2}+\frac{2\cos^2\theta}{w_0^2}} \sim 2Dq^2\,, \tag{4.37}$$

both techniques can be combined for improved accuracy.

Number fluctuation DLS-OCT can be utilized for simultaneous 2D velocimetry of sub-diffusion flows using scanning OCT systems. This is impossible for Doppler OCT or non-dilute DLS-OCT due to particle diffusion and sampling limitations. Even though the sampling frequency of adjacent B-scans is significantly reduced compared to single point measurements, it is still sufficient for resolving sub-diffusion flows since the number fluctuation decorrelation is very slow. This shows the feasibility of this technique for volumetric flow imaging even with limited acquisition rates. In contrast, it is impossible to measure 2D flow profiles with so low sampling speed at any flow velocity using Doppler OCT or non-dilute DLS-OCT. In this case the low-speed flows are dominated by diffusion, and much higher sampling rates are required for measuring faster flows.

Reliability of number fluctuation DLS-OCT increases with the increasing relative weight of the number fluctuation term in Eq. (4.21). The relative weight of this term can be increased by decreasing the particle density in the sample and/or increasing the particle radius. For a fixed particle volume fraction, increasing particle size leads to fewer particles in the scattering volume, $\langle N \rangle$, but increases scattered light power (higher SNR) per particle due to the scaling of the Mie/Rayleigh scattered intensity ($I_s \sim a^6$). The latter effect is more dominant, resulting in higher total scattered power and a larger contribution of the number fluctuation term to the normalized autocovariance function. However, a larger particle size leads to slower diffusive decorrelation. As a result the Gaussian and number fluctuation terms can have similar decorrelation ranges for the same flow speed.

Applications of number fluctuation DLS-OCT are not limited to extremely dilute samples. Our method can also be used to measure low-speed flows of typical pharmaceutical, biological or rheological suspensions that are imaged with OCT. Here we foresee two possible implementations: First, a non-dilute sample can be seeded with a small number of relatively large and highly scattering particles, ensuring low $\langle N \rangle$ but sufficient measurement SNR. In this way the number fluctuation term can be measured without changing the OCT system. The second option is to improve the number fluctuation term contrast optically by increasing the numerical aperture (NA) and reducing the scattering volume. In this case the original, unseeded sample can be used but a higher resolution OCT system is required. Note that an increase in optical resolution comes at the expense of a decrease in the effective axial working range.

Number fluctuation DLS-OCT can be used to determine the average number of scatterers in the scattering volume, $\langle N \rangle$, which is directly related to the particle concentration. This can be performed without any a-priori measurements. In this case a high axial resolution is preferable for maximizing $\langle N \rangle^{-1}$ and therefore the importance of the number fluctuation term. We expect that for a digitized OCT signal, Eq. (4.24) is only valid if the coherence waist and the axial pixel pitch are small compared to the length scales at which the local beam waist varies significantly. When using Eq. (4.27) for estimating $\langle N \rangle$, the flow decay in the measured $g_1(z,\tau)$ and $g_2(z,\tau)$ must be negligible ($\tau \ll \tau_{v_0}$). Equation (4.29), on the other hand, is independent of the flow decay time and therefore easier to implement for determining $\langle N \rangle$, but requires additional extrapolation of the data.

4.6. Conclusion

We have implemented number fluctuation DLS-OCT for measuring sub-diffusion, low-speed flows in dilute particle suspensions using the second-order autocovariance function. Our method extends the minimum measurable velocity limit compared to the standard non-dilute DLS-OCT or Doppler OCT techniques and completely removes the limitation on the minimum measurable flow due to diffusive motion of the particles. We have shown that our method is independent of the Doppler angle, is applicable to 2D flow velocimetry in a scanning OCT setup, and can be used to determine particle concentration in flowing dilute suspensions.

Data availability

Data underlying the results presented in this paper and the relevant analysis routines are available at [29].

References

[1] J. Kalkman, R. Sprik, and T. G. van Leeuwen, *Path-length-resolved diffusive particle dynamics in spectral-domain optical coherence tomography,* Physical Review Letters **105**, 198302 (2010).

[2] N. Weiss, T. G. van Leeuwen, and J. Kalkman, *Localized measurement of longitudinal and transverse flow velocities in colloidal suspensions using optical coherence tomography,* Physical Review E **88**, 042312 (2013).

[3] J. Lee, W. Wu, J. Y. Jiang, B. Zhu, and D. A. Boas, *Dynamic light scattering optical coherence tomography,* Optics Express **20**, 22262 (2012).

[4] B. K. Huang and M. A. Choma, *Resolving directional ambiguity in dynamic light scattering-based transverse motion velocimetry in optical coherence tomography,* Optics Letters **39**, 521 (2014).

[5] M. A. Choma, A. K. Ellerbee, S. Yardanfar, and J. A. Izatt, *Doppler flow imaging of cytoplasmic streaming using spectral domain phase microscopy,* Journal of Biomedical Optics **11**, 024014 (2006).

[6] S. Yazdanfar, C. Yang, M. V. Sarunic, and J. A. Izatt, *Frequency estimation precision in Doppler optical coherence tomography using the Cramer-Rao lower bound,* Optics Express **13**, 410 (2005).

[7] D. P. Chowdhury, C. M. Sorensen, T. W. Taylor, J. F. Merklin, and T. W. Lester, *Application of photon correlation spectroscopy to flowing Brownian motion systems,* Applied Optics **23**, 4149 (1984).

[8] T. W. Taylor and C. M. Sorensen, *Gaussian beam effects on the photon correlation spectrum from a flowing Brownian motion system,* Applied Optics **25**, 2421 (1986).

[9] T. G. van Leeuwen, D. J. Faber, and M. C. Aalders, *Measurement of the axial point spread function in scattering media using single-mode fiber-based optical coherence tomography,* IEEE JOURNAL OF SELECTED TOPICS IN QUANTUM ELECTRONICS **9**, 227 (2003).

[10] E. Koch, J. Walther, and M. Cuevas, *Limits of Fourier domain Doppler-OCT at high velocities,* Sensors and Actuators A **156**, 8 (2009).

[11] M. A. Choma, A. K. Ellerbee, C. Yang, T. L. Creazzo, and J. A. Izatt, *Spectral-domain phase microscopy,* Optics Letters **30**, 1162 (2005).

[12] H. C. Hendargo, R. P. McNabb, A. Dhalla, N. Shepherd, and J. A. Izatt, *Doppler velocity detection limitations in spectrometer-based versus swept-source optical coherence tomography,* Biomedical Optics Express **2**, 2175 (2011).

[13] D. A. Boas, K. K. Bizheva, and A. M. Siegel, *Using dynamic low-coherence interferometry to image Brownian motion within highly scattering media,* Optics Epxress **23**, 319 (1997).

[14] C. S. Kim, W. Qi, J. Zhang, Y. J. Kwon, and Z. Chen, *Imaging and quantifying Brownian motion of micro- and nanoparticles using phase-resolved Doppler variance optical coherence tomography,* Journal of Biomedical Optics **18**, 030504 (2013).

[15] C. S. Johnson and D. A. Gabriel, *Laser Light Scattering* (Dover Publications, 1994).

[16] B. J. Berne and R. Pecora, *Dynamic Light Scattering* (Dover Publications, 2000).

[17] N. Uribe-Patarroyo, M. Villiger, and B. E. Bouma, *Quantitative technique for robust and noise-tolerant speed measurements based on speckle decorrelation in optical coherence tomography,* Optics Express **22**, 24411 (2014).

[18] N. Weiss, T. G. van Leeuwen, and J. Kalkman, *Simultaneous and localized measurement of diffusion and flow using optical coherence tomography,* Optics Express **23**, 3448 (2015).

[19] N. Uribe-Patarroyo, A. L. Post, S. Ruiz-Lopera, D. J. Faber, and B. E. Bouma, *Noise and bias in optical coherence tomography intensity signal decorrelation,* OSA Continuum **3**, 709 (2020).

[20] M. G. O. Gräfe, M. Gondre, and J. F. de Boer, *Precision analysis and optimization in phase decorrelation OCT velocimetry,* Biomedical Optics Express **10**, 1297–1314 (2019).

[21] D. W. Schaefer, *Dynamics of number fluctuations: Motile microorganisms,* Science **180**, 1293 (1973).

[22] E. J. Nijman, H. G. Merkus, J. C. M. Marijnissen, and B. Scarlett, *Simulations and experiments on number fluctuations in photon-correlation spectroscopy at low particle concentrations,* Applied Optics **40**, 4058 (2001).

[23] K. Cheishvili and J. Kalkman, *Scanning dynamic light scattering optical coherence tomography for measurement of high omnidirectional flow velocities,* Optics Express **30**, 23382 (2022).

[24] N. Uribe-Patarroyo and B. E. Bouma, *Velocity gradients in spatially resolved laser Doppler flowmetry and dynamic light scattering with confocal and coherence gating,* Physical Review E **94**, 022604 (2016).

[25] R. R. Vardanyan, V. K. Dallakyan, U. Kerst, and C. Boit, *Laser beam transmission and focusing inside media,* Journal of Contemporary Physics **46**, 218 (2011).

[26] A. N. Bashkatov and E. A. Genina, *Water refractive index in dependence on temperature and wavelength: a simple approximation,* in *Proceedings of the SPIE*, Vol. 5068 (2003) pp. 393–395.

[27] N. Cheng, *Formula for viscosity of glycerol-water mixture,* Industrial and Engineering Chemistry Research **47**, 3285 (2008).

[28] H. Bruus, *Acoustofluidics 1: Governing equations in microfluidics,* Lab on a Chip **11**, 3742–3751 (2011).

[29] K. Cheishvili, *Number fluctuation DLS-OCT data and analysis routines,* https://doi.org/10.5281/zenodo.6606471 (2022).

5

Multi-modal optical coherence tomography flowmetry of organ-on-chip devices

Organ-on-chip (OoC) systems are microfluidic devices for maintaining live tissue under physiologically relevant (flow) conditions. Imaging of structure and flow is important for the characterization of OoC device design and visualizing tissue/fluid interaction. Here, we present 3D tissue and flow imaging in an OoC device with multi-modal optical coherence tomography (OCT) using a combination of OCT structural imaging and flow imaging with Doppler OCT, number fluctuation dynamic light scattering OCT, and particle image velocimetry OCT. We demonstrate the feasibility of combined imaging of OoC tissue culture morphology and high flow velocities. We also measure low velocities in the OoC tissue well, showing good agreement with computational fluid dynamics simulations. Our results open up the way for studying the effect of flow on living tissue in OoC devices.

This chapter has been submitted for publication as: Devrim Tugberk[†], **Konstantine Cheishvili**[†], Peter Speets, William Quirós-Solano, Anish Ballal, Nikolas Gaio, and Jeroen Kalkman, *Multi-modal optical coherence tomography flowmetry of organ-on-chip devices*.
[†]These authors contributed equally to this work.

5.1. Introduction

Organ-on-chip (OoC) systems are microfluidic devices that biomimic the in vivo micro environment with embedded living tissues for personalizing medicine [1] and improving drug development trajectories [2]. These systems need to be biocompatible, mechanically stable, and with flow commensurable to the physiological micro environment.

Structural information of OoC geometry is important for the optimal design of the flow cell. Also, structural information about the tissue morphology is important to study its development over time. For example, measuring the tissue formation rate, morphology, and its reaction to drugs are important parameters in OoC research. This information is often obtained through imaging.

In addition to structural information, flow information is important for two aspects of the OoC. First, characterizing the OoC flow speed distribution is needed to guide the design of the OoC device to make it operate under the right physiological conditions. For example, the tissue well has to have a sufficiently high refresh rate to supply the tissue with enough nutrients. Also, the flow rates need to be physiological realistic such that drug distribution and cell interactions are similar to that in humans, something that is of key importance for drug testing and development. Second, with the implementation of biological tissue it is crucial to visualize flow-tissue interaction, for example, for quantifying realistic dynamic flows or measuring the shear rate at the tissue-fluid interface and its impact on the development of epithelial cells.

Therefore, 3D monitoring of all components of the OoC device, such as cells, tissue, fluid flow, and microfluidic geometry, is of paramount importance for obtaining information on OoC functioning. However, there are few technologies that combine the wanted combination of 3D structural imaging (sample geometry and tissue morphology) with functional imaging (fluid flow and tissue perfusion).

Structural imaging has been performed with techniques such as brightfield microscopy, quantitative phase imaging, and fluorescence microscopy [3] that mainly collect 2D structural information. A number of 3D imaging techniques have been applied such as confocal fluorescence microscopy, selective plane illumination microscopy. However, fluorescence microscopy requires tissue labeling whereas selective plane illumination microscopy needs access to the sample from all directions, something that is cumbersome for the planar geometry of OoC devices.

Flow imaging has been done with brightfield microscopy combined with spatio-temporal image correlation spectroscopy and has shown good flow results in 2D [4] and was implemented in 3D with selective plane illumination microscopy [5]. However its implementation is rather cumbersome given the planar geometry of OoC devices. Quantitative flow imaging has been performed with particle image velocimetry (PIV), which is based on tracking fluorescent beads in a flow. Using imaging from multiple directions the 3D velocity can be obtained [6]. However, PIV needs complicated equipment, a darkened measurement environment, and can only be performed in optically clear media. Moreover, it does not provide the corresponding structural information.

Optical coherence tomography (OCT) is very well suited for the combined 3D

structural and flow imaging of OoC devices. OCT is fast, label-free, and images non-invasively using a large working distance. OCT has been widely applied to image microfluidic systems since it is ideally suited with its imaging depth of up to 2 mm and axial resolution of a few micrometers. For OoC devices, OCT has been used for studying the lumen development in airways-on-chip [7], thrombus formation in vessel-on-chip [8], biofilm growth [9], and bacterial colonization [10]. OCT also has been applied to image in vitro organoid development over time [11, 12]. The high temporal resolution of OCT gives the ability of label-free high-contrast tissue imaging using speckle variance [8]. Moreover, OCT is a versatile imaging tool that can be used to measure tissue properties such as biological activity [11], cellular reorganisation [12] and tissue mechanics [13].

For OCT flow imaging, Doppler OCT is the most common approach due to its ease of implementation and sensitivity for high flow speeds. However, Doppler OCT can only measure the axial flow component and the smallest measured flow speed is limited by the random signal from the Brownian motion [14]. Particle image velocimetry OCT (PIV-OCT) has been used for measuring both axial and transverse flow components in subsequent B-scans [15, 16]. Although OCT-PIV can measure extremely small flows that are in arbitrary directions, it has lower spatial resolution, is computationally intensive, and requires cumbersome fine tuning of correlation windows to the target flow velocity components. Dynamic light scattering OCT (DLS-OCT) can measure both axial and lateral flow components [17] but, similar to Doppler OCT, cannot measure small flow speeds as the Brownian motion causes random signal fluctuations. This problem has been addressed with number fluctuation DLS-OCT [18] where the signal fluctuations are caused by individual particles moving in and out of the focus, and the number fluctuation part of the correlation function is not dependent on particle diffusion. Consequently, number fluctuation DLS-OCT allows for the measurement of extremely low total flow speeds down to around 50 µm/s. The different flow speeds, spatial resolution, and requirement for assessing the flow direction necessitate the combined efforts of various OCT flow measurement techniques.

In this work we demonstrate the versatility of OCT in measuring with multiple OCT operation modes the OoC geometry, tissue structure, and different flow speeds and directions. We do this by performing conventional OCT structural imaging and flow measurements with Doppler OCT, number fluctuation DLS-OCT, and PIV-OCT. The flow speed and velocity and speed in the OoC device well shows good agreement with computational fluid-dynamic simulations.

5.2. Methods

5.2.1. OCT structural imaging

The experiments for this research were conducted using a Thorlabs GANYMEDE II HR series spectral-domain OCT system [14]. The system bandwidth is centred at 900 nm and has an axial resolution of 3 µm in air. The OCT system is operated with an NA = 0.05 scan lens (LSM04-BB, Thorlabs). The beam waist $w_0 = 6$µm in air, defined as the e^{-1} radius of the Gaussian field profile. The OCT system was used

for structural imaging in B-scan mode.

For flow measurements, the OCT system was used in Doppler mode for high flow velocities, such as in the OoC supply channels, and in number fluctuation DLS-OCT mode for low flow velocities in the OoC well. For number-fluctuations and PIV we used 5.5 kHz A-scan rate, for Doppler mode imaging we used 36 kHz A-scan rate.

5.2.2. OCT flow measurements

The flow geometry was arranged so that the OCT beam was perpendicular to the microfluidic channel surface. Two-dimensional flow measurements were carried out by laterally scanning the OCT beam (B-scan) along the width or length of the microfluidic channel. The scan length was configured to be 3.1 mm, encompassing 200 lateral pixels, while the number of axial pixels was 1024. A sequence of 2000 consecutive B-scans was obtained with a sampling time step of $\Delta t = 40$ ms. The pixel sizes in the lateral and axial directions, denoted as Δx and Δz, were 15.6 and 1.8 µm, respectively. Here, z corresponds to the optical depth and not the physical depth.

DLS-OCT total velocity measurements

The total flow velocity was determined using number-fluctuation DLS-OCT [18, 19]. The second-order normalized autocovariance function was computed from the OCT signal intensity time series as a function of lateral, x, and axial position, z. Due to a relatively large sampling time, diffusive decay could not be detected, and only the number-fluctuation term was obtained. The number-fluctuation intensity autocovariance function is

$$g_2(x,z,\tau) = \frac{(\kappa(x,z)-1)\, e^{-\frac{v_0(x,z)^2 \sin^2\theta(x,z)\tau^2}{w_z^2}} e^{-\frac{2v_0(x,z)^2\cos^2\theta(x,z)\tau^2}{w_r(z)^2}}}{\left(\kappa(x,z)-2+\left(1+\frac{1}{\mathrm{SNR}(x,z)}\right)^2\right)\left(2^{3/2}N(x,z)+1\right)}, \tag{5.1}$$

where $v_0(x,z)$ is the total velocity, $\mathrm{SNR}(x,z)$ is the signal-to-noise ratio, $N(x,z)$ is the average number of particles within the scattering volume, $w_r(z)$ is the local Gaussian beam waist, w_z is the coherence function waist, $\theta(x,z)$ denotes the Doppler angle ($90° - \theta$ is the angle between the velocity vector and the optical axis), and $\kappa(x,z)$ is the kurtosis of the noise-subtracted complex field distribution [19]. As seen in Eq. (5.1), a fit of the autocovariance function could not distinguish between variations in velocity v_0 and variations in angle θ. To eliminate the dependence of the autocorrelation function on the Doppler angle θ, the Gaussian spectral apodization window width, σ_k, was varied to equalize the lateral and axial flow decay rates at every axial voxel, such that $\sqrt{2}w_z = w_r(z)$. Consequently, the measured intensity autocorrelation functions were fitted using

$$g_2(x,z,\tau) = A(x,z)e^{-v_0(x,z)^2\tau^2\left(\frac{\sin^2\theta}{w_z(z)^2}+\frac{2\cos^2\theta}{w_r(z)^2}\right)} = A(x,z)e^{-\frac{2v_0(x,z)^2\tau^2}{w_r(z)^2}}, \tag{5.2}$$

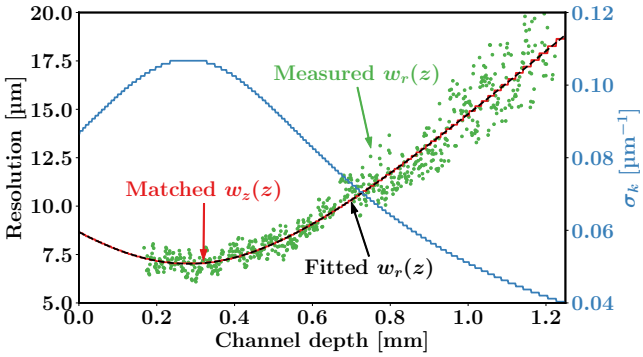

Figure 5.1: Measured and fitted Gaussian beam width as a function of depth, along with the matched coherence length and spectral apodization window.

where $A(x,z)$ is the amplitude factor for the intensity autocorrelation function incorporating all the pre-terms in Eq. (5.1). In this case, the fit parameters are $A(x,z)$ and $v_0(x,z)$.

For every axial voxel, a spectral apodization window width $\sigma_k(z)$ was implemented such that $(\sigma_k(z)n_k)^{-1} = \sqrt{2}w_z(z) = w_r(z)$. The refractive index $n_k = 1.33$ of water was used since the aqueous particle suspension was very dilute. The effect of dispersion on the coherence length was neglected. The Gaussian beam shape, $w_r(z)$, was calibrated by scanning the beam over the stationary particle suspension, following the procedures described in Refs. [18, 19]. The local beam waist, the matched coherence waist, and the spectral apodization window width are shown in Fig. 5.1. The beam shape $w_r(z)$ was fitted using $w_r(z) = w_0\sqrt{1 + (z - z_0)^2/z_R^2}$. The measured beam shape from Fig. 5.1 is a good match with the Gaussian fit.

PIV-OCT directional velocity measurements

In-plane velocity vectors were determined by implementing PIV-OCT. Laterally and axially resolved OCT B-scan intensity images were divided into smaller windows, $I(\epsilon,\eta,t)$, each containing 4 lateral and 32 axial pixels covering a square area of 62 µm × 44 µm. For each window, the time-dependent normalized unbiased 2D cross-covariance matrix was computed for every image pair using

$$\rho(m,n,t) = \frac{\left\langle \left(I(\epsilon,\eta,t) - \bar{I}_{\epsilon,\eta}(t)\right)\left(I(\epsilon+m,\eta+n,t+N\Delta t) - \bar{I}_{\epsilon,\eta}(t+N\Delta t)\right)\right\rangle_{\epsilon,\eta}}{\sigma_{\epsilon,\eta}(t)\sigma_{\epsilon,\eta}(t+N\Delta t)\,(4-|m|)\,(32-|n|)}, \tag{5.3}$$

where ϵ,η are lateral and axial pixel numbers within the window reference frame, $\sigma_{\epsilon,\eta}$ is the standard deviation over a window, m and n represent the relative pixel shifts in the corresponding directions, and N is the number of B-scans by which two frames are temporally separated. The obtained correlation coefficients were temporally averaged, resulting in the mean 2D cross-correlation coefficient $\bar{\rho}_t(m,n)$.

For each window, the lateral velocity v_x was computed by finding the lateral index of the maximum of $\overline{\rho}_t(m,n)$, denoted as $m_{\max}$, while the axial velocity was determined by the axial index of the maximum, denoted as $n_{\max}$. The lateral and axial velocities were then determined using

$$v_x = \frac{m_{\max}\Delta x}{N\Delta t} \qquad \text{and} \qquad v_z = \frac{n_{\max}\Delta z}{n_k N\Delta t}. \tag{5.4}$$

In our analysis, we used $N = 5$ for calculating v_z and $N = 20$ for calculating v_x, except at the channel center, where we used $N = 15$ for calculating both velocity components. The minimum sampling time between two images is 202 ms when $N = 5$. This is significantly larger than the time required for acquiring the intensity image of one window, which is approximately 0.7 ms. Therefore, particle motion within this time window was neglected.

5.2.3. Doppler OCT measurements

Doppler OCT measurements were performed on the main device channels where the flow was high. The pump discharge rate was set to 25 µl/min for all conditions. We measured the flow with Doppler-OCT in the main flow channel using Intralipid as tracer particles in two different OoCs. Doppler-OCT flow measurements were implemented using the phase-resolved method as described in [14].

5.2.4. Organ-on-chip samples

Flow measurements were performed on inCHIPit™ OoC devices (inCHIPit™–1C, BIOND Solutions B.V., Delft, the Netherlands). The inCHIPit™ OoC device consists of a single poly(dimethylsiloxane) (PDMS) microfluidic channel, with a porous membrane on the ceiling of the channel that leads to a static culture well, see Fig. 5.2. The flow going in and out of the system, via the inlet and outlet respectively, is the driving force of fluid movement inside the system and the porous membrane geometry creates an active perfusion flow (inside the static culture well).

PDMS is a soft polymer used in the inCHIPit™ device due to its bio-compatibility, gas permeability, optical transparency, chemical inertness, low-costs, and elasticity [20]. The hydrophobic surface of PDMS, originating from the presence of the organic methyl groups, caused clogging of the membrane pores. Therefore we increased the hydrophilicity of PDMS via plasma surface modification [21]. We treated the surface with an oxygen plasma (0.22 mBar) for 3 minutes (Atto, Diener, Germany). The exposure to the oxygen plasma replaces the methyl groups on the PDMS with hydroxyl groups to create polar silanol groups, making the surface hydrophilic. This can decrease the water contact angle of PDMS by 30° or more, depending on the treatment time, significantly improving cell adhesion onto the surface, and increasing the ease of fluid, and its constituents, passing through the porous PDMS membrane. The increased PDMS hydrophilicity in combination with appropriate cell-adhesive coating and the aforementioned standalone benefits of PDMS create a microenvironment that allows the culturing of cells. The hydrophilic effects induced via plasma treatment are temporary and wear off depending on factors such as the PDMS chemistry and OoC storage method. The hydrophilic hydroxyl

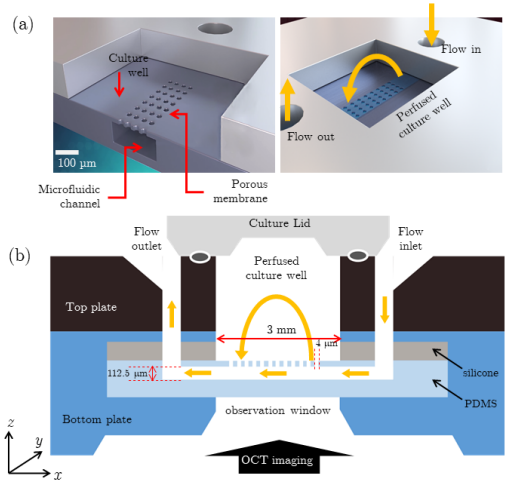

Figure 5.2: (a) Computer rendered images of the inCHIPit™-1C displaying the cross-section of the microfluidic channel, porous membrane, the static culture well, and the direction of flow from the inlet, through the microfluidic channel pores, creating a perfusion area, and back out from the outlet. (b) Cross-sectional view of the of the inCHIPit™-1C, the flow directions, dimensions, and OCT observation window.

groups are highly reactive and can react with molecules found in air, reverting back into a hydrophobic state in 1-2 days for our PDMS.

5.2.5. Computational fluid dynamics simulations

Numerical computational fluid dynamics (CFD) simulations were performed using the finite element method software COMSOL Multiphysics®v5.6 to model the flow behaviour of the inCHIPit™ OoC device from BIOND Solutions B.V. The developed model computationally solved the Navier-Stokes equations neglecting the inertial term. This is valid since the Stokes flow problem is considered to be under steady-state pressure-driven conditions and is expected to remain under steady-state for the envisioned applications of the device. The OoC device geometry comprises five main parts: inlet, outlet, microchannel, porous membrane and well. The dimensions of these parts are set according to the measured dimensions of the inCHIPit™ device and are shown in Table 5.1. Figure 5.3(a) shows an example of the simulated flow geometry. The corresponding boundary conditions along with the material properties were set. Water was employed as the fluid of interest with a viscosity value 10^{-3} Pa·s at 20 °C. A boundary condition of laminar flow was set at the inlet for the different flow rates of interest. At the outlet an open boundary with null normal stress was used. The walls of the well, channels, and porous membrane were set assuming a no slip condition for the fluid velocity.

The geometry was meshed with 6012570 elements with an average element quality of 0.6854 for different element types (tetrahedral, triangular). An image of

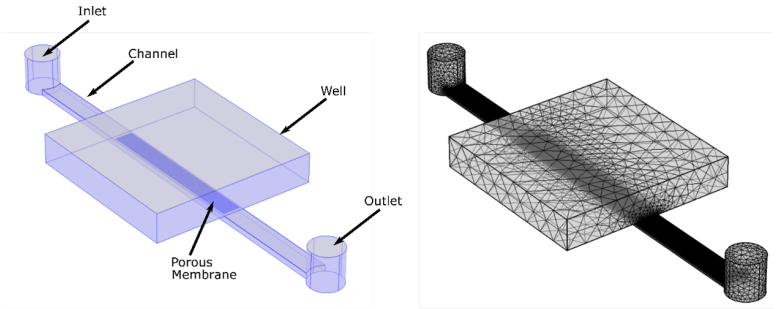

Figure 5.3: (left) Geometry of the inCHIPit™ in COMSOL Multiphysics and the corresponding boundary conditions set for the computation of the velocity field under steady-state conditions. (right) Meshed geometry of the inCHIPit™ in COMSOL Multiphysics.

Table 5.1: Parts and dimensions of the computationally modeled inCHIPit™ device.

Part	Feature	Dimension [µm]
Inlet and Outlet	Diameter	600
	Height	630
Microchannel	Length	7200
	Width	370
	Height	100
Porous Membrane	Thickness	6
	Pore diameter	4
Well	Length	3000
	Width	3000
	Height	525

the meshed geometry is shown in Fig. 5.3(b). The computation was carried out in a server with two cores Intel(R) Xeon(R) CPU E-54667 v3 @ 2.00GHz and 32 GB RAM memory, for an average computation time of 3 hours for most of the simulations. All components of the flow speed were calculated and used for comparison to the measurements.

5.3. Results

5.3.1. Flow in a single channel OoC system

To show the versatility of combined OCT morphology and flow measurements we first studied cell morphology and flow inside the OoC device. Human umbilical vein endothelial cells (HUVECs) were cultured in the microfluidic channel and arising retinal pigment epithelial cells (ARPE19) were cultured in the static culture well. Upon reaching a stable and matured adhesion to the PDMS, all cell cultures were fixated with paraformaldehyde.

Fig. 5.4(a,b) shows the OCT structural and flow speed images of the open channel. The open channel has no pores nor cells and shows some minor elastic channel

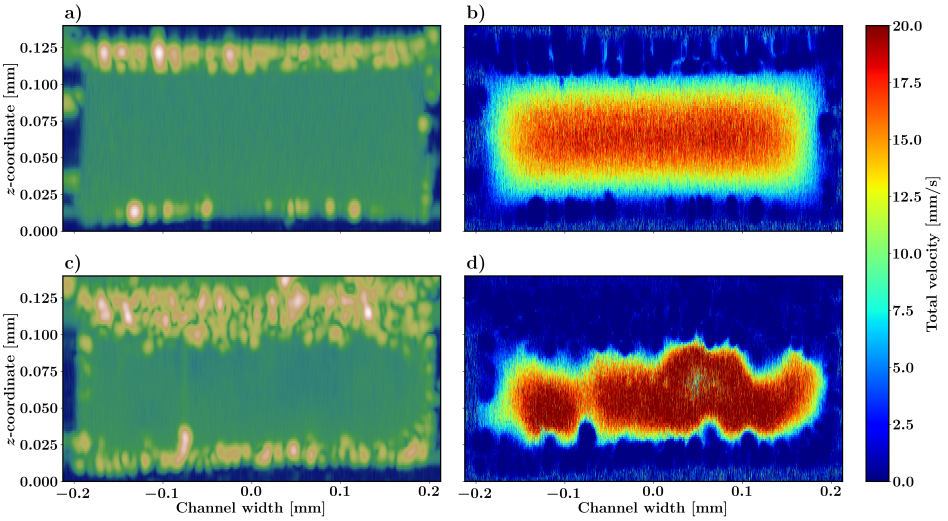

Figure 5.4: Cross-sectional B-scan intensity in dB scale perpendicular through the flow channel for the channel (a) with no pores and (c) with the presence of epithelial cells protruding from the culture well into the channel through the porous membrane. (b,d) Corresponding Doppler OCT flow measurements of the lumen.

deformation. In this case the flow is laminar and the flow speed is calculated based on the Doppler angle of the OoC flow channel. Figure 5.4(c,d) shows the structural and flow OCT image of the channel constricted by the growing tissue. In the constricted channel the epithelial cells grow inside the culture well and clogged the porous membrane. The cells essentially allowed the OoC to act as a channel with no pores. Even though the contrast between the original channel and the cell monolayer is low, the flow channel can still be observed in the structural image. The flow image in Fig. 5.4(d) clearly shows the constriction of the channel as the channel lumen becomes smaller and the flow speed increases (measurement at constant discharge rate). Note that in the case of lumen restrictions, the flow does not necessarily need to be in the direction of the flow channel, and the absolute flow speeds may be slightly off.

Although the Doppler OCT method is easy to implement and can measure the flow in the channels without much problems, measuring the flow speed in the OoC well was close to impossible under realistic flow conditions. Hence, we implemented number fluctuation DLS-OCT and PIV-OCT to measure the flow also in these spaces with the same OCT system.

5.3.2. Flow in the OoC well

Figures 5.5 and 5.6 show a comparison of the CFD simulations to the combined number-fluctuation DLS-OCT and PIV-OCT measurements inside the OoC culture well. The flow profile along the symmetry plane along the microchannel from the inlet to the outlet is shown in Fig. 5.5(a) for the OCT measurements and in Fig. 5.5(b)

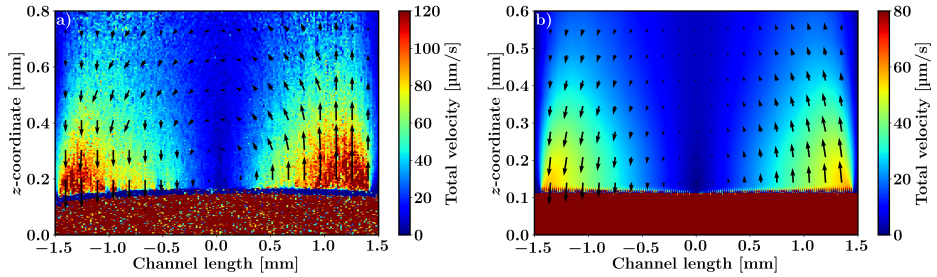

Figure 5.5: (a) Total velocity distribution along the channel length derived from number fluctuation DLS-OCT with superimposed in-plane velocity vectors measured using PIV-OCT. (b) Corresponding CFD simulations.

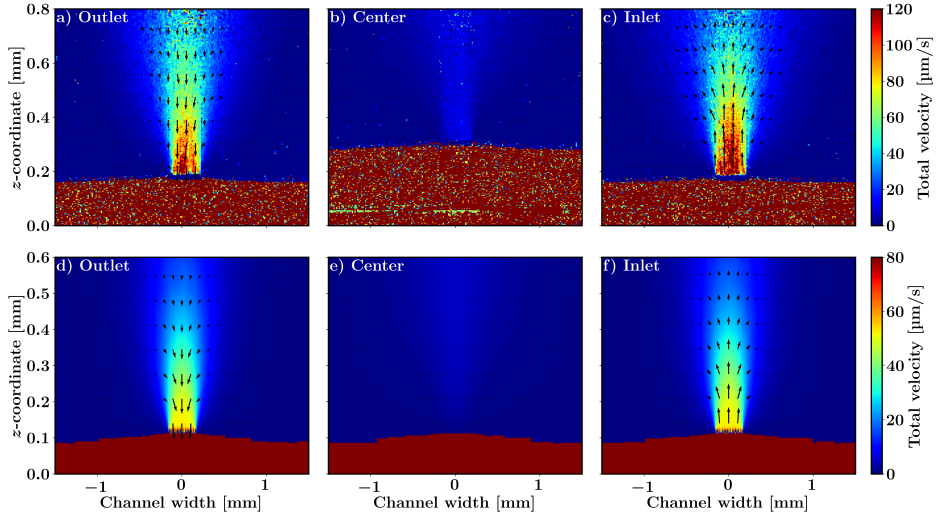

Figure 5.6: (a,b,c) Total velocity distribution along the channel width derived from number fluctuations, accompanied by in-plane velocity vectors measured using particle tracking. (d,e,f) Corresponding CFD simulations.

for the CFD simulations. The presented measurements are only sensitive to the low flow speeds in the well; the higher flow speeds in the microchannel can be quantified separately with Doppler OCT (similar to the data in Fig. 5.4). The flow enters the channel from the right where most of the flow enters the well through the porous membrane. In the well, the flow spreads out and the flow speed decreases. Near the outlet the flow speed again increases as the fluid goes out from the well into the channel. Overall there is a good qualitative agreement between the simulations and the measurements showing similar flow directions as well as flow distributions. There is less absolute quantitative agreement, with the simulated flow speeds being approximately 50% lower than the measured flow speeds.

The flow profile perpendicular to the line from the inlet to the outlet in Fig. 5.6 shows the flow entering the well at the inlet and exiting the well from the outlet. In the middle of the well, the z-component of the flow is almost completely absent, which is what one would expect for this plane. Again there is a good qualitative agreement between the simulations and the measurements showing similar flow directions as well as flow distributions, but less absolute quantitative agreement, with the simulated flow speeds being approximately 50% lower than the measured flow speeds. Note that the measurements in the center clearly show the bulging out of the porous membrane from the channel into the well caused by the fluid pressure acting on the flexible PDMS porous membrane.

5.4. Discussion

We demonstrated structural and functional measurements in an OoC system using multiple OCT imaging modes such as OCT, Doppler-OCT, PIV-OCT and DLS-OCT flow.

Our demonstration of in vitro OoC Doppler-OCT flow measurements, as shown in Fig. 5.4, opens up a way to study the effect of relatively high flows on in vivo tissue growth and development (we performed these measurements on dead tissue due to lab restrictions). The flow stimulates the cells residing on the cell-adhesive coated substrate with flow-induced shear stress whereas the pores provide a 3D microenvironment where the cells can sense the architecture and attach accordingly. In addition to the flow being an excellent flow/tissue contrast mechanism, the greatest value for such OCT measurements is in the quantification of blood flow and shear rates. For example, OCT flow measurements in the (micro) vasculature of vessel-on-chip or tumor-on-chip may be used to measure the shear rate in vivo. Shear rate is a biologically relevant stimulus for vessel modification sensed by the epithelial cells lining the vessel wall, which is important in the study of atherosclerosis, effects of high blood pressure, and vascular remodeling.

We successfully demonstrated the challenging task to measure the flow speed and velocity at the low flows speeds that are present in the OoC well. Comparison with CFD calculations, as shown in Fig. 5.5(a) and 5.6(a,b,c), gave good qualitative agreement, however, quantitatively, the measured velocities are approximately 1.5 times greater than those in the simulations. We attribute this disagreement to a flow geometry that is not identical to the rectangular designed shape as we observed that due to the pressure of the pump the elastic PDMS membrane deformed, as can be seen in the elevation in the middle of the flow channel in Fig. 5.6(b,e). The bulging of the channel is mainly due to the lack of mechanical support at the center of the channel and the low pressure inside the culture well (relative to the microchannel) due to the partially sealing lid that isolates the culture well from the environment. The lid allows air to escape from the culture well which creates a small 'air leak' in the system that causes the channel bulges into the culture well due to the relatively low pressure and consequently this leads to more fluid traveling through the culture well and hence a higher velocity. Another consequence of the bulging channel is a variability in the pore sizes of the porous membrane along the channel. These variations are difficult to model, thereby emphasizing the need for

in-situ flow measurements for flow performance calibration of OoC devices.

In Fig. 5.5(a) and 5.6(a,b,c), we utilized from the same data both number-fluctuation DLS-OCT, to measure the total flow speed, and PIV-OCT for directional velocities. The magnitude of the total velocity obtained with PIV-OCT matches well to the values obtained with number-fluctuation measurements. Although, PIV-OCT offers the advantage of capturing in-plane 2D velocity vectors it has some drawbacks over DLS-OCT. First, the spatial resolution of PIV-OCT flow imaging is significantly reduced due to the required spatial windowing which is especially prominent when the flow is highly confined such as in the well inlet and outlet regions. Second, PIV-OCT requires careful tuning of the temporal separation between windows ($N\Delta t$), the temporal window size, and the lateral window size to be able to measure a particular flow speed and direction. Third, the computational overhead is large due to the need for 2D cross-correlation analysis. Number-fluctuation DLS-OCT is a more robust method, requires no parameter optimization, and is readily applicable to the original resolution of the data obtained. However, it is sensitive only to the total velocity and cannot capture individual velocity components. The combination of PIV-OCT and number fluctuation DLS-OCT can be used to get good low resolution quantitative assessment of the flow direction with number fluctuation DLS-OCT supplementing this with high resolution total flow speed data.

Stable and consistent flow measurements of an OoC with pores turned out to be a big challenge due to scattering particles clogging the pores of the system. The flow through the system was rapidly fluctuating due to the clogging of pores and the consequential build-up of pressure that resulted in some pores becoming unclogged and clogged again. After various experimental trials, it was deduced that the highly hydrophobic nature of the PDMS caused the clogging. We could visibly observe that the highly hydrophobic surface of PDMS essentially created such a high repelling force to the particles that the 4 μm pores of the system were not accessible for the particle suspension. Even particles of 200 nm in diameter would not pass through the pores, either creating clogs or simply rolling over the pores. The clogging of the pores created unstable flow environments within the OoC and reproducible OCT measurements were impossible due to the sporadic nature of the clogging. This problem was overcome with surface plasma treatment of the entire OoC, which is a standard treatment procedure for OoCs to improve cell adhesion on PDMS.

In conclusion, we demonstrated versatile multi-mode OCT structural and flow imaging in an OoC device. Doppler-OCT, PIV-OCT, and number fluctuation DLS-OCT supplement each other and are applicable to image the flow and velocity in different speed regimes that are in different parts of the OoC device.

5.5. Acknowledgments

This work was funded by NWO domain Applied and Engineering Sciences with the project number 17988 and P17-24, project 6. This project was funded in part by a contribution from the National Growth Fund program NXTGEN Hightech.

Data availability

The data underlying the results presented in this paper, along with the relevant number-fluctuation DLS-OCT analysis routines, are available at [22].

References

[1] A. van den Berg, C. L. Mummery, R. Passier, and A. D. van der Meer, *Personalised organs-on-chips: functional testing for precision medicine,* Lab Chip **19**, 198 (2019).

[2] E. W. Esch, A. Bahinski, and D. Huh, *Organs-on-chips at the frontiers of drug discovery,* Nat. Rev. Drug Discov. **14**, 248 (2015).

[3] B. C. Buchanan and J. Y. Yoon, *Microscopic imaging methods for organ-on-a-chip platforms,* Micromachines **13**, 328 (2022).

[4] M. Travagliati, S. Girardo, D. Pisignano, F. Beltram, and M. Cecchini, *Easy monitoring of velocity fields in microfluidic devices using spatiotemporal image correlation spectroscopy,* Analytical Chemistry **85**, 8080–8084 (2013).

[5] N. G. Ceffa, M. Bouzin, L. D'Alfonso, L. Sironi, C. A. Marquezin, F. Auricchio, S. Marconi, G. Chirico, and M. Collini, *Spatiotemporal image correlation analysis for 3D flow field mapping in microfluidic devices,* Anal. Chem. **90**, 2277–2284 (2018).

[6] G. E. Elsinga, F. Scarano, B. Wieneke, and B. W. van Oudheusden, *Tomographic particle image velocimetry,* Experiments in fluids **41**, 933 (2006).

[7] Z. Liu, S. Mackay, D. M. Gordon, J. D. Anderson, D. W. Haithcock, C. J. Garson, G. J. Tearney, G. M. Solomon, K. Pant, B. Prabhakarpandian, S. M. Rowe, and J. S. Guimbellot, *Co-cultured microfluidic model of the airway optimized for microscopy and micro-optical coherence tomography imaging,* Biomed. Opt. Express **10**, 5414 (2019).

[8] C. Cuartas-Vélez, H. H. T. Middelkamp, A. D. van der Meer, A. van den Berg, and N. Bosschaart, *Tracking the dynamics of thrombus formation in a blood vessel-on-chip with visible-light optical coherence tomography,* Biomed. Opt. Express **14**, 5642 (2023).

[9] N. Weiss, K. El Tayeb El Obied, J. Kalkman, R. Lammertink, and . . T.G. van Leeuwen 7, *Measurement of biofilm growth and local hydrodynamics using optical coherence tomography,* Biomedical Optics Express **7**, 3508 (2016).

[10] L. Yuan, P. de Haan, B. W. Peterson, E. D. de Jong, E. Verpoorte, H. C. van der Mei, and H. J. Busscher, *Visualization of bacterial colonization and cellular layers in a gut-on-a-chip system using optical coherence tomography,* Microscopy and Microanalysis **26**, 1211 (2020).

[11] Y. Ming, S. Hao, F. Wang, Y. R. Lewis-Israeli, B. D. Volmert, Z. Xu, A. Goestenkors, A. Aguirre, and C. Zhou, *Longitudinal morphological and functional characterization of human heart organoids using optical coherence tomography,* Biosensors and Bioelectronics **207**, 114136 (2022).

[12] T. Monfort, S. Azzollini, J. Brogard, M. Clémençon, A. Slembrouck-Brec, V. Forster, S. Picaud, O. Goureau, S. Reichman, O. Thouvenin, and K. Grieve, *Dynamic full-field optical coherence tomography module adapted to commercial microscopes allows longitudinal in vitro cell culture study,* Comm. Biol. **6**, 992 (2023).

[13] J. H. Mason, L. Luo, Y. Reinwald, M. Taffetani, A. Hallas-Potts, C. S. Herrington, V. Srsen, C.-J. Lin, I. A. Barroso, Z. Zhang, Z. Zhang, A. K. Ghag, Y. Yang, S. Waters, A. J. E. Haj, and P. O. Bagnaninchi, *Debiased ambient vibrations optical coherence elastography to profile cell, organoid and tissue mechanical properties,* Communications Biology **6**, 543 (2023).

[14] K. Cheishvili and J. Kalkman, *Scanning dynamic light scattering optical coherence tomography for measurement of high omnidirectional flow velocities,* Optics Express **30**, 23382 (2022).

[15] S. Jonas, D. Bhattacharya, M. K. Khokha, and M. A. Choma, *Microfluidic characterization of cilia-driven fluid flow using optical coherence tomography-based particle tracking velocimetry,* Biomed. Opt. Express **2**, 2022 (2011).

[16] A. Buchsbaum, M. Egger, I. Burzic, T. Koepplmayr, M. Aigner, J. Miethlinger, and M. Leitner, *Optical coherence tomography based particle image velocimetry (OCT-PIV) of polymer flows,* Optics and Lasers in Engineering **69**, 40 (2015).

[17] N. Weiss, T. G. van Leeuwen, and J. Kalkman, *Localized measurement of longitudinal and transverse flow velocities in colloidal suspensions using optical coherence tomography,* Physical Review E **88**, 042312 (2013).

[18] K. Cheishvili and J. Kalkman, *Sub-diffusion flow velocimetry with number fluctuation optical coherence tomography,* Optics Express **31**, 3755 (2023).

[19] K. Cheishvili, B. Rieger, and J. Kalkman, *Precision and bias in dynamic light scattering optical coherence tomography measurements of diffusion and flow,* Biomedical Optics Express **15**, 1288 (2024).

[20] H. Kutluk, E. E. Bastounis, and I. Constantinou, *Integration of extracellular matrices into organ-on-chip systems,* Advanced Healthcare Materials **12**, 2203256 (2023).

[21] J. Zhou, A. V. Ellis, and N. H. Voelcker, *Recent developments in pdms surface modification for microfluidic devices,* Electrophoresis **31**, 2 (2010).

[22] K. Cheishvili and D. Tugberk, *Organ-on-chip DLS-OCT data and analysis routines,* https://doi.org/10.5281/zenodo.14293638 (2024).

6

Precision and bias in dynamic light scattering optical coherence tomography measurements of diffusion and flow

We quantify the precision and bias of dynamic light scattering optical coherence tomography (DLS-OCT) measurements of the diffusion coefficient and flow speed for first and second-order normalized autocovariance functions. For both diffusion and flow the measurement precision and accuracy are severely limited by correlations between the errors in the normalized autocovariance function. We demonstrate a method of mixing statistically independent normalized autocovariance functions at every time delay for removing these correlations. The mixing method reduces the uncertainty in the obtained parameters by a factor of two but has no effect on the standard error of the mean. We find that the precision in DLS-OCT is identical for different averaging techniques, but that the lowest bias is obtained by averaging the measured correlation functions before fitting the model parameters. With our correlation mixing method it is possible to quantify the precision in DLS-OCT and verify whether the Cramer-Rao bound is reached.

This chapter has been published as: **Konstantine Cheishvili**, Bernd Rieger, and Jeroen Kalkman, *Precision and bias in dynamic light scattering optical coherence tomography measurements of diffusion and flow*, Biomedical Optics Express 15(2), 1288-1310 (2024).

6.1. Introduction

Dynamic light scattering optical coherence tomography (DLS-OCT) relies on the measurement of fluctuations of scattered light and coherence gating to obtain simultaneous depth-resolved information about diffusive and translational motion of particles. Initially, DLS-OCT was used for measuring diffusion coefficients [1] and flow speeds of particle suspensions [2–5]. Later, several improvements have been suggested for increasing the DLS-OCT flow velocity dynamic range [6, 7].

DLS-OCT has the advantage over phase-resolved Doppler OCT that a flow can be measured for zero Doppler angle. It can also be used for particle sizing where the particle size is determined from the estimated diffusion coefficient using the Stokes-Einstein relation. The combined flow and diffusion estimation is particularly interesting for in-line particle sizing during process control [8]. Sensitivity and precision of phase-resolved Doppler OCT has been widely studied and reported in literature [9–12]. However, there is very little information available about the precision and bias of DLS-OCT diffusion and flow measurements. These are crucial for reliable measurements, especially in medical and pharmaceutical applications. Effects of noise and bias in OCT on the measured autocorrelation function have been reported [13], but their influence on the underlying parameters remains unclear.

In this work we perform simulations, measurements, and a theoretical analysis to quantify the precision and bias of diffusion and flow measurements using DLS-OCT. In our analysis, we consider both the first and second-order normalized autocovariance functions, $g_1(z,\tau)$ and $g_2(z,\tau)$, diffusive particle motion, and, for both dilute and non-dilute suspensions, translational particle motion. We derive analytical expressions for the highest attainable precision using the Cramer-Rao bound and compare them with the obtained results. We also assess the bias for different averaging techniques.

6.2. Theory

The geometry for OCT diffusion and flow measurements is described in [6, 7]. The propagation of the optical beam is described by a Gaussian beam along the z-direction. We assume that the scattering process is stationary.

6.2.1. Correlation functions for particle diffusion

For a non-flowing particle suspension, the normalized depth-dependent autocovariance of the OCT complex-valued signal in a backscattering geometry, including the effect of SNR, is given by [3, 4, 13–15]

$$g_1(z,\tau) = \frac{\langle E(z,t)E^*(z,t+\tau)\rangle_t}{\langle I(z,t)\rangle_t} = \frac{e^{-Dq^2\tau}}{1+\frac{1}{\mathrm{SNR}(z)}} = A_1(z)\, e^{-Dq^2\tau}, \qquad (6.1)$$

where $E(z,t)$ is the depth and time-dependent complex-valued OCT signal, $I(z,t)$ is the OCT signal intensity, τ is the autocovariance time lag, $A_1(z)$ is the autocovariance amplitude containing the effect of a diminishing signal-to-noise with depth [13], $\mathrm{SNR}(z)$ is the depth-dependent experimental signal-to-noise ratio[7,

13], D is the particle diffusion coefficient given by Stokes–Einstein equation, and $q = 2nk_0$ is the scattering wavenumber for the OCT backscattering probe configuration with the incident light wavenumber in vacuum k_0 and the medium refractive index n. Equation (6.1) for $g_1(z,\tau)$ is also known as the first-order autocorrelation function where $\langle E(z,t)\rangle_t = \langle E^*(z,t)\rangle_t = 0$. The signal-to-noise correction describes the non-zero time lag autocorrelation. At $\tau = 0$, the normalized correlation coefficient is unity.

The autocorrelation function of the mean-subtracted OCT signal intensity, also known as the Pearson correlation or autocovariance, decays twice as fast than $g_1(z,\tau)$ [1, 15] and can be expressed with the normalized second-order autocovariance using the Siegert relation [16, 17]

$$g_2(z,\tau) = \frac{\left\langle \left(I(z,t) - \langle I(z,t)\rangle_t\right)\left(I(z,t+\tau) - \langle I(z,t)\rangle_t\right)\right\rangle_t}{\langle I(z,t)\rangle_t^2} \approx$$
$$\left|g_1(z,\tau)\right|^2 = \frac{e^{-2Dq^2\tau}}{\left(1 + \frac{1}{\mathrm{SNR}(z)}\right)^2} = A_2(z)\, e^{-2Dq^2\tau}, \tag{6.2}$$

where $A_2(z)$ is a depth-dependent amplitude factor for the intensity autocorrelation function. For a mean-subtracted intensity autocovariance, the Siegert relation states that $g_2(z,\tau)$ is the square of $|g_1(z,\tau)|$. In Eq.(6.2) we have assumed that the average number of particles in the scattering volume, N_s, is sufficiently large $(N_s \gg 1)$ [16–19]. This ensures that the particle probability distribution in the scattering volume and the scattered light fluctuations follow Gaussian statistics. For a non-flowing particle suspension this requirement is almost always satisfied whenever the backscattered OCT signal intensity from every voxel is high [7].

6.2.2. Correlation functions for particle flow

For diffusing and flowing particle suspensions the first-order normalized autocovariance function magnitude is

$$\left|g_1(z,\tau)\right| = A_1(z)\, e^{-Dq^2\tau} e^{-\frac{v^2(z)\sin^2\theta\,\tau^2}{2w_z^2}} e^{-\frac{v^2(z)\cos^2\theta\,\tau^2}{w_0^2}}, \tag{6.3}$$

where $v(z)$ is the depth-dependent total flow speed, θ is the Doppler angle, w_z is the coherence function waist, w_0 is the Gaussian beam waist in focus, and $A_1(z)$ is the same SNR correction factor as given in Eq. (6.1). We take the absolute value to get rid of the phase component in $g_1(z,\tau)$ originating from the particle translational motion along the optical axis[2–4].

For flow measurements we focus on the second-order normalized autocovariance function, $g_2(z,\tau)$, that does not depend on the phase, is easier to implement, and can also be implemented in phase-unstable OCT systems. Here, we differentiate between very dilute and non-dilute sample regimes. For the flowing non-dilute particle suspensions, where the number of particles in the scattering

volume, N_s, is much greater than one, $g_2(z,\tau)$ is again obtained using the Siegert relation [3, 4, 6, 14, 15]

$$g_2(z,\tau) \approx \left|g_1(z,\tau)\right|^2 = A_2(z)e^{-2Dq^2\tau}\, e^{-\frac{v^2(z)\sin^2\theta\,\tau^2}{w_z^2}}\, e^{-\frac{2v^2(z)\cos^2\theta\,\tau^2}{w_0^2}}, \tag{6.4}$$

where $A_2(z)$ is the same SNR correction factor as given in Eq. (6.2). Here, we have neglected the effect of a gradient of the axial velocity on the autocovariance function [20]. In the non-dilute regime the scattering process is strictly Gaussian [7].

In dilute suspensions, the expected number of particles in the scattering volume can be significantly lower than 1. Therefore, for stationary particles certain depth voxels would give zero signal. However, due to the translational particle motion, the scattering signal is obtained from every voxel during the acquisition time. When the number of particles in the scattering volume is very low, the scattering process becomes non-Gaussian, and the Siegert relationship does not apply anymore [18, 21, 22]. In the dilute case with $N \lesssim 1$, the second-order normalized autocovariance is [7, 13, 19]

$$g_2(z,\tau) = \frac{A_3(z)2^{3/2}N_s(z)}{2^{3/2}N_s(z)+1}\left[e^{-2Dq^2\tau}e^{-\frac{v^2(z)\sin^2\theta\tau^2}{w_z^2}}e^{-\frac{2v^2(z)\cos^2\theta\tau^2}{w_0^2}} + \frac{1}{2^{3/2}N_s(z)}e^{-\frac{v^2(z)\sin^2\theta\tau^2}{w_z^2}}e^{-\frac{2v^2(z)\cos^2\theta\tau^2}{w^2(z)}}\right], \tag{6.5}$$

in which $g_1(z,\tau)$ can be incorporated as follows

$$g_2(z,\tau) = \frac{A_3(z)2^{3/2}N_s(z)}{2^{3/2}N_s(z)+1}\left[\frac{\left|g_1(z,\tau)\right|^2}{A_1^2(z)} + \frac{1}{2^{3/2}N_s(z)}e^{-\frac{v^2(z)\sin^2\theta\tau^2}{w_z^2}}e^{-\frac{2v^2(z)\cos^2\theta\tau^2}{w^2(z)}}\right]. \tag{6.6}$$

Here, $A_3(z)$ is given by

$$A_3(z) = \frac{\kappa(z)-1}{\kappa(z)-2+\left(1+\frac{1}{\mathrm{SNR}(z)}\right)^2}, \tag{6.7}$$

where $w(z)$ is the radius of the local beam waist, $N_s(z)$ is the average depth-dependent number of particles in the scattering volume [7, 19], and $\kappa(z)$ is the kurtosis of the noise-subtracted complex field distribution. The kurtosis can also be expressed as a ratio of the average squared noise-subtracted intensity to the squared mean noise-subtracted intensity. It can be obtained using the measured OCT signal intensity $I(z,t)$ and the signal-to-noise ratio,

$$\kappa(z) = 2 + \left(1+\frac{1}{\mathrm{SNR}(z)}\right)^2\left(\frac{\langle I^2(z,t)\rangle_t}{\langle I(z,t)\rangle_t^2} - 2\right), \tag{6.8}$$

which simplifies to $\kappa(z) = 2$ for the Gaussian scattering process with $A_2(z) = A_3(z) = \left(1+\frac{1}{\mathrm{SNR}(z)}\right)^{-2}$. The kurtosis can be depth-dependent for the non-Gaussian

process due to different signal intensities and particle flow speeds at different depths. In our previous study [7] we assumed $\kappa(z) = 2$, even though the scattering process was non-Gaussian. This made our analysis simpler considering that $\kappa(z)$ minimally affects $A_3(z)$ when the signal-to-noise ratio is sufficient. Here equations (6.5-6.8) use no assumptions on the scattering process, $\kappa(z)$, and do not impose any restrictions on the number of particles.

6.2.3. Precision of diffusion and flow estimation

Precision is defined as the spread of the measurement around the mean and can be quantified by the square root of the measurement variance. For DLS-OCT the precision is governed by random errors, i.e., unpredictable changes in the measured intensity. Since the particle diffusion coefficient and the flow speed are determined by fitting the models from Sec. 6.2.1 and Sec. 6.2.2 to the measured $g_1(z,\tau)$ and $g_2(z,\tau)$, the precision of the fit parameters is determined by the random errors of the normalized autocovariance function at different time delays. The maximum obtainable precision in the fit parameters is determined by the Cramer-Rao lower bound (CRLB). It is computed by inverting the Fisher information matrix [23]. For calculating the Cramer-Rao lower bound the probability distribution functions of $g_1(z,\tau)$ and $g_2(z,\tau)$ must be known. The correlation coefficients from a long time series data are approximately normally distributed [24–26]. Typical diffusion or flow measurements contain at least thousands of temporal sampling points, which is more than enough to assume that $g_1(z,\tau)$ and $g_2(z,\tau)$ are normally distributed at every time delay. In general, errors (residuals) at different time delays can be correlated. Calculating the CRLB becomes challenging because we don't know the error correlations and their impact on the model bias. To address this, we assume uncorrelated residuals. In this case, for M observations $g(z,\tau_1), g(z,\tau_2), \dots g(z,\tau_M)$ with N model (fit) parameters $p_1, p_2, \dots p_N$, the Fisher matrix F is an $N \times N$ symmetric matrix given by

$$F_{ij} = \sum_{m=1}^{M} \frac{1}{\sigma^2(z,\tau_m)} \frac{\partial g(z,\tau_m)}{\partial p_i} \frac{\partial g(z,\tau_m)}{\partial p_j}, \tag{6.9}$$

where τ_m is the discretized τ for index m. The observations depend on the model parameters and have a variance $\sigma^2(z,\tau_m)$. In our analysis the observations are $g_1(z,\tau_m)$ or $g_2(z,\tau_m)$ and the summation is performed over all considered time delays.

The covariance matrix of the model parameters is obtained by inverting the Fisher information matrix. Consequently, the variances of our model parameters, $\sigma_{p_j}^2$, are represented by the diagonal entries of the covariance matrix. This relationship is described by the equation

$$\sigma_{p_j}^2 = \left(F^{-1}\right)_{jj}. \tag{6.10}$$

Precision of estimating the diffusion coefficient

For a non-flowing particle suspension the diffusion coefficient is determined by fitting Eq. (6.1) to the real part of $g_1(z,\tau_m)$, with $A_1(z)$ and D being the fit (model)

parameters. The lowest attainable variance CRLB in the fitted diffusion coefficient, assuming uncorrelated noise in the Fisher information matrix, is given by

$$\sigma^2_{\mathrm{CRLB},\,D_{\Re(g_1)}}(z) = \frac{\sum_{m=1}^{M} \frac{e^{-2Dq^2\tau_m}}{\sigma^2_{\Re(g_1)}(z,\tau_m)}}{\sum_{m=1}^{M} \frac{A_1^2(z)q^4\tau_m^2 e^{-2Dq^2\tau_m}}{\sigma^2_{\Re(g_1)}(z,\tau_m)} \sum_{m=1}^{M} \frac{e^{-2Dq^2\tau_m}}{\sigma^2_{\Re(g_1)}(z,\tau_m)} - \left(\sum_{m=1}^{M} \frac{A_1(z)q^2\tau_m e^{-2Dq^2\tau_m}}{\sigma^2_{\Re(g_1)}(z,\tau_m)}\right)^2}, \tag{6.11}$$

where $\sigma^2_{\Re(g_1)}(z,\tau_m)$ represents the variance of the real part of $g_1(z,\tau_m)$, which is half of the variance of the complex $g_1(z,\tau_m)$. It can be obtained with simulations or measurements and can also be derived analytically using

$$\sigma^2_{\Re(g_1)}(z,\tau_m) = \underbrace{\frac{1}{2}\left(\frac{\langle I(z,t)I(z,t+\tau_m)\rangle_t}{\langle I(z,t)\rangle_t^2} - \frac{\langle E(z,t)E^*(z,t+\tau_m)\rangle_t^2}{\langle I(z,t)\rangle_t^2}\right)}_{\text{variance in the real part of } g_1(z,\tau_m)} \times$$
$$\frac{1}{M}\underbrace{\left(1-\Re\left(g_1(z,\tau_m)\right)^2\right)^2}_{\text{unexplained variance}}\underbrace{\left(1+2\sum_{\tau_m>0}\Re\left(g_1(z,\tau_m)\right)^2\right)}_{\text{long-lag correction}} = \tag{6.12}$$
$$\frac{1}{2M}\left(1+2\sum_{\tau_m>0}\Re\left(g_1(z,\tau_m)\right)^2\right)\left(1-\Re\left(g_1(z,\tau_m)\right)^2\right)^2,$$

where M is the total number of temporal sampling points (time series length). The first term represents the variance in the real part of the field autocorrelation and is equal to one half, the second term is a correction for the explained variance in the Pearson correlation coefficient [24–28], and the third term is a long-lag correction for the effect of the correlation magnitude on the variance [29]. As expected, $\sigma^2_{\Re(g_1)}(z,\tau_m) = 0$ when $\Re\left(g_1(z,\tau_m)\right) = 1$. Even though $g_1(z,\tau_m)$ is complex in nature, we only consider its real part when fitting the diffusion coefficient. According to Eq. (6.1), in non-flowing suspensions, the imaginary part $\Im\left(g_1(z,\tau_m)\right)$ is pure noise and contains no information about the particle diffusion. Therefore, in phase-stable systems it is always beneficial to use the real part $\Re\left(g_1(z,\tau_m)\right)$ instead of the absolute value $\left|g_1(z,\tau_m)\right|$.

A similar analysis can be performed with $g_2(z,\tau_m)$. In this case we use Eq. (6.2) for fitting with model parameters D and $A_2(z)$. The Cramer-Rao lower bound on the variance of the diffusion coefficient, when using the second-order normalized

autocovariance function, is

$$\sigma^2_{\mathrm{CRLB},D_{g_2}}(z) = \frac{\sum_{m=1}^{M} \frac{e^{-4Dq^2\tau_m}}{\sigma^2_{g_2}(z,\tau_m)}}{\sum_{m=1}^{M} \frac{4A_2^2(z)q^4\tau_m^2 e^{-4Dq^2\tau_m}}{\sigma^2_{g_2}(z,\tau_m)} \sum_{m=1}^{M} \frac{e^{-4Dq^2\tau_m}}{\sigma^2_{g_2}(z,\tau_m)} - \left(\sum_{m=1}^{M} \frac{2A_2(z)q^2\tau_m e^{-4Dq^2\tau_m}}{\sigma^2_{g_2}(z,\tau_m)}\right)^2}, \tag{6.13}$$

with $\sigma^2_{g_2}(z,\tau_m)$ being the variance of $g_2(z,\tau_m)$ given by

$$\sigma^2_{g_2}(z,\tau_m) = \frac{\left(1-g_2^2(z,\tau_m)\right)^2}{M} \left(\frac{\left\langle \left(I(z,t)-\langle I(z,t)\rangle_t\right)^2 \left(I(z,t+\tau_m)-\langle I(z,t)\rangle_t\right)^2 \right\rangle_t}{\langle I(z,t)\rangle_t^4} - \frac{\left\langle \left(I(z,t)-\langle I(z,t)\rangle_t\right)\left(I(z,t+\tau_m)-\langle I(z,t)\rangle_t\right) \right\rangle_t^2}{\langle I(z,t)\rangle_t^4} \right) \left(1+2\sum_{\tau_m>0} g_2(z,\tau_m)^2\right) = \frac{1+4g_2(z,\tau_m)+3g_2(z,\tau_m)^2}{M} \left(1+2\sum_{\tau_m>0} g_2^2(z,\tau_m)\right)\left(1-g_2(z,\tau_m)^2\right)^2 . \tag{6.14}$$

Here the higher order (3rd and 4th) intensity autocorrelation functions were calculated using theory derived by Lemieux et al. [30]. This analysis is limited to the Gaussian scattering process. Equation (6.14) incorporates the Siegert relation and relies on the fact that the diffusive $g_1(z,\tau_m)$ is real-valued.

Precision of velocity estimation

The velocity of a non-dilute flowing particle suspension can be obtained by fitting Eq. (6.4) at every depth z to the measured $g_2(z,\tau_m)$. In this case $v(z)$ and $A_2(z)$ are the model parameters, while D, w_0, w_z, and θ are assumed to be exactly known a-priori (calibrated). The minimum achievable variance of the flow speed v is given by

$$\sigma^2_{\mathrm{CRLB},v_{g_2}}(z) = \frac{\sum_{m=1}^{M} \frac{e^{-2v^2(z)B\tau_m^2-4Dq^2\tau_m}}{\sigma^2_{g_2}(z,\tau_m)}}{\sum_{m=1}^{M} \frac{4A_2^2(z)v^2(z)B^2\tau_m^4 e^{-2v^2(z)B\tau_m^2-4Dq^2\tau_m}}{\sigma^2_{g_2}(z,\tau_m)} \sum_{m=1}^{M} \frac{e^{-2v^2(z)B\tau_m^2-4Dq^2\tau_m}}{\sigma^2_{g_2}(z,\tau_m)} - \left(\sum_{m=1}^{M} \frac{2A_2(z)v(z)B\tau_m^2 e^{-2v^2(z)B\tau_m^2-4Dq^2\tau_m}}{\sigma^2_{g_2}(z,\tau_m)}\right)^2}, \tag{6.15}$$

$$\text{with} \quad B = \frac{2\cos^2\theta}{w_0^2} + \frac{\sin^2\theta}{w_z^2}, \tag{6.16}$$

where $\sigma^2_{g_2}(z,\tau_m)$ can also be computed analytically similar to Eq. (6.14) using [30]. However, in this case phase terms of $g_1(z,\tau_m)$ need to be taken into account.

For a dilute suspension the velocity can be determined by fitting Eq. (6.5) to the measured $g_2(z,\tau_m)$. In this case $v(z)$ and $A_3(z)$ are the model parameters, while D, w_0, $w(z)$, w_z, $N_s(z)$ and θ are assumed to be known in advance. The minimum achievable variance of the flow speed is given by

$$\sigma^2_{\text{CRLB}_{\text{dilute}},v_{g_2}}(z) = \frac{\sum_{m=1}^{M} \frac{1}{\sigma^2_{g_2}(z,\tau_m)} \left(\frac{\partial g_2(z,\tau_m)}{\partial A_3(z)}\right)^2}{\sum_{m=1}^{M} \frac{1}{\sigma^2_{g_2}(z,\tau_m)} \left(\frac{\partial g_2(z,\tau_m)}{\partial A_3(z)}\right)^2 \sum_{m=1}^{M} \frac{1}{\sigma^2_{g_2}(z,\tau_m)} \left(\frac{\partial g_2(z,\tau_m)}{\partial v(z)}\right)^2 - \left(\sum_{m=1}^{M} \frac{1}{\sigma^2_{g_2}(z,\tau_m)} \frac{\partial g_2(z,\tau_m)}{\partial A_3(z)} \frac{\partial g_2(z,\tau_m)}{\partial v(z)}\right)^2}, \tag{6.17}$$

with

$$\frac{\partial g_2(z,\tau_m)}{\partial A_3(z)} = \frac{2^{3/2}N_s(z)}{2^{3/2}N_s(z)+1}\left(e^{-v^2(z)B\tau_m^2-2Dq^2\tau_m} + \frac{e^{-v^2(z)C(z)\tau_m^2}}{2^{3/2}N_s(z)}\right), \tag{6.18}$$

$$\frac{\partial g_2(z,\tau_m)}{\partial v(z)} = -\frac{2A_3(z)v(z)\tau_m^2 2^{3/2}N_s(z)}{2^{3/2}N_s(z)+1}\left(Be^{-v^2(z)B\tau_m^2-2Dq^2\tau_m} + \frac{Ce^{-v^2(z)C(z)\tau_m^2}}{2^{3/2}N_s(z)}\right), \tag{6.19}$$

$$\text{and} \quad C(z) = \frac{2\cos^2\theta}{w(z)^2} + \frac{\sin^2\theta}{w_z^2}, \tag{6.20}$$

where $\sigma^2_{g_2}(z,\tau_m)$ can no more be calculated using an equation similar to Eq. (6.14) using [30] due to a non-Gaussian scattering process.

For comparison, the minimum achievable variance of the flow speed when using $|g_1(z,\tau_m)|$ from Eq. (6.3) is independent of the particle concentration and given by

$$\sigma^2_{\text{CRLB},v_{|g_1|}}(z) = \frac{\sum_{m=1}^{M} \frac{e^{-v^2(z)B\tau_m^2-2Dq^2\tau_m}}{\sigma^2_{|g_1|}(z,\tau_m)}}{\sum_{m=1}^{M} \frac{A_1^2(z)v^2(z)B^2\tau_m^4 e^{-v^2(z)B\tau_m^2-2Dq^2\tau_m}}{\sigma^2_{|g_1|}(z,\tau_m)} \sum_{m=1}^{M} \frac{e^{-v^2(z)B\tau_m^2-2Dq^2\tau_m}}{\sigma^2_{|g_1|}(z,\tau_m)} - \left(\sum_{m=1}^{M} \frac{A_1(z)v(z)B\tau_m^2 e^{-v^2(z)B\tau_m^2-2Dq^2\tau_m}}{\sigma^2_{|g_1|}(z,\tau_m)}\right)^2}. \tag{6.21}$$

6.2.4. Bias of diffusion and flow estimation

Bias in DLS-OCT is determined by systematic errors in the correlation function and is a measure of the accuracy of the method. The bias is not random but leads to a consistent over or under estimation of the fit parameter. The systematic errors

arise when the model parameters in DLS-OCT are determined by fitting the models from Sec. 6.2 to the measured $g_1(z,\tau_m)$ and $g_2(z,\tau_m)$. These error sources are:

- **Estimation bias** in $g_2(z,\tau_m)$ due to subtraction of the sample mean instead of the true mean from the OCT signal intensity. This introduces an almost constant offset to the normalized autocovariance function given by [31]

$$g_{2_{\text{biased}}}(z,\tau_m) = g_{2_{\text{true}}}(z,\tau_m) - \left(\Pi_{M,m} + \frac{m}{M-m}\left(\Pi_{M,0} - \Pi_{M,m}\right)\right), \tag{6.22}$$

with

$$\Pi_{M,m} = \frac{1}{M(M-2m)} \sum_{i=1}^{M} \sum_{j=m+1}^{M-m} g_{2_{\text{true}}}(z,\tau_{|i-j|}), \tag{6.23}$$

where $g_{2_{\text{biased}}}(z,\tau_m)$ and $g_{2_{\text{true}}}(z,\tau_m)$ are biased and unbiased correlation coefficients, respectively. Calculation of the bias requires a-priori knowledge of a true correlation coefficient, which is not possible in practice. The estimation bias term in Eq. (6.22) is independent of the correlation coefficient and depends only on the correlation decay rate, SNR, and M. It can be reduced by increasing the intensity time series length with respect to the characteristic decay time of $g_2(z,\tau_m)$. As reported in literature [13], the estimation bias (also referred to as the statistical bias) also affects the amplitude and decay rate of $g_2(z,\tau_m)$ and even contains a random component which is not included in Eq. (6.22). This randomness can be reduced by averaging multiple $g_2(z,\tau_m)$. Theoretically both $g_1(z,\tau_m)$ and $g_2(z,\tau_m)$ suffer from the additional estimation bias when subtracting a DC term from the OCT interference spectra before inverse Fourier transformation, if the DC term is estimated from the interference time series itself. In our analysis this effect is neglected.

- **Sampling distribution bias** in $g_1(z,\tau_m)$ and $g_2(z,\tau_m)$ is caused by the slight skewness of the correlation coefficient distribution [28] leading to a bias of the sample mean with respect to the true value. This bias depends on the correlation coefficient and decreases with increasing time series length as the distribution better approaches a normal distribution. A simple correction factor for this bias is given by [25, 26, 28]

$$g_{\text{biased}}(z,\tau_m) = g_{\text{true}}(z,\tau_m)\left(1 - \frac{1 - g^2_{\text{true}}(z,\tau_m)}{2M}\right), \tag{6.24}$$

which is negligible for long acquisitions. For example, the sampling distribution bias for our diffusion measurements in Sec. 6.5.1 is of the order of 0.01% of the correlation coefficient and can be disregarded without any corrections.

- **Curve fitting bias** in $g_1(z,\tau_m)$ and $g_2(z,\tau_m)$ is caused by the use of incorrect fit models. For example, the exponential fit curves from Sec. 6.2 cannot be negative at any time delay, whereas measured $g_1(z,\tau_m)$ and $g_2(z,\tau_m)$ can be, due to their probability distributions. So, fits to $g_1(z,\tau_m)$ and $g_2(z,\tau_m)$ with

asymmetric noise will be slightly biased, which can happen if random errors are correlated along τ_m. This bias can be lowered by increasing the time series length and reducing the variance of $g_1(z,\tau_m)$ and $g_2(z,\tau_m)$. Additional fit bias arises if a wrong model is used in the analysis, i.e., a non-dilute model for very dilute suspensions, static fit models for flowing samples, etc. Furthermore, the models are based on assumptions that may be invalid. For example, we assume that the mean scattering wavenumber q is exactly known and that the scattering process is stationary. The polydispersity in particle size and refractive index can also add to the bias. Estimation bias also adds to the fit bias since it introduces a constant offset that cannot be incorporated in the models.

The bias for a sufficiently large M is predominantly represented by estimation and curve fitting errors. Since it affects the normalized autocovariance functions and not directly the model parameters, its influence on the fitted diffusion coefficient and the flow speed cannot be evaluated analytically. Predicting the bias is also impossible experimentally due to a lack of a-priori knowledge and is only feasible using simulations. In addition, systematic errors make our estimators from Sec. 6.2 biased which affect the random errors and prevents us from reaching the maximum precision of our model parameters.

6.3. OCT signal simulations for flow and diffusion

In simulations we generate a complex OCT signal scattered from an ensemble of particles with random (diffusion) and directional (flow) motion. The signal intensity and the normalized autocovariance functions are subsequently calculated. This is repeated N_b times which allows us to compute the autocorrelation variances at every time delay.

6.3.1. Simulation of diffusion

Noiseless time-dependent complex field scattered from N_p diffusing particles is simulated using

$$E_0(t) = \sum_{j=1}^{N_p} e^{-2ik_0 n z_j(t)}, \tag{6.25}$$

where $z_j(t)$ is the j^{th} particle axial position at time t due to the Brownian motion generated using normally distributed steps with $\sigma = \sqrt{2D\Delta t}$. The initial particle positions $z_j(0)$ are uniformly distributed in space. In Eq. (6.25) we have neglected the effect of the PSF on the scattered field fluctuations [3], considered motion solely in the depth direction, and assumed that all particles have an identical scattering cross section. The effects of Brownian motion in the lateral direction can be disregarded since they occur on a timescale much longer than that assessed with DLS-OCT.

Inclusion of the noise in the scattered field then leads to [32, 33]

$$E(z,t) = E_0(t) + e^{i\varphi(t)}\sqrt{\frac{\left\langle \left|E_0(t)\right|^2 \right\rangle_t}{\mathrm{SNR}(z)}}, \tag{6.26}$$

where $\varphi(t)$ is a time-dependent random phase angle uniformly distributed between 0 to 2π. Note that this is only a good approximation when SNR $\gg 1$ because we assume that field magnitude fluctuations are negligible and the noise originates purely from the random phase angle.

6.3.2. Simulation of flow

The scattered field from suspensions flowing perpendicular to the beam optical axis is simulated by replacing $E_0(t)$ in Eq. (6.26) with

$$E_0(z,t) = \sum_{j=1}^{N_p} e^{-2ik_0 n z_j(t)} e^{\frac{-2(x_j+v(z)t)^2}{w^2(z)}} e^{\frac{-ik_0(x_j+v(z)t)^2}{R^2(z)}}, \tag{6.27}$$

where $v(z)$ is the depth-dependent transverse bulk velocity, $w(z)$ is the local beam waist, $R(z)$ the radius of curvature of the Gaussian beam, and x_j is the uniformly distributed initial random transverse position of j^{th} particle. The additional factor 2 in the radial PSF function is due to coupling efficiency of the scattered light in a confocal setup [2, 3, 34].

As we solely model the transverse flow, leading to identical decorrelation regardless of its direction within the transverse plane, we consider only one lateral dimension, denoted as x. This allows us to reduce the computational complexity and the number of required particles to be modeled. The particles are simulated with random, uniformly distributed x-positions between $-L(z)$ and $+L(z)$ given by

$$L(z) = \frac{N_p\sqrt{\pi}w_0}{4N_s(z)}, \tag{6.28}$$

where $N_s(z)$ is the number of particles in the scattering volume and N_p is the total number of simulated particles. Equation (6.28) guarantees that the number of particles in the scattering volume is always $N_s(z)$ and does not depend on N_p. The scattering volume (length) for 1D flow simulations is an integral of the intensity PSF over all space [7, 19] and equals to $\sqrt{\pi}w_0/2$. Since we confine our modeling to the x-dimension spanning from $-L(z)$ to $+L(z)$, as the particles move with the bulk velocity $v(z)$ and exit the simulated space, they are reintroduced based on the periodic boundary conditions.

Simulations using Eq. (6.27) are valid for arbitrary particle concentrations. For non-dilute particle suspensions with $N_s \gg 1$, the normalized flow autocovariance functions from Sec. 6.2.2 depend only on the beam waist in focus and are indepen-

dent of $w(z)$ and $R(z)$. In this case Eq. (6.27) simplifies into

$$E_0(z,t) = \sum_{j=1}^{N_p} e^{-2ik_0 n z_j(t)} e^{\frac{-2(x_j+v(z)t)^2}{w_0^2}}, \tag{6.29}$$

with w_0 being the beam waist in focus. Therefore, the simulations of non-dilute flowing suspensions do not require a-priori knowledge of any other beam shape parameter except w_0. Even though the models in this section are given for the transverse flow, they can be readily extended to incorporate the flow component along the beam optical axis.

6.4. Materials and Methods

6.4.1. OCT system

The experiments were performed using a Thorlabs GANYMEDE II HR series spectral domain OCT system, which has been described in detail in our previous works [6, 7]. The acquisition rate was 5.5 kHz for diffusion and dilute flow measurements (low-speed), and 36 kHz for non-dilute flow measurements (high-speed). The acquired signal spectrum was measured with a spectrometer with 2048 pixels. The maximum imaging depth in air is 1.87 µm. After acquisition, the measured spectrum was first resampled to a linearly-sampled wavenumber domain and then apodized using a Gaussian filter. After the apodization, the measured coherence function waist in sample was $w_z = 2.11$ µm. We have neglected the effect of a gradient of the axial velocity on the autocovariance function for two reasons [20]. First, the Doppler angle in this work is essentially zero ($\theta \approx 0$). Second, our optical resolution is high both in axial and transverse directions compared to the flow channel dimensions. Hence, the flow velocity within PSF can be assumed to be constant.

The OCT system is operated with a scan lens (LSM04-BB, Thorlabs) in a confocal setup with a manufacturer provided focal spot size of $w_0 = 6$ µm in air which was validated by axial confocal response measurements [6, 7]. The system has NA $= 0.05$. Depending on the angle of incidence, refractive index contrast and Gaussian beam parameters, w_0 and $w(z)$ vary somewhat because of the passage of the beam through the various interfaces [35]. Therefore, for flow measurements $w(z)$ and w_0 were calibrated using the procedures described in [6, 7]. Since for the given OCT setup the coherence length is small and the NA is very low, it can be assumed that the scattering angle is $180°$ and the scattering wavenumber q in the correlation analysis is constant at $q = 2nk_0$.

6.4.2. Averaging strategies

We acquire N_b separate OCT interference time traces, $S(k_0, t_m)$, each having a length of M, to compute N_b normalized autocovariance functions. Measurements conducted under identical conditions can be averaged. The processing and averaging steps of DLS-OCT are illustrated in Fig. 6.1. Nonlinear curve fitting is utilized, truncating the autocorrelation functions when they reach zero and are fully decorrelated. From N_b measurements, three distinct approaches are used to derive the

average model parameters:

- This first approach (method 1), represented by the orange arrow, involves fitting our models to each $g_1(z, \tau_m)$ and $g_2(z, \tau_m)$ and subsequently averaging the resulting N_b parameters. We denote this method as $\overline{D}$ and $\overline{v}$ for diffusion and flow measurements, respectively, and it is also referred to as the standard method by us.
- The second approach (method 2), indicated by the red arrow, is to average N_b normalized autocovariance functions and perform the curve fitting procedure on the averaged data. This approach is denoted as $D_{\overline{g}}$ and $v_{\overline{g}}$ for diffusion and flow measurements, respectively.
- The third approach (method 3), denoted by the blue arrow, is a mixing method developed by us. It begins by creating an $N_b \times M$ matrix containing N_b statistically independent autocorrelation functions along each row. Subsequently, the j^{th} column is circularly shifted by an integer number $j-1$, with the shifting being performed in the same direction for every column. This process generates a resultant 2D matrix where each row represents a mixed autocorrelation function containing only one correlation coefficient from any single time trace. Finally, our models are fitted to the N_b mixed autocorrelation functions, and the obtained parameters are averaged. This method is denoted as mixed $\overline{D}$ and mixed $\overline{v}$ for diffusion and flow measurements, respectively. The mixing method is illustrated in Fig. 6.2 using simple autocorrelation functions with $N_b = M = 3$. The superscript indicates the statistically independent measurements.

For a single time trace measurement the precision is given by the standard deviation (σ_D and σ_v), but when averaging multiple measurements the precision is given by the standard error of the mean ($\sigma_{\text{average } D}$ and $\sigma_{\text{average } v}$). Averaging N_b uncorrelated measurements lowers the variance by a factor of N_b. For positively correlated measurements, the decrease is slower.

When averaging the fitted model parameters, σ_D^2 and σ_v^2 are reduced upon averaging, whereas when averaging the autocorrelation functions, $\sigma_{g_1}^2$ and $\sigma_{g_2}^2$ are

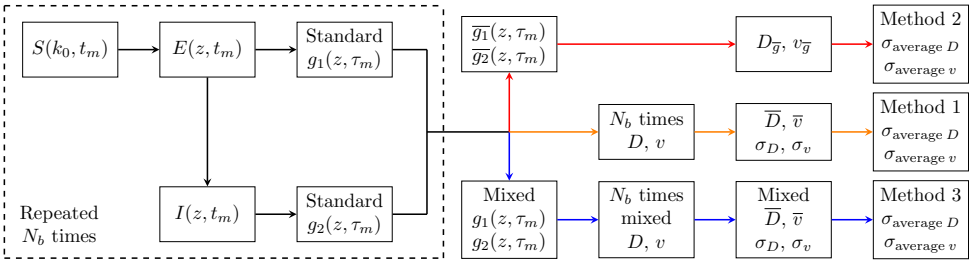

Figure 6.1: Data processing steps for obtaining D and v from OCT data with different averaging techniques.

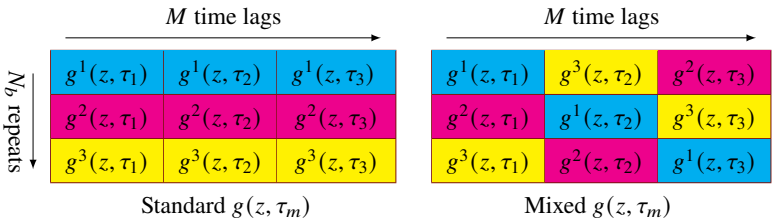

Figure 6.2: Schematic overview of the calculation of standard and mixed autocorrelation functions.

scaled at all time delays and the noise is reduced. As Eq. (6.11, 6.13, 6.15, 6.17) show, multiplying $\sigma^2_{g_1}$ or $\sigma^2_{g_2}$ by a constant N_b^{-1} at every τ_m results in the identical scaling of σ^2_D and σ^2_v. This holds true for both uncorrelated and correlated random variables. As the averaging sequence does not influence the noise correlation, for unbiased or even slightly biased estimators identical overall precision is expected for the first and second approaches. In the third approach, if the autocorrelation noise at different time delays is correlated, we anticipate that the mixing process will eliminate the correlation in the noise.

Bias cannot be improved by averaging. However, one of the sources of the bias is the estimation bias which, according to Sec. 6.2.4, exhibits some random nature. Hence, mixing or averaging the correlation functions can reduce this variability. Therefore, we study the bias for all three averaging schemes. The bias is generally very small compared to the measurement uncertainty, and due to a lack of a-priori information it can only be quantified using simulations.

6.4.3. Diffusion measurements

For diffusion measurements the acquisition rate was 5.5 kHz which is the highest sensitivity setting of our OCT system. All measurements are performed using monodisperse 50 nm radius silica particles with a volume fraction $f_v \approx 1\%$, provided by CWK (Chemiewerk Bad Köstritz GmbH, Germany). In total 1100 depth-resolved measurements were performed with a time series length of 4096 points covering $T = 0.74$ s. From this data 1100 correlation functions $g_1(z,\tau_m)$ and $g_2(z,\tau_m)$ were calculated at every depth. For diffusion analysis only the real part of $g_1(z,\tau_m)$ was used. Since the OCT sensitivity decreases in depth [36], a usable depth-range of 0.92 mm was chosen where the fitted diffusion coefficients were constant and where the single scattering regime holds. The reference diffusion coefficient was calculated by fitting Eq. (3.3) to the mean $\Re\big(g_1(z,\tau_m)\big)$ and averaging the resulting diffusion coefficients over the chosen depth range, resulting in $D_0 = 4.02 \pm 0.02$ µm^2/s which corresponded to a mean particle radius of 53 nm. The SNR at every depth was calculated based on Eq. (3.3) using the fitted $A_1(z)$. Simulations were performed using the same parameters as input. In total 10000 simulations were performed for each SNR. Simulated variances were used for calculating the Cramer-Rao lower bounds using Eq. (6.11) and Eq. (6.13). Precision as a function of SNR for both diffusion measurements and simulations was determined by computing the standard deviation and the standard error of the mean in the fit-

ted diffusion coefficient both when using $\Re\big(g_1(z,\tau_m)\big)$ and $g_2(z,\tau_m)$. The bias for different averaging schemes was assessed using simulations.

6.4.4. Flow measurements

The flow was generated using a syringe pump with a variable discharge rate (Fusion 100, Chemyx, Inc.). The flow geometry was aligned so that $\theta \approx 0°$. This minimized the velocity gradient effect on the correlation [20] and simplified the beam waist calibration. Other than that, the effect of a nonzero Doppler angle on DLS-OCT is minimal because of similar optical resolutions in axial and transverse directions.

Non-dilute flow measurements

For non-dilute flow measurements we used 20 mL syringe (Terumo Europe NV) and OCT acquisition rate of 36 kHz. Diluted Intralipid solutions were used as a sample with a particle volume fraction $f_v \approx 0.6\%$. The flow passes through a quartz rectangular flow cell with internal dimensions of 0.2 mm depth and 10 mm width (type 45-F, Starna Scientific). M-scan 1D measurements were performed at the center width of the flow cell as a function of depth with discharge rates of 1.5 and 2 mL/min. The beam focus was moved away from the center depth of the sample to increase the number of particles in the scattering volume and reduce the effect of number fluctuations [18, 19]. The particle diffusion coefficient and the beam waist in focus were calibrated using a $g_2(z,\tau_m)$ based on lateral scanning over the static sample [6] and were found to be $D = 1.40 \pm 0.09$ μm^2/s and $w_0 = 8.08 \pm 0.31$ μm, respectively. The flow speed was determined by fitting Eq. (6.3,6.4) to the measured or simulated first and second-order autocovariance functions. The depth-dependent SNR was calculated from the fitted autocovariance magnitude. In total 1000 measurements and 10000 simulations were performed with a time series length of 4096. The average depth-dependent flow velocities and SNR values from measurements were used as the input for simulations. Simulated variances were used for calculating the Cramer-Rao lower bounds both for $\big|g_1(z,\tau_m)\big|$ and $g_2(z,\tau_m)$. The bias for different averaging schemes was also determined using simulations.

Dilute flow measurements

Dilute flow measurements were performed with the second-order normalized autocovariance function using the number fluctuations analysis. The OCT acquisition rate was 5.5 kHz and a 5 mL syringe (BD Plastipak) was used. Experiments were performed using a monodisperse suspension of polystyrene particles with volume fraction $f_v \approx 0.006\%$ and expected particle radius of $230 - 250$ nm, provided by InProcess-LSP. The flow passes through a quartz rectangular flow cell with internal dimensions of 0.5 mm depth and 10 mm width (type 45-F, Starna Scientific). M-scan 1D measurements were performed at the center width of the flow cell as a function of depth at discharge rates of 0.15 and 0.225 mL/min. In contrast to our previous work, where only the number fluctuation term was used [7], here we use the full model from Eq. (6.5).

The particle diffusion coefficient was determined (calibrated) in the stationary suspension using $\Re\big(g_1(z,\tau_m)\big)$ and Eq. (3.3). The obtained diffusion coefficient of

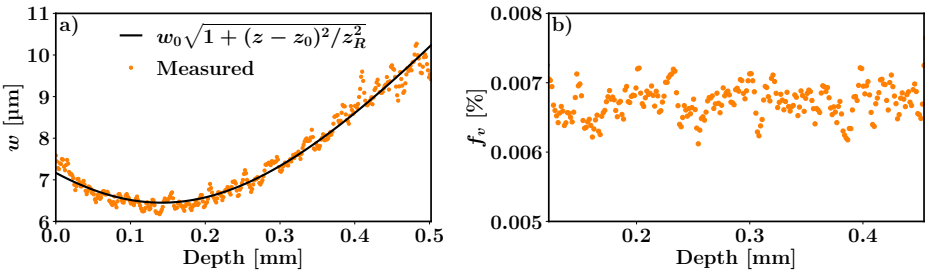

Figure 6.3: Obtained (a) beam shape $w(z)$ and (b) particle volume fraction f_v as a function of depth.

$D_0 = 1.00 \pm 0.03$ µm^2/s corresponded to an average particle radius of 220 nm. The beam shape calibration procedure was identical to that in [7], but the analysis was slightly different because of using the full autocorrelation model. The SNR at every depth was calculated by fitting Eq. (6.3) to the measured $|g_1(z,\tau_m)|$. The kurtosis was determined using Eq. (6.8). Then $A_3(z)$ was found based on Eq. (6.7) using the known SNR and kurtosis. Finally, Eq. (6.6) was fitted to the measured $g_2(z,\tau_m)$ with $N_s(z)$ and $w(z)$ being the fit parameters and using $A_3(z)$, SNR, and the measured $|g_1(z,\tau_m)|$. The obtained beam shape $w(z)$ was fitted using $w(z) = w_0\sqrt{1+(z-z_0)^2/z_R^2}$, with w_0, z_0, and z_R being the free parameters equaling 6.45 ± 0.02 µm, 187 ± 3 µm and 293 ± 3 µm, respectively. The particle volume fraction f_v was computed using $w(z)$, D_0, w_z and $N_s(z)$ according to [7]. It is given in Fig. 6.3(a,b) along with the obtained $w(z)$.

The obtained $w_z(z)$ and $N_s(z)$ were used in subsequent number fluctuation flow measurements. In total, 750 measurements were performed each with a time series length of 8192. The flow speed was determined by fitting Eq. (6.5) to the measured second-order autocovariance function with $A_3(z)$ and $v(z)$ being the free parameters. Simulations for the dilute regime were not performed due to the adverse effects of boundary conditions and long computational times. Therefore, the measured variances were used for calculating the Cramer-Rao bounds. Even though number fluctuations are only present in $g_2(z,\tau_m)$, for comparison the CRLB for $|g_1(z,\tau_m)|$ was also determined.

6.5. Results

6.5.1. DLS-OCT diffusion measurement

Depth dependent diffusion measurements were performed on a static particle suspension. Examples of measured $\Re(g_1(z,\tau_m))$ and $g_2(z,\tau_m)$ for SNR $= 100$ are shown in Fig. 6.4(a). Observe here that the autocorrelation functions do not oscillate around the mean, but, instead, consistently remain above or below it for some time. From N_b measured normalized autocovariance curves (signal ACF), the normalized autocovariances of errors (error ACF) in the measured and simulated

$\Re\big(g_1(z,\tau_m)\big)$ and $g_2(z,\tau_m)$ were calculated using

$$\rho_e(z,\tau_e) = \frac{\big\langle \big(g(z,\tau_m) - \overline{g}(z,\tau_m)\big)\big(g(z,\tau_m+\tau_e) - \overline{g}(z,\tau_m+\tau_e)\big)\big\rangle_{\tau_m}}{\sigma_e^2(z)}, \qquad (6.30)$$

where $g(z,\tau_m)$ is the measured normalized autocovariance function, $\overline{g}(z,\tau_m)$ is its average from N_b measurements, and $\sigma_e^2(z)$ is the variance of $g(z,\tau_m) - \overline{g}(z,\tau_m)$ along the τ_m axis.

Figure 6.4(c,d) illustrates that in standard autocorrelation functions, errors at different time delays exhibit strong correlation. This means that the magnitude and direction of errors in $\Re\big(g_1(z,\tau_m)\big)$ or $g_2(z,\tau_m)$ at small τ_m significantly affect the errors at larger τ_m, which can be observed from the fact that any single autocorrelation function is consistently above or below the mean autocorrelation function. As described in Sec. 6.4.2, we implement a novel way of reducing these correlations or even completely eliminating them by mixing different autocorrelation functions at every τ_m. The number of independent autocorrelation functions used for mixing is denoted by N_{mix}. To fully get rid of the correlations N_{mix} must be greater or equal to the number of sampling points it takes for $\Re\big(g_1(z,\tau_m)\big)$ and $g_2(z,\tau_m)$ to go to zero. For $g_2(z,\tau_m)$ it takes fewer realizations to eliminate correlations because it decays twice as fast.

Figure 6.4(b-d) show that for a single fully mixed $\Re\big(g_1(z,\tau_m)\big)$ and $g_2(z,\tau_m)$ with sufficiently large N_{mix} the errors at different τ_m are completely uncorrelated. As a result, the measured mixed autocorrelation data oscillate approximately around

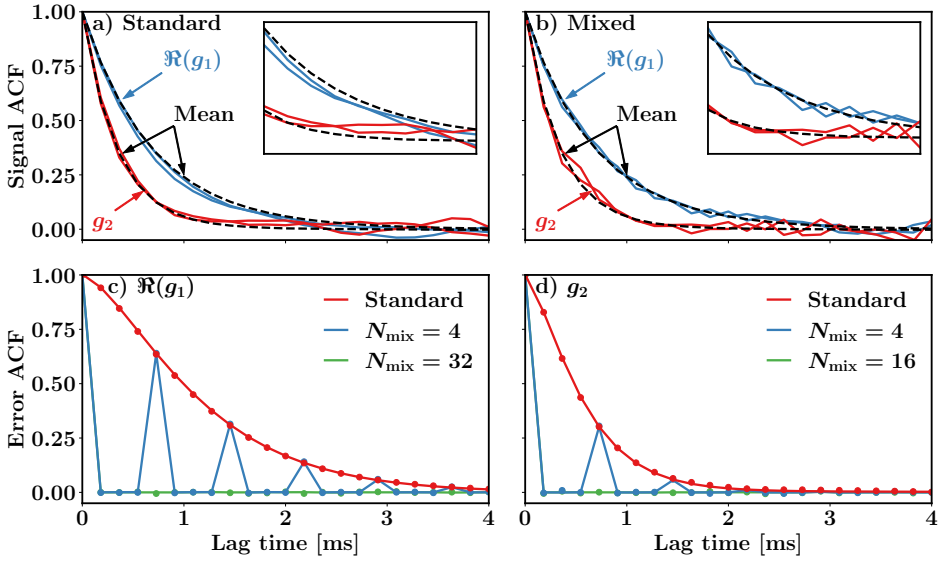

Figure 6.4: Example (a) standard and (b) mixed autocorrelation functions (signal ACF) for SNR = 100. (c,d) Measured (points) and simulated (lines) error ACF, $\rho_e(z,\tau_e)$.

the mean as a function of τ_m. With standard (unmixed) measurements, as shown in Fig. 6.4(a), error ACF is nonzero and every measured $\Re\big(g_1(z,\tau_m)\big)$ and $g_2(z,\tau_m)$ deviates from the mean autocorrelation function. Figure 6.4(c,d) show that once the autocorrelation functions are sufficiently mixed (e.g. $N_{\text{mix}} = 32$), error ACF becomes a delta function. At intermediate mixing ratios ($N_{\text{mix}} = 4$) error ACF becomes periodic as the correlations reappear at later time points.

Precision in diffusion estimation

Next, we look at the diffusion estimation precision from a single autocorrelation measurement. To estimate the precision, the autocorrelation variance at every time delay needs to be known. Figure 6.5(a,b) show measured, simulated, and analytical variances from Eq. (6.12,6.14) for the diffusive $\Re\big(g_1(z,\tau_m)\big)$ and $g_2(z,\tau_m)$ at different SNR values. All three match relatively well with each other. The variances are higher for larger SNR values, but, in this case the correlation coefficients are also larger. Even though the variances of $\Re\big(g_1(z,\tau_m)\big)$ and $g_2(z,\tau_m)$ are comparable at larger time delays, $\sigma^2_{g_2}(z,\tau_m)$ is significantly larger at small τ_m. The different shape of $\sigma^2_{g_2}(z,\tau_m)$ and its sharp increase at small τ_m is due to the mean subtraction from the intensity time series.

Figure 6.6(a,b) show measured and simulated standard deviations in the fitted diffusion coefficient from a single correlation function, as well as the Cramer-Rao lower bound calculated with Eq. (6.11) and (6.13), where the z-dependence is converted to SNR. The results are based on 10000 simulations and 1100 measurements. Here D_0 was calculated from the measured $\Re\big(g_1(z,\tau_m)\big)$ as described in Sec. 6.4.3 and subsequently used as input for simulations. The obtained σ_D strongly depends on whether the errors in our normalized autocovariance functions are correlated. The obtained σ_D from the standard measurements is several factors larger than the Cramer-Rao lower bound. After mixing the resulting σ_D matches very well with the Cramer-Rao bound and we achieve the most precise determination of the diffusion coefficient possible. The measured and simulated σ_D overlap each other except for $g_2(z,\tau_m)$ at very low SNR values. Here the simulations underestimates the error. The lowest spread in the fitted D, given by σ_D, is obtained when mixing the

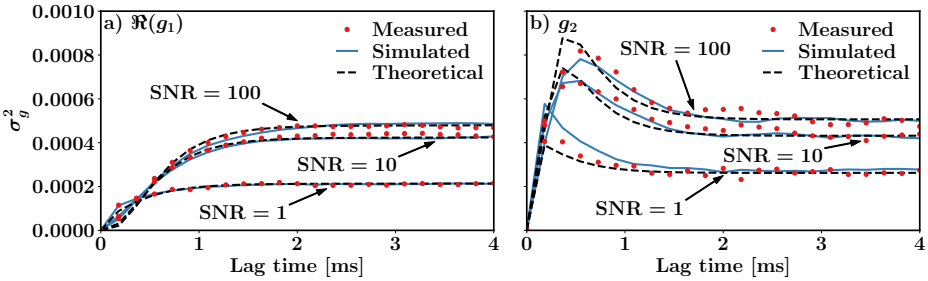

Figure 6.5: Measured, simulated, and analytical variances of diffusion only (a) $g_1(z,\tau_m)$ and (b) $g_2(z,\tau_m)$.

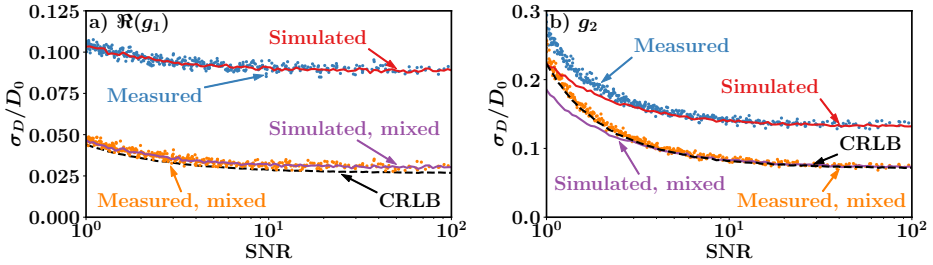

Figure 6.6: Measured (points) and simulated (lines) standard deviation for estimating the diffusion coefficient from a single autocorrelation function and the corresponding Cramer-Rao lower bound for (a) $g_1(z,\tau_m)$ and (b) $g_2(z,\tau_m)$.

normalized autocovariance functions for removing the error correlations. However, this requires many measurements, as shown in Fig. 6.6(a,b), and is therefore less relevant for practical applications with few measurements. Typically, the number of DLS-OCT measurements is on the order of 5-10.

Figure 6.7(a,b) show the standard deviation (spread) in the diffusion coefficient obtained from fitting a single correlation function as a function of the number of measurements N_b. For conventional DLS-OCT measurements without mixing, σ_D is constant as expected for independent measurements. When employing auto-correlation mixing we see that σ_D decreases with increasing N_b until reaching the

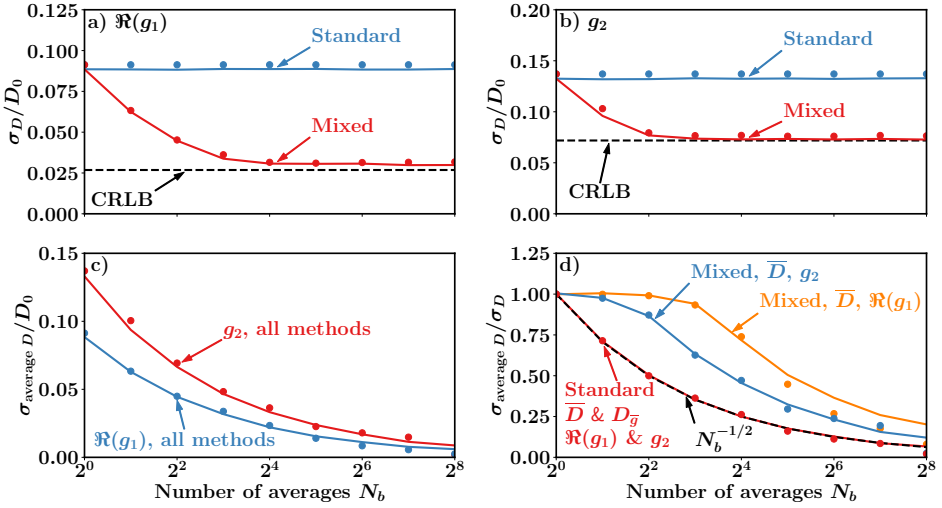

Figure 6.7: (a,b) Standard deviation and (c,d) standard error of the fitted diffusion coefficient as a function of the number of averaged correlation functions for SNR = 100. Points correspond to DLS-OCT measurements and lines denote simulations.

CRLB and after which it remains constant with N_b. For $g_2(z, \tau_m)$ it takes fewer measurements for σ_D to reach the CRLB.

In DLS-OCT measurements are averaged to improve the precision. In this case the measurement precision is given by the standard error of the mean, $\sigma_{\text{average } D}$. Figure 6.7(c) shows simulated and measured standard error of the mean diffusion coefficient, $\sigma_{\text{average } D}$, as a function of N_b for different averaging techniques. The standard error of the mean is identical for all three averaging methods, even though σ_D itself is different depending on error correlations. The decrease is proportional to ${N_b}^{-1/2}$. Figure 6.7(d) shows how $\sigma_{\text{average } D}$ is related to σ_D for the three different averaging techniques. For the standard analysis we see that $\sigma_{\text{average } D} = \frac{\sigma_D}{\sqrt{N_b}}$ for both averaging methods. However, when mixing the normalized autocovariance functions, we notice that $\sigma_{\text{average } D} > \frac{\sigma_D}{\sqrt{N_b}}$ as the fitted diffusion coefficients now become statistically interdependent. Here $\sigma_{\text{average } D}$ initially decreases very slowly with N_b and then starts to reduce faster above a certain N_b. This coincides with the N_b at which the CRLB is reached in Fig. 6.7(a,b). In Fig. 6.7(d) there is a small discrepancy between measurements and simulations at large N_b which caused by the lack of sufficient number of averaged measurements.

Bias in diffusion estimation

The bias in the average diffusion coefficient is determined by comparing the averaged D to a ground truth. We average 1100 and 10000 values of D in measurements and simulations, respectively. With this large set of averages we can assume that the random errors are negligible and only the systematic errors remain. Fig-

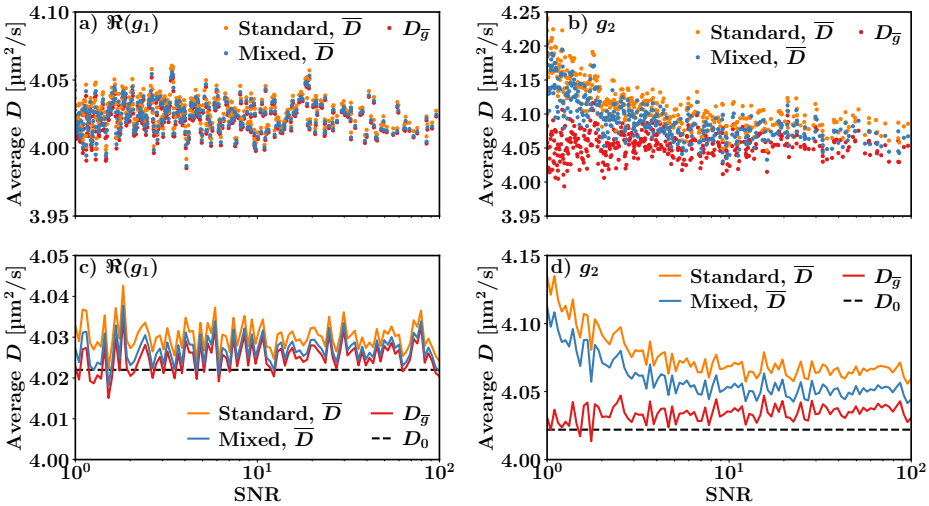

Figure 6.8: Diffusion coefficients as a function of SNR and averaging scheme determined using (a,b) measurements and (c,d) simulations.

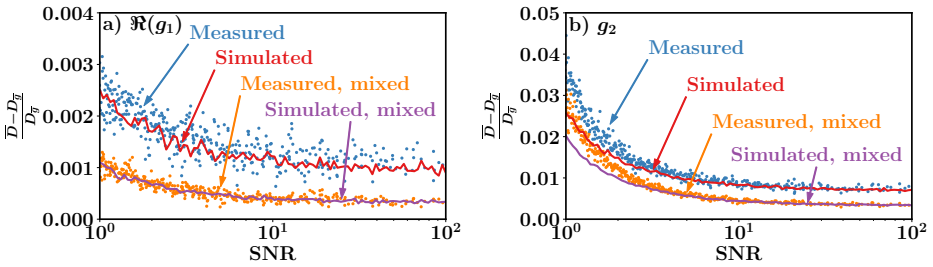

Figure 6.9: Measured (points) and simulated (lines) relative bias in the diffusion coefficient as a function of SNR for (a) $\Re(g_1(z,\tau_m))$ and (b) $g_2(z,\tau_m)$.

ure 6.8(a,b) shows the measured diffusion coefficients as a function of SNR for both $\Re(g_1(z,\tau_m))$ and $g_2(z,\tau_m)$ with different averaging schemes. Figure 6.8(c,d) show the same results but obtained using simulations. In this case the input D_0 is also displayed. Both in measurements and simulations we can observe that mixing different correlation functions slightly reduces the bias. However, the lowest bias is obtained for $D_{\bar{g}}$ when averaging the correlation functions. This is more evident for $g_2(z,\tau_m)$. The differences for the three techniques are minimal for $\Re(g_1(z,\tau_m))$. Overall, the bias is much smaller and less affected by SNR when using $\Re(g_1(z,\tau_m))$ compared to $g_2(z,\tau_m)$.

Trends from both measurements and simulations in Figures 6.8(a,b) and 6.8(c,d) are similar, however for the measurements we lack a-priori knowledge of the ground truth D_0. Therefore, it is not possible to compare the bias directly between measurements and simulations. This can be rectified on a relative basis by not comparing the absolute deviation from D_0, but the relative bias with respect to the most accurate method (correlation averaging). Figure 6.9(a,b) displays the relative bias when averaging the fitted diffusion coefficients with respect to averaging $\Re(g_1(z,\tau_m))$ and $g_2(z,\tau_m)$ first and then fitting the diffusion coefficient. The obtained measurements and simulations are in perfect agreement except for $g_2(z,\tau_m)$ at very low SNR values. This emphasizes the reliability of our simulations and that they can be used for determining the absolute bias.

The bias of the mean diffusion coefficient from Fig. 6.8(c,d) is determined by averaging over a large number of simulations. Figure 6.10(a,b) show simulated systematic errors as a function of the number of averaged measurements N_b for $\Re(g_1(z,\tau_m))$ and $g_2(z,\tau_m)$. For $\Re(g_1(z,\tau_m))$the bias is very low and almost independent of N_b, as expected. The bias is more significant for $g_2(z,\tau_m)$. Figure 6.10(b) shows the estimation bias due to mean subtraction modeled using Eq. (6.22). This is the main source of bias for $g_2(z,\tau_m)$ which is absent in $\Re(g_1(z,\tau_m))$. The estimation bias also contains a random component which averages out with increasing number of measurements. As a result, the bias in $g_2(z,\tau)$ initially decreases with N_b until reaching the minimum and then remains constant. Overall, the bias is minimal when averaging the autocorrelation functions. The

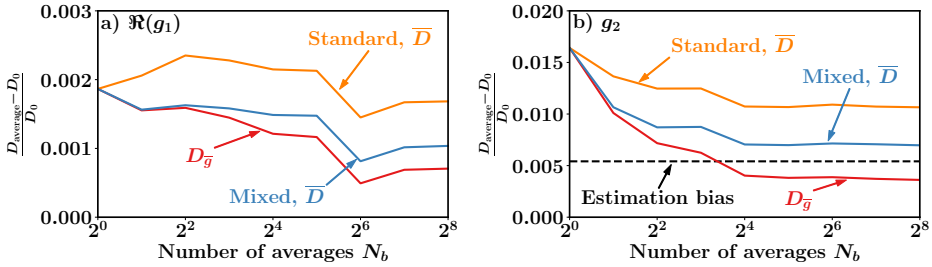

Figure 6.10: Simulated bias of the fitted diffusion coefficient as a function of the number of used correlation functions at SNR = 100 for (a) $\Re(g_1(z,\tau_m))$ and (b) $g_2(z,\tau_m)$.

second best technique is mixing the autocorrelation functions before the curve fitting and averaging the fitted diffusion coefficients. The worst approach is to the fit model parameters to the standard autocorrelation functions and then average them.

6.5.2. Non-dilute DLS-OCT flow measurement

Precision analysis of flow was performed for DLS-OCT $|g_1(z,\tau_m)|$ and $g_2(z,\tau_m)$ measurements of a laminar transverse flow corrected for diffusion. Figure 6.11(a,b) show measured and simulated variances at different flow speeds in the channel, good agreement between the two is observed. The variances are higher with lower flow speeds, but do not depend much on the SNR. The highest SNR value in the channel was above 100, and the lowest was 6. This is sufficiently high to neglect the SNR dependence of σ_v for plotting purposes and display it only as a function of the flow speed. Velocity profiles, shown in Fig. 6.12(a), were obtained by averaging the measured correlation functions and were subsequently used as ground-truth input for simulations.

Figure 6.12(c,d) show measured and simulated standard deviation in the fitted flow speed as a function of velocity. Results are obtained using both the standard

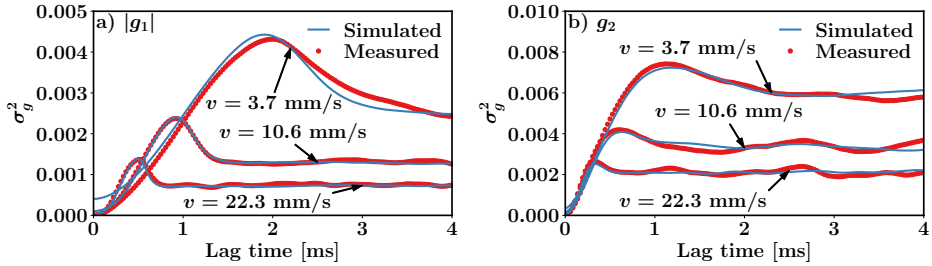

Figure 6.11: Measured and simulated variances for flow (with a fixed and calibrated diffusion coefficient) of (a) $|g_1(z,\tau_m)|$ and (b) $g_2(z,\tau_m)$.

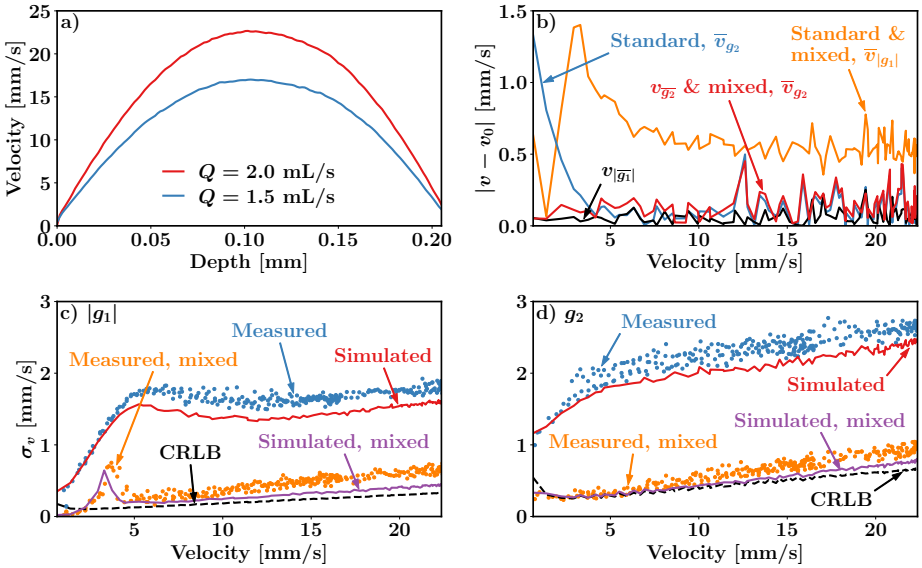

Figure 6.12: Non-dilute flow measurements. (a) Measured flow profiles. (b) Simulated bias in the fitted velocity. Measured and simulated σ_v using (c) $|g_1(z,\tau_m)|$ and (d) $g_2(z,\tau_m)$ and the corresponding CRLB.

method with correlated errors and the mixing technique with uncorrelated errors are given. Similar to diffusion, mixing decreases the spread in the obtained velocity. For comparison, the Cramer-Rao lower bounds for $g_2(z,\tau_m)$ and $|g_1(z,\tau)|$, calculated using Eq. (6.15) and (6.21), are also displayed. The theoretical Cramer-Rao bound for $|g_1(z,\tau)|$ is lower than for $g_2(z,\tau_m)$. For both methods there is a good agreement between measurements and simulations. The obtained σ_v from measurements and simulations is significantly improved when mixing removes the error correlations and matches well with the Cramer-Rao bound, especially for $g_2(z,\tau_m)$. In general, the standard deviation in the flow speed decreases with lower velocities. However, it does not decrease to zero and has a certain minimum value. Below the threshold velocity σ_v starts to increase because of diffusion. This is only clearly visible when the errors are not correlated.

Figure 6.12(b) displays the simulated bias for different averaging schemes both for $|g_1(z,\tau)|$ and $g_2(z,\tau_m)$. The bias was calculated with respect to the simulation input which included both depth-dependent velocity and SNR profiles. The simulated bias is lowest when averaging the complex $g_1(z,\tau_m)$, taking the absolute value and then fitting $v(z)$. This is denoted by the black curve. The second lowest bias is obtained when averaging $g_2(z,\tau_m)$ and then fitting $v(z)$ or when mixing $g_2(z,\tau_m)$, fitting and averaging $v(z)$. In this case the errors are identical and given by the red curve. This approach is only marginally less accurate than the former method. The third best method relies on using the standard $g_2(z,\tau_m)$, fitting and

then averaging $v(z)$. This approach is less accurate than the second best method only at low flow speeds. The largest bias is obtained when using $|g_1(z,\tau)|$ to fit $v(z)$ and then average the obtained velocities. In this case the sample population is significantly skewed and the mixing method has virtually no effect.

6.5.3. Dilute DLS-OCT flow measurement

Similar to non-dilute, we analyse precision of dilute DLS-OCT flow measurements where the effect of diffusion is absent in $g_2(z,\tau_m)$. Also for this case we obtained the variance of the correlation function for different flow speeds. The results look similar to the non-dilute case, except there is no overshoot at small τ_m. Figure 6.13(a,b) show dilute flow measurements using the second-order normalized autocovariance function incorporating the number fluctuations. Velocity profiles are shown in Fig. 6.13(a) which were again obtained by averaging the measured correlation functions. The lowest SNR value in the channel was again around 6, and the highest was above 100. In Fig. 6.13 we have again neglected the SNR dependence for the same reasons as mentioned in Sec. 6.5.2 and plot σ_v only as a function of the velocity.

Figure 6.13(b) shows the measured standard deviation in the fitted flow speed as a function of velocity. Results using both the standard $g_2(z,\tau_m)$ with correlated errors and the mixed $g_2(z,\tau_m)$ with uncorrelated errors are given. Measurements using $|g_1(z,\tau_m)|$ are not shown because they are too noisy and have a significantly larger σ_v. For comparison, the Cramer-Rao lower bounds for $g_2(z,\tau_m)$, calculated with Eq. (6.17), and $|g_1(z,\tau_m)|$, calculated with Eq. (6.21), are also displayed. Here we used the measured variances of $\sigma^2_{g_2}(z,\tau_m)$ and $\sigma^2_{|g_1|}(z,\tau_m)$ for calculating the Cramer-Rao lower bounds. The Cramer-Rao bound for $g_2(z,\tau_m)$ is considerable lower than for $|g_1(z,\tau_m)|$ and agrees very well with our measurements. When using $g_2(z,\tau_m)$ the velocity standard deviation decreases, with decreasing velocity, to zero. However, this is not the case with $|g_1(z,\tau_m)|$. As the Cramer-Rao lower bound shows, σ_v increases dramatically at lower flower speeds when using $|g_1(z,\tau_m)|$. This happens because $|g_1(z,\tau_m)|$ in Eq. (6.3) is ultimately limited by particle diffusion and is independent of number fluctuations. The second-order

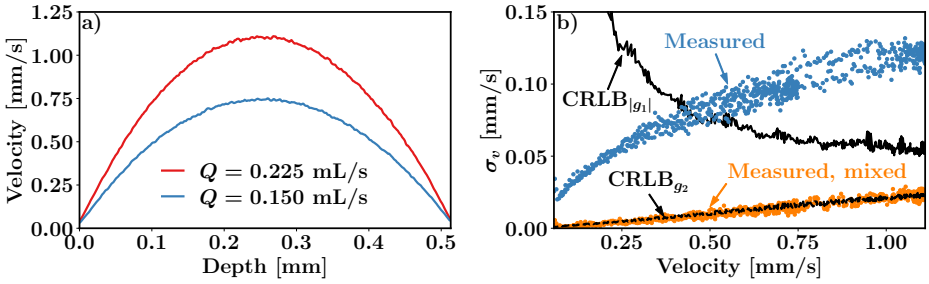

Figure 6.13: Dilute flow measurements. (a) Measured flow profiles using $g_2(z,\tau_m)$. (b) Measured σ_v using $g_2(z,\tau_m)$ and the corresponding CRLB.

normalized autocovariance function in Eq. (6.5), on the other hand, contains the number fluctuation term that is independent D. This increases the velocity precision for this method at extremely low flow speeds. For number fluctuation DLS-OCT no bias analysis is performed because of boundary condition limitations and increasing computational complexity of our simulations.

6.6. Discussion

In this work we review autocorrelation averaging and mixing techniques for reducing random and systematic errors. In the absence of an analytical model for error correlations, only using the mixing method suggested by us, it is possible to quantify the precision in DLS-OCT and verify whether the CRLB is reached. In diffusion measurements using the average real part of $g_1(z,\tau_m)$ results in the highest accuracy and precision. In flow measurements it is more reliable and convenient to use the average $g_2(z,\tau_m)$ because it is not affected by the sampling distribution bias, does not depend on phase and can be implemented in phase-unstable systems. It is important to note that mixing and/or averaging of the autocorrelation functions can only be performed using the autocorrelation functions with the same SNR (and identical optical or sample properties). For single scattering diffusion measurements where D is constant as a function of depth (SNR), we can also average the measurements with different signal-to-noise ratios. In this case the measured $g_1(z,\tau_m)$ and $g_2(z,\tau_m)$ first have to be noise-corrected [13] before any further processing.

6.6.1. DLS-OCT diffusion estimation

Random error correlations in $\Re\big(g_1(z,\tau_m)\big)$ and $g_2(z,\tau_m)$ are the main reason for σ_D not reaching the theoretical Cramer-Rao bound. Once these correlations are removed by mixing, the standard deviation in the fitted diffusion coefficient is reduced significantly and reaches the CRLB. The improvement is bigger for larger SNR values since $\Re\big(g_1(z,\tau_m)\big)$ and $g_2(z,\tau_m)$ are lower in the presence of more noise and hence the random errors are less correlated. The improvement with mixing is less for $g_2(z,\tau_m)$ because it decays faster and therefore correlations play less of a role in the precision. We can conclude that faster decorrelations and smaller autocovariance magnitudes, i.e., more noisy measurements, are less affected by mixing. We have not derived analytical expressions for ρ_e, but our observations suggest that it depends on the autocorrelation decay rate and also experiences a delta function noise decorrelation at $\tau_m = 0$.

Even though the improvement in σ_D due to mixing is significant, practical applications of the mixing technique for increasing the measurement precision are limited. In order to reduce some of the error correlations we need at least two measurements. Mixing just 2 measurements already provides us with a significant improvement in σ_D. However, the precision of the average diffusion coefficient when using multiple measurements is given by the standard error of the mean, $\sigma_{\text{average } D}$, which is identical for all averaging techniques with or without mixing the correlation functions. So, even though σ_D is significantly lower when mixing the autocorrelation functions, it does not decrease as fast with averaging because the

mixed autocorrelation functions are not statistically independent anymore. As a result, the fitted diffusion coefficients are also interdependent and $\sigma_{\text{average } D} \neq \frac{\sigma_D}{\sqrt{N_b}}$. When $\Re\left(g_1(z,\tau_m)\right)$ or $g_2(z,\tau_m)$ are not mixed, $\sigma_{\text{average } D}$ is proportional to $N_b^{-1/2}$ because every fitted D is independent. With mixing we basically move the error correlations from $\Re\left(g_1(z,\tau_m)\right)$ and $g_2(z,\tau_m)$ to the fitted D. Therefore, the actual measurement precision is identical for all averaging methods and cannot be improved any further.

We noticed that systematic errors are much larger when using $g_2(z,\tau_m)$ compared to $\Re\left(g_1(z,\tau_m)\right)$ and are dominated by the estimation bias. Averaging N_b measurements slightly reduces the bias in $g_2(z,\tau_m)$ but only to a certain limit, beyond which the errors remain constant. This is probably caused by variability and randomness in the estimation bias which averages out and diminishes with increasing N_b. We have mentioned that in phase-stable systems it is always preferable to utilize $\Re\left(g_1(z,\tau_m)\right)$ instead of $\left|g_1(z,\tau)\right|$. Using $\left|g_1(z,\tau)\right|$ adversely affects the bias because the autocorrelation coefficients are always positive. This leads to a higher sampling distribution bias which is otherwise negligible. Overall, random errors are larger than systematic errors unless we average thousands of measurements.

There is an asymptotic dependence of precision and bias on SNR. Therefore, the benefits of using extremely high signal-to-noise ratios are rather limited. As Fig. 6.6(b) and Fig. 6.9(b) show, there is a mismatch between simulations and measurements at very low SNR when using $g_2(z,\tau_m)$. This is caused by the specific noise model used in our simulations [33] that is based on the assumption that the signal intensity is much larger than the noise intensity. However, this assumption is not valid at low SNR values. As a result, this noise model overestimates $A_2(z)$ at low SNR values, leading to the lower σ_D.

6.6.2. DLS-OCT flow estimation

Both in dilute and non-dilute flow measurements, the standard deviation (spread) in the fitted velocity is significantly reduced when the error correlations are removed. In non-dilute flows, σ_v decreases with decreasing velocity and then starts to increase at very low flow speeds. A minimum in the error occurs because the diffusive limit is reached. At this stage, any further reduction in the velocity does not affect autocorrelation functions or their variances. According to Eq. (6.15), the velocity is explicitly included in the denominator of $\sigma^2_{\text{CRLB},v}$. As a result, σ_v starts to increase when the diffusive limit is reached. This behaviour is overshadowed by error correlations and is only visible when employing correlation function mixing.

For non-dilute flow the Cramer-Rao bound for $g_2(z,\tau)$ is slightly lower than the simulated σ_v at larger velocities, which itself is marginally lower than the measured σ_v. The difference between simulations and the Cramer-Rao bound is probably because of the Siegert approximation. In this case, the approximate number of particles in the scattering volume is around 49 both in simulations and measurements. This could be sufficiently low to violate the large number of particle assumption and have a small effect on $g_2(z,\tau_m)$. Furthermore, the offset between measurements and simulations can be caused by galvo or pump instabilities. The Cramer-Rao

bound of $|g_1(z,\tau)|$ shows that on paper it is possible to achieve higher precision in non-dilute flow measurements when using $g_1(z,\tau)$ instead of $g_2(z,\tau)$. However, in practice this is more problematic. The mismatch among measurements, simulations and the Cramer-Rao bound at all velocities is considerably larger for $|g_1(z,\tau)|$ compared to $g_2(z,\tau)$. This is largely caused by the bias of the sampling distribution and the limited phase stability.

Theoretically, the lowest bias in non-dilute flow measurements can also be achieved when using $|g_1(z,\tau)|$ by averaging the complex autocorrelation functions first, then taking the absolute value, and then fitting $v(z)$. However, getting rid of the sampling distribution bias when taking the absolute value requires sufficient averaging of the complex $g_1(z,\tau_m)$. In our work we averaged 1000 autocorrelation functions which in real-time flow measurements is impossible. Insufficient averaging will result in oscillations with $|g_1(z,\tau_m)| > 0$. In this work we have not investigated the dependence of the sampling distribution bias on the number of measurements. However, it is clear that with fewer measurements it is preferred to use $g_2(z,\tau)$ as it does not suffer from the population skewness.

Similar to diffusion, random velocity errors in flow measurements are also generally larger than systematic errors. However, at very low speeds both errors become comparable. Despite some advantages of $|g_1(z,\tau_m)|$, for practical reasons it is more convenient to use $g_2(z,\tau_m)$ in non-dilute flows. In dilute low-speed flows it is always preferable to use $g_2(z,\tau_m)$ because it is not limited by the particle diffusion.

6.7. Conclusion

We have investigated precision and bias of diffusion coefficient and flow speed measurements using DLS-OCT based on the first and second-order normalized autocovariance functions. We found that errors in the autocovariance functions are strongly correlated. This significantly reduces the precision and bias of fit parameters and prevents us from reaching the Cramer-Rao lower bound. We demonstrated that mixing different autocovariance functions at every time delay before the curve fitting procedure reduces the standard deviation in the fitted parameters and reaches the Cramer-Rao lower bound. This proves the validity of our DLS-OCT models. When using the mixing technique the correlations are transferred to the fitted parameters and the standard error of the mean remains unchanged. We conclude that the precision in DLS-OCT is identical for all averaging techniques and ultimately limited by correlations between the random variables. The bias is lowest when averaging the measured normalized autocovariance functions before fitting the model parameters.

Data availability

Data underlying the results presented in this paper and the relevant analysis routines are available at [37].

References

[1] J. Kalkman, R. Sprik, and T. G. van Leeuwen, *Path-length-resolved diffusive particle dynamics in spectral-domain optical coherence tomography,* Physical Review Letters **105**, 198302 (2010).

[2] V. J. Srinivasan, H. Radhakrishnan, E. H. Lo, E. T. Mandeville, J. Y. Jiang, S. Barry, and A. E. Cable, *OCT methods for capillary velocimetry,* Biomedical Optics Express **3**, 612 (2012).

[3] N. Weiss, T. G. van Leeuwen, and J. Kalkman, *Localized measurement of longitudinal and transverse flow velocities in colloidal suspensions using optical coherence tomography,* Physical Review E **88**, 042312 (2013).

[4] J. Lee, W. Wu, J. Y. Jiang, B. Zhu, and D. A. Boas, *Dynamic light scattering optical coherence tomography,* Optics Express **20**, 22262 (2012).

[5] B. K. Huang and M. A. Choma, *Resolving directional ambiguity in dynamic light scattering-based transverse motion velocimetry in optical coherence tomography,* Optics Letters **39**, 521 (2014).

[6] K. Cheishvili and J. Kalkman, *Scanning dynamic light scattering optical coherence tomography for measurement of high omnidirectional flow velocities,* Optics Express **30**, 23382 (2022).

[7] K. Cheishvili and J. Kalkman, *Sub-diffusion flow velocimetry with number fluctuation optical coherence tomography,* Optics Express **31**, 3755 (2023).

[8] R. Besseling, M. Damen, J. Wijgergans, M. Hermes, G. Wynia, and A. Gerich, *New unique PAT method and instrument for real-time inline size characterization of concentrated, flowing nanosuspensions,* European Journal of Pharmaceutiral Sciences **133**, 2005 (2019).

[9] S. Yazdanfar, C. Yang, M. V. Sarunic, and J. A. Izatt, *Frequency estimation precision in Doppler optical coherence tomography using the Cramer-Rao lower bound,* Optics Express **13**, 410 (2005).

[10] H. C. Hendargo, R. P. McNabb, A. Dhalla, N. Shepherd, and J. A. Izatt, *Doppler velocity detection limitations in spectrometer-based versus swept-source optical coherence tomography,* Biomedical Optics Express **2**, 2175 (2011).

[11] C. S. Kim, W. Qi, J. Zhang, Y. J. Kwon, and Z. Chen, *Imaging and quantifying Brownian motion of micro- and nanoparticles using phase-resolved Doppler variance optical coherence tomography,* Journal of Biomedical Optics **18**, 030504 (2013).

[12] M. G. O. Gräfe, M. Gondre, and J. F. de Boer, *Precision analysis and optimization in phase decorrelation OCT velocimetry,* Biomedical Optics Express **10**, 1297–1314 (2019).

[13] N. Uribe-Patarroyo, A. L. Post, S. Ruiz-Lopera, D. J. Faber, and B. E. Bouma, *Noise and bias in optical coherence tomography intensity signal decorrelation,* OSA Continuum **3**, 709 (2020).

[14] N. Uribe-Patarroyo, M. Villiger, and B. E. Bouma, *Quantitative technique for robust and noise-tolerant speed measurements based on speckle decorrelation in optical coherence tomography,* Optics Express **22**, 24411 (2014).

[15] N. Weiss, T. G. van Leeuwen, and J. Kalkman, *Simultaneous and localized measurement of diffusion and flow using optical coherence tomography,* Optics Express **23**, 3448 (2015).

[16] B. J. Berne and R. Pecora, *Dynamic Light Scattering* (Dover Publications, 2000).

[17] C. S. Johnson and D. A. Gabriel, *Laser Light Scattering* (Dover Publications, 1994).

[18] D. P. Chowdhury, C. M. Sorensen, T. W. Taylor, J. F. Merklin, and T. W. Lester, *Application of photon correlation spectroscopy to flowing Brownian motion systems,* Applied Optics **23**, 4149 (1984).

[19] T. W. Taylor and C. M. Sorensen, *Gaussian beam effects on the photon correlation spectrum from a flowing Brownian motion system,* Applied Optics **25**, 2421 (1986).

[20] N. Uribe-Patarroyo and B. E. Bouma, *Velocity gradients in spatially resolved laser Doppler flowmetry and dynamic light scattering with confocal and coherence gating,* Physical Review E **94**, 022604 (2016).

[21] D. W. Schaefer, *Dynamics of number fluctuations: Motile microorganisms,* Science **180**, 1293 (1973).

[22] E. J. Nijman, H. G. Merkus, J. C. M. Marijnissen, and B. Scarlett, *Simulations and experiments on number fluctuations in photon-correlation spectroscopy at low particle concentrations,* Applied Optics **40**, 4058 (2001).

[23] S. M. Kay, *Fundamentals of Statistical Signal Processing Estimation Theory* (Prentice Hall, 1998).

[24] H. Hotelling, *New light on the correlation coefficient and its transforms,* Journal of the Royal Statistical Society **15**, 193 (1953).

[25] H. E. Soper, *On the probable error of the correlation coefficient to a second approximation,* Biometrika **9**, 91 (1913).

[26] G. Shieh, *Estimation of the simple correlation coefficient,* Behavior Research Methods **42**, 906 (2010).

[27] A. L. Bowley, *The standard deviation of the correlation coefficient,* Biometrika **23**, 31 (1928).

[28] T. Gnambs, *Brief note on the standard error of the Pearson correlation,* (2022), preprint.

[29] P. Arun, S. A. Lincon, and N. Prabhakaran, *Standard error of the sample autocorrelation as a measure of 'non-stationarity',* Middle-East Journal of Scientific Research **9**, 2778 (2016).

[30] P. A. Lemieux and D. J. Durian, *Investigating non-Gaussian scattering processes by using nth-order intensity correlation functions,* Optical Society of America **16**, 1651 (1999).

[31] B. O'Neill, *How to estimate the autocorrelation function?* https://stats.stackexchange.com/q/343524 (2018).

[32] M. A. Choma, A. K. Ellerbee, C. Yang, T. L. Creazzo, and J. A. Izatt, *Spectral-domain phase microscopy,* Optics Letters **30**, 1162 (2005).

[33] M. A. Choma, A. K. Ellerbee, S. Yardanfar, and J. A. Izatt, *Doppler flow imaging of cytoplasmic streaming using spectral domain phase microscopy,* Journal of Biomedical Optics **11**, 024014 (2006).

[34] T. G. van Leeuwen, D. J. Faber, and M. C. Aalders, *Measurement of the axial point spread function in scattering media using single-mode fiber-based optical coherence tomography,* IEEE JOURNAL OF SELECTED TOPICS IN QUANTUM ELECTRONICS **9**, 227 (2003).

[35] R. R. Vardanyan, V. K. Dallakyan, U. Kerst, and C. Boit, *Laser beam transmission and focusing inside media,* Journal of Contemporary Physics **46**, 218 (2011).

[36] J. Kalkman, *Fourier-domain optical coherence tomography signal analysis and numerical modeling,* International Journal of Optics **2017**, 1 (2017).

[37] K. Cheishvili, *Precision and bias in DLS-OCT data and analysis routines,* https://doi.org/10.5281/zenodo.8124454 (2023).

7

Measuring particle diffusion in multiple scattering media using dynamic light scattering optical coherence tomography

In this study we conducted dynamic light scattering optical coherence tomography (DLS-OCT) simulations and measurements to investigate multiple scattering in Intralipid 20% and 10 wt.% polystyrene suspension. Our analysis of autocorrelation functions revealed significant deviations from single exponential decay at intermediate path lengths and scattering events. By employing a double exponential fit model, we enhanced the accuracy of diffusing wave spectroscopy (DWS) estimate and expanded the path-length range suitable for reliable determination of single scattering diffusion coefficient. Additionally, we utilized OCT intensity attenuation to derive concentration-dependent scattering coefficients. Intralipid exhibited behavior consistent with single scattering models up to a depth of 0.5 mm, yielding a well-matched attenuation coefficient. In contrast, the polystyrene suspension, characterized by stronger multiple-scattering effects, posed challenges in accurately determining its attenuation coefficient.

7.1. Introduction

Dynamic light scattering optical coherence tomography (DLS-OCT) relies on the autocorrelation of fluctuations in the scattered light signal and coherence gating to obtain depth-resolved information about the diffusive and directional motion of particles. Without particle flow and in the single scattering limit, the decay rate of the exponentially decaying autocorrelation function is proportional to the particle diffusion coefficient. Coherence gating suppresses multiple scattering and allows for the study of diffusive dynamics at large depths and in concentrated samples [1–3] within the single-scattering regime, where light is scattered once before detection.

Coherence gating in DLS-OCT does not fully suppress multiple scattering, but more importantly, its possibility for path-length-resolved diffusion estimation enables the determination of the single and multiple scattering regimes from the depth-resolved data. Bizheva et al. [2] showed that at small path lengths, single scattering dominates, resulting in a constant autocorrelation decay rate with depth, while at large path lengths, light is fully diffuse and scatters multiple times before detection. In this multiple-scattering regime, the autocorrelation decay rate is described by diffusive wave spectroscopy (DWS) theory [4, 5] and increases linearly with path length.

However, there is a transition region at intermediate path lengths, where light has scattered more than once but is not yet diffuse. In this region, neither single scattering nor multiple scattering DWS theory accurately describes the autocorrelation decay rate. In this work, we employ a combined single and multiple scattering model to improve diffusion estimation for an intermediate number of scattering events. We perform both simulations and measurements in dense particle suspensions to show that the autocorrelation function in this transitional regime is not purely single exponential. The use of a double exponential fit model improves the DWS estimate and extends the path-length range where the single-scattering approach can be used. We also performed OCT intensity attenuation measurements to determine scattering coefficient, which provides additional insight into the scattering anisotropy of the sample.

7.2. Theory

The geometry for OCT diffusion and attenuation coefficient measurements is described in [6, 7], see Figs. 3.1 and 4.1. The optical beam is described by a Gaussian beam along the z-direction. The path length travelled by light in the sample is given by s, where $s = 2z$ in the single scattering limit where z denotes the physical depth of the sample from the interface. We assume that the diffusion process is stationary.

7.2.1. DLS-OCT in the multiple scattering regime

For a particle suspension, the path-length dependent first-order temporal autocorrelation of the backscattered OCT complex-valued signal due to particle diffusion is

given by [8–12]

$$g_1(s,\tau) = \frac{\langle E(s,t)E^*(s,t+\tau)\rangle_t}{\langle I(s,t)\rangle_t} = A(s)e^{-\Omega(s)\tau}, \tag{7.1}$$

where $E(s,t)$ is the path-length and time-dependent complex-valued OCT signal, $I(s,t)$ is the OCT signal intensity, τ is the autocovariance time lag, $A(s)$ is the autocovariance amplitude containing the effect of depth-dependent signal-to-noise ratio [12] (see definition in Eq. 6.1), and $\Omega(s)$ is the autocorrelation decay rate. Within the single scattering approximation, the autocorrelation decay rate does not depend on the path length and is given by

$$\Omega(s) = Dq^2, \tag{7.2}$$

where D is the particle diffusion coefficient, and $q = 2nk_0$ represents the scattering wavenumber for the OCT backscattering probe configuration with the incident light wavenumber in vacuum k_0 and the medium refractive index n. The autocorrelation of a mean-subtracted OCT intensity within the Siegert approximation is then given by [13, 14]

$$g_2(s,\tau) = A(s)^2 e^{-2\Omega(s)\tau}. \tag{7.3}$$

In an optically dense medium where light undergoes multiple scattering events before detection, Eq. (7.2) is no longer valid. For fully diffuse incident light, the decay rate of the autocorrelation is given by [2, 4, 5]

$$\Omega(s) = 2n^2k_0^2D\frac{s}{l^*}, \tag{7.4}$$

where l^* denotes the photon transport mean free path. The photon transport mean free path l^* is related to the photon mean free path l through [5]

$$l^* = \frac{l}{\langle 1-\cos\theta\rangle} = \frac{l}{1-g}, \tag{7.5}$$

where θ represents the scattering angle, $g = \langle\cos\theta\rangle$ is the scattering anisotropy, and $\langle\ldots\rangle$ denotes an ensemble average over many scattering events. The inverse of the photon mean free path is called the scattering coefficient, denoted as $\mu_s = l^{-1}$. Similarly, the inverse of the photon transport mean free path is known as the reduced scattering coefficient, $\mu_s^* = {l^*}^{-1}$. In Eq. (7.4) and (7.5), all quantities pertain to single-particle properties (independent scattering) and do not include dependent scattering effects [4, 5, 15]. Standard DLS measurements are not path-length resolved and require integration of Eq. (7.4) over all path lengths to determine the scattering rate. However, in DLS-OCT, the signal is obtained as a function of path length, which enables the use of Eq. (7.4) to describe the path-length dependent decorrelation rate.

In DLS-OCT, both single-scattered and multiple-scattered contributions are detected where the relative contribution of each depends on various optical and sample parameters [16]. The autocorrelation decay rate of single-scattered light is

constant as a function of path length, whereas for multiple-scattered light, it increases with path length as described in Eq. (7.4). Carminati et al. [17] suggested splitting the temporal autocorrelation function $g_1(z,\tau)$ into single and multiple scattering terms,

$$g_1(s,\tau) = \underbrace{A_s(s)e^{-Dq^2\tau}}_{\text{single scattering}} + \underbrace{\sum_{m>1} A_m(s)e^{-2mn^2k_0^2D\frac{l}{l^*}\tau}}_{\text{multiple scattering}}, \tag{7.6}$$

where m is the number of scattering events. The average number of scattering events is related to the path length through $\langle m\rangle = \frac{s}{l}$. Even though for a given path length $\langle m\rangle$ takes on a single value, this restriction does not apply to the integer m, leading to an infinite number of exponentials in Eq. (7.6). Hence, using Eq. (7.6) with infinitely many exponentials as a fit model is problematic. From our experience, a double exponential model is sufficient to fit any DLS-OCT first-order autocorrelation function [18]. Adding a third or higher-order exponential cannot capture any further details of the autocorrelation function and merely increases the fit uncertainty. A more advanced method would be to use Laplace analysis, similar as has been used in determining particle size polydispersity [19]. Hence, we introduce a double exponential fit model

$$g_1(s,\tau) = \underbrace{A_1(s)e^{-\Omega_1(s)\tau}}_{\text{slower mode}} + \underbrace{A_2(s)e^{-\Omega_2(s)\tau}}_{\text{faster mode}}, \tag{7.7}$$

where Ω_1 and Ω_2 are the decay rates for single scattering and higher-order scattering processes, respectively, and A_1 and A_2 are the corresponding exponential amplitudes. We expect Eq. (7.7) to describe $g_1(s,\tau)$ from samples transitioning to multiple scattering better than Eq. (7.1). Similarly, the simplified second-order normalized autocovariance function, containing only two exponential decays, can be expressed as follows:

$$g_2(s,\tau) = \underbrace{B_1(s)e^{-2\Omega_1(s)\tau}}_{\text{slower mode}} + \underbrace{B_2(s)e^{-2\Omega_2(s)\tau}}_{\text{faster mode}}, \tag{7.8}$$

where B_1 and B_2 denote the exponential amplitudes.

7.2.2. Intensity attenuation

The decorrelation rate Ω in the multiple scattering limit depends on the photon mean free path l, which is the inverse of μ_s, the independent scattering coefficient that determines OCT signal attenuation in depth. However, μ_s can only be used to model signal attenuation in a concentration-independent scattering regime. To estimate OCT intensity attenuation in samples with high particle concentration, dependent-scattering effects due to interactions between scatterers must be considered. In concentrated particle suspensions, the attenuation can be very strong and is the most dominant factor in the intensity reduction of the single scattered light in the sample. For dependent scattering in concentrated suspensions, the OCT intensity

inside the sample is given by [20–26]

$$I(z) = I_0 \cdot \underbrace{e^{-2\mu_s^{\text{dep}} z}}_{\text{attenuation}} \times \underbrace{\left(\frac{\sin(\delta k \cdot z \cdot n) \cdot e^{-2z^2 n^2 \sigma_r^2}}{z \cdot n} \right)^2}_{\text{roll-off}} \times \underbrace{\left(1 + \left(\frac{z - z_0}{\alpha \cdot z_R} \right)^2 \right)^{-1}}_{\text{confocal}}, \quad (7.9)$$

where μ_s^{dep} is the concentration-dependent scattering coefficient, which accounts for wavefield interactions from light scattered from different particles in the medium, including interference effects and spatial correlations in particle positions that modify the scattering behavior compared to the independent scattering regime. The spectral width of the pixel is denoted by δk, while σ_r represents the spectral resolution in terms of the standard deviation of the Gaussian lineshape [24]. In addition, z_0 is the focus position, $z_R = nk_0 w_0^2/2$ is the Rayleigh length, and α is a scaling factor of the Rayleigh length [25, 27]. The intensity roll-off factor arises from k-domain integration and the finite spectral resolution [24], and the confocal factor describes the depth-dependent light collection efficiency of the focused Gaussian beam [25].

The exponent of the attenuation term in Eq. (7.9) should contain $\mu_s^{\text{dep}} + \mu_a$, where μ_a is the sample absorption coefficient. However, for samples used in this work $\mu_s^{\text{dep}} \gg \mu_a$, allowing us to neglect the effect of absorption. Therefore, for spherical scattering particles, the total attenuation coefficient equals the dependent scattering coefficient μ_s^{dep} and is given by

$$\mu_s^{\text{dep}} = \frac{3 f_v}{2a^3} \int_0^{\pi} \sigma_s(\theta) S(f_v, \theta) \sin\theta \, d\theta \,, \quad (7.10)$$

where f_v is the particle volume fraction, a is the particle radius, $\sigma_s(\theta)$ is the differential scattering cross-section, which can be determined using Mie theory, and $S(f_v, \theta)$ is the structure factor, which for hard spheres can be calculated using the Percus-Yevick approximation [28–30].

7.3. Simulations

To model the effect of multiple scattering we developed a basic 1D simulation model that generates a time-dependent complex OCT signal scattered from an ensemble of particles exhibiting random diffusive motion along the direction of light propagation. Subsequently, we calculate the OCT signal along with the first- and second-order normalized autocovariance functions. To reduce the autocorrelation variance, this process is repeated N_b times. The resulting autocorrelation functions are then averaged before being fitted with our models from Sec. 7.2.1 to obtain the autocorrelation decay rate. In our simulations, we used a time series length of 32768, a particle radius of 150 nm (corresponding to the average particle radius in Intralipid), an acquisition rate of 36 kHz, and $N_b = 300$.

In contrast to the dilute particle suspension simulation detailed in Chapter 6, a noiseless time-dependent complex field scattered from diffusing particles is simu-

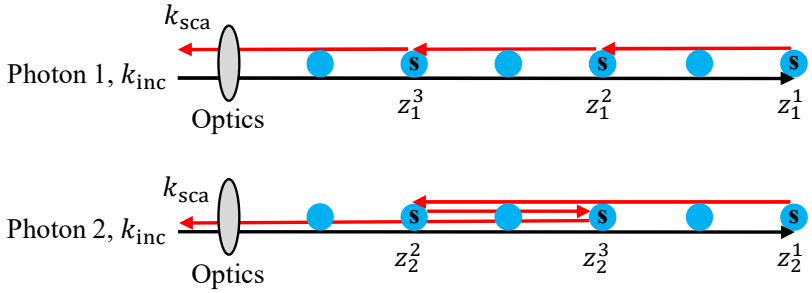

Figure 7.1: Schematics of multiple scattering DLS-OCT simulations with $N_p = 6$, $N_l = 2$, and $m = 3$.

lated by summing the complex field over all path lengths, instead of particle positions, using

$$E_0(t) = \sum_{j=1}^{N_l} e^{ik_0 n s_j(t)}, \tag{7.11}$$

where the summation is performed over N_l randomly generated photons. Figure 7.1 shows a schematic representation of our simulations. We simulate N_p Brownian particles that are randomly distributed in depth at locations $z_j^{1\ldots N_p}$.

The path of each photon from Eq. (7.11) is generated by scattering m times from m randomly selected particles. Here, we show this for 2 photons, 6 Brownian particles, denoted by blue circles, and 3 scattering events. Particles that scatter light are denoted by the symbol "**s**". The black arrow represents the illuminating light with wavenumber k_{inc}, and the red vector k_{sca} represents the detected light scattered from the last (third) particle. For photon 1, there is no back-and-forth scattering, which is quite unprobable in the case of a large number of scattering events. Photon 2, on the other hand, represents a more realistic scenario, where light scatters back and forth before being detected. As a result, the photon accumulates more phase that leads to an increase in the speed of the fluctuation, which is exactly what affects the decay rate in the multiple scattering regime.

For each photon, we generate the total traveled path length s_j. Subsequently, the particle positions are moved due to Brownian motion, which is generated using normally distributed discrete steps with $\sigma = \sqrt{2D\Delta t}$, where Δt is the inverse of the acquisition rate. By repeating this process for every time step and calculating the total path length, we obtain $s_j(t)$ that represents the time-dependent total path length traveled. While particles move due to diffusion, the scattering pattern, i.e. on which particle each photon is scattered, remains unchanged over time to reduce computational cost. In our simulations, we used $N_l = 100$ and $N_p = 100$. We assume isotropic and lossless particle scattering. For each photon, the total traveled path length is given by:

$$s_j(t) = z_j^1(t) + z_j^m(t) + \sum_{c=2}^{m-1} z_j^{c+1}(t) - z_j^c(t), \tag{7.12}$$

where $z_j^c(t)$ is the axial position of the c^{th} particle from a total of m random scattering particles for the j^{th} photon. All other assumptions and conditions remain identical to those laid out in Chapter 6.

Simulations using Eq. (7.11) can be performed for an arbitrary number of scattering events, m. By directly controlling m in these simulations, we can induce multiple scattering events, which leads to an increase in the mean photon path length. This influences the autocorrelation functions when there is back-and-forth scattering between the particles. Consequently, changes in the position of intermediate scatterers affect the total traveled path length. In 1D simulations, this effect occurs only when $m > 2$. In 2D or 3D simulations, this effect can occur starting from $m = 2$. Therefore, for 1D simulations, the cases $m = 2$ and $m = 1$ are identical, both corresponding to single scattering with a decay rate $\Omega = Dq^2$. For $m > 2$ scattering events, we expect the decay rate for multiple-scattered light in our simulations to be $\Omega = 2mn^2k_0^2D\langle 1 - \cos\theta\rangle$. In our 1D simulations, we found that $\langle\cos\theta\rangle = -0.33$. This result is due to the nature of 1D simulations, and we expect $\langle\cos\theta\rangle = 0$ for isotropic 2D and 3D simulations.

7.4. Materials and Methods

7.4.1. OCT system

The experiments were performed using a Thorlabs GANYMEDE II HR series spectral domain OCT system, which has been described in detail in our previous works [6, 7, 18, 31]. The acquisition rate was 5.5 kHz for calibration measurements (low-speed, higher sensitivity), and 36 kHz for diffusion measurements (high-speed, lower sensitivity). The acquired signal spectrum was measured with a spectrometer with 2048 pixels. The maximum imaging depth in air is 1.87 mm. After acquisition, the measured spectrum was first resampled to a linearly-sampled wavenumber domain and then apodized using a Gaussian filter. After the apodization, the measured coherence function waist in sample was $w_z = 2.11$ µm. The OCT system is operated with a scan lens (LSM04-BB, Thorlabs) in a confocal setup with a manufacturer-provided focal spot size of $w_0 = 6$ µm in air and NA $= 0.05$. Since for the given OCT setup the coherence length is small and the NA is very low, it can be assumed that the scattering angle is $180°$ and the scattering wavenumber q in the correlation analysis is constant at $q = 2nk_0$.

7.4.2. Particle suspensions

For our diffusion measurements, we used two samples: Intralipid 20% (Sigma-Aldrich, product number I141) and a relatively monodisperse 10 wt.% aqueous polystyrene particle suspension (Applied Microspheres, PIN number 60490-100). The polystyrene particles have a mean diameter of 488 nm, a size coefficient of variation of 5%, and a refractive index of 1.59 (at a wavelength of 589 nm). Both samples were used at their original concentration for the diffusion measurements. For beam shape calibration measurements, the samples were diluted with water until the number-fluctuation signal was sufficiently strong. In all measurements, similar to our previous works [6, 7, 31], particle suspensions were placed in a rectangular

quartz flow cell with internal dimensions of 1 mm depth and 10 mm width (type 45-F, Starna Scientific). The temperature was 25 degrees Celsius. For dilute calibration measurements, we used the refractive index of 1.33. For concentrated sample measurements, we used a refractive index of 1.36 for Intralipid [32] and 1.35 for the polystyrene suspension, estimated using the Lorentz-Lorenz formula [33, 34]. All concentration dependent scattering coefficients for Intralipid were calculated using phenomenological equations derived from measurements from Ref. [32]. For the polystyrene sample, the scattering properties were modelled based on Mie theory [35] and Eq. (7.10), incorporating the structure factor from Chapter 2.

7.4.3. Calibration measurements

DLS-OCT diffusion measurements require no calibration. However, to calculate the attenuation coefficients from the OCT intensity profile, the intensity profile must be corrected for the sensitivity roll-off and confocal response [21–23, 36]. Sensitivity roll-off, shown in Fig. 7.2(a), was calculated using the reflection from the flow cell edge and fitted with Eqs. 17 and 18 from [24]. This was done by changing the OCT reference path length, which resulted in different axial positions of the flow cell reflection with varying signal magnitude levels due to sensitivity roll-off. The measurements match very well with the fit model used. Numerical dispersion compensation was performed as described in [36–38] to compensate for the dispersion of the flow cell glass.

Even though we know the manufacturer-provided focal spot size w_0, the exact beam shape depends on the angle of incidence, refractive index contrast, and Gaussian beam parameters, w_0 and $w(z)$ vary somewhat due to the passage of the beam through various interfaces [39]. Additionally, there are conflicting results in

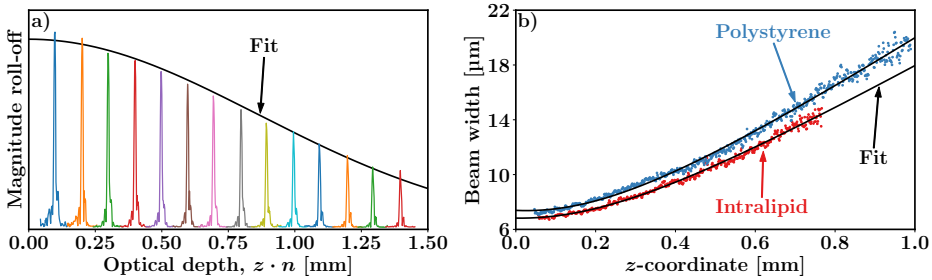

Figure 7.2: OCT calibration measurements. Measured and fitted (a) complex field magnitude roll-off and (b) OCT beam shape in diluted samples.

Sample	w_0 [µm]	z_0 [mm]	α
Polystyrene	7.37 ± 0.05	0.03 ± 0.01	1.52 ± 0.02
Intralipid	6.82 ± 0.04	0.01 ± 0.01	1.86 ± 0.03

Table 7.1: OCT beam shape parameters calibrated using number-fluctuation DLS-OCT.

the literature about the Rayleigh length pre-factor in the Gaussian beam coupling equation [22, 25, 27]. Therefore, $w(z)$ and w_0 were calibrated using the procedures described in [6, 7, 31] using the number fluctuation dependence on the local beam waist $w(z)$ in $g_2(z,\tau)$ measured for diluted particle suspensions. For beam shape calibration measurements, we acquired 300 time series, each with 8192 sampling points at a 5.5 kHz scan rate. The obtained beam shape $w(z)$ was fitted using $w(z) = w_0\sqrt{1+(z-z_0)^2/(\alpha z_R)^2}$, with $z_R = k_0 w_0^2 n/2$ with w_0, z_0, and α as fit parameters. The fitted $w(z)$ was subsequently used for OCT intensity normalization. The measured and fitted beam shapes are displayed in Fig. 7.2(b), and the obtained Gaussian beam parameters are given in Table 7.1. Note the significant difference in α between the two samples. Since the samples were measured on different days and have different refractive indices, variations in the flow cell alignment, angle, and focus position likely contributed to small differences in w_0, z_0 and subsequently α between the polystyrene and Intralipid samples. For both samples, focus positions were adjusted to be close to the interface. From our experience, that position increases the contribution of single-scattered light and most effectively suppresses multiple scattering.

7.4.4. Diffusion measurements

For the diffusion measurements, the acquisition rate was set to 36 kHz to resolve the faster-decaying autocorrelation functions due to multiple scattering. For both samples, 300 time series were acquired. For Intralipid, the time series was 32768 data points long, while for the polystyrene suspension, it was 65536 data points long. From this data, the average autocorrelation function $g_1(s,\tau)$ was calculated at every depth. In the diffusion analysis, we used only the real part of $g_1(s,\tau)$, as the imaginary part of $g_1(s,\tau)$ contains no information about particle diffusion, as described in Sec. 7. We utilized Eq. (7.1) for the single exponential fit with $A(s)$ and $\Omega(s)$ as free parameters, and Eq. (7.7) for double exponential fit with $A_1(s)$, $A_1(s)$, $\Omega_1(s)$, and $\Omega_2(s)$ as fit parameters. Fits were performed for the range of τ for which $g_1(s,\tau) > 0.01$.

For both samples, the single scattering diffusion coefficient, D, was calculated over the path-length (s) range where the decay rate was constant—beyond the path length for which the wall-drag effect occurs and up to the path length where the onset of multiple scattering occurs. The chosen path-length ranges for Intralipid and polystyrene samples were $38-159$ µm and $30-41$ µm, respectively. For the polystyrene particle suspension, the obtained $D = 0.99 \pm 0.02$ µm^2/s corresponded to a particle size of 493 ± 6 nm, which agrees well with the manufacturer-provided particle size of 488 nm. This agreement suggests that the effects of particle interactions on D are negligible, likely because the particle volume concentration is not too high. In contrast, the Intralipid diffusion coefficient was $D = 0.76 \pm 0.01$ µm^2/s, which is roughly half of that of dilute Intralipid. This discrepancy is attributed to the higher particle volume concentration in Intralipid, which affects D differently in monodisperse and polydisperse particle suspensions [18].

7.4.5. Attenuation measurements

For attenuation measurements, we calculated the average OCT intensity profile as a function of z-coordinate for both samples at their original concentration. After normalizing the intensities for roll-off and confocal sensitivity, we fitted Eq. (7.9), with I_0 and μ_s^{dep} as free parameters. Since Eq. (7.9) is valid only in the single scattering regime, we truncated the intensity profiles to the same z-ranges as in Sec. 7.4.4 (with $z = s/2$) to ensure we were in the exponentially decaying range.

7.5. Results

Figures 7.3(a-d) summarize the results obtained from simulations. Figs. 7.3(a,b) show the simulated $g_1(\tau)$ and $g_2(\tau)$ for different numbers of scattering events, along with double exponential fits using Eqs. (7.7) and (7.8), respectively. The obtained autocorrelation functions exhibit single exponential behavior for very low and very large numbers of scattering events. However, for an intermediate number of scattering events, $g_1(\tau)$ and $g_2(\tau)$ are no longer purely exponential. Multi-exponential behavior is more pronounced in $g_1(\tau)$.

Figures 7.3(c,d) display the fitted decay rates for $g_1(\tau)$ and $g_2(\tau)$ as a function of the number of scattering events. As mentioned in Sec. 7.3, we can only use double exponential fit models for $m > 2$. It can be observed that for $3 \leq m \leq 10$, Ω_2 (the faster mode) from the double exponential model matches better with

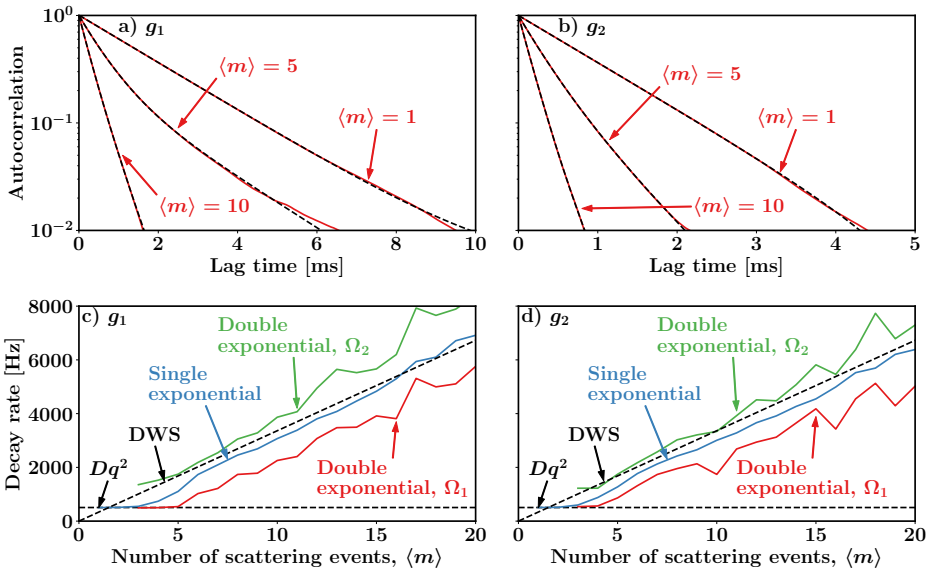

Figure 7.3: Multiple scattering OCT decorrelation simulations. Simulated and fitted (a) $g_1(\tau)$ and (b) $g_2(\tau)$ for different numbers of scattering events. Fitted decay rate for (c) $g_1(\tau)$ and (d) $g_2(\tau)$ using single and double exponential fit models.

the DWS theory [2] compared to using a single exponential fit. Furthermore, for $3 \leq m \leq 5$, Ω_1 (the slower mode) from the double exponential fit matches with the single scattering Dq^2, whereas the single-exponential decay rate already deviates from it when $m \geq 4$. For a large number of scattering events, such as $m > 10$, the decay becomes purely single exponential, and using a double exponential fit model is less effective than using a single exponential fit.

Figures 7.4(a-d) display the results obtained from DLS-OCT measurements. We employed Eqs. (7.1) and (7.7) for single and double exponential fits, respectively. Figures 7.4(a,b) show the measured and fitted autocorrelation functions at different path lengths for Intralipid and polystyrene suspensions, respectively. While both samples exhibit double exponential behavior, it is more pronounced for Intralipid. This double exponential behavior is not due to size polydispersity, as it is not observable in dilute samples. At very low path lengths, similar to simulations with a low number of scattering events, the autocorrelation is linear on a logarithmic scale, which indicates a single exponential decay rate as is the case for the single-scattering regime. However, as the path-length increases, the double exponential nature becomes more evident. At large path lengths, the autocorrelation approaches a pure single exponential, akin to a large number of scattering events in our simulations.

Figures 7.4(c,d) show as solid and dashed lines the estimated single and multiple scattering diffusive decay rates, respectively. The single scattering rate Dq^2

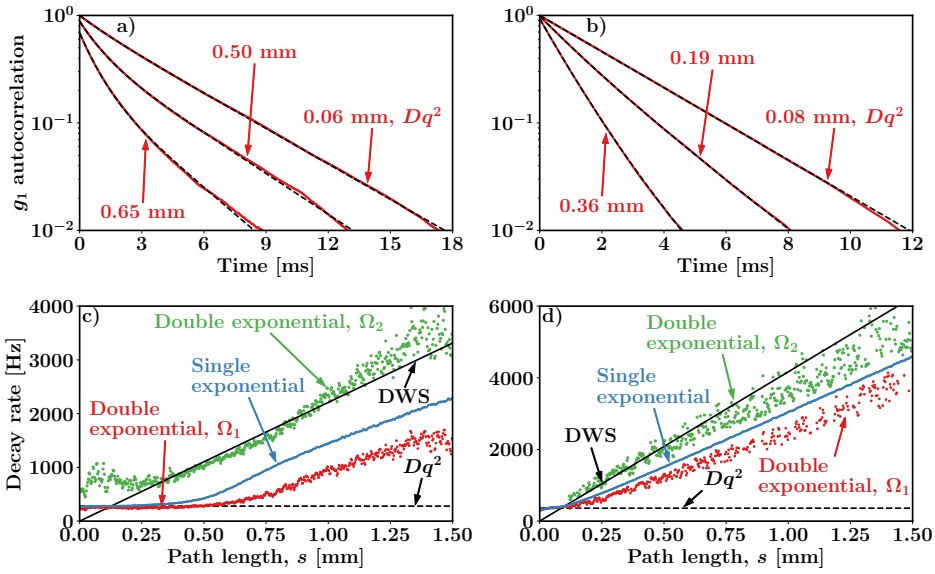

Figure 7.4: Multiple scattering DLS-OCT decorrelation measurements. Measured and fitted $g_1(s,\tau)$ at different path lengths for (a) Intralipid and (b) polystyrene particle suspension. Fitted decay rate for (c) Intralipid and (d) polystyrene particle suspension using single and double exponential fit models.

was determined using the measured single scattering diffusion coefficients from Sec. 7.4.4. The DWS estimate was calculated using Eq. (7.4), where the independent reduced scattering coefficient μ_s^* was forward-modelled as described in Sec. 7.4.2. Utilizing the double exponential fit model from Eq. (7.7) provides two advantages. First, the decay rate of the faster decaying exponential aligns better with the DWS theory compared to the single exponential fit. Second, the s-range over which the decay rate of the slower decaying exponential matches the single scattering estimate is larger. For Intralipid, there is a good agreement of Ω_2 with the DWS theory, and the single scattering s-range is approximately 3.5 times larger compared to using a single exponential model. In the case of the polystyrene suspension, higher fit noise is evident for the double exponential model. However, there is a clear improvement towards the DWS theory, although a small mismatch between the estimated and measured decay rates remains. For polystyrene an extension of the single scattering path-length range was not observed.

Figures 7.5(a,b) show the fitted autocorrelation mode amplitudes from Eq. (7.7) for Intralipid and polystyrene samples, respectively. In this case, A_1 corresponds to the mode amplitude of the slow decaying single scattering exponential, and A_2 is the amplitude of the faster decaying multiple scattering exponential. For Intralipid, the modes are well separated, with $A_1 > A_2$ for path length values below 0.5 mm. Up to this path length, the decay rate Ω_1 from Fig. 7.4(c) matches the single scattering Dq^2. Beyond a path length of 0.5 mm, A_1 becomes smaller than A_2, coinciding with the deviation of Ω_1 from the single scattering theory shown in Fig. 7.4(c). In the case of the polystyrene suspension, the mode amplitudes are not as well separated. At very low path length, $A_1 > A_2$, which also corresponds to a very limited single scattering path-length range in Fig. 7.4(d). However, above a path length of 0.25 mm, the mode amplitudes are similar and evidently more noisy compared to those of Intralipid.

Figure 7.5(c) shows the OCT intensity attenuation in depth for both samples

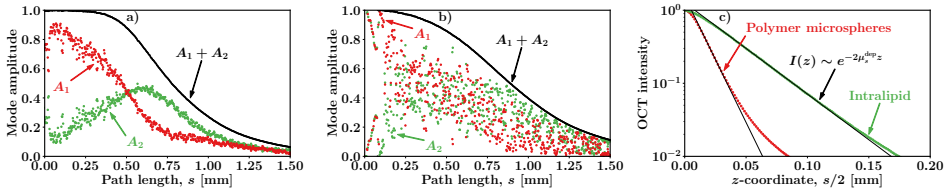

Figure 7.5: Measurements in the multiple scattering regime. Fitted DLS-OCT autocorrelation mode amplitudes for (a) Intralipid and (b) polystyrene suspension. (c) Roll-off and confocal-corrected OCT intensity attenuation in both samples.

Sample	OCT fitted μ_s^{dep} [mm^{-1}]	Theoretical μ_s^{dep} [mm^{-1}]
Polystyrene	39.7 ± 0.2	61.1
Intralipid	14.4 ± 0.1	15.9

Table 7.2: Fitted and estimated (theoretical) OCT attenuation (scattering) coefficients.

after corrections for roll-off and confocal sensitivity factors. Fits using single scattering exponential models are also shown. For the Intralipid sample, the intensity profile remains linear up to a depth range of 0.15 mm, with slight deviations from this model near the end of this range. In contrast, the polystyrene suspension exhibits much stronger and increasingly nonlinear intensity attenuation, indicating a greater contribution from multiple scattering. The linear range of the OCT signal for the polystyrene suspension is significantly shorter. The fitted OCT attenuation coefficients and corresponding theoretical estimates are given in Table 7.2. For Intralipid, the fitted μ_s^{dep} is very close to the estimated value. However, for polystyrene sample, the deviation between the theoretical and measured μ_s^{dep} is much larger.

7.6. Discussion

In this work, we presented DLS-OCT simulations and measurements in the multiple scattering regime using Intralipid 20% and concentrated polystyrene suspension. At specific path lengths, we found that the measured first-order autocorrelation functions deviate significantly from a single exponential decay, and a double exponential fit model is more appropriate and provides better estimates for both DWS and single scattering decay rates for Intralipid. However, for the polystyrene sample, the DWS measurement did not fully match the theoretical model. Additionally, we obtained dependent scattering coefficients from the intensity attenuation. The results were consistent with the theoretical estimates for Intralipid but less so for the polystyrene sample.

As our simulations and measurements showed, single exponential fit models are applicable to multiple scattering samples primarily at very small and large path lengths, corresponding to low and high numbers of scattering events. At intermediate numbers of scattering events, occurring at moderate path lengths, the autocorrelation functions clearly exhibit multi-exponential behavior, with $g_1(\tau)$ showing a stronger deviation from a pure single exponential compared to $g_2(\tau)$. In such cases, using a double exponential fit model is preferable. This approach offers two main advantages: firstly, the decay rate of the slower exponential better matches with the single scattering Dq^2 and is a valid description over a broader depth range. Secondly, the decay rate of the faster exponential aligns more closely with diffusing wave spectroscopy (DWS) theory at any path length, including the transition region. Thus, employing a double exponential model reduces bias and enables simultaneous determination of the particle diffusion coefficient D in the single scattering regime and the reduced independent scattering coefficient μ_s^* through DWS. Generally, fitting a double exponential model requires more averaging (higher N_b) to reduce noise in the autocorrelation function and disentangle the different decay rates. In the multiple scattering regime, the results for both decay rates should not always be taken at face value, and their accuracy must always be verified by assessing the fit quality. If the single exponential fit proves inadequate and $g_1(\tau)$ or $g_2(\tau)$ display multi-exponential behavior, using a double exponential model is always preferred. This approach can significantly reduce premature deviations of the fitted decay rate from the single scattering theory.

We conducted multiple scattering measurements on Intralipid 20% and a 10 wt.%, 9.5% volume fraction polystyrene suspension. Despite the lower volume fraction of the polystyrene suspension, compared to Intralipid, both diffusion and attenuation measurements indicated that the polystyrene sample exhibited significantly higher multiple scattering contributions that are present even at lower path lengths. However, the polystyrene particles are approximately twice as large and the refractive index of the polystyrene particles, $n = 1.59$, is also higher than that of soybean oil, which predominates in Intralipid particles. Therefore, particle size and refractive index contrast are likely the primary factors contributing to the polystyrene sample being more in the multiple scattering regime. In addition, the relatively higher monodispersity of the polystyrene particles compared to the more polydisperse Intralipid suspension should not be underestimated. It would also be interesting to investigate whether size polydispersity affects the relation between single and multiple scattering.

The OCT attenuation coefficient and results from DWS measurements agreed well with estimates for Intralipid 20% from literature [32]. For the polystyrene particle suspension, the DWS measurement gave a μ_s^* that is slightly lower than expected, and the OCT attenuation coefficient μ_s^{dep} was approximately 1.5 times lower than the modeled value. One of the primary reasons behind this discrepancy we attribute to the presence of multiple scattering effects in the OCT measurement. Since, the theoretical estimates are primarily based on the single scattering assumption and do not fully account for multiple scattering contributions. In the case of Intralipid, the sample remains within the single scattering regime until the OCT intensity is largely attenuated, thus aligning well with single scattering theoretical predictions. However, for the polystyrene suspension, the OCT intensity decay with depth is significantly non-exponential, limiting the range over which μ_s^{dep} can be accurately determined and increasing uncertainty in the fit parameter. This challenge can be partially addressed by incorporating multiple scattering attenuation models [40]. However, these models introduce additional fit parameters and complexity, which can pose challenges during the fitting process. Another contributing factor is the method of estimating μ_s^{dep}: while the Intralipid attenuation coefficient estimate was derived from an empirical model based on measurements, for the polystyrene suspension we utilized Mie theory and Eq. (7.9). The estimated dependent μ_s^{dep} for Intralipid is approximately 2.4 times lower than the independent μ_s. However, for the polystyrene suspension, the difference is only a factor of 1.4, which warrants further investigation. Therefore, refining the estimation method of μ_s^{dep} for the polystyrene particle suspension could help narrow the gap between measurement and theory. Additionally, when calculating the volume fraction of polystyrene particles from their weight content, we neglected the thickness of the electrical double layer and treated the particles as hard spheres. However, we have not verified this assumption using reference measurements similar to our previous work [18]. Therefore, an incorrect volume fraction value can also be an important factor contributing to the mismatch with the theoretical estimates.

One of the advantages of using simultaneous OCT autocorrelation and attenu-

ation measurements is the ability to obtain the anisotropy factor g. In DLS-OCT, employing a double-exponential fit allows us to determine the particle diffusion coefficient D and the independent reduced scattering coefficient μ_s^*. From attenuation measurements, we can derive μ_s^{dep}. Therefore, if we can relate these two quantities through g, similar to how μ_s and μ_s^* are related, we can subsequently calculate g.

7.7. Conclusion

In this study, we conducted DLS-OCT simulations and measurements to investigate multiple scattering in Intralipid 20% and polystyrene suspensions. Our analysis of autocorrelation functions revealed pronounced deviations from single exponential decay at intermediate path lengths and scattering events. By employing a double exponential fit model, we enhanced the accuracy of diffusing wave spectroscopy (DWS) estimates and expanded the path-length range suitable for reliable determination of single scattering diffusion coefficients. Additionally, we utilized OCT intensity attenuation to derive scattering coefficients. Intralipid exhibited behavior consistent with single scattering models until significant attenuation, yielding a well-matched attenuation coefficient. In contrast, the polystyrene suspension, characterized by stronger multiple scattering effects, posed challenges in accurately determining its attenuation coefficient. This underlines the importance of refining methods to account for multiple and dependent scattering contributions in dense particle suspensions.

References

[1] J. Kalkman, R. Sprik, and T. G. van Leeuwen, *Path-length-resolved diffusive particle dynamics in spectral-domain optical coherence tomography,* Physical Review Letters **105**, 198302 (2010).

[2] K. K. Bizheva, A. M. Siegel, and D. A. Boas, *Path-length-resolved dynamic light scattering in highly scattering random media: The transition to diffusing wave spectroscopy,* Physical Review E **58**, 7664 (1998).

[3] D. A. Boas, K. K. Bizheva, and A. M. Siegel, *Using dynamic low-coherence interferometry to image Brownian motion within highly scattering media,* Optics Epxress **23**, 319 (1997).

[4] D. J. Pine, D. A. Weitz, J. X. Zhu, and E. Herbolzheimer, *Diffusing-wave spectroscopy: dynamic light scattering in the multiple scattering limit,* Journal De Physique **51**, 2101 (1990).

[5] D. A. Weitz and D. J. Pine, *Diffusing-wave spectroscopy,* in *Dynamic Light Scattering: The Method and Some Applications*, edited by W. Brown (Clarendon Press, 1993) p. 652–782.

[6] K. Cheishvili and J. Kalkman, *Scanning dynamic light scattering optical coherence tomography for measurement of high omnidirectional flow velocities,* Optics Express **30**, 23382 (2022).

[7] K. Cheishvili and J. Kalkman, *Sub-diffusion flow velocimetry with number fluctuation optical coherence tomography,* Optics Express **31**, 3755 (2023).

[8] J. Lee, W. Wu, J. Y. Jiang, B. Zhu, and D. A. Boas, *Dynamic light scattering optical coherence tomography,* Optics Express **20**, 22262 (2012).

[9] N. Uribe-Patarroyo, M. Villiger, and B. E. Bouma, *Quantitative technique for robust and noise-tolerant speed measurements based on speckle decorrelation in optical coherence tomography,* Optics Express **22**, 24411 (2014).

[10] N. Weiss, T. G. van Leeuwen, and J. Kalkman, *Localized measurement of longitudinal and transverse flow velocities in colloidal suspensions using optical coherence tomography,* Physical Review E **88**, 042312 (2013).

[11] N. Weiss, T. G. van Leeuwen, and J. Kalkman, *Simultaneous and localized measurement of diffusion and flow using optical coherence tomography,* Optics Express **23**, 3448 (2015).

[12] N. Uribe-Patarroyo, A. L. Post, S. Ruiz-Lopera, D. J. Faber, and B. E. Bouma, *Noise and bias in optical coherence tomography intensity signal decorrelation,* OSA Continuum **3**, 709 (2020).

[13] B. J. Berne and R. Pecora, *Dynamic Light Scattering* (Dover Publications, 2000).

[14] C. S. Johnson and D. A. Gabriel, *Laser Light Scattering* (Dover Publications, 1994).

[15] Z. Fahimi, F. J. Aangenendt, P. Voudouris, J. Mattsson, and H. M. Wyss, *Diffusing-wave spectroscopy in a standard dynamic light scattering setup,* Physical Review E **96**, 062611 (2017).

[16] G. R. Untracht, M. Chen, P. Wijesinghe, J. Mas, H. T. Yura, D. Marti, P. E. Andersen, and K. Dholakia, *Spatially offset optical coherence tomography: Leveraging multiple scattering for high-contrast imaging at depth in turbid media,* Science Advances **9**, 1 (2023).

[17] R. Carminati, R. Elaloufi, and J.-J. Greffet, *Beyond the diffusing-wave spectroscopy model for the temporal fluctuations of scattered light,* Physical Review Letters **92**, 213903 (2004).

[18] K. Cheishvili, R. Besseling, M. Hermes, and J. Kalkman, *Wavenumber-dependent dynamic light scattering optical coherence tomography measurements of collective and self-diffusion,* Optics Express **32**, 19963 (2024).

[19] A. G. Mailer, P. S. Clegg, and P. N. Pusey, *Particle sizing by dynamic light scattering: Non-linear cumulant analysis,* Journal of Physics Condensed Matter **27** (2015).

[20] B. Ghafaryasl, K. A. Vermeer, J. Kalkman, T. Callewaert, J. F. de Boer, and L. J. van Vliet, *Analysis of attenuation coefficient estimation in Fourier-domain OCT of semi-infinite media,* Biomedical Optics Express **11**, 6093 (2020).

[21] B. Ghafaryasl, K. A. Vermeer, J. Kalkman, T. Callewaert, J. F. de Boer, and L. J. van Vliiet, *Attenuation coefficient estimation in Fourier-domain OCT of multi-layered phantoms,* Biomedical Optics Express **12**, 2744 (2021).

[22] P. Gong, M. Almasian, G. van Soest, D. M. de Bruin, T. G. van Leeuwen, D. D. Sampson, and D. J. Faber, *Parametric imaging of attenuation by optical coherence tomography: review of models, methods, and clinical translation,* Journal of Biomedical Optics **25**, 040901 (2020).

[23] J. Kübler, V. S. Zoutenbier, G. Buist, J. Fischer, , A. Amelink, and J. F. de Boer, *Confocal corrected attenuation coefficient imaging in phantoms and in vivo using chromatic focal shift calibration,* Biomedical Optics Express **14**, 5282 (2023).

[24] J. Kalkman, *Fourier-domain optical coherence tomography signal analysis and numerical modeling,* International Journal of Optics **2017**, 1 (2017).

[25] T. G. van Leeuwen, D. J. Faber, and M. C. Aalders, *Measurement of the axial point spread function in scattering media using single-mode fiber-based optical coherence tomography,* IEEE JOURNAL OF SELECTED TOPICS IN QUANTUM ELECTRONICS **9**, 227 (2003).

[26] M. Almasian, N. Bosschaart, T. G. van Leeuwen, and D. J. Faber, *Validation of quantitative attenuation and backscattering coefficient measurements by optical coherence tomography in the concentration-dependent and multiple scattering regime,* Journal of Biomedical Optics **20**, 121314 (2015).

[27] G. Buist, M. Debiasi, A. Amelink, and J. F. de Boer, *Theoretical and experimental determination of the confocal function of OCT systems for accurate calculation of sample optical properties,* Biomedical Optics Express **15**, 2937 (2024).

[28] M. S. Wertheim, *Exact solution of the Percus-Yevick integral equation for hard spheres,* Physical Review Letters **10**, 321 (1963).

[29] E. Leutheusser, *Exact solution of the Percus-Yevick equation for a hard-core fluid in odd dimensions,* Physica A **127**, 667 (1984).

[30] D. J. Kinning and E. L. Thomas, *Hard-sphere interactions between spherical domains in diblock copolymers,* Macromolecules **17**, 1712–1718 (1984).

[31] K. Cheishvili, B. Rieger, and J. Kalkman, *Precision and bias in dynamic light scattering optical coherence tomography measurements of diffusion and flow,* Biomedical Optics Express **15**, 1288 (2024).

[32] B. Aernouts, R. V. Beers, R. Watté, J. Lammertyn, and W. Saeys, *Dependent scattering in Intralipid® phantoms in the 600-1850 nm range,* Optics Express **22**, 6086 (2014).

[33] W. Heller, *Remarks on refractive index of mixture rules,* The Journal of Physical Chemistry **69**, 1123–1129 (1965).

[34] P. N. A. Speets and J. Kalkman, *Measuring optical properties of clear and turbid media with broadband spectral interferometry,* Applied Optics **62**, 4349 (2023).

[35] S. Jacques and S. Prahl, *Mie scattering calculator,* https://omlc.org/calc/mie_calc.html (2018).

[36] W. Drexler and J. G. Fujimoto, *Dynamic Light Scattering* (Springer, 2008).

[37] X. Attendu, R. M. Ruis, C. Boudoux, T. G. van Leeuwen, and D. J. Faber, *Simple and robust calibration procedure for k-linearization and dispersion compensation in optical coherence tomography,* Journal of Biomedical Optics **24**, 056001 (2019).

[38] M. Wojtkowski, V. J. Srinivasan, T. H. Ko, J. G. Fujimoto, A. Kowalczyk, and J. S. Duker, *Ultrahigh-resolution, high-speed, Fourier domain optical coherence tomography and methods for dispersion compensation,* Optics Express **12**, 2404 (2004).

[39] R. R. Vardanyan, V. K. Dallakyan, U. Kerst, and C. Boit, *Laser beam transmission and focusing inside media,* Journal of Contemporary Physics **46**, 218 (2011).

[40] L. Thrane, H. T. Yura, and P. E. Andersen, *Analysis of optical coherence tomography systems based on the extended Huygens–Fresnel principle,* Journal of the Optical Society of America A **17**, 484 (2000).

8

Summary and outlook

8.1. Summary

Particle sizing and flow measurement using dynamic light scattering optical coherence tomography (DLS-OCT) present numerous challenges, particularly in concentrated and/or flowing suspensions. In this work, we address several important challenges encountered in DLS-OCT:

- Particle interactions in concentrated suspensions introduce dependencies of the diffusion coefficient on factors such as the duration of the motion being analyzed, the wavenumber, and the concentration, thereby complicating the extraction of particle size.
- Multiple scattering in concentrated suspensions imposes limitations on the accurate estimation of the diffusion coefficient.
- High flow speeds increase uncertainty in particle sizing and limit the depth at which the diffusion coefficient can be reliably determined.
- Low flow speeds cannot be determined due to particle diffusion limitations.
- Acquisition time limitations impose restrictions on the maximum flow speed and minimum particle size that can be measured.
- Unavailability of models to estimate precision and bias in diffusion and flow measurements complicates the quantification of uncertainty in DLS-OCT.

In concentrated suspensions the relationship between particle size and the diffusion coefficient is not adequately described by the simple Stokes-Einstein equation and becomes dependent on multiple factors. Accurate determination of particle size thus necessitates diffusion coefficient measurements across a wide range of wavenumbers and the application of sophisticated rheological models to describe the complex interactions within the suspension that affect particle transport dynamics. To address this challenge, we developed a broadband DLS-OCT system encompassing wavelengths from 350 to 1000 nm, as described in Chapter 2. By inverting hard-sphere rheological models, we were able to derive the particle size from the collective diffusion coefficient measured over an extensive wavenumber range. Furthermore, we demonstrate how the measurements of different diffusion modes can be used to assess the number-based particle size polydispersity in concentrated suspensions.

Measurement of higher flow speeds and particle sizing in fast-flowing suspensions using DLS-OCT become problematic due to detector sampling limitations. When the decay of the autocorrelation function is too rapid, it prevents the extraction of flow speed and particle size information. In Chapter 3 of this work, we incorporated beam scanning—a standard feature in many OCT systems—to extend the capabilities of DLS-OCT flow imaging beyond its current limitations. This approach allowed us to increase the flow dynamic range by a factor of two, significantly surpassing the limits of Doppler OCT. In addition, beam scanning enabled more accurate measurement of particle sizes in flowing suspensions, even further

from the flow cell edge, which is advantageous for applications in the process industry.

Particle diffusion limitations in DLS-OCT and Doppler OCT make it impossible to measure low flow speeds in particle suspensions. At these flow velocities, the autocorrelation function is dominated by diffusive decay. In Chapter 4, we introduced the concept of number fluctuations in the DLS-OCT intensity autocorrelation function to address this challenge. This development enabled us to measure extremely low, particle diffusion-limited flow speeds and concentrations in dilute suspensions, both in 1D and 2D. In addition, number-fluctuation DLS-OCT allows for the measurement of beam shape within the particle suspension, something that requires an elaborate calibration in conventional OCT.

Chapter 5 demonstrates the implementation of number-fluctuation DLS-OCT, as discussed in Chapter 4, for measuring 2D flow profiles in organ-on-chip (OoC) devices. Conventional Doppler OCT and DLS-OCT could not be used for flowmetry due to the lower flow speeds encountered in these chips. Additionally, the flow direction is unknown and varies within the chip, posing challenges for velocity measurements. To address these issues, we developed a numerical method to equalize the axial and transverse OCT resolutions at every position and eliminate the dependence on the Doppler angle in the autocorrelation function. This innovation enabled us to measure absolute velocities in 2D using number fluctuations. Furthermore, we implemented particle image velocimetry (PIV) on the OCT data and superimposed our number-fluctuation measurements with in-plane velocity vectors.

Quantification of precision and bias in DLS-OCT is crucial for reliable particle sizing and flow characterization. Despite the known influence of signal-to-noise ratio (SNR) on autocorrelation functions, their impact on the quantification of flow speed, particle size, and diffusion coefficient has not been thoroughly studied. In Chapter 6 of this work, we conducted a comprehensive investigation of precision and bias in DLS-OCT measurements of diffusion and flow. We discovered that errors in autocorrelation functions are strongly temporally correlated, posing challenges for uncertainty quantification and reaching the fundamental precision limit imposed by the Cramer-Rao lower bound. To address this issue, we developed an innovative signal mixing method to eliminate these correlations. Once the error correlations were removed, the standard deviation in the obtained diffusion coefficient or flow speed matched the Cramer-Rao lower bound. This achievement enables verification of whether optimal precision in these parameters has been reached, which is vital in the process industry.

Multiple scattering in DLS-OCT complicates the particle sizing process, particularly in dense media where the range of single scattering optical path length (OPL) is severely limited. Conversely, diffusing-wave spectroscopy (DWS) models encounter challenges at intermediate optical path lengths and numbers of scattering events. In Chapter 7 of this work, we conducted an extensive study focusing on diffusion measurements and simulations in samples exhibiting multiple scattering effects. Our investigation revealed that autocorrelation functions at intermediate numbers of scattering events are not purely exponential but are better described by a double exponential model. The use of a double exponential model improves the

accuracy of DWS estimates and extends the range of single scattering OPL suitable for estimating the diffusion coefficient.

8.2. Outlook on particle sizing

Accurate particle sizing in (flowing) suspensions using DLS-OCT is limited by various factors, as outlined earlier in this chapter. While this work improved in many of these areas, several possible further advancements remain unexplored, which we discuss in this section.

8.2.1. Particle sizing in flowing suspensions

Chapter 3 presented scanning DLS-OCT to improve particle sizing and velocity dynamic range in flowing suspensions. This technique can be implemented for in-line particle sizing by optimizing the scan speed during the measurement process. In addition, some flowing suspensions in the process industry tend to agglomerate near the flow cell edges, necessitating measurements farther from the edge for accurate particle sizing. Scanning DLS-OCT can be very useful in such scenarios by moving the location of least flow decorrelation a distance away from the wall.

Dynamic scan speed optimization

As discussed in Chapter 3, the effect of beam scanning in reducing flow decorrelation depends on the scan speed and direction. For laminar flow and alignment of equal magnitude scan and flow vectors, flow decorrelation is essentially zero. However, this requires some knowledge of the flow geometry and expected velocities. For automatic particle sizing using scanning DLS-OCT, it is essential that beam scan speed optimization happens during the measurement process. The goal is to equalize flow and scan speeds at a specific depth position to eliminate flow decay and maximize the accuracy of the obtained diffusion coefficient. The axial position can be chosen based on the distance from the edge of the flow cell or cuvette. We implemented an automatic scan speed optimization routine in the NanoFlowSizer, a DLS-OCT particle sizing device manufactured by InProcess-LSP. The flow geometry was identical to the one described in Chapter 3. The approach is as follows: First, we choose the distance from the flow cell edge where we want to improve the particle sizing estimate by specifying the range of axial voxels for which the optimization must be performed. Second, we choose a beam scan speed and direction (angle). Third, we perform N_b different DLS-OCT measurements, each with an acquisition time of $N_a \Delta t$, where N_a is the number of A-lines and Δt is the sampling time. In the fourth step, we calculate the average second-order normalized autocovariance function over the chosen voxel range and obtain the decay time τ_{decay} at which the autocorrelation magnitude reaches a lower limit set by us (e.g. 0.1 or 0.01). We repeat steps 2-4 within the optimization loop until the minimum of τ_{decay}^{-1} is found. This corresponds to the lowest decay rate at the chosen axial position, where, in principle, the flow decorrelation is absent and only diffusive decay remains. Therefore, automatic scan speed optimization in DLS-OCT suppresses flow decay at a specific axial position and makes particle sizing more reliable.

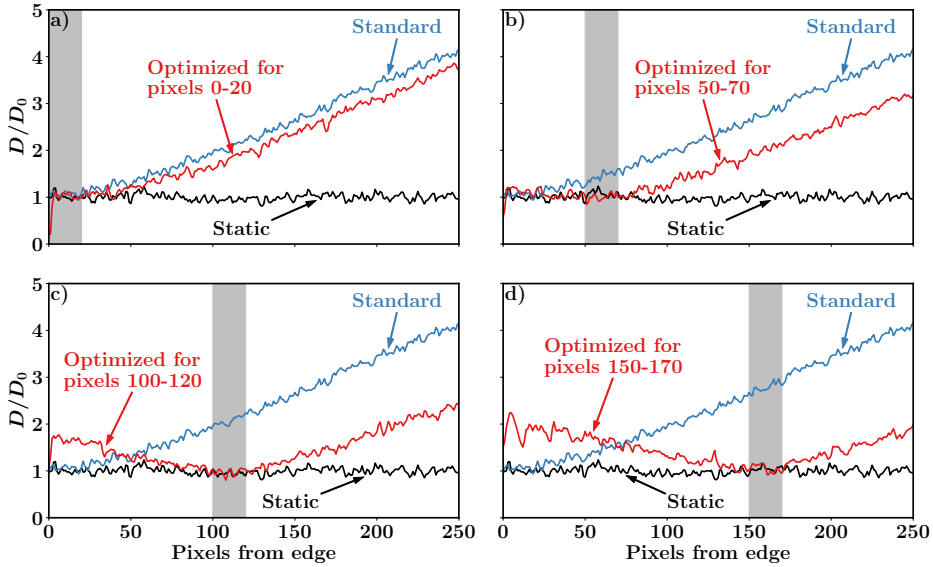

Figure 8.1: Comparison of in-line DLS-OCT diffusion measurements with and without beam scan speed optimization, alongside static measurements. The shaded area corresponds to the position where the optimization was performed.

We performed our optimization measurements using the integrated cylindrical flow cell of the NanoFlowSizer, which has a diameter of nearly 2 mm. Therefore, we expect a typical parabolic Poiseuille velocity profile. Figure 8.1(a-d) shows DLS-OCT diffusion measurements with and without optimization. The black curve corresponds to static diffusion measurements under no-flow conditions, the blue curves correspond to standard measurements under flow without beam scanning, and the red curves correspond to inflow measurements with the optimized scan speed. Shaded regions denote the pixel range for which the scan speed optimization was performed, and D_0 denotes the average diffusion coefficient from static measurements. For better comparison, we only fit the exponential of the diffusion decorrelation to the obtained autocorrelation functions, without any flow correction. We have not quantified the flow profile, but the suspension velocity farther from the edge is sufficiently high to affect the fitted diffusion coefficient. As expected, static diffusion measurements are constant in depth. For standard in flow measurements, the obtained diffusion coefficient is accurate only close to the edge, which is where the flow speeds are zero due to the no-slip condition. However, as we move farther from the edge, the bias in the diffusion coefficient dramatically increases with increasing flow speed. In the case of scanning DLS-OCT, the obtained diffusion coefficient matches with D_0 at the locations where the optimization was performed, irrespective of the flow speed. This is clearly visible at larger depths in Fig. 8.1(c,d).

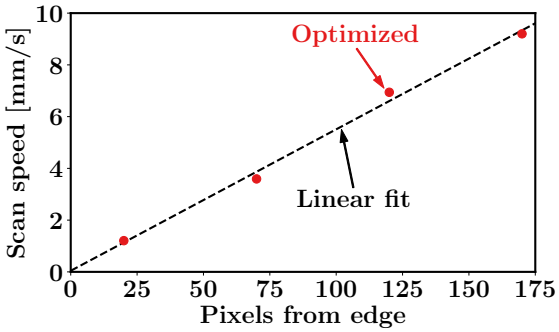

Figure 8.2: Optimized scan speed as a function of distance from the flow cell edge.

Figure 8.2 displays the optimized scan speed as a function of position from the edge where the optimization was performed. The obtained scan speed equals the flow speed at the optimization position. Since the flow cell is relatively wide, the flow speed is approximately linear with depth, which explains why the optimized scan speed increases linearly with the distance from the edge. Besides improving the diffusion coefficient (particle size) estimate, we also obtain the suspension flow speed at the optimization location using scanning DLS-OCT. In a typical measurement configuration of the NanoFlowSizer, the lateral scanning direction is aligned to the flow cell so that the Doppler angle θ is essentially always zero. Therefore, during the optimization process, only the scan speed and orientation (forward or backward) are optimized, not the scan angle. For more complex geometries with unknown alignment, the scan angle can also be included as an additional optimization parameter.

8

Off-wall particle sizing

As Fig. 8.1(a-d) shows, the standard DLS-OCT approach without beam scanning already provides a good estimate of the diffusion coefficient for flowing particle suspensions close to the flow cell edge. Therefore, it may seem that the scanning implementation is unnecessary. However, this is not entirely true. In the process industry, it is sometimes desirable to avoid particle sizing near the edges of the flow cell. This can be due to two reasons: first and foremost, the sample close to the edge has the lowest flow speed and refreshes the slowest. Therefore, in-line measurements cannot be performed as quickly, and the sample near the edge may not represent the actual, up-to-date particle suspension. Second, there might be cases where, due to the wall-drag effect [1] or particle sticking, the diffusion coefficient of particles close to the interface decreases. This effect is less consistent and may only occur under certain conditions. The extent of this reduction depends on the particle shape, type, concentration, size, and OCT resolution [1]. Therefore, a wrongful estimate of the diffusion coefficient near the wall introduces bias in the particle size. Scanning DLS-OCT effectively mitigates this bias by enabling

accurate measurements of the diffusion coefficient away from the edge. This capability ensures more representative and reliable particle sizing in various industrial applications.

Effect of turbulence on particle sizing

Despite the effectiveness of scanning DLS-OCT in mitigating dominant flow decay, the presence of turbulent fluctuations and mixing at high suspension flow speeds poses significant challenges for particle sizing. In turbulent flows, the velocity fluctuates around its mean value, affecting the estimation of the particle diffusion coefficient, even when the average flow speed remains constant. The velocity fluctuations caused by turbulence induce additional particle displacement, which temporally resembles random diffusive motion [2, 3]. Consequently, turbulence leads to an increased mean squared displacement (MSD) and, correspondingly, an elevated effective particle diffusion coefficient [4]. While turbulence does not alter the flow decay rate due to the consistent average flow speed, it does increase diffusive decorrelation, resulting in underestimation of particle size.

Since turbulence-induced fluctuations resemble those caused by diffusion, they cannot be mitigated using scanning DLS-OCT. Further research is needed to calibrate their effect on the diffusion coefficient as a function of particle size (or D_0), Reynolds number, and potentially other parameters such as particle concentration and size polydispersity. Addressing this issue holds promise for enabling particle sizing using DLS-OCT in turbulence-limited flows, presenting an intriguing avenue for future exploration.

8.2.2. Particle sizing using Doppler OCT

Doppler OCT is the gold standard for measuring flow speeds of particle suspensions and is extensively covered in Chapters 3 and 4. Doppler OCT measures the average depth-resolved phase change of the OCT signal, which is directly proportional to the axial velocity of the particle suspension. In a single-scattering regime, the average phase change is independent of particle concentration and size; it is only affected by multiple scattering [5]. Therefore, it is thought that Doppler OCT cannot be used for particle sizing.

Phase changes in Doppler OCT are influenced by particle Brownian motion. As the particle diffusion coefficient increases (or particle size decreases), the distribution of phase changes broadens [6, 7]. Consequently, this broadening leads to an increased uncertainty in the average phase change and in the flow velocity [8–10]. Therefore, the shape of the phase change distribution in Doppler OCT contains information about particle size and polydispersity. The phase change distribution from the complex OCT signal can be calculated using Eqs. (3.17) and (4.32).

Figure 8.3(a-c) shows simulated OCT phase change distributions for the optical parameters of our Thorlabs OCT system using a 36 kHz sampling time. Figure 8.3(a) displays the phase change distribution for monodisperse particles with different radii. The phase change distribution spreads out with decreasing particle size, with more values being wrapped as the particle size decreases (i.e., larger than π). Since smaller particles exhibit a larger diffusion coefficient, this leads to

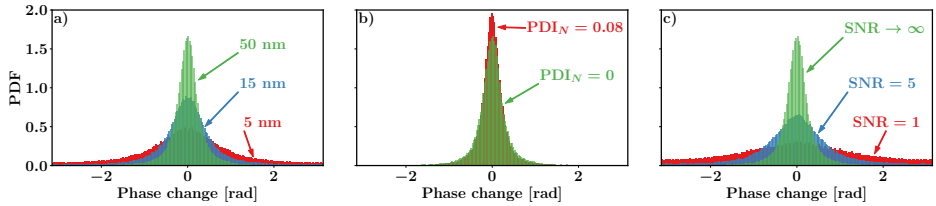

Figure 8.3: Phase change distribution as a function of particle radius, size polydispersity and SNR. (a) Monodisperse particles, SNR → ∞. (b) 50 nm particles, SNR → ∞. (c) 50 nm monodispere particles.

bigger phase changes for the given sampling time. Figure 8.3(b) shows phase change distributions for Gaussian-distributed particle sizes with an average radius of 50 nm and varying number-based particle size polydispersity indices, as described by Eq. (2.19). Increasing particle size polydispersity narrows down the phase change distribution, which is somewhat contradictory to expectations. Figure 8.3(c) presents phase change distributions for 50 nm particles at different SNR values. As the SNR decreases, the distribution spreads out. This is caused by noise, which has a uniform phase-change distribution

The phase change distribution contains information about the particle radius, size polydispersity, and the experimental signal-to-noise ratio. However, multiple parameters can have a similar effects on the distribution, making the determination of one parameter problematic without the knowledge of the others. In addition, it is important to quantify the shape of the distribution, its variance, and other key parameters. This is also challenging, as the distribution tends to change shape for lower SNR and particle size values. Finally, the propagation of the OCT field variance to the variance of the phase change distribution is non-trivial, because Eqs. (3.17) and (4.32) contain ratios of quantities that are centered around zero for non-flowing samples, for which simple uncertainty propagation techniques fail.

Even though we cannot use the phase change distribution directly, we can still utilize Eqs. (3.17) and (4.32) to obtain information about the particle size. For the complex OCT signal $a(t)$, we can express the ratio of the variances of the imaginary and real parts of $a(t) \times a^*(t+\tau)$ using

$$\frac{\sigma^2_{\Im\left(a(t)\times a^*(t+\tau)\right)}}{\sigma^2_{\Re\left(a(t)\times a^*(t+\tau)\right)}} = \frac{1 - A^2 e^{-2Dq^2}}{1 + A^2 e^{-2Dq^2}}, \tag{8.1}$$

where $A = \left(1 + \frac{1}{\mathrm{SNR}}\right)^{-1}$ is the first-order autocorrelation amplitude, D is the particle diffusion coefficient, q is the scattering wavenumber, and τ is the lag time. Equation (8.1) can be rearranged in the form of

$$\left(1 - \frac{\sigma^2_{\Im\left(a(t)\times a^*(t+\tau)\right)}}{\sigma^2_{\Re\left(a(t)\times a^*(t+\tau)\right)}}\right)\left(1 + \frac{\sigma^2_{\Im(a(t)\times a^*(t+\tau))}}{\sigma^2_{\Re\left(a(t)\times a^*(t+\tau)\right)}}\right)^{-1} = A^2 e^{-2Dq^2\tau} = g_2(\tau), \tag{8.2}$$

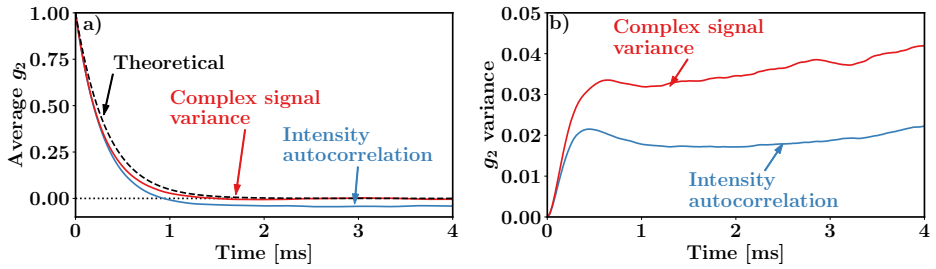

Figure 8.4: Simulations for 50 nm radius particles with a time series length of 512 and a scan rate of 36 kHz. (a) Average $g_2(\tau)$ and (b) variance in $g_2(\tau)$.

which is none other than the second-order normalized autocovariance, $g_2(\tau)$, within the Siegert approximation.

Even though Eq. (8.2) looks identical to $g_2(\tau)$, it is not calculated using the autocorrelation of the mean-subtracted OCT intensity but instead is based on the variances of the complex OCT field. As a result, it does not suffer from the estimation bias from Eq. (6.22) acquired when subtracting the mean from the intensity time series in Eq. (6.2) estimated from the intensity time series itself. Therefore, for shorter intensity time series with higher estimation bias, it could be beneficial to use Eq. (8.2) rather than Eq. (6.2) to calculate $g_2(\tau)$.

Figure 8.4(a,b) shows simulated second-order autocorrelation functions for 50 nm radius particles, calculated using intensity autocorrelation and complex signal variance with Eqs. (6.2) and (8.1), respectively. In this case, the number of temporal sampling points is 512, with an acquisition rate of 36 kHz. Figure 8.4(a) displays the average $g_2(\tau)$ calculated using both methods. Averaging was performed over a large number of realizations to eliminate random errors in $g_2(\tau)$. A constant offset due to estimation bias in $g_2(\tau)$ obtained using intensity autocorrelation is clearly visible, causing the autocorrelation function to dip below the zero line and become negative. This bias is absent in $g_2(\tau)$ calculated using the variance method we propose. However, as mentioned in Chapter 6, shorter time series lengths can also influence the decay rate of the autocorrelation function due to contrast bias [11], which arises from the dependence of speckle contrast on the ensemble size in the autocorrelation. This effect distorts $g_2(\tau)$, as observed in Figure 8.4(a). Autocorrelation functions calculated using both methods are equally affected by contrast bias in the decay rate due to shorter time-series lengths. Consequently, Eq. (8.1) is expected to suffer similarly from contrast bias as Eq. (6.2). Typically, contrast bias is insignificant for long acquisition times in DLS-OCT, but becomes more pronounced for very short time series lengths.

As discussed in Chapter 6, random errors in $g_2(\tau)$ dominate estimation bias for realistic acquisition times and averaging. The random errors are expressed using the variance in $g_2(\tau)$. Figure 8.4(b) shows the variance in $g_2(\tau)$ for both methods. The variance is significantly lower for the standard method of calculating $g_2(\tau)$ using intensity autocorrelation. Therefore, the advantage of the variance model is

evident only for very short time series lengths with higher amounts of averaging, where estimation bias dominates over random errors. Even though such conditions are less realistic in typical particle sizing applications, Eq. (8.2) could be useful in high flow speed scenarios where long acquisition times are not required.

8.2.3. Particle sizing in the multiple scattering regime

Chapter 7 of this work focused on DLS-OCT in the multiple scattering regime. In this case, the autocorrelation decay rate is better described by a sum of several exponentials, where the decay rate of the fastest exponential follows the diffusing-wave spectroscopy (DWS) theory and can be converted to particle size. The contribution of this term becomes dominant with increasing optical path length (OPL). However, at shallow OPL, lower-order scattering modes can dominate and make the estimation of the DWS decay rate problematic, even when using double-exponential models suggested by us.

Particle sizing using spatially offset DLS-OCT

Recently, Untracht et al. [12] demonstrated the possibility of laterally offsetting OCT incident and collection fields to increase the contribution of multiple scattered light at all depths. This approach proved to be effective in enhancing the signal-to-noise ratio at larger depths. The spatial offset can be varied, which in turn affects the ratio of multiple to single scattered light. This approach holds significant promise in the context of particle sizing in the DWS limit. By introducing spatial offset, we can achieve two objectives: first, we can obtain the DWS decay rate more accurately even at lower optical path lengths using the double-exponential fit model discussed in Chapter 7. Second, we may not need to fit the double-exponential model at larger OPL values due to the overwhelming contribution of multiple scattered light, thus simplifying and enhancing the reliability of the fitting process. Spatially offset DLS-OCT can be used to study the transition of the diffusive decay rate from single to multiple scattering in more detail. However, it can only enhance the contribution of multiple scattered light and, therefore, cannot improve particle sizing accuracy in a single scattering regime.

Particle sizing using cross-correlation DLS-OCT

The standard DLS method is limited by multiple scattering and is typically used for low-concentration samples. However, two-color [13, 14] and cross-correlation [15] DLS techniques have been employed to overcome this limitation. Two-color DLS measures particle size by cross-correlating scattered intensity fluctuations at different wavelengths. The obtained correlation function is more independent of multiple scattering and contains only the contribution from single-scattered light. Cross-correlation DLS is similar but uses scattered light detected at two different angles with the same scattering wavenumber q instead of using two different wavelengths. These approaches can also be implemented in DLS-OCT. We can select the signals at different wavenumbers from the OCT spectrum and cross-correlate them to reduce the effect of multiple scattering. Choosing the right spectral separation for two-color DLS-OCT and the optimal scattering angle for maximizing imaging depth in cross-correlation DLS-OCT are promising topics for further research.

Particle sizing using spatiotemporal image correlation OCT

In order to determine particle size using DLS-OCT, we obtain depth-resolved first- or second-order temporal autocorrelation functions. These autocorrelation functions are fitted using models, resulting in a depth-resolved particle diffusion coefficient. Spatial information is not used in the fit; that is, the correlation of scattering signals at different depths is not taken into account. The advantage of this approach is that the fit parameters can be obtained as a function of depth. However, the disadvantage is that any spatial correlation present in the signal is disregarded.

In DLS-OCT, the complex field and intensity scattered from the particle suspension are not only temporally correlated but also spatially correlated. Spatiotemporal image correlation spectroscopy (STICS) has been used to measure particle motion from a series of laser scanning microscopy images [16]. STICS can be readily extended to OCT. The spatial correlation of the OCT signal from moving particles is directly related to the decay of the temporal autocorrelation functions $g_1(\tau)$ and $g_2(\tau)$ caused by flow in the axial direction. The spatial correlation decay rate is equivalent to the temporal decay rate with a certain axial velocity. In this case, the spatial lag parameter $d = nv_z\tau$, where v_z is the particle axial velocity, τ is the lag time, and n is the suspension refractive index. The spatial lag parameter d is the optical path length of a single OCT voxel. For purely diffusive particles without any bulk motion, the two-dimensional spatiotemporal autocorrelation function of the complex field is given by

$$g_{1_{2D}}(d,\tau) = \frac{\langle E(z,t)E^*(z+d,t+\tau)\rangle_{z,t}}{\langle I(z,t)\rangle_t} = Ae^{-Dq^2\tau}e^{-\sigma^2 d^2}e^{i2k_0 d}, \tag{8.3}$$

and of the intensity by

$$g_{2_{2D}}(d,\tau) = A^2 e^{-2Dq^2\tau}e^{-2\sigma^2 d^2}, \tag{8.4}$$

where σ is the wavenumber standard deviation of the Gaussian source spectrum defined in Chapter 3, and k_0 is the source center vacuum wavenumber. The variation of the OCT intensity as a function of depth was neglected in our analysis because it is much slower than the spatial decay in $g_{1_{2D}}$ and $g_{2_{2D}}$.

Figure 8.5(a,b) shows the magnitudes of the first and second-order 2D spatiotemporal correlation functions measured in intralipid 20% using our Thorlabs OCT system. Temporal lag corresponds to the lag time of the standard $g_1(\tau)$ or $g_2(\tau)$, while spatial lag corresponds to the axial separation in optical path length units. To calculate the spatiotemporal correlation function, we need to select the depth (optical path length, OPL) range containing our sample. In our analysis, we selected the OPL range between 0.05 and 0.87 mm. The first point corresponds to the edge of the flow cell, and the last point corresponds to the position where both $g_1(\tau)$ and $g_2(\tau)$ obtained using standard DLS-OCT could be reliably fitted. It is worth noting that the real or imaginary parts of $g_{1_{2D}}$ contain dips below zero which are not visible in the figure because we show the absolute values.

Figure 8.6 displays the diffusion coefficient obtained using standard DLS-OCT and spatiotemporal image correlation OCT. With 2D autocorrelation functions from

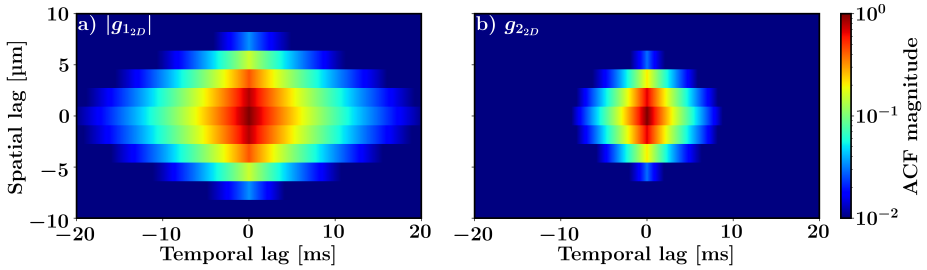

Figure 8.5: 2D spatiotemporal correlation functions, (a) $g_{1_{2D}}$ and (b) $g_{2_{2D}}$, measured in Intralipid 20%.

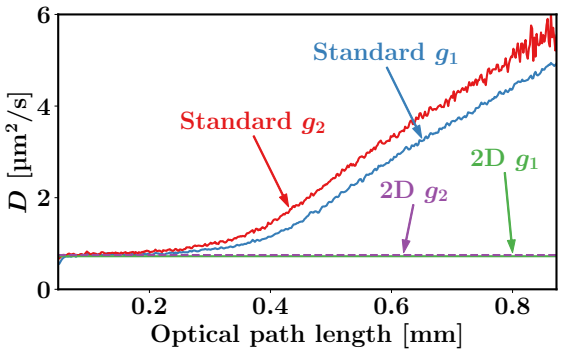

Figure 8.6: Diffusion coefficient of 20% Intralipid obtained using standard DLS-OCT and spatiotemporal image correlation OCT.

8

Eqs. (8.3) and (8.4), we obtain a single diffusion coefficient. In contrast, standard DLS-OCT provides diffusion coefficients as a function of optical path length (OPL). For both $g_1(\tau)$ and $g_2(\tau)$, the diffusion coefficient increases with OPL due to multiple scattering effects [17]. At very low OPL values, it decreases due to the wall-drag effect [1]. Therefore, the measured D coincides with D_0 only over a narrow OPL range, between 0.10-0.19 mm. The diffusion coefficient obtained using spatiotemporal image correlation OCT matches this single scattering D_0 value. Overall, we observe no significant effects of multiple scattering on the results obtained using 2D spatiotemporal correlation functions.

The contribution of multiple scattered light varies with optical path length (OPL), while signal fluctuations due to single scattering remain consistent. Reduction of the diffusion coefficient due to the wall-drag effect occurs primarily at low OPL values. Therefore, when combining data across the entire axial range to obtain the 2D spatiotemporal correlation function, we expect it to reflect characteristics that are not specific to individual axial voxels. Consequently, the 2D correlation function only captures information about free diffusion in a single-scattering regime. This observation aligns with the findings in Fig. 8.6. It could also be the case

that single scattered intensity dominates the total intensity, whereas this may not hold true at all depths for 1D depth-resolved analysis. Furthermore, the difference between using first- or second-order correlation functions is much smaller compared to standard DLS-OCT.

Spatiotemporal image correlation OCT holds promise as a technique for particle sizing. Further research is needed to explore its potential for improving particle sizing in samples with a high degree of multiple scattering or spatially variable diffusion coefficients. The advantage of using spatiotemporal correlation functions lies in their potential resilience to multiple scattering, as they capture fluctuations in scattered light over a broader range of optical path lengths (OPL). While Eqs. (8.3) and (8.4) can be extended to account for flow effects, it remains unclear how varying flow speeds within the chosen OPL range would impact measurements. In standard DLS-OCT measurements, we assume a constant flow speed across axial voxels due to the very small pixel size. However, since our 2D correlation functions encompass the entire OPL range, such assumptions in STICS are valid only under conditions of spatially uniform flow. In typical pharmaceutical or research applications, flow speeds can vary significantly with spatial position. Therefore, the application area of spatiotemporal image correlation OCT under flow conditions may be limited.

8.2.4. Particle sizing using q-dependent DLS-OCT

Chapter 2 presented wavenumber-dependent DLS-OCT collective and self-diffusion measurements conducted using our custom-built backscattering DLS-OCT system, which operates over a broad wavelength range. These measurements are instrumental for estimating particle size in concentrated suspensions. The uncertainty in the obtained size directly correlates with the setup's q-range and acquisition rate. In addition, particle diffusion in concentrated suspensions can be measured using a transmission DLS-OCT system.

Improving acquisition rate and q-range of DLS-OCT

The wavenumber range of a DLS-OCT system hinges on factors like the source spectrum bandwidth, the sensitivity of the detector (typically a spectrometer with camera) across different wavelengths, and the scattering angle, as detailed by Eq. (1.3). In backscattering DLS-OCT, where the scattering angle is set at $180°$, the system achieves its maximum scattering wavenumber q and the maximum wavenumber range over which measurements can be made with a fixed source spectrum. A higher q implies faster decay rates in autocorrelation functions, which in turn sets a lower limit on the measurable particle size, constrained by the spectrometer's sampling time. While extending the sampling rate can enable the detection of smaller particles using the same scattering wavenumber, increasing the spectrometer's acquisition rate across a broad wavelength range poses significant challenges. For instance, obtaining a commercially available spectrometer with a rate faster than 4.5 kHz spanning from 350 to 1000 nm proved unfeasible. Custom design of such spectrometers is challenging particularly due to the requirement of obtaining high spectral resolution over a broad bandwidth.

One strategy to reduce the limitation imposed by the acquisition rate in DLS-OCT is to reduce the scattering angle θ. By lowering θ, the system can mitigate sampling limitations in measuring diffusion of smaller particles due to a reduced q and slower decay rates of autocorrelation functions. However, this adjustment also narrows the achievable q-range. Therefore, finding an optimal scattering angle is crucial; it must balance maintaining a sufficient wavenumber range for accurate q-dependent measurements while ensuring that the scattering wavenumber is low enough to avoid sampling constraints for the specific particle size of interest. Adjusting θ also impacts the scattered intensity, particularly in concentrated suspensions, where scattering anisotropy plays a significant role. Ideally, implementing a variable-angle DLS-OCT setup could offer flexibility in optimizing these parameters, but this approach introduces complexities in system design and alignment. Another potential strategy involves using multiple scattering arms with different angles, though this approach increases setup complexity and requires synchronized spectrometers, which can add to overall costs.

Integrating differential dynamic microscopy with transmission OCT

In Chapter 1, we briefly introduced the technique called differential dynamic microscopy (DDM), which can be used for particle sizing. DDM is a q-dependent technique typically operating in the transmission configuration. It utilizes a 2D camera to capture intensity fluctuations as a function of position, which corresponds to the Fourier pair of the radial scattering wavenumber. However, depending on the experimental setup, alternative configurations may also be employed. The light scattered by particles is detected over a range of scattering angles in the numerical aperture of the objective. The absolute scattering wavenumber, or scattering vector magnitude in DDM, can be expressed as

$$q = \sqrt{q_z^2 + q_r^2} = \frac{4\pi n}{\lambda_0} \sin(\theta/2) \,, \tag{8.5}$$

where q_z is the component of the scattering vector along the optical axis, and q_r is the Fourier pair of the radial position in the intensity image. In transmission DDM, q_z is typically small and close to zero, while θ ranges from zero degrees to the maximum scattering angle within the collection optics, which cannot exceed $90°$. The application of DDM is limited by factors such as sample thickness, concentration, and multiple scattering.

We can overcome the limitations of DDM by combining it with OCT, thereby leveraging the strengths of both techniques to measure the diffusion coefficient of concentrated particle suspensions over a broad q-range, resulting from variations in scattering angles within the objective, while OCT's coherence gating reduces the constraints posed by sample thickness, particle concentration, and multiple scattering. DDM-OCT can be implemented in either the transmission or backscattering configuration to ensure a unique mapping of the radial components of scattering wavenumbers q_r to the absolute scattering wavenumber q. In this case, besides the influence of the objective, q_z is further influenced by the OCT spectral resolution.

In DDM-OCT, resolving the scattered light both spectrally (for OCT) and spatially (for DDM) is essential. This can be achieved using either full-field swept-source OCT or line-scan spectral-domain OCT. The DDM-OCT wavenumber range can be increased both optically and spectrally. Optically, the q-range is increased by enhancing the objective NA, which allows access to higher and lower scattering angles for transmission and backscattering configurations, respectively. Spectrally, the q-range can be expanded by increasing the source spectral bandwidth, which directly influences the range of accessible wavenumbers through Eq. (8.5). Based on Eq. (8.5) and the possible scattering angles, we found that it is easier and more effective to extend the wavenumber range by increasing the NA for transmission DDM-OCT, while for the backscattering configuration, it is more efficient to extend it spectrally. We concluded that DDM-OCT in the backscattering configuration offers no significant improvement over DLS-OCT in enhancing the q-range. However, in the transmission configuration, DDM-OCT can be highly advantageous. In this case, a narrow bandwidth source is sufficient, since the q-range is mainly determined by the objective NA. Additionally, in the transmission configuration, scattering wavenumbers are smaller, which alleviates sampling time and detector speed limitations. Therefore, investigating DDM-OCT in the transmission configuration can be particularly interesting for particle sizing in concentrated suspensions due to reduced sampling limitations, simpler optics from using a relatively narrow bandwidth source, and access to a large q-range.

8.3. Outlook on number-fluctuation DLS-OCT

Incorporating number fluctuations into the second-order normalized autocovariance function opens up additional possibilities beyond standard DLS-OCT. With number-fluctuation DLS-OCT, we can measure 2D flow fields of particle suspensions below the particle diffusion limits. This technique also enables the measurement of particle concentrations in dilute particle suspensions. Further research using number fluctuations presents more potential avenues for exploration.

8.3.1. Improving 2D flow imaging with faster B-scan rates

Number-fluctuation DLS-OCT can be used to simultaneously measure 2D flow profiles of low flow speeds by analyzing subsequent B-scans. Chapters 4 and 5 demonstrate the implementation and applications of number-fluctuation DLS-OCT for characterizing flow fields below the diffusion limit, which are impossible to measure using standard DLS-OCT or Doppler OCT techniques. However, even at low flow velocities, number-fluctuation DLS-OCT is constrained by the limited sampling rate of B-scans. This increases measurement uncertainty and limits the maximum velocities the technique can accurately measure. For our scanning DLS-OCT system, where the beam physically moves to acquire B-scans, the 2D acquisition rate is 45 Hz with 100 A-scans per B-scan and 25 Hz with 200 A-scans per B-scan. Increasing the number of A-scans within a B-scan reduces the scan rate but enhances spatial resolution.

The OCT B-scan acquisition rate can be significantly improved by implementing

line-scan spectral-domain DLS-OCT. In such a setup, a light sheet is focused over a line of interest using cylindrical lenses. The scattered light is detected using a fast 2D camera, where the light is spectrally dispersed over one dimension of the camera, while it is spatially imaged using another dimension [18]. In this case, the B-scan acquisition rate is limited only by the camera frame rate. For advanced 2D cameras, sampling rates can be on the order of several kHz or higher. This improvement will likely eliminate all sampling limitations for 2D imaging of sub-diffusion flow speeds. For very fast 2D cameras, one can also implement full-field swept-source OCT for 3D flow imaging. However, compared to standard scanning OCT systems, both line-scan and full-field OCT setups incur significantly higher setup complexity and costs.

8.3.2. Beam shape characterization in scattering media

For quantitative flow speed measurements in dilute particle suspensions, as described in Chapters 4, 5, and 6, the beam shape needs to be determined (calibrated). Also the beam shape is required for intensity normalization, as shown in Chapter 7, to determine the sample attenuation coefficient. When operating our DLS-OCT system in B-scan mode with a carefully chosen scan speed, we can accurately determine the beam shape in the sample as a function of depth using number fluctuations. In the context of this work, the obtained Gaussian beam shape was only a calibration parameter and was not studied separately.

However, number-fluctuation DLS-OCT can directly measure the beam shape $w(z)$ in the scattering medium. This is of particular interest for OCT applications involving attenuation coefficient estimation, particle sizing, and super-resolution techniques [19]. In OCT, the beam shape or point-spread function is measured in air, or in water, against a moving reflector [20], and the results (beam waist at focus, Rayleigh length) are used to estimate the beam shape in any arbitrary sample. In most cases the beam shape can be approximated as a Gaussian beam of which the beam waist is parameterized as

$$w(z) = w_0 \sqrt{1 + \frac{(z - z_0)^2}{\alpha \cdot z_R^2}}, \tag{8.6}$$

where w_0 is the beam waist at focus, z_0 is the focus position, z is the distance from focus, $z_R = \frac{\pi w_0^2 n}{\lambda}$ is the Rayleigh length, n is the suspension refractive index, λ is the incident light wavelength in vacuum, and α is a scaling factor of the Rayleigh length. Leeuwen et al. [20] determined that in OCT, $\alpha = 1$ for specular reflections and $\alpha = 2$ for diffuse reflections. Reflections from particles in the suspension have been considered as diffuse reflections, for which $\alpha = 2$ has been employed in attenuation coefficient measurements [20, 21]. However, recently, Buist et al. [22] claimed that $\alpha = 1$ irrespective of the sample or object used. This contradicts established practices in OCT and requires further verification.

Number fluctuation DLS-OCT enables the determination of the scaling factor α in different samples. In dilute polystyrene and polymer particle suspensions from

Chapters 6 and 7, respectively, we obtained $\alpha = 1.5$. For dilute Intralipid measurements from Chapter 7, we found $\alpha = 1.9$, which is much closer to 2. Factors such as focus depth [22], particle size, polydispersity, and possibly concentration effects are suspected to influence α. The focus depth was virtually identical in both samples from Chapter 7, suggesting this was not a significant factor. Our polystyrene and polymer particles were monodisperse with a radius of around 250 nm, while Intralipid particles were quite polydisperse with an average radius of about 150 nm. In all cases, the beam shape was determined in very dilute samples. Therefore, it is intriguing to explore why α varies among these samples. Additionally, studying the beam shape in more concentrated suspensions using number fluctuations by seeding them with a low number of large particles could provide further insights. Further research in this field using number-fluctuation DLS-OCT could overcome current measurement limitations, clarify the OCT beam shape in scattering media, and establish the scaling factor for the Rayleigh length.

8.3.3. Effects of particle size polydispersity

Chapters 4 and 6 detail the dependence of $g_2(\tau)$ on the average number of particles in the scattering volume, $\langle N \rangle$. As the number of particles in the scattering volume decreases, the magnitude of the number-fluctuation term in $g_2(\tau)$ increases. Notably, the magnitude and decay rate of the number-fluctuation term are independent of the particle size and its polydispersity. However, we suspect that the magnitude of the number-fluctuation term may actually depend on the particle size polydispersity. The equations provided in Chapters 4 and 6 that relate the magnitude of the number-fluctuation term to $\langle N \rangle$ are valid for monodisperse particle suspensions. Therefore, it would be interesting to investigate whether particle size polydispersity affects the magnitude of the number-fluctuation term.

Figure 8.7 shows the simulated number-fluctuation term of $g_2(\tau)$ for monodisperse and polydisperse particle suspensions. The simulation parameters include an OCT scan rate of 5.5 kHz, a time series length of 32768 time steps, a particle

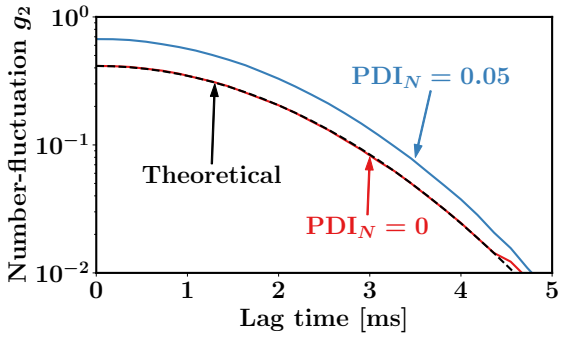

Figure 8.7: Number-fluctuation part of the normalized second-order autocovariance function simulated for monodisperse and polydisperse samples.

velocity of 1.8 mm/s, and $\langle N \rangle = 1$. The polydisperse particles have a Gaussian number-based size distribution with $\mathrm{PDI}_N = 0.05$. As expected, the simulation for monodisperse particles matches the theoretical predictions from Chapters 4 and 6. However, the magnitude of the number-fluctuation term of $g_2(\tau)$ is considerably larger for the polydisperse particle suspension. It appears that as polydispersity increases, the effective $\langle N \rangle$ decreases, resulting in an increased magnitude of the number-fluctuation term in $g_2(\tau)$. This could be caused by the fact that with increasing size polydispersity the intensity scattered by larger particles dominates the scattering process. Consequently, the effective number of particles is reduced because the intensity scattered by smaller particles is essentially undetected. Therefore, developing new models to account for particle-size polydispersity in the magnitude of the number-fluctuation term in $g_2(\tau)$ is an interesting future research direction.

References

[1] K. Ishii, T. Iwai, and H. Xia, *Hydrodynamic measurement of Brownian particles at a liquid-solid interface by lowcoherence dynamic light scattering,* Optics Express **18**, 7390 (2010).

[2] H. Bereovici, P. Constantin, C. Foias, and O. P. Manley, *Exponential decay of the power spectrum of turbulence,* Journal of Statistical Physics **80**, 579–602 (1995).

[3] P. J. W. Roberts and D. R. Webster, *Turbulent diffusion,* in *Environmental Fluid Mechanics Theories and Application*, edited by H. H. Shen, A. H. Cheng, K. Wang, M. H. Teng, and C. C. K. Liu (ASCE, 2002).

[4] P. Lesaffre, M. Gerin, and P. Hennebelle, *Effects of turbulent diffusion on the chemistry of diffuse clouds,* Astronomy & Astrophysics **469**, 949–961 (2007).

[5] J. Kalkman, A. V. Bykov, D. J. Faber, and T. G. van Leeuwen, *Multiple and dependent scattering effects in Doppler optical coherence tomography,* Optics Express **18**, 3833 (2010).

[6] B. J. Berne and R. Pecora, *Dynamic Light Scattering* (Dover Publications, 2000).

[7] C. S. Johnson and D. A. Gabriel, *Laser Light Scattering* (Dover Publications, 1994).

[8] S. Yazdanfar, C. Yang, M. V. Sarunic, and J. A. Izatt, *Frequency estimation precision in Doppler optical coherence tomography using the Cramer-Rao lower bound,* Optics Express **13**, 410 (2005).

[9] D. A. Boas, K. K. Bizheva, and A. M. Siegel, *Using dynamic low-coherence interferometry to image Brownian motion within highly scattering media,* Optics Epxress **23**, 319 (1997).

[10] C. S. Kim, W. Qi, J. Zhang, Y. J. Kwon, and Z. Chen, *Imaging and quantifying Brownian motion of micro- and nanoparticles using phase-resolved Doppler variance optical coherence tomography,* Journal of Biomedical Optics **18**, 030504 (2013).

[11] N. Uribe-Patarroyo, A. L. Post, S. Ruiz-Lopera, D. J. Faber, and B. E. Bouma, *Noise and bias in optical coherence tomography intensity signal decorrelation,* OSA Continuum **3**, 709 (2020).

[12] G. R. Untracht, M. Chen, P. Wijesinghe, J. Mas, H. T. Yura, D. Marti, P. E. Andersen, and K. Dholakia, *Spatially offset optical coherence tomography: Leveraging multiple scattering for high-contrast imaging at depth in turbid media,* Science Advances **9**, 1 (2023).

[13] P. N. Segrè and P. N. Pusey, *Scaling of the dynamic scattering function of concentrated colloidal suspensions,* Physical Review Letters **77**, 771 (1996).

[14] P. N. Segrè and P. N. Pusey, *Dynamics and scaling in hard-sphere colloidal suspensions,* Physica A **235**, 9 (1997).

[15] F. Westermeier, B. Fischer, W. Roseker, G. Grübel, G. Nägele, and M. Heinen, *Structure and short-time dynamics in concentrated suspensions of charged colloids,* The Journal of Chemical Physics **137**, 114504 (2012).

[16] B. Hebert, S. Costantino, and P. W. Wiseman, *Spatiotemporal image correlation spectroscopy (STICS) theory, verification, and application to protein velocity mapping in living CHO cells,* Biophysical Journal **88**, 3601 (2005).

[17] K. K. Bizheva, A. M. Siegel, and D. A. Boas, *Path-length-resolved dynamic light scattering in highly scattering random media: The transition to diffusing wave spectroscopy,* Physical Review E **58**, 7664 (1998).

[18] L. Han, B. Tan, L. Schmetterer, and K. Bizheva, *Localized transverse flow measurement with dynamic light scattering line-scan OCT,* Biomedical Optics Express **14**, 883 (2023).

[19] J. de Wit, G. O. Glentis, and J. Kalkman, *Computational 3D resolution enhancement for optical coherence tomography with a narrowband visible light source,* Biomedical Optics Express **14**, 3532 (2023).

[20] T. G. van Leeuwen, D. J. Faber, and M. C. Aalders, *Measurement of the axial point spread function in scattering media using single-mode fiber-based optical coherence tomography,* IEEE JOURNAL OF SELECTED TOPICS IN QUANTUM ELECTRONICS **9**, 227 (2003).

[21] B. Ghafaryasl, K. A. Vermeer, J. Kalkman, T. Callewaert, J. F. de Boer, and L. J. van Vliiet, *Attenuation coefficient estimation in Fourier-domain OCT of multi-layered phantoms,* Biomedical Optics Express **12**, 2744 (2021).

[22] G. Buist, M. Debiasi, A. Amelink, and J. F. de Boer, *Theoretical and experimental determination of the confocal function of OCT systems for accurate calculation of sample optical properties,* Biomedical Optics Express **15**, 2937 (2024).

Acknowledgements

My PhD research journey would not have been possible without the unwavering support of my friends, colleagues, and especially my family. They have stood by me, believing in me even during moments when I doubted myself. Their encouragement and steadfast belief in my abilities have been instrumental in reaching this milestone. I am deeply grateful to everyone who has been part of this journey.

First, I would like to thank my supervisor and promoter, Jeroen. Striking a balance between providing sufficient support and freedom to a PhD candidate is challenging, but you managed it remarkably well. Your approach will serve as an exemplary model for me. I had complete freedom to pursue new ideas, yet I could always rely on your knowledge and experience, which greatly boosted my confidence in myself and my work. I am very grateful for your support and guidance. I want to thank my promoter, Bernd. Although we did not meet daily, your concise feedback and advice were crucial, playing a pivotal role in one of our publications. Despite both our national football teams losing to Spain in the Euro 2024 finals, I am glad they did not face each other, which might have affected our relationship.

I extend my sincere gratitude to our colleagues and supporters at InProcess-LSP. Rut, your feedback and guidance have been invaluable and inspiring, particularly in deepening my understanding of colloids and particle sizing. It was a pleasure discussing new findings with you, which has significantly enriched my knowledge. Michiel, your pivotal support and collaborative efforts on a technical level have greatly contributed to my progress, especially through our work in implementing new ideas and findings in Oss. Marko, Nick, Michiel Damen, Carl, Ali, Remy, and Walter, thank you for your resources, enthusiasm, and constant support. The welcoming environment at InProcess has profoundly influenced my motivation.

I would like to thank NWO for supporting this project. Kirsten, thank you for organizing user meetings and providing us with the latest information about NWO grants and opportunities. Input and feedback from user committee members were crucial for the success of our research. Alfons, Panos (Panagiotis), Marcel, and Fried, thank you for participating in user meetings and providing direct yet invaluable comments and feedback. I would especially like to mention Panos for always being present in meetings and giving motivating feedback. Alfons, I would like to thank you and Kelly for your support in performing reference measurements.

One man, no man—it would have been impossible to carry out my research without the support of coworkers, fellow PhDs, postdocs, BEP, and MEP students. Jos, Peter, Qingru, Wenxiu, Alim, Huangcheng, Isabel, Linda, Enya, Sobhan, Hamed, Vahid, Loes, Valeri, Spozmai, Yutong, and Agis, thank you for creating a friendly environment where I always felt welcome. It was always a pleasure to come to the office, have strictly non-work-related conversations, and become an expert in new fields over lunch. Jos, I appreciate the jump start you gave me on OCT in the early

stages of my PhD. This was crucial during the COVID period when there were few people in the office, and it increased the efficiency of my work going forward.

Annelies and Angela, thank you for your invaluable assistance in organizing wonderful events and handling practical matters for our department, which greatly contributed to my well-being and motivation. Ron, your support in designing custom mounts and fixtures for my optical setup was essential; without it, my work would have required significantly more time and resources. Ronald, your help with ICT-related issues, combined with your humor, brought a lively atmosphere to our department. Miriam, I deeply appreciate your feedback and helpful conversations. Sjoerd, thank you for your guidance, both personally and for the entire department, during my time at TU Delft. Additionally, my gratitude extends to the cleaners and other staff who maintained our building, creating a pleasant working environment. To everyone else who has been part of my journey at TU Delft, even if I haven't mentioned you individually, your contributions are deeply appreciated. Thank you all for making my experience at TU Delft truly memorable and rewarding.

I would like to thank my friends outside TU Delft for their unwavering support throughout this journey. Although it's difficult to see many of them regularly because they live abroad, their encouragement has meant a lot to me. While I cannot name everyone individually, their support has been invaluable.

I am deeply blessed and lucky to have my mom, Khatuna, in my life. I wouldn't have accomplished this PhD without her unwavering support and the many sacrifices she made for my education. She has always put me first, ensuring I had the best opportunities. Mom, you are the epitome of what a parent should be. Thank you for everything. I would also like to thank my brother David, my sister Nino, her husband Nika, my uncle David, his wife Olga, my aunt Leila, my mother-in-law Irma, and her mother Tsira for their unwavering support. Your encouragement and assistance have been invaluable throughout this journey. I would like to dedicate this work to the memory of my father, David, whose love, support, and encouragement have always been with me. Though he is no longer with us, his guidance and values continue to inspire me every day. I am deeply grateful for everything he did for me. I also dedicate this work to the memory of my grandfather, also David, whose wisdom and support have been a constant source of inspiration. His legacy continues to influence my life and work.

Tata, my beautiful wife and the love of my life, I am incredibly fortunate to have you by my side. Your unwavering trust and belief in me resonate constantly in my mind, giving me an unfair advantage. My love for you grows deeper with each passing day. Together, we have achieved so much, especially after moving to the Netherlands during challenging times, and my PhD research stands as a significant milestone in our journey together. David, my son, whom I am immensely proud of, has been a constant source of motivation. I strive to set a positive example for him, and I believe my PhD journey will ignite his passion for education. Being with you both has helped me realize what truly matters in this life, and that is you.

Finally, and most importantly, I want to thank God for giving me the strength and determination to navigate through my PhD research, and for blessing me with timely luck. I am deeply grateful for His guidance throughout this journey.

Curriculum Vitæ

Konstantine CHEISHVILI

21-04-1993 Born in Tbilisi, Georgia.

Education

2011-2014 Bachelor of Science in Physics
Jacobs University Bremen

2014-2016 Master of Science in Aerospace Engineering
Delft University of Technology
Thesis: Development and validation of an end-to-end simulator for frequency scanning filtered Rayleigh scattering techniques
Supervisors: dr. G. Stockhausen and dr. F.F.J. Schrijer

2020-2024 Doctor of Philosophy in Applied Physics
Delft University of Technology
Thesis: Advancements in dynamic light scattering optical coherence tomography particle sizing and flowmetry
Promotors: dr. J. Kalkman and prof. dr. B. Rieger

List of Publications

5. Devrim Tugberk, **Konstantine Cheishvili**, Peter Speets, William Quirós-Solano, Anish Ballal, Nikolas Gaio, and Jeroen Kalkman, *Multi-modal optical coherence tomography flowmetry of organ-on-chip devices*, manuscript has been submitted for publication.

4. **Konstantine Cheishvili**, Rut Besseling, Michiel Hermes, and Jeroen Kalkman, *Wavenumber-dependent dynamic light scattering optical coherence tomography measurements of collective and self-diffusion*, Optics Express 32(11), 19963-19983 (2024), doi: 10.1364/OE.521702.

3. **Konstantine Cheishvili**, Bernd Rieger, and Jeroen Kalkman, *Precision and bias in dynamic light scattering optical coherence tomography measurements of diffusion and flow*, Biomedical Optics Express 15(2), 1288-1310 (2024), doi: 10.1364/BOE.505847.

2. **Konstantine Cheishvili** and Jeroen Kalkman, *Sub-diffusion flow velocimetry with number fluctuation optical coherence tomography*, Optics Express 31(3), 3755-3773 (2023), doi: 10.1364/OE.474279.

1. **Konstantine Cheishvili** and Jeroen Kalkman, *Scanning dynamic light scattering optical coherence tomography for measurement of high omnidirectional flow velocities*, Optics Express 30(13), 23382-23397 (2022), doi: 10.1364/OE.456139.

TU Delft
ISBN 978-94-6366-995-5